HABILITATION A DIRIGER DES RECHERCHES EN SCIENCES

Université Paris VII - Denis Diderot

Quelques écoulements de petites échelles dans le noyau liquide terrestre

Emmanuel Dormy

Soutenue le 18 novembre 2002, devant le jury composé de Messieurs

Jean-Louis LE MOUËL	Directeur,
Claude JAUPART	Rapporteur interne,
Stéphane FAUVE	Rapporteur externe,
Keith MOFFATT	Rapporteur externe,
Claude BASDEVANT	Examinateur,
Henri-Claude NATAF	Examinateur.

Table des matières

I Curriculum Vitae **3**

II Activités d'encadrement **5**

III Résumé **7**

IV Exposé synthétique **9**

1 Etudes laminaires **9**
1.1 Couches limites 9
1.1.1 Couche d'Ekman 9
1.1.2 Couche de Hartmann 10
1.1.3 Couche d'Ekman-Hartmann 10
1.1.4 Singularités équatoriales 11
1.2 Couches de cisaillement 15
1.2.1 Couche de Stewartson 15
1.2.2 Couche en super-rotation 17

2 Etudes non-lineaires **18**
2.1 Stabilité non-linéaire de la couche d'Ekman-Hartmann 18
2.2 Première instabilité de la couche d'Ekman-Hartmann 22

V Perspectives **26**

VI Liste des travaux et publications **28**

VII Publications sur cinq ans **29**

Earth and Planetary Science Letters, 160-1-2, *15-30*, **1998.** **30**

Nonlinearity, 12, *181-199*, **1999.** **46**

Journal of Computational Physics, 151, *676-683*, **1999.** **65**

Geochemistry, Geophysics and Geosystems, 1, *62*, **2000.** **73**

Physics of the Earth and Planetary Interiors, 124-3-4, *283-294*, **2001.** **115**

Physics of the Earth and Planetary Interiors, 128-1-4, *25-34*, **2001.** **127**

Journal of Fluid Mechanics, 452, *263-291*, **2002.** **137**

Première partie

Curriculum Vitae

Emmanuel Dormy

Expérience

Oct. 1999	**Chargé de Recherche** (1ère classe) au Centre National de la Recherche Scientifique, dans l'U.M.R. 7577 de l'Institut de Physique du Globe de Paris.
1999	Recherches post-Doctorales, au service d'Astrophysique (DAPNIA) du C.E.A. avec Tahar Amari.
1997-1998	Recherches post-Doctorales à l'University of California Los Angeles (U.C.L.A.), avec le professeur Paul H. Roberts.
Nov. 1997	**Doctorat** soutenu avec la mention très honorable avec félicitations, à l'Institut de Physique du Globe de Paris sur la *Modélisation numérique de la dynamo terrestre*. Directeur de thèse : Dominique Jault.
1995-1997	Monitorat de l'Enseignement Supérieur au Département de Mathématiques du Palais de la Découverte. Ecriture et réalisation d'un cycle de conférences grand public sur l'analyse numérique.
Juin 1994	**D.E.A.** de Mathématiques, option Mathématiques Appliquées, avec mention, à l'Université de Nice Sophia-Antipolis.
	Ingénieur de l'Ecole Supérieure en Sciences Informatiques de l'Université de Nice Sophia-Antipolis, option Calcul Scientifique.
1994	Mise au point d'un modèle hiérarchique, en arbre binaire, pour l'étude statistique de la turbulence développée. Stage de trois mois, effectué sous la direction de Claude Basdevant et Peter Frick, au Laboratoire de Météorologie Dynamique à l'Ecole Normale Supérieure de Paris.
1993	Mise au point d'une méthode de type Volumes Finis utilisant des grilles alternées, pour l'étude de la propagation d'ondes élastiques, puis simulations sur *Connection Machine 5*. Stage de quatre mois au département de Sismologie de l'I.P.G.P. sous la direction d'Albert Tarantola.

Communications

London Mathematical Society Symposium , août 2002, Durham, U.K.
Geophysical Fluid Dynamics Program, juillet 2002, Woods Hole, U.S.A.
European Geophysical Society, avril 2002, Nice, France.
American Geophysical Union, mai 2001, Boston, U.S.A.
European Geophysical Society, mars 2001, Nice, France.
Study of the Earth Deep Interior, juillet 2000, Exeter, G.-B.
American Geophysical Union, décembre 1999, San Francisco, U.S.A.
Int. Assoc. of Geomagnetism and Aeronomy, juillet 1999, Birmingham, G.-B.
American Geophysical Union, décembre 1998, San Francisco, U.S.A.
Society for Industrial and Applied Mathematics, juillet 1998, Toronto, Canada.
American Geophysical Union, décembre 1997, San Francisco, U.S.A.
Int. Association of Geomagnetism and Aeronomy, août 1997, Uppsala, Suède.
European Union of Geosciences, EUG 9, mars 1997, Strasbourg, France.
21st Annual Conference on Mathematical Geophysics, juin 1996, Santa Fe, U.S.A.

Autres Activités & Distinctions

2002 Obtention du rattachement de mon laboratoire au réseau *Marie Curie* de l'Union Européenne (*Marie Curie Training Site*). Responsable du programme ainsi négocié.

2001-2003 Co-lauréat avec Emmanuel Grenier (U.M.P.A., E.N.S.-Lyon) de l'ACI Jeunes Chercheurs "Aspects mathématiques de la Géodynamo".

2000-2002 Trésorier de l'UMR-7577 (C.N.R.S.).

2000 Lauréat du *Doornbos Memorial Prize*, attribué par le commité S.E.D.I. (**S**tudy of the **E**arth's **D**eep **I**nterior) de l'*International Union of Geodesy and Geophysics*.

1998 Réalisation d'un programme de référence (*Benchmark*) pour la prospective en calcul vectoriel de l'I.D.R.I.S. (Institut du Développement et des Ressources en Informatique Scientifique - C.N.R.S.).

1997 Lauréat de la bourse Lavoisier du Ministère des Affaires Etrangères.

1996-1997 Développement, puis mise à jour (*Webmaster*) du serveur "web" de l'European Union of Geosciences (EUG) (`http://eost.u-strasbg.fr/EUG/`).

Deuxième partie
Activités d'encadrement

Encadrement du Stage de DEA de Vincent Morin
DEA Dynamique des Fluides et Transferts
Cohabilitation entre les Universités de Paris-Sud (Paris XI), P. et M. Curie (Paris VI), D. Diderot (Paris VII), l'Ecole Polytechnique, l'Ecole Supérieure de Physique et de Chimie Industrielles de Paris.
4 mars 2002 - 28 juin 2002

Nous avons développé durant ce stage une approche introduite par Philippe Cardin et Julien Aubert (L.G.I.T., Grenoble) à deux dimensions pour la convection dans une sphère en rotation rapide. L'originalité de notre travail a consisté à appliquer cette approche pour la convection près du seuil. Nous avons pu explorer des valeurs du nombre d'Ekman inaccessibles en trois dimensions, tant dans le domaine linéaire que dans le domaine non-linéaire. Ces nouveaux résultats ont permis de mettre à jour de nouvelles difficultés numériques, comme celle liée à une très grande vitesse de phase ω (supérieure à 10^5) qui gène la convergence numérique. En effet les études numériques précédentes n'avaient pas pu atteindre de telles valeurs du nombre d'Ekman et n'avaient donc pas été confrontées à ce problème. Aucune bifurcation sous-critique n'a été observée, mais des oscillations périodiques en temps de l'énergie, inattendues aussi près du seuil, viennent mettre en péril l'existence même de celle-ci. Ces oscillations n'étaient pas prévues par la théorie et l'impact de leur existence, sur la possibilité d'obtenir une courbe de bifurcation sous-critique, reste à déterminer. Nous allons poursuivre ce travail en essayant d'explorer de nouvelles valeurs (encore plus petites) du nombre d'Ekman, et d'effectuer un échantillonnage plus précis en nombre de Rayleigh près du seuil, un article est en préparation. Vincent Morin va poursuivre en thèse à l'I.P.G.P.

Encadrement du Stage de DEA de Anis Bsaissa
DEA Méthodes Numériques pour les Modèles des Milieux Continus
Ecole Normale Supérieure de Cachan.
17 mai 2002 - fin septembre 2002.

Pour pouvoir étudier numériquement le problème de la dynamo cinématique dans la sphère, on utilise généralement l'approche spectrale. L'usage d'un champ de vitesse discontinu, demande de pouvoir résoudre ces quations avec une méthode de type volumes finis. Cette approche soulève au moins deux questions majeures : la construction d'un schéma permettant de conserver $\nabla \cdot B = 0$ pour tout temps (ce qui n'est pas trivial lorsque l'on discrétise les équations) et la construction de conditions aux limites propres pour la raccordement à un champ potentiel.

Ce stage a intégré une partie pratique (réalisation d'un mailleur et résolution par volumes finis d'une équation parabolique scalaire) et une réflexion théorique sur l'implémentation des conditions aux limites. Il est actuellement en fin de rédaction.

Enseignement

2000-2001
DEA de Géophysique Interne
Institut de Physique du Globe de Paris
3h de cours : “Introduction à la Magnétohydrodynamique”.

2001-2002
DEA de Géophysique Interne
Institut de Physique du Globe de Paris
6h de cours : “Dynamique des Fluides en rotation”.

DEA de Mathématiques (MN2MC)
Ecole Normale Supérieure de Cachan
10h de cours : “Fluides en rotation et magnétohydrodynamique”.

2002-2003 (année en cours)
DEA de Géophysique Interne
Institut de Physique du Globe de Paris
6h de cours : “Dynamique des Fluides en rotation”.

DEA de Mathématiques (MN2MC)
Ecole Normale Supérieure de Cachan
10h de cours : “Fluides en rotation et magnétohydrodynamique”.

Cours de l’Ecole Doctorale de Sciences de la Terre
Université de Paris VII / Institut de Physique du Globe de Paris
10h de cours : “Origine du champ magnétique terrestre”.

Troisième partie

Résumé

De nombreux modèles numériques de dynamo ont récemment été proposés. Ces modèles concernent des régimes de paramètres extrêmement éloignés de ce que l'on connaît des caractéristiques du noyau liquide terrestre. Utilisant des approximations diverses, ils donnent des résultats souvent extrêmement différents entre eux bien qu'ils semblent produire, en surface, des champs magnétiques comparables à celui de notre planète. Il faut donc travailler à la réalisation de modèles numériques plus proches des équilibres significatifs de la Terre.

Le noyau liquide terrestre est caractérisé par une très faible viscosité et un équilibre dominant entre deux forces majeures : les forces magnétiques (force de Laplace) et les effets de la rotation (force de Coriolis). Mon objectif est de parvenir à la description de l'action dynamo (génération auto-excitée de champ magnétique) pour cet équilibre. Les modèles actuellement disponibles souffrent tous d'une valeur très largement surestimée de la viscosité. Il a été montré (Roberts, Academic Press, 1978) que dans le régime asymptotique des faibles viscosités, la séquence de bifurcation lorsque le paramètre de contrôle (le nombre de Rayleigh) croît est décrite par trois branches successives. La première bifurcation est naturellement la bifurcation convective (sans champ magnétique), cette bifurcation serait sous-critique (Soward, Geophys. Astrophys. Fluid Dyn., 9, 1977). Si le nombre de Rayleigh est encore augmenté les mouvements deviennent assez vigoureux pour entretenir un champ magnétique (bifurcation dynamo). Ce champ est alors faible, c'est-à-dire que son intensité est fixée par les forces visqueuses. Si le nombre de Rayleigh est encore suffisamment augmenté cette branche disparaît et la solution dynamo "saute" via une croissance rapide du champ ("runnaway growth") sur une branche à champ fort. Cette branche est caractérisée par un équilibre magnétostrophique et correspondrait au mécanisme en jeu dans le noyau de notre planète. La solution sur cette branche doit différer significativement de celle sur la branche à champ faible. Ainsi, une fois sur cette branche, l'action dynamo peut être maintenue même si le nombre de Rayleigh est diminué en dessous de sa première valeur critique (correspondant à l'instabilité convective). Ce scénario théorique n'a bien sur de sens que si la viscosité est très faible (quasiment négligeable) et il n'a jamais pu être vérifié sur les études numériques. Fort de ces considérations théoriques, mon objectif est de décrire l'action dynamo dans le régime magnétostrophique applicable au problème géophysique. L'approche utilisée consiste à étudier des problèmes de complexité croissante en s'assurant à chaque étape que le comportement asymptotique à été atteint.

Nous avons mis en évidence (voir Dormy, Jault, Cardin, 1998) l'existence d'une nouvelle structure correspondant à une couche de cisaillement en super-rotation. Nous avons depuis obtenu avec le professeur Andrew Soward (Département de Mathématiques, Université d'Exeter, Grande-Bretagne) la description mathématique de ce nouvel équilibre "magnéto-visqueux" (Dormy, Jault, Soward, 2001). L'étude asymptotique a mené à un système couplé d'équations différentielles (à deux dimensions) qui n'a pas pu être résolu analytiquement. La résolution numérique des équations du système discret correspondant a été obtenue (sur le Cray du C.C.R. Jussieu). L'accord avec les simulations est à présent excellent.

Devant la récente abondance des modèles numériques de dynamos publiés (voir Dormy et al. 2000), le professeur Ulrich Christensen de l'Université de Göttingen en Allemagne a proposé de coordonner un "benchmark" international autour de cas tests afin de vérifier la validité des différents codes existants. Les chercheurs français sur ce domaine (à Paris et à Grenoble) n'avaient pas souhaité présenter

de modèles numériques de géodynamo (essentiellement car nous pensons, pour les raisons exposées ci-dessus, que ces régimes de paramètres ne sont pas appropriées à l'étude de la dynamo terrestre). Nous avons cependant voulu saisir cette occasion de valider notre code sphérique. Les modifications nécessaires ont donc été apportées au programme avec l'aide de Julien Aubert (qui a effectué sa thèse à Grenoble). Nous avons reproduit avec succès les résultats demandés pour ce Benchmark (Christensen et al. 2001).

L'interaction avec les observations paléomagnétiques, archéomagnétiques et géomagnétiques est très importante pour l'étude de ces problèmes. Les connaissances sur le champ magnétique terrestre et sa variabilité temporelle ont considérablement progressé ces dernières années. J'ai efectué avec Jean-Pierre Valet et Vincent Courtillot un travail de revue sur les connaissances observationnelles du champ magnétique terrestre ainsi que sur les modèles numériques existants (Dormy et al., 2000).

La collaboration avec les équipes de mathématiques appliquées françaises (Emmanuel Grenier, à présent à l'U.M.P.A. E.N.S.-Lyon et Benoît Desjardins à présent C.E.A./D.I.F.) se sont renforcées par l'obtention d'une ACI jeunes chercheurs (dont j'assure la co-direction pour la Géophysique avec Emmanuel Grenier pour les Mathématiques). Nos travaux en commun ont donné lieu à deux publications sur les critères de stabilité puis d'instabilité des couches limites à la frontière noyau-manteau. Une troisième étude utilisant les modèles de champ construit sur les observations est en cours. Nos collaborations s'élargissent actuellement aux outils numériques pour la modélisation de la géodynamo.

Quatrième partie

Exposé synthétique

Je présente dans cet exposé synthétique l'aspect de mes recherches concernant les couches limites et couches de cisaillement dans des écoulements fluides en rotation et en magnétohydrodynamique. Cela ne représente qu'une partie de mes recherches (l'intégralité des articles publiés depuis cinq ans est inclue en fin de document), mais permet d'illustrer l'approche utilisée qui repose sur une interaction forte entre les modèles numériques et les études théoriques, menées en collaboration avec des mathématiciens (Pr. Andrew Soward en Grande-Bretagne, Pr. Emmanuel Grenier à Lyon et Dr. Benoît Desjardins à Paris).

1 Etudes laminaires

Je commence cet exposé par la dérivation très classique des couches limites d'Ekman et de Hartmann. Puis je présente la couche mixte Ekman-Hartmann influencée à la fois par la rotation et par le champ magnétique. Enfin j'insisterai sur les singularités introduites par la géométrie sphérique sur ces couches.

1.1 Couches limites

1.1.1 Couche d'Ekman

A la fin du $XIX^{\text{ième}}$ Fridtjof Nansen observe lors d'une expédition polaire que les icebergs dérivent dans l'océan à 90° des vents dominants... Cela mena son étudiant Vagn Ekman à développer une théorie des courants de surface prenant en compte la rotation de la Terre...

Décomposons la vitesse en un écoulement moyen et un correcteur de couche limite $\mathbf{u} = \mathbf{U}_o + \mathbf{u}'$. Par commodité, on peut introduire la notation complexe $\mathcal{V} = u'_x + \mathrm{i}\, u'_y$ (où z est la direction normale au bord). En négligeant les variations horizontales (tangentes au bord) devant les variations verticales (normales) et faisant l'hypothèse que le gradient de pression ne varie pas à travers la couche limite, on obtient l'équation de $\mathcal{V}$:

$$E\, \partial_{zz} \mathcal{V} = \mathrm{i}\, \mathcal{V}\,. \tag{1}$$

Le nombre d'Ekman E doit ici être construit en ne tenant compte que de la composante de $\mathbf{\Omega}$ normale au bord (comme les variations horizontales sont négligées, l'effet des composantes horizontales de $\mathbf{\Omega}$ s'annule pour la construction du profil).

Il est alors naturel de mettre à l'échelle les longueurs dans la direction normale au bord $z = \lambda\zeta$, avec $\lambda = \sqrt{2\,E}$:

$$\zeta = \sqrt{2\,E}\, z\,,$$

l'équation (1) se re-écrit alors

$$\frac{\partial^2 \mathcal{V}}{\partial \zeta^2} = 2\,\mathrm{i}\, \mathcal{V}\,. \tag{2}$$

dont la solution décroissant à l'infini est naturellement

$$\mathcal{V} \propto e^{-\zeta\,(1+\mathrm{i})}\,, \tag{3}$$

c'est le profil de spirale d'Ekman.

A la surface des océans, c'est la contrainte qui est imposée, elle s'oriente à la base du profil d'Ekman comme $-(1+\mathrm{i})\, e^{-\zeta\,(1+\mathrm{i})}$, alors que le transport intégré sur

l'ensemble de la couche s'écrit $-\frac{1}{(1+\mathrm{i})}\, e^{-\zeta\,(1+\mathrm{i})}$. D'où l'angle de 90° rapporté par Nansen.

Dans le cas où le déplacement est imposé au bord (par exemple à la surface du noyau liquide terrestre, si l'on néglige les effets magnétiques), en introduisant $\mathcal{V}_o = U_{ox} + \mathrm{i}\, U_{oy}$, on a

$$\mathcal{V} = -\mathcal{V}_o\, e^{-\zeta\,(1+\mathrm{i})}\,. \tag{4}$$

En utilisant l'incompressibilité du fluide

$$\partial_x u + \partial_y v + \frac{1}{\lambda}\,\partial_\zeta w = 0\,. \tag{5}$$

On écrit alors (sans faire l'hypothèse d'un Ω normal)

$$\frac{1}{\lambda}\,\partial_\zeta w = \left(\underbrace{\partial_x U_{ox}\cos\zeta}_{(a)} + \underbrace{\partial_x U_{oy}\sin\zeta}_{(b)} - \underbrace{\partial_y U_{ox}\sin\zeta}_{(c)} + \underbrace{\partial_y U_{oy}\cos\zeta}_{(b)} \right) e^{-\zeta} \tag{6}$$

Après intégration, les termes (b)&(c) donnent

$$\mathbf{n}\cdot(\boldsymbol{\nabla}\wedge\mathbf{U}_o)\ , \tag{7}$$

qui est complèté quand Ω n'est pas normal au bord (car $\partial_z\mathbf{U}_o \neq \mathbf{0}$) par (a) & (d) :

$$\mathbf{n}\cdot[\boldsymbol{\nabla}\wedge(\mathbf{n}\wedge\mathbf{U}_o)]\ . \tag{8}$$

On a donc d'une manière g'nérale un terme de pompage

$$[w] = \lambda\,\mathbf{n}\cdot\boldsymbol{\nabla}\wedge[\mathbf{n}\wedge\mathbf{U}_o + \mathrm{sign}(\mathbf{n}\cdot\boldsymbol{\Omega})\,\mathbf{U}_o]\ . \tag{9}$$

1.1.2 Couche de Hartmann

En procédant comme précédemment et en introduisant le nombre de Hartmann M et en décomposant $\mathbf{B} = \mathbf{B}_o + \mathbf{B}'$ et $\mathcal{B} = \mathbf{B}'_x + \mathrm{i}\,\mathbf{B}'_y$, il vient

$$\begin{cases} \partial_{zz}\mathcal{V} + M\,\partial_z\mathcal{B} = 0\,, \\ \partial_{zz}\mathcal{B} + M\,\partial_z\mathcal{V} = 0\,. \end{cases} \tag{10}$$

Posons à présent $\mathcal{A} = \partial_z\mathcal{V}$,

$$\partial_{zz}\mathcal{A} = M^2\,\mathcal{A}\,. \tag{11}$$

Posons $z = \lambda\zeta$, avec $\lambda = M^{-1}$:

$$\partial_{\zeta\zeta}\mathcal{A} = \mathcal{A}\,, \tag{12}$$

D'où

$$\mathcal{A} \propto e^{-\zeta}\,. \tag{13}$$

C'est le profil exponentiel des couches de Hartmann.

1.1.3 Couche d'Ekman-Hartmann

En procédant comme nous venons de le faire et en étudiant l'équation du correcteur de couche limite, il vient

$$\begin{cases} -E\,\partial_{zz}\mathcal{V} + \mathrm{i}\,\mathcal{V} = \Lambda\,\partial_z\mathcal{B}\,, \\ \partial_z\mathcal{V} + \partial_{zz}\mathcal{B} \quad = 0\,, \end{cases} \tag{14}$$

où Λ est le nombre d'Elsasser. En différentiant la première équation et en substituant, il vient

$$-E\,\partial_z^3\mathcal{V} + \mathrm{i}\,\partial_z\mathcal{V} + \Lambda\,\partial_z\mathcal{V} = 0\,. \tag{15}$$

Posons comme précédement $\mathcal{A} = \partial_z\mathcal{V}$,

$$E\,\partial_z^2\mathcal{A} = (\Lambda + \mathrm{i})\;\mathcal{A}. \tag{16}$$

Effectuons à présent la mise à l'échelle $z = \lambda\zeta$, (où λ, la taille de la couche limite n'est pas encore connue).

$$E\,\partial_\zeta^2\mathcal{A} = \lambda^2\,(\Lambda + \mathrm{i})\;\mathcal{A}\,, \tag{17}$$

dont la solution est sous la forme $\mathcal{A} \propto e^{-\zeta\,(1+\mathrm{i}\,X)}$, il vient

$$1 - X^2 + 2\,\mathrm{i}\,X = \frac{\lambda^2}{E}\,(\Lambda + \mathrm{i})\;. \tag{18}$$

Comme

$$\left(1 - \tan^2\frac{\tau}{2}\right)\,\tan\tau = 2\,\tan\frac{\tau}{2}\,, \tag{19}$$

on peut poser $X = \tan\frac{\tau}{2}$, avec $\tan\tau = \Lambda^{-1}$. D'où

$$\tan\frac{\tau}{2} = \sqrt{\Lambda^2+1} - \Lambda = \frac{1}{\Lambda + \sqrt{\Lambda^2+1}}\,. \tag{20}$$

On a alors

$$\lambda = \sqrt{2\,E\,\tan\frac{\tau}{2}}\,. \tag{21}$$

Le profil d'Ekman-Hartmann s'écrit donc

$$\begin{cases} u = e^{-\zeta}\,\left[-U_o\cos(\zeta\tan\frac{\tau}{2}) - V_o\sin(\zeta\tan\frac{\tau}{2})\right]\,, \\ v = e^{-\zeta}\,\left[U_o\sin(\zeta\tan\frac{\tau}{2}) - V_o\cos(\zeta\tan\frac{\tau}{2})\right]\,. \end{cases} \tag{22}$$

On note au passage les comportements limites. Pour $\Lambda \longrightarrow 0$, on a $\tan\tau \longrightarrow \infty$ et $\tan(\tau/2) \longrightarrow 1$, on retrouve donc le profil d'Ekman. Pour $\Lambda \longrightarrow \infty$, on a $\tan(\tau/2) \longrightarrow 0$ et on retrouve donc le profil de Hartmann.

1.1.4 Singularités équatoriales

Considérons tout d'abord la singularité équatoriale de la couche d'Ekman. La structure précise de cette singularité n'est pas connue analytiquement. Une solution numérique semble envisageable (voir perspectives). En revanche les mises à l'échelle de cette couche peuvent facilement être obtenus analytiquement.

En écrivant (sous l'hypothèse axi-symmétrique)

$$\mathbf{u} = s\Omega\boldsymbol{\phi} + \boldsymbol{\nabla}\wedge\frac{\psi}{s}\boldsymbol{\phi}$$

et en prenant le rotationel des équations de Navier-Stokes,

$$\frac{\partial\Omega}{\partial z} \propto E\,\frac{\partial^4\psi}{\partial s^4}\,. \tag{23}$$

Le double rotationnel permet d'écrire

$$\frac{\partial}{\partial z}\frac{\partial^2\psi}{\partial s^2} \propto E\,\frac{\partial^4\Omega}{\partial s^4}\,. \tag{24}$$

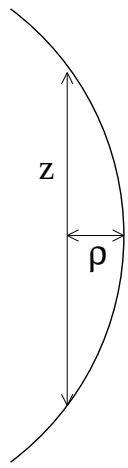

FIG. 1: *Relation géométrique :* $\rho = z^2$

Comme $w \propto \dfrac{\partial \psi}{\partial s}$, en intégrant la seconde équation, on obtient

$$\frac{\partial \Omega}{\partial z} \propto E \, \frac{\partial^3 w}{\partial s^3} \, , \tag{25}$$

$$\frac{\partial w}{\partial z} \propto E \, \frac{\partial^3 \Omega}{\partial s^3} \, . \tag{26}$$

Ce qui implique directement que l'échelle horizontale ρ associée à une échelle verticale z s'écrit

$$\rho \sim (Ez)^{1/3} \, . \tag{27}$$

On note immédiadement que pour une échelle verticale $z \sim \mathcal{O}(1)$, on retrouve la mise à l'échelle usuelle en $E^{1/3}$.

De plus la géométrie sphérique impose (voir figure 1) :

$$\rho = z^2 \tag{28}$$

(Il s'agit simplement du premier terme du dévelopement de Taylor). Donc

$$z^2 \sim (Ez)^{1/3} \, ,$$

$$z^{5/3} \sim E^{1/3} \, . \tag{29}$$

Ce qui donne finalement

$$\boxed{z \sim E^{1/5}} \tag{30}$$

et

$$\boxed{\rho \sim E^{2/5}} \tag{31}$$

Vérifions à présent la reconnection propre entre la couche d'Ekman régulière et cette singularité. Comme nous l'avons vu, la couche d'Ekman régulière se met à l'échelle comme

$$\delta_E \sim (E/\overline{\theta})^{1/2} \, , \tag{32}$$

où $\overline{\theta}$ est la latitude (i.e. $\theta = \pi/2 - \overline{\theta}$).

Par conséquent, une mise à l'échelle en $\overline{\theta} \sim E^{1/5}$ implique

$$\delta_E \sim (E^{1-1/5})^{1/2} \, ,$$

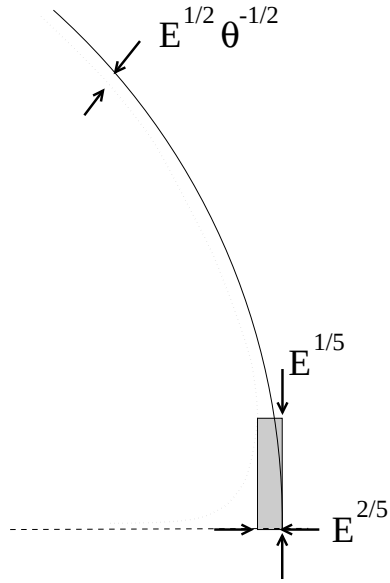

FIG. 2: *Mise à l'échelle pour la singularité de la couche d'Ekman.*

$$\delta_E \sim E^{2/5} \sim \rho \,. \tag{33}$$

Ce qui est bien l'épaisseur de la singularité (voir figure 2).

Considérons à présent la singularité de la couche de Hartmann, en exploitant comme précédemment les équations de Navier-Stokes, on écrit

$$(\mathbf{B}_o \cdot \nabla)\, b \propto \nu \Delta u \,, \tag{34}$$

L'équation d'induction, quant à elle, permet d'écrire

$$(\mathbf{B}_o \cdot \nabla)\, u \propto \eta \Delta b \,. \tag{35}$$

Ainsi, comme B est vertical à l'équateur (pour un champ dipolaire)

$$M \frac{\partial b}{\partial z} \propto \frac{\partial^2 u}{\partial s^2} \,, \tag{36}$$

$$M \frac{\partial u}{\partial z} \propto \frac{\partial^2 b}{\partial s^2} \,. \tag{37}$$

Ce qui entraîne naturellement

$$\rho \sim \left(M^{-1}\, z\right)^{1/2} \,. \tag{38}$$

Utilisons comme précedemment l'argument géométrique (28), on obtient

$$z^2 \sim \left(M^{-1}\, z\right)^{1/2} \,, \tag{39}$$

et donc

$$\boxed{z \sim M^{-1/3}} \,, \tag{40}$$

exploitant à nouveau la relation géométrique, on écrit

$$\boxed{\rho \sim M^{-2/3}} \,. \tag{41}$$

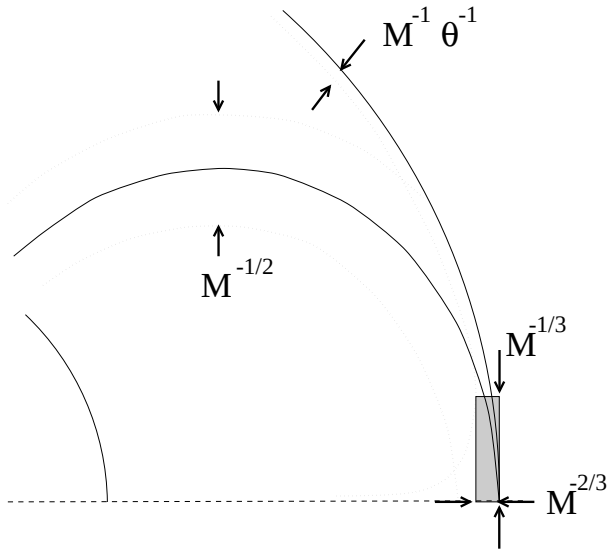

FIG. 3: *Mise à l'échelle pour la singularité de la couche de Hartmann.*

Nous pouvons, comme précédemment vérifier la reconnection à la couche de Hartmann régulière. Celle-ci se met à l'échelle comme

$$\delta_M \sim M^{-1}\overline{\theta}^{-1}\,. \tag{42}$$

Donc, $\overline{\theta} \sim M^{-1/3}$ implique

$$\delta_M \sim M^{-1+1/3}\,,$$

$$\delta_M \sim M^{-2/3} \sim \rho\,. \tag{43}$$

Ce qui est bien l'épaisseur de la singularité (voir figure 3).

Considérons enfin la couche mixte, dite d'Ekman-Hartmann (significative des équilibres opérant dans le noyau liquide terrestre). En suivant la couche régulière à mesure que l'on s'approche de l'équateur, la couche régulière d'Ekman s'élargit comme

$$\delta_E \sim (E/\overline{\theta})^{1/2}\,. \tag{44}$$

La couche régulière de Hartmann, quand à elle s'élargit comme

$$\delta_M \sim M^{-1}\overline{\theta}^{-1}\,. \tag{45}$$

Elles sont donc toutes deux de taille comparable ($\delta_E \sim \delta_M$) lorsque

$$\overline{\theta} \sim M^{-2}\,E^{-1} = \Lambda^{-1}\,. \tag{46}$$

Quand $\overline{\theta}$ devient inférieur à cette valeur, la taille de la couche de Hartmann augmente plus rapidement que celle de la couche d'Ekman. La couche mixte dégénère donc en couche d'Ekman simple.

En notant que cette valeur ($\overline{\theta} \sim \Lambda^{-1} \sim \mathcal{O}(1)$) est plus grande pour la Terre que $M^{-1/3}$ ou $E^{1/5}$, cela justifie l'usage d'une couche d'Ekman régulière au voisinage de la singularité.

En conséquence, la couche mixte d'Ekman-Hartmann pour des paramètres réalistes pour la Géophysique est bien définie jusqu'à des latitudes de l'ordre de

$$\overline{\theta} \sim E^{1/5} \simeq 10^{-3}\,, \tag{47}$$

où elle devient singulière.

1.2 Couches de cisaillement

Même pour de très faibles valeurs de la viscosité, les effets visqueux ne sont pas toujours négligeables loin des bords. Lorsqu'un cisaillement visqueux apparait loin des bords on parle de "couche de cisaillement". Je présente ici deux exemples de telles couches, dans le cas en rotation et dans le cas magnétohydro-dynamique.

1.2.1 Couche de Stewartson

Considérons le problème de Couette sphérique dans un référentiel en rotation. Supposons que la sphère interne tourne plus vite $(1+\varepsilon)\Omega$ que la sphère externe Ω. On se place dans le référentiel de la sphère externe, et on fixe l'unité de temps de sorte que la sphère interne ait une vitesse angulaire unitaire dans ce référentiel. Ce problème a été décrit analytiquement par I. Proudman (Journal of Fluid Mechanics, **1**, 505, 1956) et par K. Stewartson (Journal of Fluid Mechanics, **26**, 131, 1966) pour les couches de cisaillement.

Si la vitesse à l'extérieur du cylindre tangent est naturellement nulle dans ce référentiel, la vitesse à l'intérieur de ce cylindre est moins triviale à déterminer (c'est le travail de Proudman).

En notant T le haut d'une colonne fluide et B le bas de la même colonne de hauteur h, on note que pour une coquille de rapport d'aspect α

$$\begin{cases} \cos\theta_T = \sqrt{1-(s/\alpha)^2}\,, \\ \cos\theta_B = \sqrt{1-s^2}\,. \end{cases} \tag{48}$$

La couche d'Ekman impose à la frontière inférieure

$$2\psi_B = -\frac{E^{1/2}s^2}{\sqrt{\cos\theta_B}}(1-\Omega) \tag{49}$$

et à la frontière supérieure

$$2\psi_T = \frac{E^{1/2}s^2}{\sqrt{\cos\theta_T}}\Omega \tag{50}$$

En égalant $\psi = \psi_T = \psi_B$, il vient à l'intérieur du cylindre tangent

$$1-\Omega = \frac{(1-s^2)^{1/4}}{(1-s^2)^{1/4}+(1-(s/\alpha)^2)^{1/4}} \tag{51}$$

et

$$2\psi = -\frac{s^2\sqrt{E}}{(1-s^2)^{1/4}+(1-(s/\alpha)^2)^{1/4}}\,. \tag{52}$$

Notons que $\Omega \longrightarrow 1$ quand $s \longrightarrow 1$, ce qui induit donc une singularité de volume pour cette solution. Ce comportement de synchronisation avec la sphère interne a été reproduit pour la première fois numériquement dans Dormy et al. 1998.

Cette singularité au cylindre tangent est accommodée par la viscosité sous la forme de trois couches imbriquées (on appelle abusivement l'ensemble de ces trois couches la "couche de Stewartson").

Les deux premières de ces trois couches sont dites quasi-géostrophique. Elles respectent la géostrophie de : $\Omega = \Omega(\rho)$ où $s-1=\rho$. Pour ψ, on écrit

$$\psi = \frac{z-z_B(\rho)}{h(\rho)}\psi_T(\rho) + \frac{z_T(\rho)-z}{h(\rho)}\psi_B(\rho)\,. \tag{53}$$

En moyennant selon z la composant azimutale de Navier-Stokes, on a

$$E\,\partial_{\rho\rho}\Omega = -\frac{2}{h}(\psi_T-\psi_B) \tag{54}$$

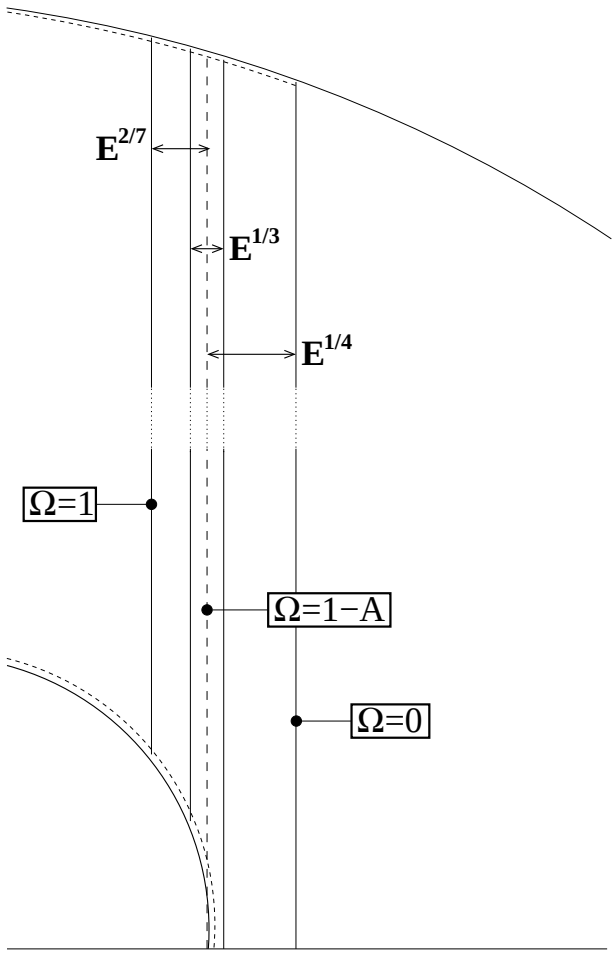

FIG. 4: *La structure imbriquée de la couche de Stewartson.*

A l'extérieur du cylindre tangent, on a donc

$$E\,\partial_{\rho\rho}\Omega \propto E^{1/2}\Omega\,, \tag{55}$$

qui donne donc une couche en $E^{1/4}$. A l'intérieur du cylindre tangent, l'effet de pente à la sphère interne est dominant, on a

$$E\,\partial_{\rho\rho}\Omega \propto -\frac{E^{1/2}}{(-\rho)^{1/4}}(1-\Omega)\,, \tag{56}$$

qui donne donc une couche en $E^{2/7}$.

A travers la couche en $E^{1/4}$, $\Omega(s)$ croit de 0 à $1-A$ au cylindre tangent (où A est petit). Donc sur le cylindre tangent

$$\frac{d\Omega}{ds} = \mathcal{O}(E^{-1/4})\,.$$

A travers la couche en $E^{2/7}$, Ω reste proche de l'unité avec

$$\frac{d\Omega/ds}{1-\Omega} = \mathcal{O}(E^{-2/7})\,.$$

Donc, en invoquant la continuité de Ω et celle de $d\Omega/ds$

$$A = \mathcal{O}(E^{(2/7)-(1/4)}) = \mathcal{O}(E^{1/28})\,.$$

Cette puissance d'Ekman est extrèmement petite... Malgré les petites valeurs du nombre d'Ekman atteintes pour les simulations numériques les plus poussées présentées ci-avant ($E = 10^{-8}$), on atteint seulement sur le cylindre tangent $\Omega \simeq 0.55$. En fait, même pour le noyau liquide terrestre ($E = 10^{-15}$) A ne serait pas vraiment petit !

Une troisième couche enfin est nécessaire pour réconcillier l'ensemble des dérivées, celle-ci est agéostrophique. Les équations pour cette structure sont

$$\begin{cases} -2\partial_z\psi = E\partial_{\rho\rho}\Omega\,, \\ 2\partial_z\Omega \;\; = E\partial_\rho^4\psi\,. \end{cases} \tag{57}$$

La mise à l'échelle correspondante $E^{1/3}$ pour une échelle verticale d'ordre 1 a déjà été introduite précédemment.

Ces diférentes mises à l'échelle ainsi que leur caractère quasi-géostrophique ou agéostrophique ont pu être vérifiées sur les résultats numériques (Dormy et al., 1998).

1.2.2 Couche en super-rotation

Considérons à présent le problème de Couette MHD dans un référentiel au repos. On impose un champ dipolaire axial

$$\mathbf{B}_o = \boldsymbol{\nabla} \wedge \frac{A}{s}\boldsymbol{\phi}\,, \tag{58}$$

avec $A = s^2/2r^3$. $A = A_Q$ définit la ligne de champ tangente à l'équateur.

La rotation lente de la graine Ω induit un faible champ magnétique azimutal $\mathbf{B}_\phi = R_M\mathbf{B}_o$.

La composante ϕ des équations de la magnétohydrodynamique linéarisées (petit R_M) s'écrit

$$\begin{cases} M^2\dfrac{1}{s}\,\mathbf{B}_o\cdot\boldsymbol{\nabla}\,(sB) \;+\; \Delta(s\Omega) = 0\,, \\ \qquad\qquad s\,\mathbf{B}_o\cdot\boldsymbol{\nabla}\,\Omega \;+\; \Delta B \;= 0\,. \end{cases} \tag{59}$$

Dans la limite des grands nombres de Hartmann (forts champs imposés), en négligeant les effets visqueux, la force de Laplace doit s'annuler :

$$\boldsymbol{\jmath} \wedge \mathbf{B}_o \simeq \mathbf{0} \tag{60}$$

où $\boldsymbol{\jmath} = s^{-1}\boldsymbol{\nabla} sB \wedge \boldsymbol{\phi}$. En négligeant la diffusion ohmique, le champ magnétique est gelé dans le fluide (e.g. Moffatt, Magnetic field Generation in electrically conducting fluids, 1978), ce qui implique

$$\Omega \simeq \mathcal{F}(A)\,, \qquad sB \simeq -r_o^2 M^{-1}\,\mathcal{G}(A)\,. \tag{61}$$

Il est alors commode d'introduire les variables d'Alfvén

$$V_\pm = s\Omega \pm MB$$

qui satisfont

$$\mathbf{B}_o \cdot \boldsymbol{\nabla} V_\pm \pm M^{-1}\Delta V_\pm = s^{-1}B_s V_\mp\,. \tag{62}$$

Quand $r \to r_o$ (sphère externe), la continuité de V_+ à travers la couche de Hartmann entraîne

$$s\Omega + MB \to 0\,. \tag{63}$$

Quand $r \to r_i$ (sphère interne), la continuité de V_- à travers la couche de Hartmann entraine

$$\begin{pmatrix} MB \\ s_i\Omega \end{pmatrix} \longrightarrow \begin{pmatrix} MB_i \\ s_i \end{pmatrix} + \begin{pmatrix} 1 \\ 1 \end{pmatrix} \frac{1}{\mid B_{ri} \mid} (\partial_r B)_i \tag{64}$$

d'où $\Omega \to 1$.

La solution hors couches limites et couches de cisaillement (en prenant en compte la symétrie par rapport au plan de l'équateur) est

$$\mathcal{F}(A) = 1 \quad \text{sauf en } A = A_Q\,, \tag{65}$$

$$\mathcal{G}(A) = \begin{cases} A/A_Q & \text{dans la région polaire} \\ 0 & \text{dans la région équatoriale} \end{cases} \tag{66}$$

La ligne de champ tangente à l'équateur joue donc ici un rôle très similaire à celui joué par le cylindre tangent dans le problème hydrodynamique en rotation. Les courants électriques induits sont discontinus de part et d'autre de cette ligne et il est donc nécessaire de réintroduire les diffusivités pour résoudre cette singularité.

L'équation (62) peut-être utilisée pour caractériser la couche de cisaillement qui y est associée. C'est ce que nous avons fait (en collaboration avec le Professeur Andrew Soward et Dominique Jault) dans Dormy et al. 2001.

Cette couche de cisaillement a une propriété remarquable : la vitesse angulaire y dépasse d'environ 50% la vitesse de la sphère interne (moteur des mouvements).

Malheureusement, les équations associés à cette couche ne peuvent être résolues analytiquement que dans la limite $r_i \longrightarrow r_o$. Ces équations asymptotiques peuvent toutefois être résolues numériquement dans le cas général. La figure 5 présente une comparaison entre le calcul complet en géométrie sphérique et la résolution du problème asymptotique (on peut se reporter à l'article en fin de rapport pour plus de détails). La figure 6 présente une coupe à travers la solution, qui permet une confrontation plus fine.

2 Etudes non-lineaires

Si les vitesses en jeu dans ces écoulements sont trop importantes, les non-linéarités intrinsèques doivent être réintroduites et celles-ci peuvent déstabiliser les couches. On mesure ces vitesses à l'aide d'un nombre de Reynolds, dit "de couche limite" car la longueur caractéristique y est celle du cisaillement visqueux.

2.1 Stabilité non-linéaire de la couche d'Ekman-Hartmann

La première approche consiste à démontrer la stabilité non-linéaire. Cette technique mathématique repose sur une estimation d'energie et permet de montrer qu'en dessous d'une valeur critique des paramètres de contrôle (ici le nombre de Reynolds de couche limite) une solution perturbée ne voit pas son énergie s'éloigner au cours du temps de la solution non-perturbée.

Par souci de simplicité, le raisonnement est ici mené sur la couche d'Ekman pure :

$$\varepsilon(\partial_t \mathbf{u} + \mathbf{u} \cdot \nabla \mathbf{u}) + \nabla p - E\Delta \mathbf{u} + \mathbf{e}_\Omega \times \mathbf{u} = 0,$$

$$\boldsymbol{\nabla} \cdot \mathbf{u} = 0, \qquad \mathbf{u}_{|z=0} = 0,$$

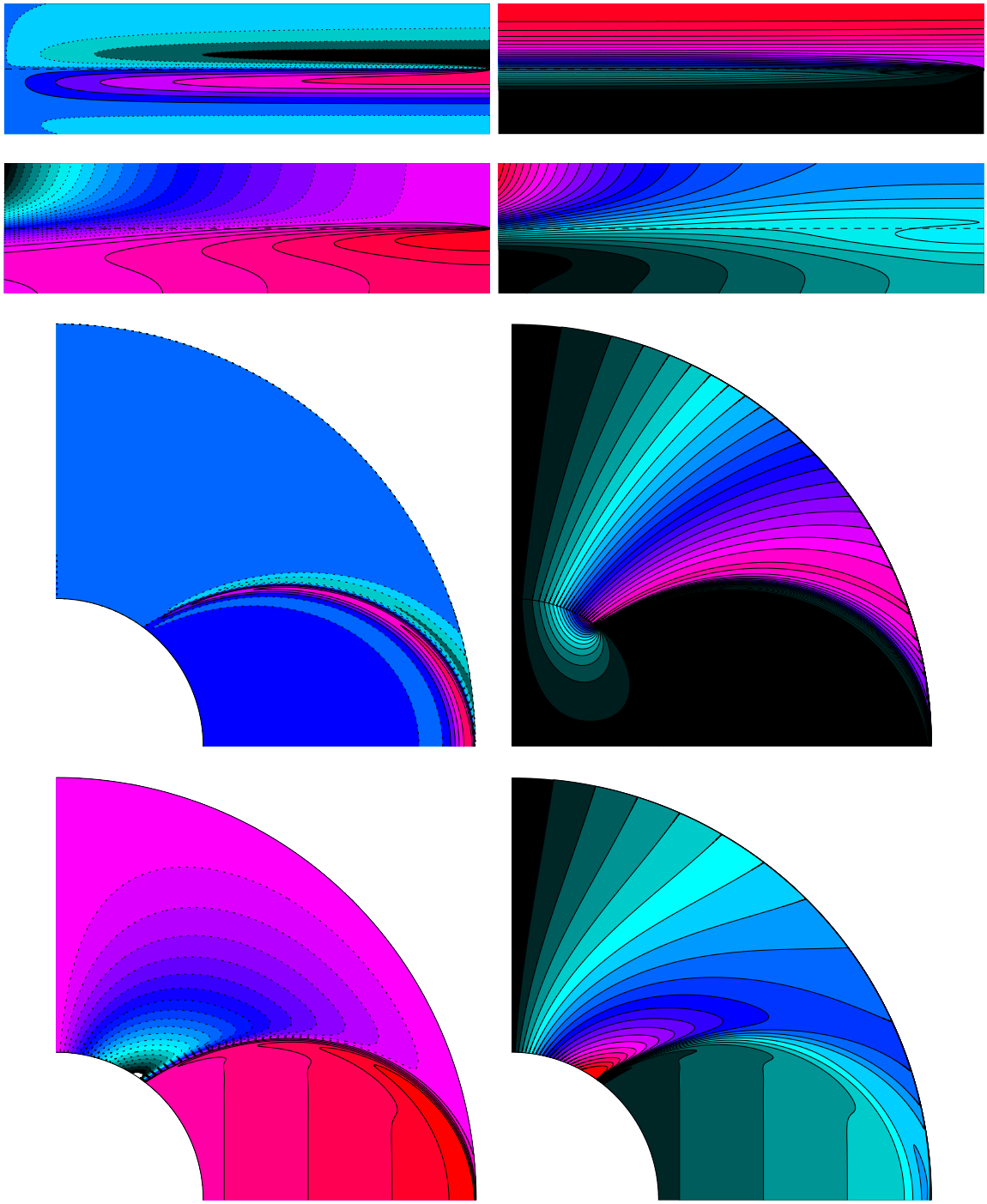

FIG. 5: *Représentation de la solution du problème de Couette MHD. L'approche asymptotique en haut (de gauche à droite* Ω, sB, V_+, V_-*) puis la résolution du problème complet pour un nombre de Hartmann de* 10^4 *(mêmes quantités).*

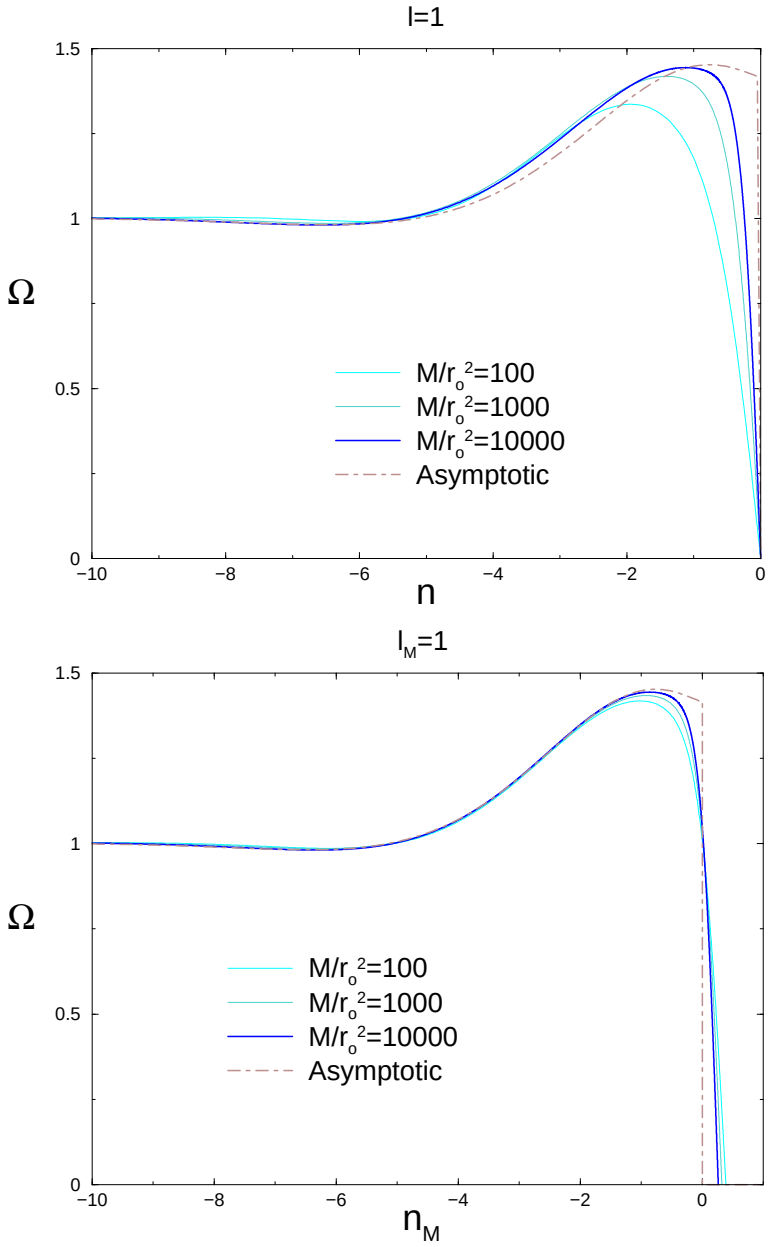

FIG. 6: *Coupes à travers la solution (asymptotique et numérique complète) dans le plan équatorial. La seconde figure a été corrigée pour tenir compte du décalage apporté par la singularité équatoriale de la couche de Hartmann (voir Dormy, Jault, Soward, 2001).*

où

$$E \sim \varepsilon^2 \to 0, \qquad \beta = \frac{E^{1/2}}{\varepsilon}.$$

Dans l'intérieur, loin du bord (le terme en β correspond à la succion d'Ekman)

$$\partial_t \mathbf{u}_o^{int} + \mathbf{u}_o^{int} \cdot \nabla \mathbf{u}_o^{int} + \beta \mathbf{u}_o^{int} + \nabla p = 0,$$

$$\boldsymbol{\nabla} \cdot \mathbf{u}_o^{int} = 0, \qquad \mathbf{u}_o^{int} \cdot \mathbf{n}_{|z=0} = 0.$$

La stabilité non-linéaire peut-être démontrée dans le sens suivant

$$\sup_{t \geq 0} \int |\mathbf{u}(t) - \mathbf{u}^{int}|^2 \leq C \int |\mathbf{u}(0) - \mathbf{u}^{int}(0)|^2.$$

L'idée principale de la démonstration réside dans l'asymptotique formelle :

$$\mathbf{u} \sim \mathbf{u}_N = \sum_{k=0}^{N} \varepsilon^k \left(\mathbf{u}_k^{int}(t,x,y,z) + \mathbf{u}_k^{BL}\left(t,x,y,\frac{z}{E^{1/2}}\right)\right).$$

Une solution approchée satisfait

$$\varepsilon(\partial_t \mathbf{u}_N + \mathbf{u}_N \cdot \nabla \mathbf{u}_N) + \nabla p_N - E\Delta \mathbf{u}_N + \mathbf{e} \times \mathbf{u}_N = O(\varepsilon^{N+1}),$$

$$\boldsymbol{\nabla} \cdot \mathbf{u}_N = 0, \qquad \mathbf{u}_{N|z=0} = 0.$$

L'étape suivante consiste à estimer l'énergie de la différence $\mathbf{v} = \mathbf{u} - \mathbf{u}_N$:

$$\frac{d}{dt}\int \frac{|v|^2}{2} + \frac{E}{\varepsilon}\int |\nabla \mathbf{v}|^2 \leq \left| \int \mathbf{v} \cdot (\mathbf{u} \cdot \nabla \mathbf{u} - \mathbf{u}_N \cdot \nabla \mathbf{u}_N) \right| + \dots$$

$$\leq C \sup_{z \geq 0} \left| z \mathbf{u}^{BL}\left(\frac{z}{E^{1/2}}\right)\right| \int |\nabla \mathbf{v}|^2 + \dots$$

$$\leq C E^{1/2} \sup |\mathbf{u}^{int}| \int |\nabla \mathbf{v}|^2 + \dots$$

D'où l'on peut déduire le critère de stabilité

$$Re_{Ekman} = \frac{\varepsilon \sup |\mathbf{u}^{int}|}{E^{1/2}} = \frac{\varepsilon}{E} \sup |\mathbf{u}^{int}| E^{1/2} = \frac{U\lambda}{\nu} \leq Re_c, \tag{67}$$

où λ dénote la taille de la couche d'Ekman.

D'une manière générale, on obtient

$$Re_{BL} = \frac{|\mathbf{U}^{BL}|_\infty L^{BL}}{\nu} \leq Re_c^{BL}. \tag{68}$$

Pour le cas Ekman-Hartmann, l'équation loin du bord est

$$\partial_t \mathbf{u}_o^{int} + \mathbf{u}_o^{int} \cdot \nabla \mathbf{u}_o^{int} + \beta \mathbf{u}_o^{int} + \nabla p = 0,$$

$$\boldsymbol{\nabla} \cdot \mathbf{u}_o^{int} = 0, \qquad \mathbf{u}_o^{int} \cdot \mathbf{n}_{|z=0} = 0,$$

avec

$$\beta = \sqrt{\frac{2E}{\varepsilon^2 \tan(\tau/2)}}$$

$$\tan\frac{\tau}{2} = \frac{1}{\Lambda + \sqrt{1+\Lambda^2}}.$$

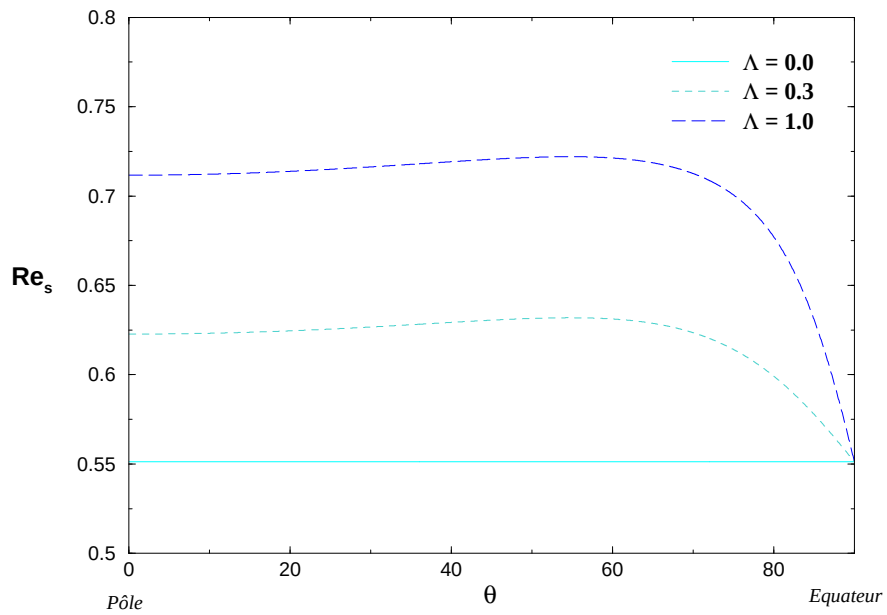

FIG. 7: *Representation du critère de stabilité non-linéaire.*

On montre que la couche est stable si

$$\|U_\infty\| \frac{\varepsilon}{\sqrt{E}} \leq Re_s(\Lambda, \theta), \tag{69}$$

car, alors

$$\sup_{t\geq 0} \int \left(|\mathbf{u}(t) - \mathbf{u}_s|^2 + \frac{\Lambda R_M}{\varepsilon} |\mathbf{b}(t) - \mathbf{b}_s|^2 \right) \leq \int \left(|\mathbf{u}(0) - \mathbf{u}_s|^2 + \frac{\Lambda R_M}{\varepsilon} |\mathbf{b}(0) - \mathbf{b}_s|^2 \right).$$

Cette expression est illustrée figure 7 (voir Desjardin, Dormy, Grenier, 1999 pour la dérivation détaillée de cette estimation).

Cette technique n'a pas permis d'établir la stabilité non-linéaire de la couche d'Ekman-Hartmann sur l'ensemble de la frontière noyau-manteau pour le régime de paramètres significatif du noyau terrestre.

2.2 Première instabilité de la couche d'Ekman-Hartmann

Puisque la stabilité non-linéaire n'a pu être établie partout près de la frontière noyau-manteau, il est intéressant de chercher à démontrer l'existance d'instabilités.

Pour cela, étudions le système linéarisé ($\mathbf{\Omega}$ est dans la direction $\mathbf{e}$ et $\mathbf{B}_o$ dans la direction $\mathbf{e}'$)

$$\begin{aligned}
\frac{\varepsilon}{\lambda}(\partial_t \mathbf{u} + \mathbf{U}\cdot\nabla\mathbf{u} + \mathbf{u}\cdot\nabla\mathbf{U}) - \frac{E}{\lambda^2}\Delta\mathbf{u} + \frac{\nabla p}{\lambda} &= \frac{\Lambda}{\lambda}(\boldsymbol{\nabla}\wedge\mathbf{b})\times\mathbf{e}' - \mathbf{e}\times\mathbf{u} \\
&+ \frac{\Lambda R_M}{\lambda}\left((\boldsymbol{\nabla}\wedge\mathbf{B}_o)\times\mathbf{b} + (\boldsymbol{\nabla}\wedge\mathbf{b})\times\mathbf{B}_o\right), \\
\frac{R_M}{\lambda}(\partial_t\mathbf{b} + \mathbf{U}\cdot\nabla\mathbf{b} + \mathbf{u}\cdot\nabla\mathbf{B}_o - \mathbf{b}\cdot\nabla\mathbf{U} - \mathbf{B}_o\cdot\nabla\mathbf{u}) &= \frac{1}{\lambda}\boldsymbol{\nabla}\wedge(\mathbf{u}\times\mathbf{e}') + \frac{1}{\lambda^2}\Delta\mathbf{b}, \\
\boldsymbol{\nabla}\cdot\mathbf{u} = 0, \qquad \boldsymbol{\nabla}\cdot\mathbf{b} &= 0.
\end{aligned} \tag{70}$$

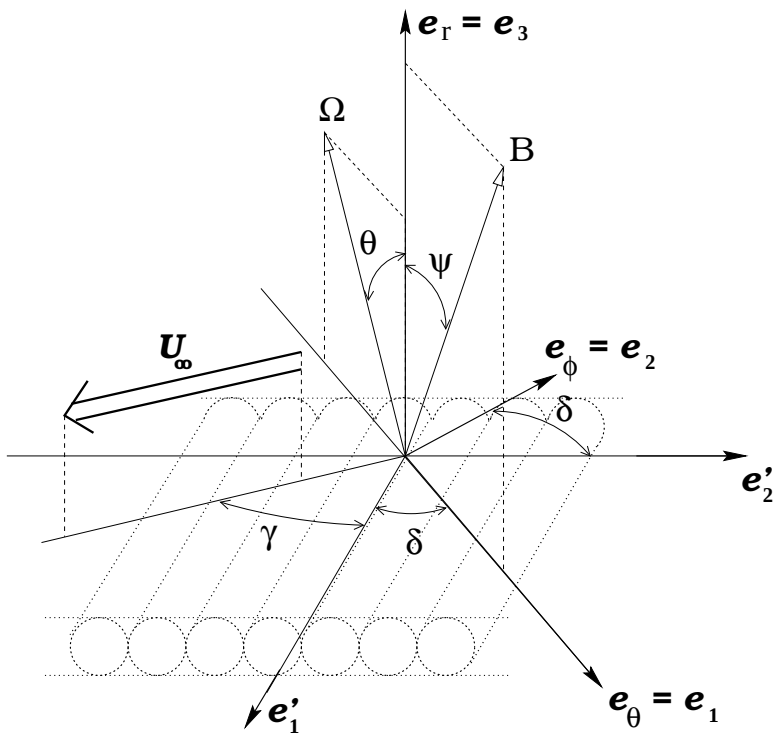

FIG. 8: *Géometrie pour l'étude locale. L'axe de rotation et le champ magnétique imposé font respectivement un angle θ et ψ avec la normale au bord. Nous cherchons une solution en onde plane progressive pour une vitesse loin du bord $\mathbf{U}_\infty$. Ces quantités font respectivement un angle δ et $\delta + \gamma$ avec le plan $(\mathbf{\Omega}, \mathbf{B}_o)$.*

Nous cherchons des solutions sous la forme d'ondes progressives

$$f(z)\exp(i\alpha(y' - ct))\,.$$

La définition des angles est précisée sur la figure 8. Nous minimisons alors Re_i en fonction des paramètres α, γ, θ.

Dans le cas $\theta = 0$ et en l'absence d'effets magnétohydrodynamiques, Lilly (1966) a montré que la couche d'Ekman devenait instable à de telles perturbations pour des nombres de Reynolds de couche limite $Re_o = \varepsilon\sqrt{2/E}$ suppérieurs à 54.16. Gilman (1971) a étendu ce résultat à la couche d'Ekman-Hartmann toujours horizontale (i.e. aux pôles) et à montré dans ce cas la stabilité linéaire pour le noyau liquide terrestre.

En développant les équations pour la perturbation (voir Desjardins et al., 2001), on note que toute la dépendance angulaire du système se résume en deux paramètres :

$$\xi = \tan\theta\,\sin\delta$$

et

$$\xi' = \tan\psi\,\sin\delta\,.$$

Notons que ces deux paramètres s'annulent dans le cas $\theta = \psi = 0$. Ainsi, alors que la construction des profils laminaires ne repose que sur les composantes normales des $\mathbf{\Omega}$ et $\mathbf{B}_o$, l'instabilité est fondamentalement influencée par leurs composantes horizontales.

Naturellement, seul le premier de ces paramètres, ξ, a du sens dans le cas non magnétique. Pour cette raison Leibovich et Lele (1985), dans leur généralisation de

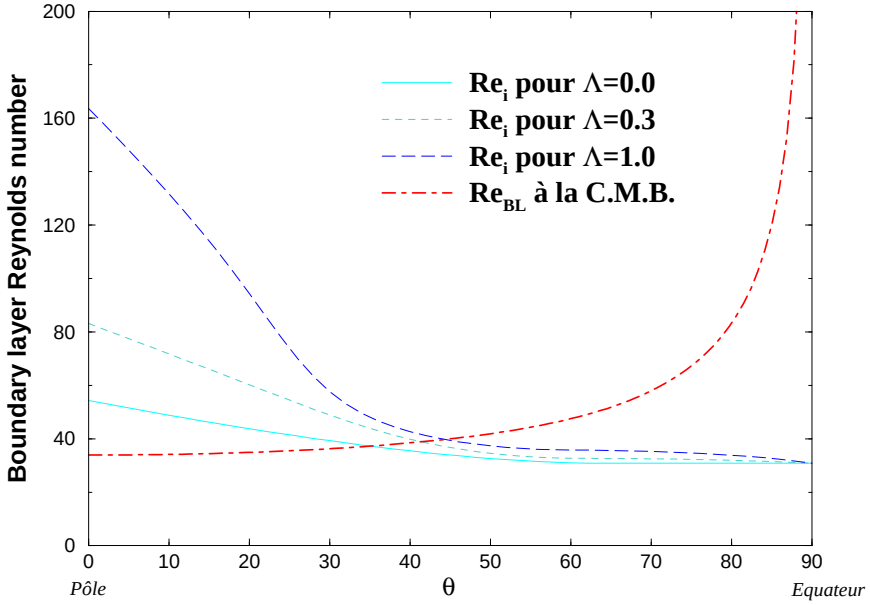

FIG. 9: *Nombre de Reynolds de couche limite au-delà duquel une instabilité est obtenue. Une estimation du nombre de Reynolds de couche limite pour la frontière noyau-manteau est également représentée pour comparaison.*

l'étude de Lilly (instabilité de la couche d'Ekman) au cas sphérique, cherchent la valeur de ξ^* qui minimise le critère d'instabilité. Pour de petites valeurs de θ (i.e. assez près des pôles), $\xi = \xi^*$ ne peut pas être réalisé et $\delta = \pi/2$ est nécessaire pour maintenir ξ aussi proche que possible de ξ^*. Une fois qu'une co-latitude critique est atteinte ($\theta^* = \mathrm{atan}(\xi^*) \simeq 63.8^o$), ξ et donc le nombre de Reynolds critique peuvent être maintenus constants ($\xi = \xi^*$) en variant δ suivant

$$\delta = \delta_1 = \mathrm{asin}\left(\frac{\xi^*}{\tan\theta}\right) .$$

Il convient de noter qu'une modification de δ en $\pi - \delta$ n'affecte pas ξ, on a donc une seconde branche solution

$$\delta = \pi - \delta_1 .$$

Dans le cas magnétohydrodynamique, l'introduction de ξ' ne permet plus de maintenir le nombre Reynolds critique constant (voir figure 9). Cependant, les deux branches de solutions continuent d'exister (voir figure 10), car la symétrie $\delta \to \pi - \delta$ n'affecte ni ξ, ni ξ'.

L'étude démontre qu'une instabilité de couche limite peut exister à la frontière noyau-manteau dans une large bande autour de l'équateur ($\overline{\theta} < 45^o$). Le rôle possible de ces instabilités sur la géodynamo reste à étudier.

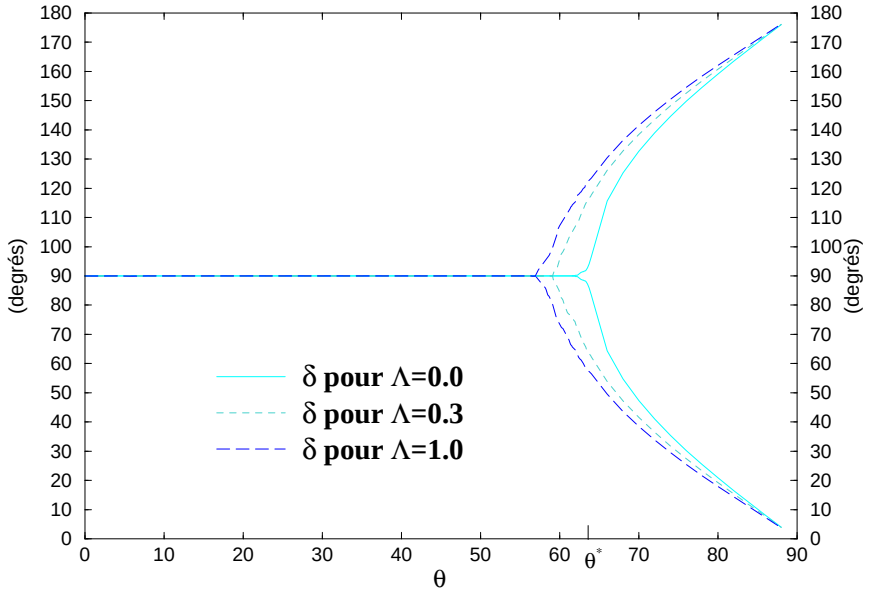

FIG. 10: *L'angle δ de l'instabilité par rapport à $\mathbf{e}_\theta$ par rapport à la co-latitude θ. L'instabilité se développe dans la direction de $\mathbf{e}_\phi$ près du pôle. Une fois passée une co-latitude critique (qui diminue avec Λ) deux branches solutions apparaissent. L'instabilité s'aligne avec $\mathbf{e}_\theta$ près de l'équateur.*

Cinquième partie

Perspectives

L'étude de l'origine du champ magnétique terrestre connaît depuis quelques années un développement rapide suite aux premières simulations de dynamo auto-excitées dans une sphère en rotation rapide (Zhang et Busse, Geophys. Astrophys. Fluid Dyn., 1988 ; Glatzmaier et Roberts, Nature, 1995). De multiples études numériques produisent à présent des modèles de dynamo dipolaires axiales. Cependant tous ces modèles fonctionnent dans des régimes de paramètres très éloignés de celui significatif du noyau liquide terrestre. Toutes ces dynamos reposent sur des effets mettant en oeuvre des forces visqueuses très largement surévaluées. Le nombre d'Ekman (mesurant l'effet des forces visqueuses par rapport aux effets de rotation) y est surestimé d'un coefficient dépassant le milliard. Les écoulements associés à ces équilibres "magnéto-visqueux" sont apparemment beaucoup moins efficaces pour la génération de champ magnétique que ceux correspondant à l'équilibre "magnétostrophique" (i.e. entre forces magnétiques et effets de rotation) attendu dans la Terre. En effet, pour pouvoir étudier l'effet dynamo, toutes les études publiées ont été obligées de sous-estimer la diffusivité magnétique (terme destructeur du champ magnétique) d'un coefficient supérieur au million. Il a été démontré (Christensen et coll., Geophys. J. Int., 1999) que ce coefficient est bien relié à l'erreur introduite sur le nombre d'Ekman. Il est donc raisonnable de penser que la géométrie des solutions numériques de dynamo obtenues à ce jour ainsi que leurs modes de fonctionnement diffèrent grandement de ceux en oeuvre à l'intérieur de notre planète. Nous avons publié un article de revue (Dormy, Valet et Courtillot, 2000) qui met en évidence ces difficultés.

Pour prendre part au progrès dans cette voie, j'envisage de poursuivre les études simplifiées avec une forte interaction entre simulations numériques et approches analytiques. J'expose ci-dessous quelques un de ces projets, ainsi qu'un projet à plus long terme consistant à développer un nouvel outil numérique pour ce problème.

Singularité de la couche d'Ekman

Si la singularité de la couche de Hartmann en $M^{-1/3}$, $M^{-2/3}$ peut être résolue analytiquement (e.g. Dormy, Jault, Soward, 2001), il n'en est pas de même de la singularité équatoriale de la couche d'Ekman. Nous travaillons actuellement, le professeur Andrew Soward et moi à la résolution numérique du problème asymptotique associé.

Convection au seuil dans une coquille sphérique

Nous avons pu étudier numériquement la convection au seuil et montrer que le comportement asymptotique ne pouvait être atteint que pour de très faibles valeurs du nombre d'Ekman (travail effectué avec Dominique Jault et Philippe Cardin). Nous nous attachons actuellement à l'étude de la structure radiale au seuil pour différents problèmes. Les calculs effectués ont permis des progrès (en collaboration avec le Professeur Andrew Soward et le Professeur Christopher Jones (tous deux de l'Université d'Exeter en Grande-Bretagne). Nous avons obtenu une description asymptotique correcte pour le mode de convection en chauffage différentiel, pour lequel la sphère interne, c'est-à-dire la graine, influence la convection contrairement au problème classique en chauffage uniforme dans une sphère pleine. Nous avons également obtenu les termes de correction à l'ordre dominant pour des conditions aux limites en surface libre (sans stress) comme pour des conditions de non glisse-

ment. Celles-ci sont actuellement en cours de validation. Un article pour Journal of Fluid Mechanics présentant ces résultats est en préparation.

Non-linearites sur la convection

J'ai également commencé l'étude du régime non-linéaire pour les équations intégrées selon l'axe de rotation (quasi-géostrophique) en chauffage uniforme (stage de DEA de Vincent Morin). Pour ce régime des désaccords persistent entre les simulations numériques et les études asymptotiques (portant sur le caractère sous-critique de la bifurcation convective). Ces désaccords pourraient être dus simplement à l'utilisation de paramètres trop élevés pour être représentatifs d'un régime asymptotique.

Approche numérique pour le régime magnétostrophique

Les codes numériques développés pour étudier la géodynamo utilisent dans leur quasi-totalité une approche spectrale. Cette approche a permis de réels progrès, mais on en atteint actuellement les limites. Les très faibles valeurs de viscosités qu'il faut considérer autorisent la présence de couches de cisaillement très fines. Si l'on néglige les effets visqueux devant les effets de rotation, on peut même voir apparaître des singularités de volumes dans la solution. La présence de ces cisaillements nécessite une résolution spectrale globalement élevée. Une méthode de raffinement local serait évidemment plus adaptée. Le problème de l'effet dynamo est fortement non-linéaire, la méthode usuelle d'estimation des non-linéarités repose sur une collocation qui est très coûteuse avec les méthodes d'harmoniques sphériques (difficulté liée à la transformée de Legendre). Enfin les méthodes spectrales se prêtent très mal à la parallélisation par décomposition de domaine. Pour toutes ces raisons, il est essentiel de travailler à la construction de méthodes locales et adaptatives. La méthode des volumes finis est extrêmement prometteuse. Cette méthode permet sous certaines conditions (Balsara, J. Comput. Phys., 174, 614, 2001) de maintenir le caractère solénoïdal du champ magnétique (en vérifiant lors de la construction numérique des opérateurs que la divergence d'un rotationel s'annule exactement).

Il est évident lorsque l'on considère le régime de paramètres pertinent qu'il s'agit d'un système raide. Il a été démontré théoriquement que la limite $E \to 0$ est singulière pour l'écoulement MHD et que le champ magnétique doit alors satisfaire une contrainte supplémentaire (la contrainte de Taylor: intégrale nulle de la composante angulaire de la force de Laplace sur un cylindre géostrophique). Les difficultés théoriques pour la construction de cette nouvelle approche sont nombreuses: équation hyperbolique pour le transport thermique, méthodes numériques stables dans les régimes de rotation rapide, conditions aux limites magnétiques (raccordement à un champ potentiel), paramétrisation des effets liés aux couches limites visqueuses (couches limites actives), méthode numérique satisfaisant la contrainte de Taylor. Pour m'engager dans cette voie, je dispose du code numérique à trois dimensions reposant sur une approche spectrale. Ce code a été validé lors d'un récent benchmark international. Cet outil sera très utile lors du dévelop-pement de l'approche proposée puisqu'il permettra la validation de chaque étape du développement.

Sixième partie

Liste des travaux et publications

Publications

Rang A

A super-rotating shear layer in magnetohydrodynamic spherical Couette flow
Emmanuel Dormy, Dominique Jault, Andrew Soward,
Journal of Fluid Mechanics, **452**, 263–291, 2002.

A numerical dynamo benchmark
U.R. Christensen, J. Aubert, P. Cardin, Emmanuel Dormy, S. Gibbons, G.A. Glatzmaier, E. Grote, Y. Honkura, C. Jones, M. Kono, M. Matsushima, A. Sakuraba, F. Takahashi, A. Tilgner, J. Wicht and K. Zhang,
Physics of the Earth and Planetary Interiors, **128**, 25–34, 2001.

Instability of Ekman-Hartmann Boundary Layers, with application to the fluid flow near the Core-Mantle Boundary
Benoît Desjardins, Emmanuel Dormy, Emmanuel Grenier,
Physics of the Earth and Planetary Interiors, **123**, 15–27 ; **124**, 283-294, 2001.

Numerical models of the geodynamo and observational constraints
Emmanuel Dormy, Jean-Pierre Valet, and Vincent Courtillot,
Geochemistry, Geophysics and Geosystems (G-cubed), **1**, 62, 2000.

An Accurate Compact Treatment of Pressure for Colocated Variables
Emmanuel Dormy
Journal of Computational Physics, **151**, 676–683, 1999.

Stability of Mixed Ekman-Hartmann Boundary Layers
Benoît Desjardins, Emmanuel Dormy, Emmanuel Grenier,
Nonlinearity, **12**, 2, 181–199, 1999.

MHD flow in a slightly differentially rotating spherical shell, with conducting inner core, in a dipolar magnetic field
Emmanuel Dormy, Philippe Cardin et Dominique Jault,
Earth and Planetary Science Letters, **160**, 1-2, 15–30, 1998.

Binary tree models of high-Reynolds-number turbulence
Erik Aurell, Emmanuel Dormy et Peter Frick,
Physical Review E, **56**, 2, 1692–1698, 1997.

Numerical Simulation of Elastic Wave Propagation Using a Finite Volume Method
Emmanuel Dormy, Albert Tarantola,
Journal of Geophysical Research, **100**, B2, 2123–2133, 1995.

Autres

Introduction aux expériences numériques
Emmanuel Dormy,
Revue du Palais de la Découverte, **24**, 235, 27–41, 1996.
republié dans
Découverte, **294**, 30-44, 2002.

Septième partie

Publications sur cinq ans

ELSEVIER

Earth and Planetary Science Letters 160 (1998) 15–30

EPSL

MHD flow in a slightly differentially rotating spherical shell, with conducting inner core, in a dipolar magnetic field

Emmanuel Dormy [a,*], Philippe Cardin [b,c,1], Dominique Jault [a,c]

[a] *IPGP, 4 place Jussieu, F-75252 Paris, France*
[b] *ENS, 24 rue Lhomond, F-75231 Paris, France*
[c] *CNRS, Paris, France*

Received 17 March 1997; revised version received 7 April 1998; accepted 24 April 1998

Abstract

Motion is generated in a rotating spherical shell, by a slight differential rotation of the inner core. We show how the numerical solution tends, with decreasing Ekman number, to the asymptotic limit of Proudman [J. Fluid Mech. 1 (1956) 505–516]. Starting from geophysically large values, we show that the main qualitative features of the asymptotic solution show up only when the Ekman number is decreased below 10^{-6}. Then, we impose a dipolar and force-free magnetic field with internal sources. Both the inner core and the liquid shell are electrically conducting. The first effect of the Lorentz force is to smooth out the change in angular velocity at the tangent cylinder. As the Elsasser number is further increased, the Proudman–Taylor constraint is violated, Ekman layers are changed into Hartmann type layers, shear at the inner sphere boundary vanishes, and the flow tends to a bulk rotation together with the inner sphere. Unexpectedly, for increasing strength of the field, there is a super-rotation (the angular velocity does not reach a maximum at the inner core boundary but in the interior of the fluid) localized in an equatorial torus. At a given field strength, the amplitude of this phenomenon depends on the Ekman number and tends to vanish in the magnetostrophic limit. © 1998 Elsevier Science B.V. All rights reserved.

Keywords: dynamos; Earth; magnetic field; induction; models

1. Introduction

As we try to model the Earth's dynamo, we face successive difficulties. In particular, the kinematic viscosity of the fluid is very low and this lets other forces dominate viscous diffusion except on very short scales. We hope that the study of some simplified problems will shed light on the numerical difficulties associated with the limit of small Ekman numbers. We present here a study of such a problem, axisymmetric, where all motions are generated by differentially rotating boundaries in the presence of an imposed magnetic field. We will study the steady solution for a wide range of parameters, and try to infer conclusions on the asymptotic limit. The solution involves nice examples of boundary and internal shear layers driven by Ekman pumping and/or Hartmann electric currents.

* Corresponding author. Present address: I.G.P.P. University of California, Los Angeles, CA 90024-1567, USA.
E-mail: dormy@math.ucla.edu
[1] Present address: L.G.I.T., B.P. 53, F-38041 Grenoble, France.

0012-821X/98/$19.00 © 1998 Elsevier Science B.V. All rights reserved.
PII S0012-821X(98)00078-8

For one part (in the absence of a magnetic field), the motivation of this work is to use our three-dimensional convection code on a simple problem, easier to solve, and for which the asymptotic solution is well understood after the work of Proudman [1] and Stewartson [2]. This allows us to test the performances and the limitations of our approach. This problem, though much easier then 3D MHD convection (it is axisymmetric, no heat equation considered), is nevertheless attractive since it possesses a non-trivial solution in the asymptotic limit of vanishing viscosity. Moreover, this problem presents a singularity at the cylinder tangent to the inner core which is a major difficulty for a spherical numerical code to deal with. In this respect, we complete the previous numerical study of Hollerbach [3] restricted to larger Ekman values.

On the other hand, the problem has not been studied before in the presence of a magnetic field and with a conducting inner core. Hopefully, this numerical study may guide future analytical works. Kleeorin et al. [4] have already studied analytically a similar problem, but for an insulating inner core. This makes an important difference but they have been nevertheless able to compare some features of their solution with our numerical findings.

Finally, recent claims of a discovery of a differential rotation of the Earth's inner core [5,6] adds, if necessary, further motivation to understand better the flow between slightly differentially rotating spheres, and the effects of an imposed magnetic field on this flow.

2. Modelling

An incompressible fluid of kinematic viscosity ν, density ρ, magnetic diffusivity η, magnetic permeability μ_0, is enclosed between two spheres. The inner solid body is rotating slightly faster than the outer sphere (Fig. 1). Their rotation rates are, respectively, $(1+\varepsilon)\Omega$ and Ω. The equations are written in the rotating frame where the outer sphere is at rest.

Using the outer sphere radius r_o as length scale, the period of angular rotation of the inner sphere with respect to the outer one $[\varepsilon\Omega]^{-1}$ as unit of time, and the maximum amplitude of the imposed magnetic field $\boldsymbol{B_0}$ at the outer sphere to scale magnetic field $\boldsymbol{B}$,

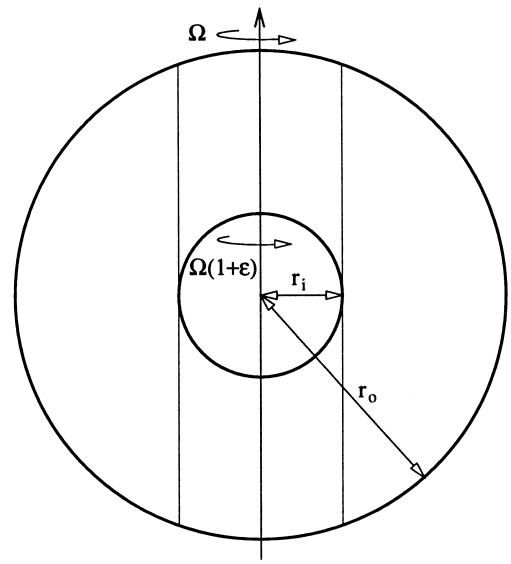

Fig. 1. The geometry of the problem is represented here in a meridional plane. The flow is driven by a slight differential rotation between the inner and the outer spheres, and remains axisymmetric.

the momentum equation and the induction equation write:

$$\begin{cases} \varepsilon\left(\dfrac{\partial \boldsymbol{u}}{\partial t} + \boldsymbol{u}\nabla\,\boldsymbol{u}\right) = -\nabla\pi + E\Delta\boldsymbol{u} - 2\boldsymbol{z}\wedge\boldsymbol{u} \\ \qquad\qquad + \Lambda P_{\mathrm{m}}^{-1}E\varepsilon^{-1}(\nabla\wedge\boldsymbol{B})\wedge\boldsymbol{B} \\ \nabla\cdot\boldsymbol{u} = 0 \\ \dfrac{\partial\boldsymbol{B}}{\partial t} = \nabla\wedge(\boldsymbol{u}\wedge\boldsymbol{B}) \\ \qquad\qquad + P_{\mathrm{m}}^{-1}E\varepsilon^{-1}\Delta\boldsymbol{B} \\ \nabla\cdot\boldsymbol{B} = 0 \end{cases} \tag{1}$$

Where $\boldsymbol{z}$ is the unit vector parallel to the axis of rotation, and the centrifugal acceleration is included in π. The geometry is fully determined by the ratio r_i/r_o which has been kept constant and equal to 0.35 throughout this study. The outer boundary ($r = 1$) is insulating and rigid ($\boldsymbol{u} = 0$). The inner core has been taken as either insulating or conducting, with the same conductivity as the fluid and $\boldsymbol{u} = s\boldsymbol{e}_\phi$ where (s, ϕ, z) denote cylindrical coordinates. The dimensionless parameters are the Ekman number E, the Elsasser number Λ, and the magnetic Prandtl

number P_m:

$$E = \frac{\nu}{\Omega r_o^2}, \quad \Lambda = \frac{B_0^2}{\Omega \rho \mu \eta}, \quad P_m = \frac{\nu}{\eta} \tag{2}$$

Four dimensionless numbers, ε, E, Λ, P_m are thus necessary to describe the problem.

The computer code is written in such a way that we can investigate the effects of the nonlinear terms $\boldsymbol{u}\nabla \boldsymbol{u}$ and $\nabla \wedge (\boldsymbol{u} \wedge \boldsymbol{B})$. However, these terms play no part in the solution when ε is small enough ($\varepsilon \ll E^{1/3}$). With ε large enough, 3D instabilities are expected [7,8]. This study focuses on the linear solution. Then, the induced perturbation $\boldsymbol{b}$ to the force-free imposed field can be scaled such that:

$$\boldsymbol{B} = \boldsymbol{B}_0 + (\varepsilon P_m E^{-1})\boldsymbol{b} \tag{3}$$

and the system (Eq. 1) reduces to:

$$\begin{cases} \varepsilon \dfrac{\partial \boldsymbol{u}}{\partial t} & = -\nabla \pi + E \Delta \boldsymbol{u} - 2\boldsymbol{z} \wedge \boldsymbol{u} \\ & \quad + \Lambda(\nabla \wedge \boldsymbol{b}) \wedge \boldsymbol{B}_0 \\ \nabla \cdot \boldsymbol{u} & = 0 \\ \varepsilon P_m E^{-1} \dfrac{\partial \boldsymbol{b}}{\partial t} & = \nabla \wedge (\boldsymbol{u} \wedge \boldsymbol{B}_0) + \Delta \boldsymbol{b} \\ \nabla \cdot \boldsymbol{b} & = 0 \end{cases} \tag{4}$$

Two parameters only (E, Λ) fully determine steady state solutions. We have not investigated transient solutions and we have found (covering a large range of parameters E, Λ) that, within this frame (axisymmetric fields and $\varepsilon \ll 1$), the solution always settles down to a steady state.

3. Numerical model

Vector fields are decomposed into poloidal and toroidal parts:

$$\begin{aligned} \boldsymbol{u} &= \nabla \wedge (\nabla \wedge \boldsymbol{r} u_p) + \nabla \wedge \boldsymbol{r} u_t \\ &= \frac{1}{r \sin\theta} \nabla u_{pol} \wedge \boldsymbol{e}_\phi + u_\phi \boldsymbol{e}_\phi \end{aligned} \tag{5}$$

$$\begin{aligned} \boldsymbol{b} &= \nabla \wedge (\nabla \wedge \boldsymbol{r} b_p) + \nabla \wedge \boldsymbol{r} b_t \\ &= \frac{1}{r \sin\theta} \nabla b_{pol} \wedge \boldsymbol{e}_\phi + b_\phi \boldsymbol{e}_\phi \end{aligned} \tag{6}$$

Applying $\boldsymbol{r} \cdot \nabla \wedge$ and $\boldsymbol{r} \cdot \nabla \wedge \nabla \wedge$ to Eq.4 ,w e get the set of scalar equations:

$$\begin{cases} \varepsilon \dfrac{\partial}{\partial t} L_2 u_t & = E \Delta L_2 u_t + 2(\boldsymbol{z} \wedge \boldsymbol{r} \cdot \nabla) u_t - 2Q u_p \\ & \quad + \Lambda \boldsymbol{r} \cdot \nabla \wedge [(\nabla \wedge \boldsymbol{b}) \wedge \boldsymbol{B}_0] \\ \varepsilon \dfrac{\partial}{\partial t} L_2 \Delta u_p & = E L_2 \Delta^2 u_p + 2(\boldsymbol{z} \wedge \boldsymbol{r} \cdot \nabla) \Delta u_p \\ & \quad + 2Q u_t - \Lambda \boldsymbol{r} \cdot \nabla \wedge \nabla \\ & \quad \wedge [(\nabla \wedge \boldsymbol{b}) \wedge \boldsymbol{B}_0] \\ \varepsilon \dfrac{P_m}{E} \dfrac{\partial}{\partial t} L_2 b_t & = \Delta L_2 b_t + \boldsymbol{r} \cdot \nabla \wedge [\nabla \wedge (\boldsymbol{u} \wedge \boldsymbol{B}_0)] \\ \varepsilon \dfrac{P_m}{E} \dfrac{\partial}{\partial t} L_2 b_p & = \Delta L_2 b_p + \boldsymbol{r} \cdot \nabla \wedge (\boldsymbol{u} \wedge \boldsymbol{B}_0) \end{cases} \tag{7}$$

where L_2 is the Beltrami operator

$$\begin{aligned} L_2 &= \frac{\partial}{\partial r} r^2 \frac{\partial}{\partial r} - r^2 \Delta \\ &= -\frac{1}{\sin\theta} \frac{\partial}{\partial \theta} - \frac{1}{\sin^2\theta} \frac{\partial^2}{\partial \phi^2} \end{aligned} \tag{8}$$

and Q (introduced in Roberts [9]) is the operator defined as:

$$Q = \boldsymbol{z} \cdot \nabla - \tfrac{1}{2}(L_2 \boldsymbol{z} \cdot \nabla + \boldsymbol{z} \cdot \nabla L_2) \tag{9}$$

The scalar u_t, u_p, b_t, b_p are decomposed as:

$$X = \sum_l x_l(r) Y_l^0 \tag{10}$$

where $x_l(r)$ is sampled at discrete points. The cross products with $\boldsymbol{B}_0$ terms are computed in the physical space on Gauss collocation points, and are re-integrated in the spectral space. Vertical discretization is achieved using a Finite Difference scheme on a non-uniform grid stretched in the vicinity of the boundaries. It required 3000 shells to resolve the structures corresponding to an Ekman number of 10^{-8}. Eq. 7 is time stepped until the solution changes very little. Time integration is performed using a Crank–Nicholson scheme for diffusion terms, and an Adams–Bashforth scheme for other terms. Hence, the calculation of the diffusion term in each of Eq. 7 requires a product and an inversion of either 3- or 5-banded diagonal matrix at each time step.

4. Solution in the non-magnetic case

In a first step, we study how the solution in the non-magnetic case depends on the Ekman number E and we recover the asymptotic solution of Proudman and Stewartson [1,2].

4.1. Ekman layers

The numerical study of Ekman layers raises important problems that can be partly alleviated by using a radial grid, which is stretched in the vicinity of the two boundaries. It is essential to determine how many points are needed to resolve these viscous layers properly. Another difficulty is due to the steep gradient of the solution in these layers. Spurious oscillations often arise in the vicinity of shear layers; it is difficult to ensure that they are kept small, that they do not spoil the solution (they do not blow up), and that they do disappear in the steady state regime after time integration of transient states. Around ten points, in the layer, are found to be needed (if regularly spaced) to resolve the structure correctly with our finite difference scheme. When only three points are used, the structure of the layer is not properly solved, the calculated suction is erroneous, and this has important consequences on the main flow computed outside the layer, as can be seen on Fig. 2.

4.2. The Proudman–Stewartson solution

The problem we consider is strongly dominated by rotation. In the limit of small viscosity, all motions in the interior should satisfy the Proudman–Taylor theorem (vertically invariant flow):

$$\boldsymbol{u} = u_\phi(s)\boldsymbol{e}_\phi + \frac{1}{s}\nabla u_{\mathrm{pol}}(s) \wedge \boldsymbol{e}_\phi \tag{11}$$

The cylindrical surface that touches the inner sphere (the axis being the axis of rotation) will be referred to as the tangent cylinder. Outside the tangent cylinder, the asymptotic state is rigid rotation with the same angular velocity as the outer sphere:

$$u_\phi(s) = u_{\mathrm{pol}}(s) = 0 \tag{12}$$

Inside the tangent cylinder the angular velocity of geostrophic cylinders in the asymptotic regime is determined by the Proudman constraint in the volume and by Ekman pumping at the boundaries [1]:

$$u_\phi(s) = \frac{s(1-s^2)^{1/4}}{(1-s^2)^{1/4} + [1-(s/r_{\mathrm{i}})^2]^{1/4}} \tag{13}$$

$$u_{\mathrm{pol}}(s) = \frac{E^{1/2}s^2}{2\{(1-s^2)^{1/4} + [1-(s/r_{\mathrm{i}})^2]^{1/4}\}} \tag{14}$$

where the notations of Proudman are related to ours by:

$$\psi' = u_{\mathrm{pol}}, \quad \xi' = s u_\phi \tag{15}$$

The resulting cylindrical shear layer was investigated by Stewartson [2] who proved that it does not exert a control on the interior flow. This layer allows the flow to recirculate from one Ekman layer to the other and also accommodates the jump in azimuthal velocity. Stewartson showed that the shear layer can be divided into three nested layers. In the two outer layers, the z-dependence of u_ϕ may be neglected and interior viscous stresses on the cylinders balance viscous stresses on the boundaries. As a consequence, u_{pol} depends on z, as can be seen from the ϕ component of the momentum equation. For $s > r_{\mathrm{i}}$, the width of the layer is $O(E^{1/4})$ and both u_ϕ and u_{pol} decrease exponentially to zero. For $s < r_{\mathrm{i}}$, the width of the layer is $O(E^{2/7})$ and the s-dependence of the solution is given by Bessel and Gamma functions. The remaining discontinuity in u_{pol} is removed in the inner layer of width $O(E^{1/3})$. This layer is fully ageostrophic. Stewartson's analysis is well illustrated by the numerical study.

4.3. Numerical study

The solutions are calculated for different Ekman numbers. As the Ekman number is decreased, the singularity on the tangent cylinder develops, and more and more harmonics are required to represent the associated fields. Harmonics up to degree 1300 were needed to compute the solution for $E = 10^{-8}$. If one was to use fewer harmonics, this would lead to oscillations comparable to Gibbs phenomenon (see Morse and Feshbach [11]).

The results published by Hollerbach [3], for Ekman numbers $E_{\mathrm{H}} \geq 10^{-5}$ are reproduced (Fig. 3). We note that his Ekman number E_{H} is related to ours by:

$$E_{\mathrm{H}} = 2.37E \tag{16}$$

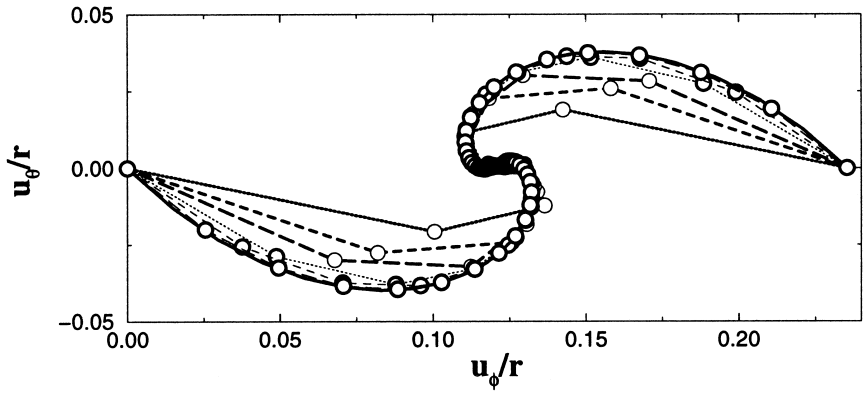

Fig. 2. Ekman spirals. u_θ/r versus u_ϕ/r for different number of grid points. $\theta = \pi/12$, $E = 10^{-5}$. These results compare very well with the linear theory [10].

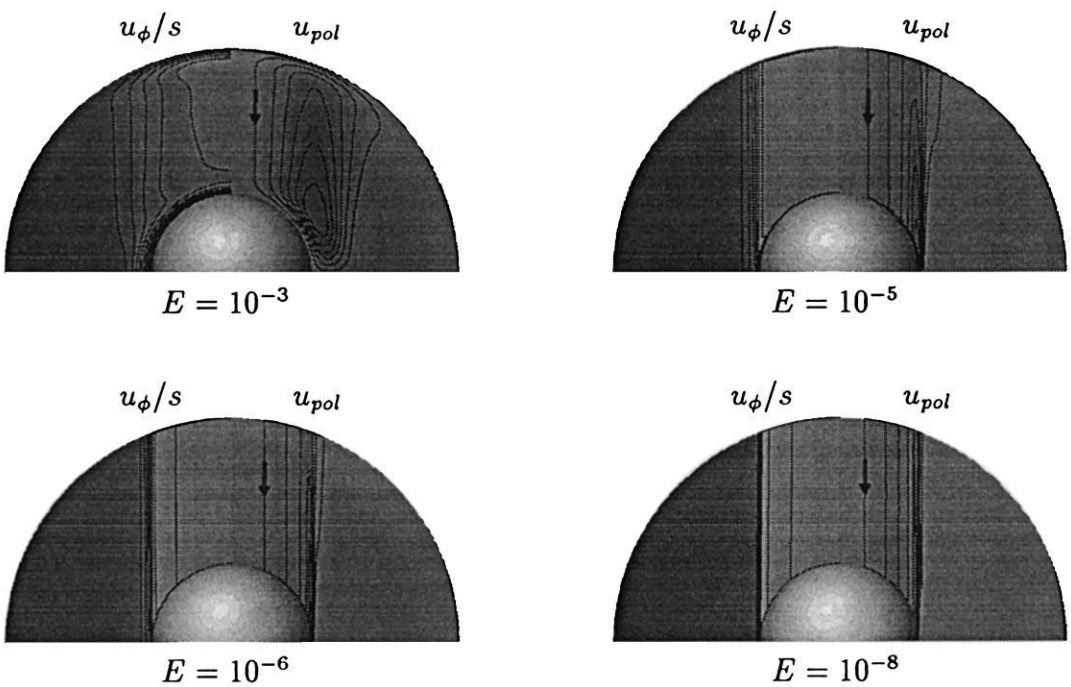

Fig. 3. Meridional section of angular velocity and $u_{\rm pol}$ for decreasing values of the Ekman number. First two figures compare very well with fig. 3 of [3]. The qualitative asymptotic behavior of flow synchronization with the inner core rotation close to $s = 0.35$ can be observed only on the two last figures.

We have recovered the interior geostrophic solution found by Proudman [1]. The meridional flow scales as $O(E^{1/2})$. The asymptotic behaviour of flow synchronization with the inner core rotation, as the tangent cylinder is approached, can be qualitatively observed only when $E \leq 10^{-6}$ (see Fig. 4). We have showed u_ϕ/s and $u_{\rm pol}$ as a function of z and r whereas we are, of course, interested by the (s,z)-structure of the solution; numerical convenience dictated our choice.

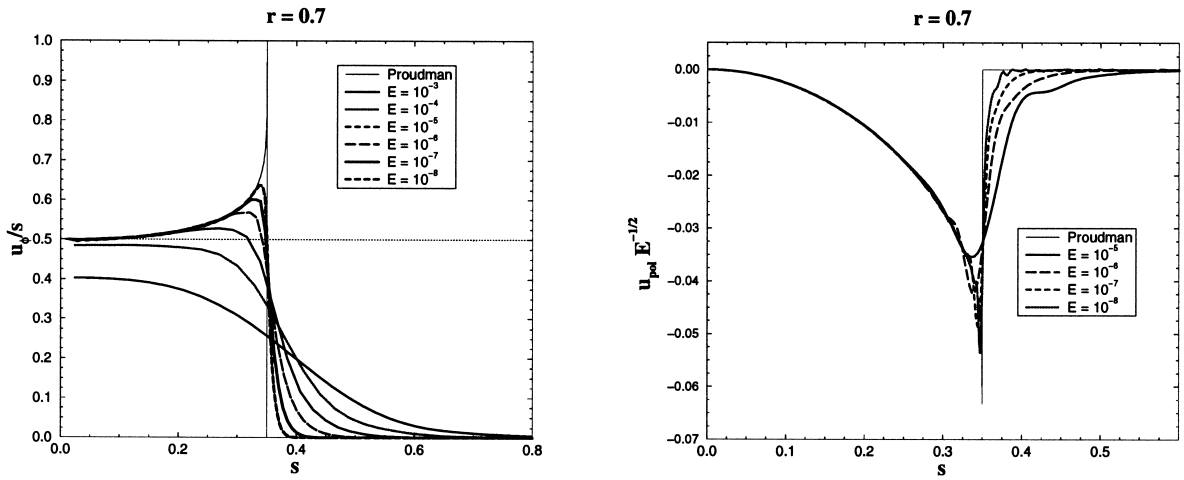

Fig. 4. Comparison with the Proudman solution. Angular velocity u_ϕ/s and poloidal scalar $u_{\rm pol}E^{1/2}$ versus s at $r = 0.7$ for different Ekman numbers. The Proudman solution is shown with a thin solid line. The angular velocity solutions for $E > 10^{-6}$ do not show the qualitative behavior of the asymptotic limit.

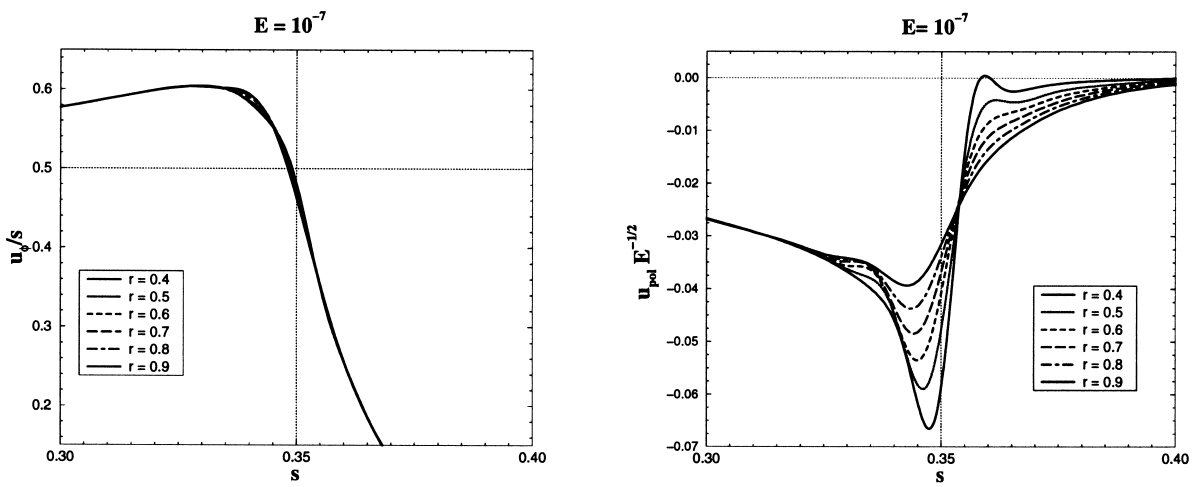

Fig. 5. Comparison with the Stewartson asymptotics. Angular velocity u_ϕ/s and poloidal field $u_{\rm pol}E^{1/2}$ versus s for different radius r. The inner ageostrophic layer of width $E^{1/3}$ is well distinguished from the outer layers where the azimuthal flow is geostrophic.

We can also study the departure from the Proudman solution in the cylindrical shear layer. Fig. 5 illustrates well the three nested layers. The inner layer of width $O(E^{1/3})$, where u_ϕ is ageostrophic, is well defined and is clearly embedded in the outer shear layers, where u_ϕ is z-independent but $u_{\rm pol}$ depends on z. The transport of fluid takes place at small z inside the tangent cylinder and at large z outside the tangent cylinder (see also Fig. 3). We have calculated the rate of exponential decrease of u_ϕ and $u_{\rm pol}$ with s for ($s > r_{\rm i}$) (Table 1). The agreement with the $E^{1/4}$ scaling of Stewartson is gratifying. In order to investigate the outer layers, we have subtracted the mainstream solution (Eqs. 13 and 14). Furthermore, we have stretched the s coordinate by the factor $E^{-2/7}$, for $s < r_{\rm i}$, and by the factor $E^{-1/4}$, for $s > r_{\rm i}$. The $O(E^{2/7})$ and $O(E^{1/4})$ scalings are vindicated (Fig. 6) inasmuch as the mainstream solution is

Table 1
$E^{1/3}$ and $E^{1/4}$ Stewartson layers

E	δ	λ_1	λ_2
10^{-5}	0.117	−23.02	19.5
10^{-6}	0.057	−38.41	33.89
10^{-7}	0.027	−73.40	63.94
10^{-8}	0.013	−129.52	106.71
	$E^{-0.32}$	$E^{-0.253}$	$E^{-0.249}$

δ is the width of the region where u_ϕ is ageostrophic. λ_1 and λ_2 are the rate of exponential decrease of, respectively, u_ϕ and $u_{\rm pol}$ outside the tangent cylinder. The last line gives the slope of the regression of these coefficients on $\log \boldsymbol{E}$.

recovered for a fixed distance to the tangent cylinder. However, the influence of the $O(E^{1/3})$ layer on $\boldsymbol{u}_{\rm pol}$ inside the tangent cylinder is also visible. Stretching now the s coordinate by $E^{-1/3}$, we characterize further the $O(E^{1/3})$ layer, whose influence on $\boldsymbol{u}_{\rm pol}$ is the strongest at small z (Fig. 7): the maxima are now aligned at a fixed distance to the tangent cylinder. Finally, Fig. 8 demonstrates that the width of the layer where $\boldsymbol{u}_\phi$ is ageostrophic scales with $E^{1/3}$ (see also Table 1) as predicted by Stewartson [2].

The scaling laws given by Stewartson apply well to the numerical solution for the range of Ekman numbers [10^{-6}, 10^{-8}], even if some features of the Stewartson solution are absent from the numerical solution. As an example, the amplitude of $E^{-1/2}\boldsymbol{u}_{\rm pol}$ increases rapidly with E^{-1} in the $E^{-1/3}$ inner layer (cf. Fig. 7), whereas Stewartson [2] predicted very slow variation ($\boldsymbol{E}^{-1/21}$). We note also that the z-dependence of $\boldsymbol{u}_{\rm pol}$ in the $E^{2/7}$ layer out of the $E^{1/3}$ inner layer is not linear as predicted (Fig. 5).

5. Magnetohydrodynamics

We now study how the flow is modified in the presence of an imposed magnetic field (Fig. 9).

5.1. The imposed magnetic field

Only current-free fields have been investigated ($\boldsymbol{J} = 0$). A current free field with external sources, when axisymmetric and dipolar, is aligned along the axis of rotation. As a consequence, shear at the tangent cylinder does not create electric currents. We have checked that, in this case, the shear at the tangent cylinder is not reduced by magnetic effects, and is even reinforced for strong fields, as the Lorentz force efficiently couples the fluid inside the tangent cylinder with the inner sphere. The asymptotic solution for large Λ consists of bulk rotation of the fluid volume inside the tangent cylinder together with the inner body and a bulk rotation of the fluid volume exterior to the cylinder together with the outer sphere (see also the recent study by Hollerbach [12]).

The problem is very different if the sources of the magnetic field are internal. For the imposed field one

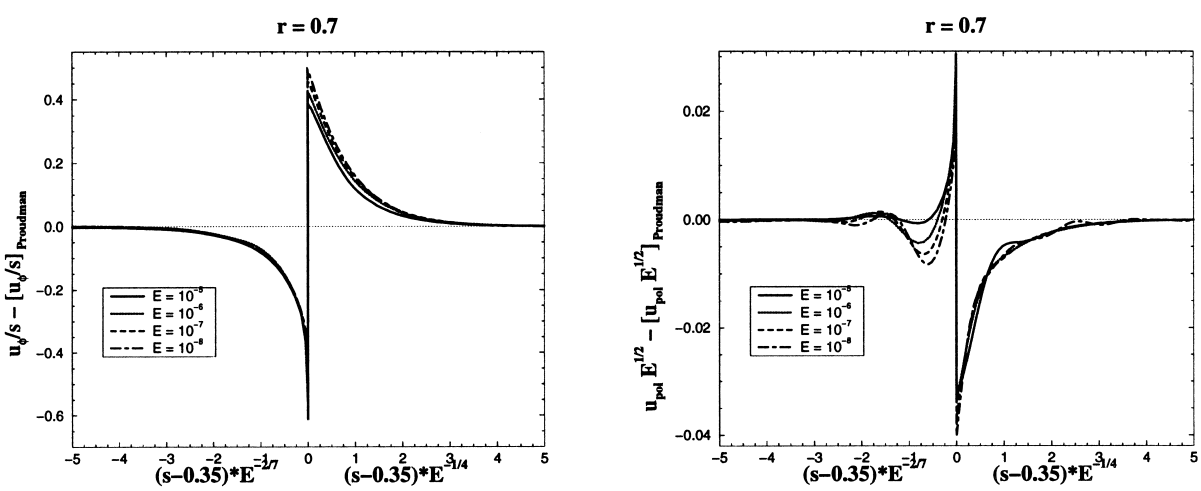

Fig. 6. The outer Stewartson layers. u_ϕ/s and $u_{\rm pol}E^{1/2}$ versus $E^{-2/7}(s-0.35)$ for $s < 0.35$ and $E^{-1/4}(s-0.35)$ for $s > 0.35$ $r = 0.7$.

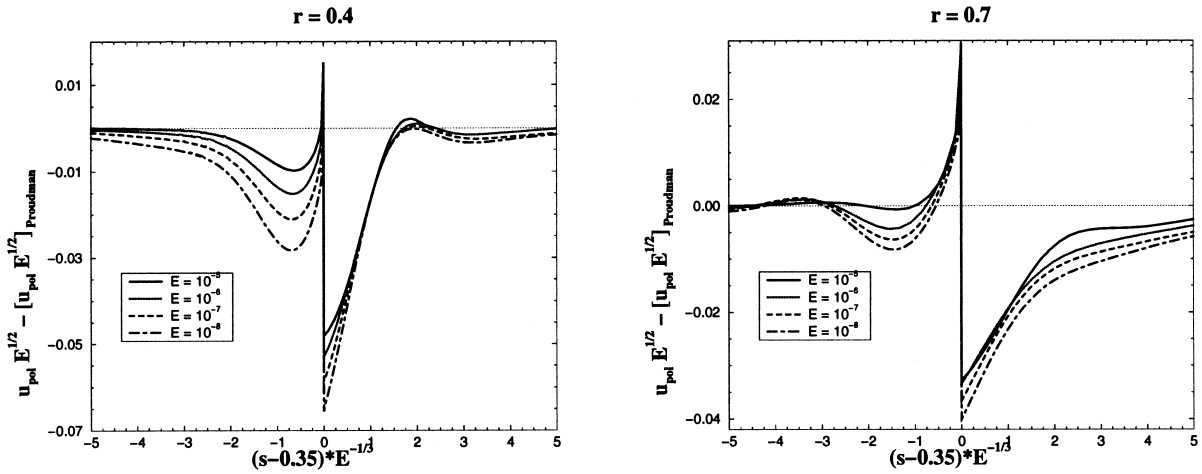

Fig. 7. The inner Stewartson layer. $u_{\mathrm{pol}}E^{1/2}$ versus $E^{-1/3}(s-0.35)$. $r = 0.4$ (left) and $r = 0.7$ (right).

then writes:

$$B_r = \frac{1}{r^3}\cos\theta, \quad B_\theta = \frac{1}{2r^3}\sin\theta \tag{17}$$

Here the magnetic field is not aligned along the axis of rotation, and will therefore cross the tangent cylinder. Important, too, is the variation of the field's magnitude: in this case the amplitude of the field, varying as r^{-3}, will be much stronger at the inner boundary. The field amplitude is 23 times larger at the inner sphere surface than at the boundary with the outer sphere. The local Elsasser number is thus 544 times greater than the value that we quote and calculate with the field at the outer boundary.

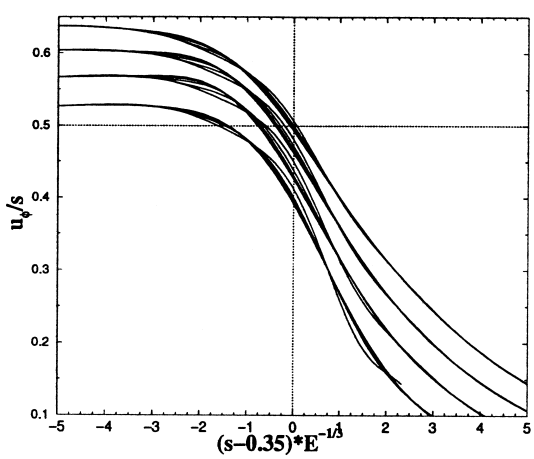

Fig. 8. The inner Stewartson layer. u_ϕ/s versus $E^{-1/3}(s-0.35)$ for different Ekman numbers ($E = 10^{-5}$, 10^{-6}, 10^{-7}, 10^{-8} from top to bottom) and different radius ($r = 0.4$, 0.5, 0.6, 0.7, 0.8, 0.9).

5.2. Comparison with previous studies and numerical tests

We present results obtained in the case of an insulating inner core in order to compare with the numerical study of Hollerbach [3]. The first effect of the magnetic force is to reduce the shear at the tangent cylinder. As the Elsasser number is increased the motion reduces to a rigid rotation with the outer sphere. Since both spheres are insulating, only viscous torques couple the solid boundaries. Fig. 10 shows how the solution evolves with increasing values of Λ at $E = 10^{-5}$. First, we see (for $\Lambda = 0$) the influence of the equatorial Ekman layer of width $E^{2/5}$ attached to the inner sphere. Comparison with [3] validates our code. The recent asymptotic study

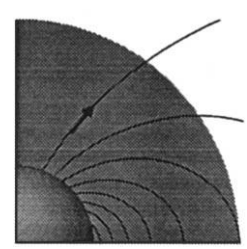

Fig. 9. The imposed magnetic induction.

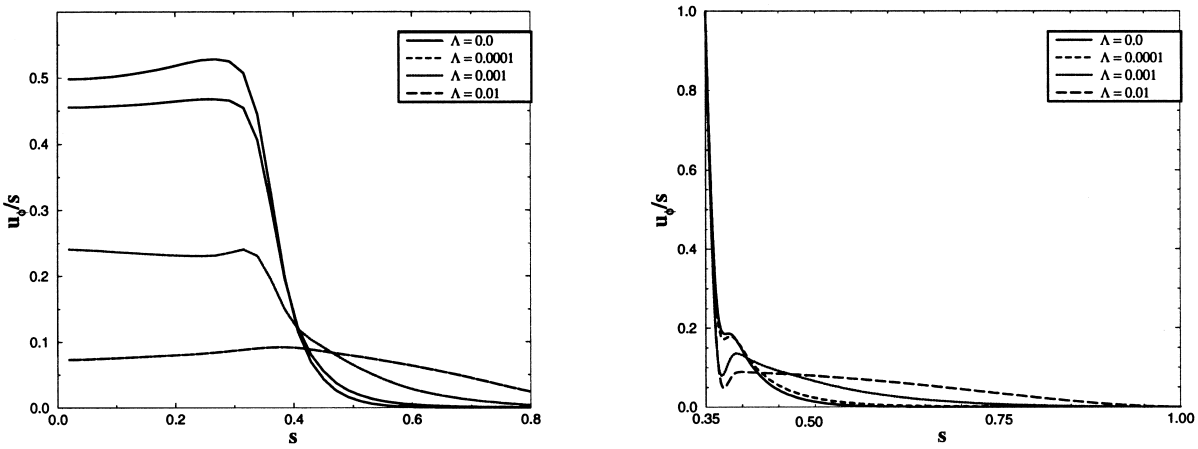

Fig. 10. Angular velocity with respect to the cylindrical radius s in the case of an insulating inner body; on the left hand side at $r = 0.75$, on the right hand side in an equatorial section. $E = 10^{-5}$.

of Kleeorin et al. [4] predicts a local minimum in angular velocity, in the vicinity of the equator of the inner body, in their strong field limit. The reversed flow can be seen on Fig. 10 (see the equatorial section). We note that they refer to a first version of our paper, in which the figures were numbered differently. Fig. 10 was referred to as Fig. 6.

We now restore finite conductivity to the inner core. The induction equation (its diffusive part) must now be solved inside the inner core, also. For non-zero Elsasser numbers, a magnetic torque applies on the inner boundary:

$$\Gamma_B = \Lambda r \iint B_r b_\phi \sin\theta \, \mathrm{d}S \tag{18}$$

Viscous torques act at both boundaries and are expressed as:

$$\Gamma_\nu = Er \iint \sin\theta r \frac{\partial}{\partial r} \frac{u_\phi}{r} \, \mathrm{d}S \tag{19}$$

Equilibrium between these torques is an additional check of our numerical calculation. They agree to within 1%.

5.3. The asymptotic state

We shall see that including a conducting inner core endows the solution with a rich variety of features. When the imposed magnetic field is strong enough, we again expect the solution to be close to a state of rigid rotation. But, now, the internal magnetic torque couples far more efficiently the fluid with the inner body than the external viscous torque with the outer body. As a consequence, most viscous effects are confined to the boundary layer attached to the outer sphere.

5.3.1. Ekman–Hartmann boundary layer

As the Elsasser number is increased from zero to $O(1)$ values, the Ekman boundary layer attached to the outer sphere gradually changes into an Hartmann type boundary layer. Boundary layers influenced by both rotation and magnetic field are reviewed by Acheson and Hide [13]. They give (in their section 5.2) a local derivation of the effect of the boundary layer on the flow and the magnetic field in the interior region when the boundary is insulating. With $\Lambda = 0$, the effect on the flow reduces to the Ekman suction. In the Hartmann limit, the normal component of $\boldsymbol{u}$ vanishes at the edge of the interior region. In between, elimination of the main flow vorticity in the expressions for u_r and j_r yields:

$$\frac{[j_r]}{[u_r]} = \frac{(\boldsymbol{B_0} \cdot \boldsymbol{r})}{B_0} \left(\left(1 + \Lambda_\perp^2\right)^{1/2} + \Lambda_\perp \right) \tag{20}$$

where $[\cdot]$ denotes jump across the boundary layer and $\Lambda_\perp$ is defined as:

$$\Lambda_\perp = \frac{1}{2\boldsymbol{z} \cdot \boldsymbol{r}} \frac{(\boldsymbol{B_0} \cdot \boldsymbol{r})^2}{B_0^2} \Lambda \tag{21}$$

Fig. 11 shows how the Ekman spirals on both boundaries are modified by magnetic effects. The

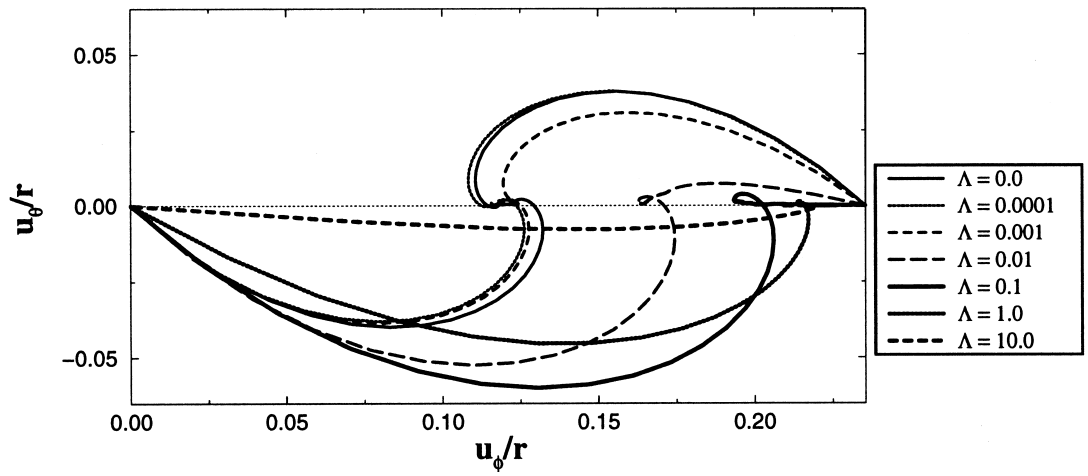

Fig. 11. Same as Fig. 2 in the presence of a magnetic field. As the Elsasser number increases, the angular velocity of the main flow approaches the angular velocity of the inner body. The θ-component of the velocity vanishes as the layers modify from Ekman type to Hartmann type.

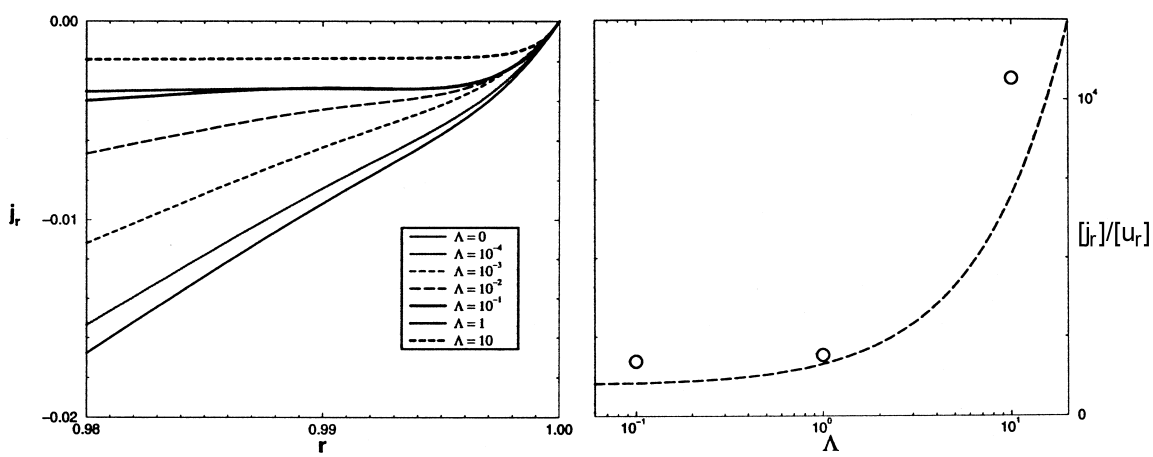

Fig. 12. The outer boundary layer for $E = 10^{-5}$ and $\theta = \pi/12$. On the left hand side, the radial electric current j_r. The current boundary layer is well characterized only for $\Lambda \geq 0.1$. On the right hand side, numerical (○) and theoretical (as given by Eq. 20) values for $[j_r]/[u_r]$ are represented.

meridional motion u_θ characteristic of the secondary flow in the Ekman layer is reduced and then suppressed as the local Elsasser number is increased to order one. Fig. 12 gives a comparison between Eq. 20 and our numerical results, for $E = 10^{-5}$ with increasing Λ at $\theta = \pi/12$.

5.3.2. Electric currents ejected from the Hartmann layer

In this section, we investigate the solution in the limit of large Elsasser numbers: the Hartmann limit. The flow is close to a state of rigid rotation and the main feature of the solution is a Hartmann boundary layer attached to the outer sphere through which the flow velocity decreases from $\sin\theta$ to 0.

We rescale the set of Eq. 4, retaining only the magnetic and viscous forces, and introducing the Hartmann number $M = (\Lambda/E)^{1/2}$. Only one parameter controls the system in this regime. Taking into account the geometry of the imposed field, and introducing $\xi = M(1-r)$ as radial boundary-layer

coordinate, we get:

$$\begin{cases} \dfrac{\partial^2 \boldsymbol{u}}{\partial \xi^2} - 2\cos\theta \dfrac{\partial \boldsymbol{b}}{\partial \xi} = 0 \\ \dfrac{\partial^2 \boldsymbol{b}}{\partial \xi^2} - 2\cos\theta \dfrac{\partial \boldsymbol{u}}{\partial \xi} = 0 \end{cases} \tag{22}$$

of which the solution is [14]:

$$\boldsymbol{u} = -\boldsymbol{b} = \sin\theta \left(1 - \mathrm{e}^{-2\cos\theta\xi}\right) \tag{23}$$

To ensure $\boldsymbol{j} \wedge \boldsymbol{B} = 0$, $\boldsymbol{b}$ has to be written:

$$\boldsymbol{b} = \frac{1}{\boldsymbol{r}\sin\theta} f\left(\frac{\sin^2\theta}{\boldsymbol{r}}\right) \tag{24}$$

Hence Eq. 23 is compatible with the bulk rotation that we have assumed as solution for the interior flow if:

$$\boldsymbol{b} = \frac{\sin\theta}{\boldsymbol{r}^2} \tag{25}$$

The equations are singular at the equator, where the magnetic field lines are parallel to the boundary.

5.3.3. The equatorial singularity

The singularity of the Hartmann layer has important consequences because it can be shown that the flux of electric currents leaving the boundary layer there does not vanish. We have not pushed the analytical study further (see Roberts [14] for a thorough investigation of such singularities) and we rely here on the numerical study to describe how the equatorial singularity affects the interior flow.

In the presence of rotation forces, the viscous layer is of Ekman type. It is also singular at the equator, where the rotation vector is parallel to the boundary. Numerical study seems necessary to unravel how rotational forces modify the Hartmann solution.

5.4. Numerical study

Fig. 13 illustrates how the flow synchronizes with the inner body as the Elsasser number is increased. For low Elsasser numbers, the electric currents are generated at the inner core and at the tangent cylinder whereas for larger values they are induced by the viscous shear at the outer boundary (see Fig. 14). For large Elsasser numbers, the numerical solution illustrates the role of the equatorial singularity. At high latitude, the electric currents flow along the lines of the imposed dipolar field. In the viscous boundary layer, they converge toward the outer equator and coming back to the inner core, they cross magnetic field lines which are parallel to the outer boundary. Indeed, the magnetic field and the electric field do not share the same symmetry with respect to the equatorial plane. This discrepancy between the symmetries of the two fields holds also in the intermediate regime where electric currents are induced by the remaining shear in the interior region. As a consequence, in the vicinity of the equatorial plane, magnetic forces do not vanish and make the interior flow depart from a state of rigid rotation. Fig. 15 shows the profile of the angular velocity in the equatorial plane for different strengths of the imposed magnetic field at $E = 10^{-5}$. The case $\Lambda = 10$ ($M = 10^3$) exemplifies departure from rigid rotation. Angular velocity reaches a maximum in the interior region. This maximum is still more pronounced at smaller Elsasser number (see $\Lambda = 0.1$, i.e. $M = 10^2$). The accelerated flow closely follows magnetic field lines. With increasing Elsasser number, the peak angular velocity migrates from the inner boundary to the outer sphere and the flow approaches a state of rigid rotation.

In order to better understand how the interior flow is accelerated, we have studied the magneto-viscous equilibrium, where the Coriolis forces are absent (see Figs. 16 and 17). As in Section 5.3.2, the system (Eq. 4) is rescaled so that the Coriolis force is eliminated in the limit $\Lambda \to \infty$, $E \to \infty$ and the remaining dimensionless number, the Hartmann number $M = (\Lambda/E)^{1/2}$ finite. Viscous shear (mainly in the outer boundary layer) generates electric Hartmann currents in the equatorial region crossing the magnetic field lines as described above. Super-rotation of the fluid is thus a magneto-viscous effect. Here, viscous forces only oppose the acceleration of the zonal flow in the equatorial region. The region of accelerated fluid has a banana shape centred on a magnetic field line. The maximum speed grows with increasing Hartmann number, in strong contrast with what is described above. Whereas a weak magnetic field ($M = 1$) changes the dynamics only slightly, a moderate magnetic field ($M = 3.16$) suffices to accelerate the equatorial interior flow. At $M = 316$ and $M = 1000$, the shear is well confined to the bound-

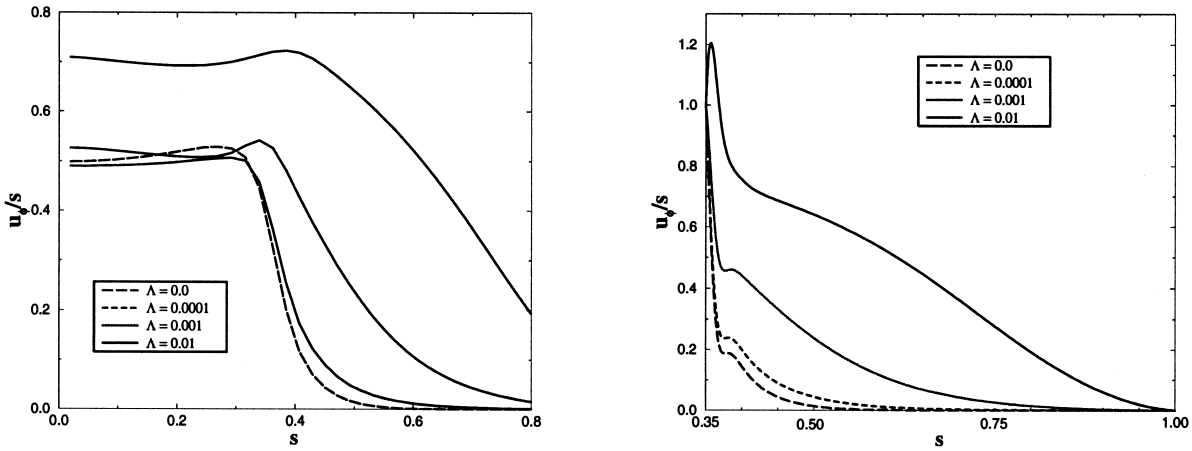

Fig. 13. Angular velocity with respect to the cylindrical radius s in the case of an conducting inner body; on the left hand side at $r = 0.75$ on the right hand side in an equatorial section. Ekman number is 10^{-5}.

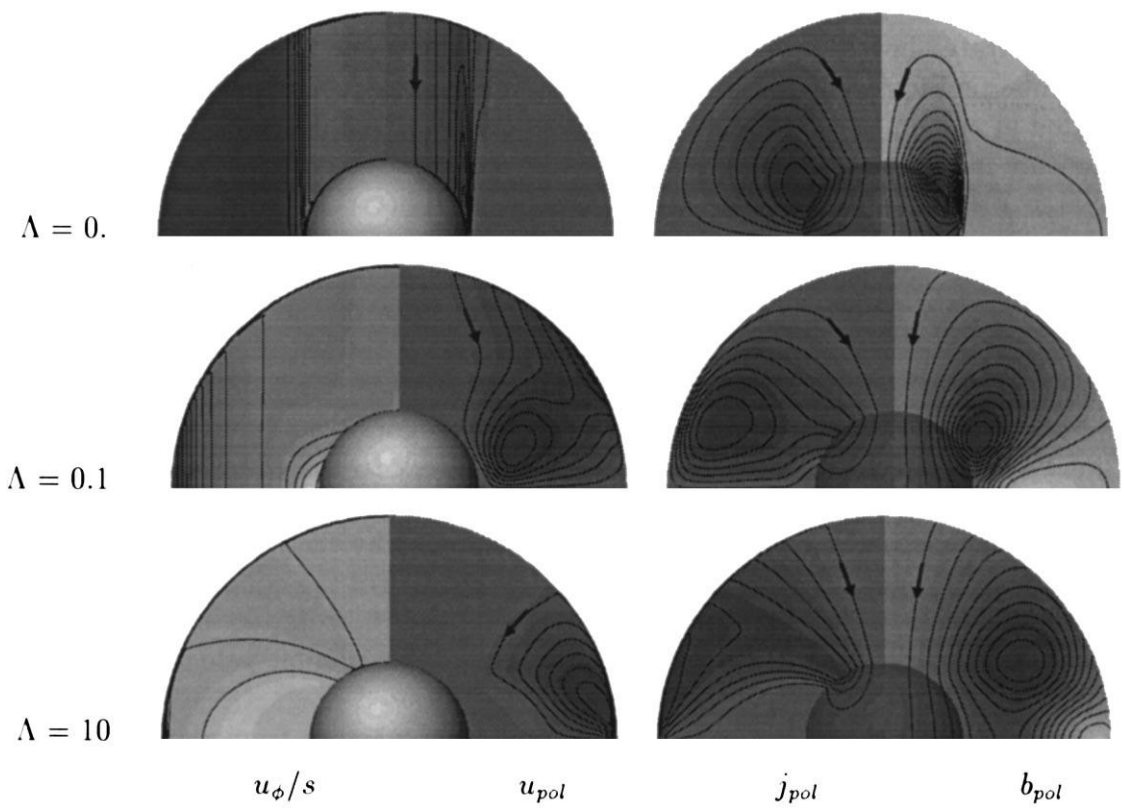

Fig. 14. Meridional sections for $E = 10^{-5}$, and increasing values of the Elsasser number.

ary layer parallel to the magnetic field line tangent to the outer sphere. The width of the sheared zone follows the $M^{-1/2}$ asymptotic law for boundary layer attached to a wall parallel to the imposed magnetic field [15]. This internal shear layer is associated with the recirculation of electric currents induced in the

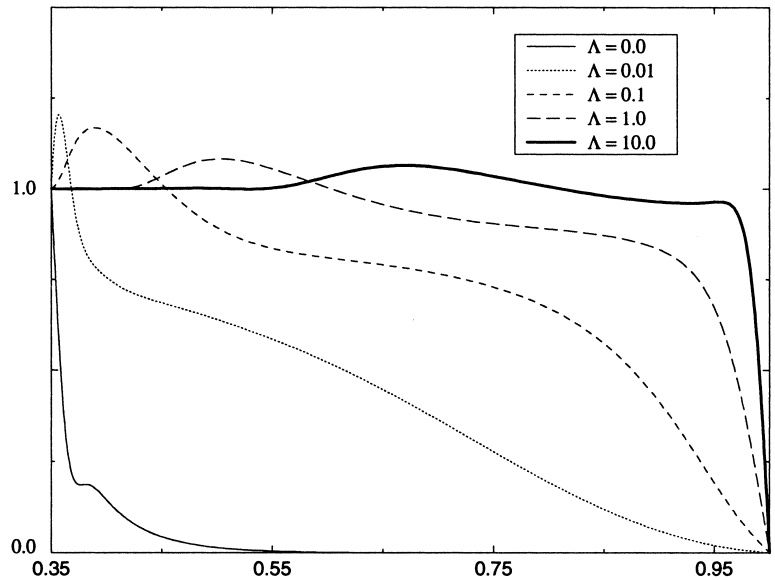

Fig. 15. Equatorial section of angular velocity at Ekman 10^{-5}. As the Elsasser number increases the flow synchronizes with the inner body. Unexpectedly the angular velocity of the flow locally exceeds the outer body's angular velocity.

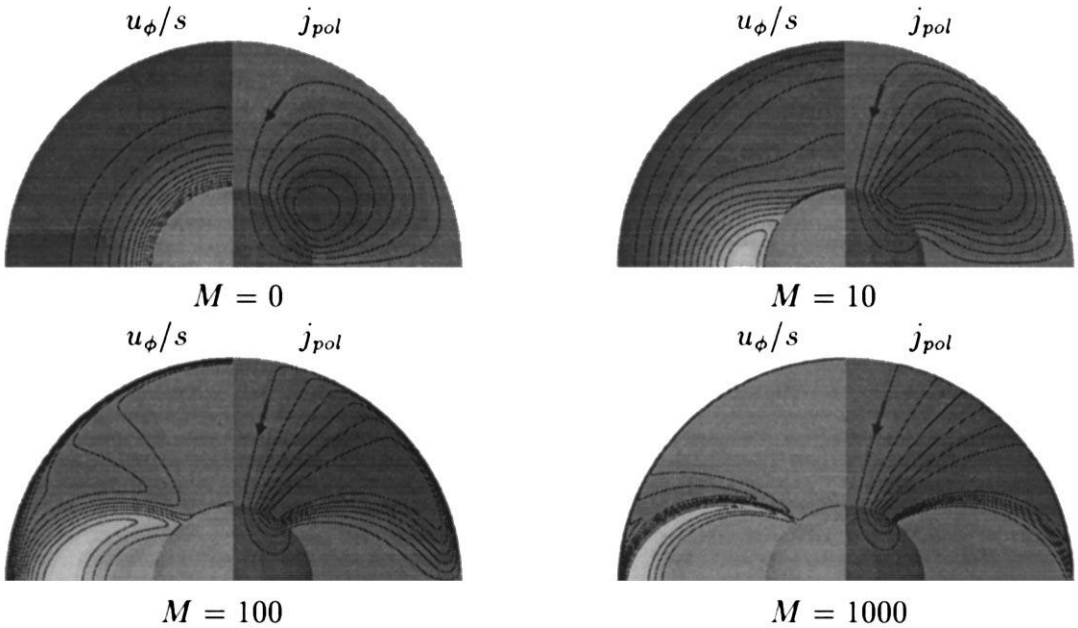

Fig. 16. Meridional representations of the zonal angular velocity u_ϕ/s and the meridional electric currents $j_{\rm pol}$ in the absence of rotational forces for increasing Hartmann numbers.

Hartmann layer as the internal Stewartson layer is associated with the recirculation of the meridional flow generated in the Ekman layers.

Comparison of the solutions with and without the rotational forces shows that they strongly inhibit the equatorial acceleration, which violates

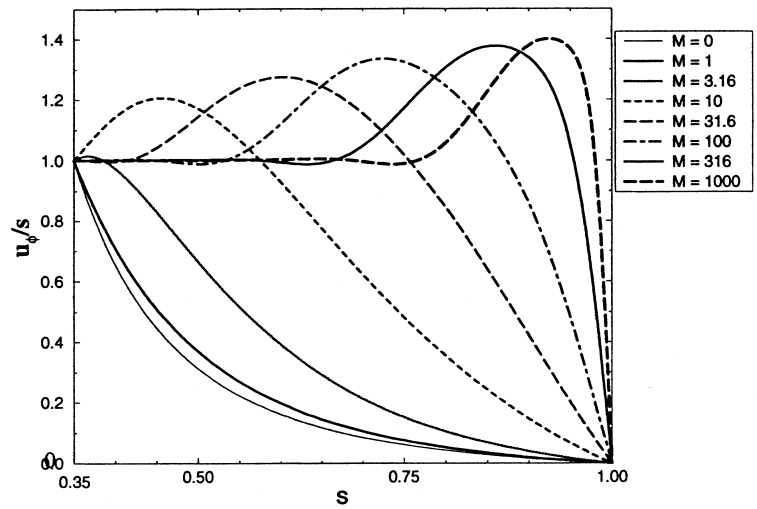

Fig. 17. Equatorial section of the angular velocity in the absence of rotational forces.

the Proudman–Taylor constraint. Besides, departure from a state of rigid rotation is less and less pronounced as viscosity is decreased (see Fig. 18). Decreasing the viscosity indeed restores the role of rotation forces, even for large Elsasser numbers.

Kleeorin et al. [4] have studied how geostrophic velocity (see Fig. 14) reduces to zero as the equator of the outer sphere is approached in the intermediate and strong field limit $E^{1/2} \ll \Lambda \ll 1$. They write the 'modified Taylor's constraint', balance between Maxwell stress in the mainstream flow and the viscous stress in the Ekman–Hartmann boundary layer. They describe a magnetic Proudman layer of width $E^{2/7}/\Lambda^{4/7}$ where viscous stress is negligible except at the top and bottom of the geostrophic cylinders. The remaining discontinuity in the geostrophic velocity is smoothed out in the viscous Stewartson $E^{2/5}$ layer attached to the equator. Kleeorin et al. [4] have compared their result with our numerical work. We note that figs. 12, 13 and 16 of that paper are now, respectively, Figs. 14, 15 and 18. Their table 2 gives the distance in our units from the outer sphere at which the rotation rate is one half the value outside the magnetic Proudman layer, according to their asymptotic theory. Only for $\Lambda = 0.1$, the $E^{2/5}$ Stewartson layer is thin compared to the magnetic Proudman layer. But the agreement between the theoretical and numerical works is striking and vindicates their analytical work.

Finally, the conducting inner body strongly influences the geometry of the electric currents. Electric currents can enter the inner body (because it is conducting) without shearing it (because it is rigid). Fig. 14 shows how the electric currents try to follow the magnetic field lines in the fluid all the way to the inner solid body where they loop back.

6. Conclusion

Very small values of the Ekman number have to be studied in order to get some insight into the asymptotic limit with a numerical study. Ekman numbers such as 10^{-5} are not small enough to describe even qualitatively the asymptotic regime, well-known in the non-magnetic case, and this conclusion holds also with strong magnetic effects. It would be helpful to develop a numerical algorithm to solve the thin boundary layers without increasing the number of grid points too much. The method used here limits the (axisymmetric) studies to E larger than 10^{-8} on some of the fastest computers available.

A new structure, defined as a maximum in the angular rotation inside the interior flow, arises in the equatorial region in the presence of an imposed field. It is present only when the solid inner body is conducting because, firstly, the main boundary layer is attached at the outer sphere and, secondly, the electric currents can loop in the inner body. This

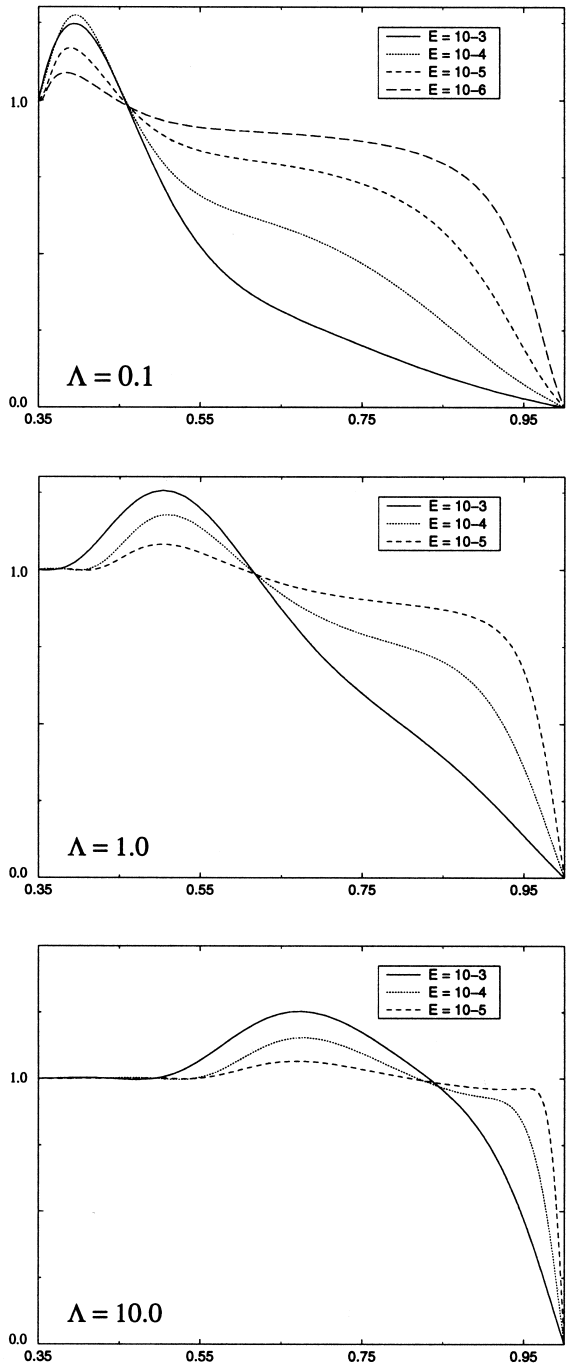

Fig. 18. Equatorial section of the angular velocity at Elsasser numbers 0.1, 1, 10 for varying Ekman numbers. One can see on each of these graphs how the amplitude of the super-rotation is controlled by viscous effects.

structure vanishes in the magnetostrophic limit but is present for Ekman number values in the range that can be investigated in the numerical geodynamo models that are being developed.

Acknowledgements

Authors wish to thank IDRIS for allowing access to Cray machines C94 and C98 through projects 960633 and 970633. We also thank the CCR Jussieu for unlimited access to a smaller Cray computer J98, which allowed us to develop and test our code, and was very useful for smaller runs. We wish to thank Andrew Soward for enlightening discussions, Henri-Claude Nataf for many useful comments and Douglas McLean for proof-reading the text. Philippe Cardin is grateful to Paul Roberts for sharing his understanding of Hartmann boundary layer singularities. ***[RO]***

References

[1] I. Proudman, The almost-rigid rotation of viscous fluid between concentric spheres, J. Fluid Mech. 1 (1956) 505–516.

[2] K. Stewartson, On almost rigid rotations, Part 2, J. Fluid Mech. 26 (1966) 131–144.

[3] R. Hollerbach, Magnetohydrodynamic Ekman and Stewartson layers in a rotating spherical shell, Proc. R. Soc. London A 444 (1994) 333–346.

[4] N. Kleeorin, I. Rogachevskii, A. Ruzmaikin, A.M. Soward, S. Starchenko, Axisymmetric flow between differentially rotating spheres in a dipole magnetic field, J. Fluid Mech. 344 (1997) 213–244.

[5] X. Song, P.G. Richards, Seismological evidence for differential rotation of the Earth's inner core, Nature 382 (1996) 221–224.

[6] W. Su, A. Dziewonski, R. Jeanloz, Planet within a planet: rotation of the inner core of the Earth, Science 274 (1996) 1883–1887.

[7] G. Dumas, A. Leonard, A divergence-free spectral expansion method for three-dimensional flows in spherical-gap geometries, J. Comput. Phys. 111 (1994) 205–219.

[8] L. Quartapelle, M. Verri, On the spectral solution of the three-dimensional Navier–Stokes equations in spherical and cylindrical regions, Comput. Phys. Commun. 90 (1995) 1–43.

[9] P.H. Roberts, On the thermal instability of a rotating fluid sphere containing heat sources, Philos. Trans. R. Soc. London A 263 (1968) 93–117.

[10] H.P. Greenspan, The Theory of Rotating Fluids, Cambridge University Press, Cambridge, 1969, 325 pp.
[11] P. Morse, H. Feshbach, Methods of Theoretical Physics, McGraw-Hill, New York, 1953, 1978 pp.
[12] R. Hollerbach, The influence of an axial field on magnetohydrodynamic Ekman and Stewartson layers, in the presence of a finitely conducting inner core, Acta Astron. Geophys. Univ. Comenianae XIX (1997) 263–275.
[13] D.J. Acheson, R. Hide, Hydromagnetics of rotating fluids, Rep. Prog. Phys. 36 (1973) 159–221.
[14] P.H. Roberts, Singularities of Hartmann layers, Proc. R. Soc. London A 300 (1967) 94–107.
[15] R. Moreau, Magnetohydrodynamics, Kluwer, Dordrecht, 1990, 313 pp.

Nonlinearity **12** (1999) 181–199. Printed in the UK PII: S0951-7715(99)94501-2

Stability of mixed Ekman–Hartmann boundary layers

B Desjardins†, E Dormy‡ and E Grenier†§

† Département de Mathématiques et d'Informatique, Ecole Normale Supérieure, 45 rue d'Ulm, 75005 Paris, France
‡ Institut de Physique du Globe de Paris, 4 place Jussieu, 75252 Paris, France
§ Laboratoire d'Analyse Numérique, CNRS URA 189, Université Paris 6, Place Jussieu, Paris, France

Received 22 May 1998
Recommended by S Fauve

Abstract. In this paper we study the nonlinear stability of Ekman–Hartmann-type boundary layers in a rotating magnetohydrodynamics flow in a half-space and between two planes. We prove rigorously that if the Reynolds number defined on boundary-layer characteristics is smaller than a critical value, the boundary layer is nonlinearly stable. It is shown that the normal component of the magnetic field increases the critical Reynolds number for instability.

AMS classification scheme numbers: 35Q35, 76U05, 76W05

1. Introduction and physical motivation

The stability of boundary-layer shear flows in magnetohydrodynamic rotating systems is of some general interest. We will concentrate our efforts in this study to the parameter range relevant for the Earth's core. The magnetohydrodynamic flow (MHD) in the Earth's core is believed to support a self-excited dynamo process generating the Earth's magnetic field. Although one has very few means of access to the deep interior of our planet, most of the parameters characterizing the dynamics in the core are quite well known [20, 21]. One can try to model the core by a spherical shell Ω filled with a conducting fluid of density ρ, kinematic viscosity ν, conductivity σ, which rotates rapidly with angular velocity Ω_0. We will only consider here phenomena occuring close to the outer bounding sphere. Important parameters are the Ekman number E, the Rossby number ε, the Elsasser number Λ and the magnetic Reynolds number θ defined introducing a typical velocity U and magnetic field B as

$$E = \nu\Omega_0^{-1}L^{-2}, \quad \varepsilon = U\Omega_0^{-1}L^{-1}, \quad \Lambda = \mathcal{B}^2\rho^{-1}\Omega_0^{-1}\mu_0^{-1}\eta^{-1}, \quad \theta = UL\eta^{-1}. \tag{1}$$

The Earth's core is believed to be in the asymptotic regime of small Ekman number ($E \simeq 10^{-15}$) and Rossby number ($\varepsilon \simeq 10^{-7}$).

Here we present the analytical study of a simplified problem. The stability of an Ekman–Hartmann layer is investigated at the boundary with a half-space $\mathbb{R}^2 \times [0, +\infty[$. We will consider the limit of small Rossby number ε at fixed Elsasser number Λ. It is natural to let $\varepsilon\theta$ go to zero as it appears to be the rescaled size of the self-induced magnetic field. Finally, we will let the Ekman number go to zero, and enforce it to be of size ε^2, in order to have a bounded and nonvanishing Ekman pumping term.

 © 1999 IOP Publishing Ltd and LMS Publishing Ltd

The stability of the Ekman–Hartmann layer at the core–mantle boundary is a critical issue in understanding how it may affect the main flow and thus the dynamo process. The stability of this layer is often assumed *a priori* in numerical works.

As the resolution of the Ekman–Hartmann boundary layers is difficult to achieve numerically [11], some models use free-slip boundary conditions to suppress those layers. Recently, Kuang and Bloxham [18] have highlighted the important effects of the boundary layers on the main flow (and field) in a computation of a hyper-viscous dynamo flow at moderate Ekman numbers.

Some other models suppress inertial and viscous effects in the momentum equation, this leads to the 'magnetostrophic' equilibrium, with the consequence of the Taylor constraint [23]. This simplification can be used to study the induction in the Earth's core [15], but leads to an underdetermination of the geostrophic flow. In practice one needs to restore viscous effects in boundary layers only, through pumping, giving a prescription for this flow.

Let us now describe the stability result. We define a boundary-layer Reynolds number by

$$Re_{BL} = u\frac{\varepsilon}{\sqrt{E}} \tag{2}$$

where u is a typical value of the rescaled velocity (and therefore of order 1). This number is the product of the typical value of the viscosity by the size $\sqrt{E}$ of the Ekman layer, divided by the viscosity E/ε. Notice that we build this Reynolds number on the size of the Ekman layer at $\Lambda = 0$ and not on the size of the Ekman–Hartman layer. This point of view clearly emphasizes the stabilizing role of the magnetic effects and the fact that the stability is controlled by only two dimensionless parameters, namely Λ and the particular combination $\varepsilon/\sqrt{E}$ (and of course on the colatitude).

As E is of order ε^2, Re_{BL} remains constant in the limiting process under consideration. We prove that the Ekman–Hartmann boundary layer is *linearly* and *nonlinearly stable* provided

$$Re_{BL} < Re_s(\Lambda, \theta_0) \tag{3}$$

where θ_0 is the colatitude, and give an explicit formula for Re_s. Of course this does not prove that the layer is unstable for $Re_{BL} \geqslant Re_s$ since Re_s is a poor bound. However, this bound seems physically nonempty, and Re_s is plotted in figure 1. We recall that as u being by definition of order 1 and as $\varepsilon \sim 10^{-7}$ and $E \sim 10^{-15}$, Re_{BL} is of order 1 and therefore completely falls within the values of Re_s given by figure 1.

This estimate on the critical Reynolds number is, however, far from being optimal. In the Ekman case ($\Lambda = 0$) for $\theta_0 = 0$, instabilities appear near $Re_{BL} = 55$ [19], and moreover the magnetic field has a stabilizing effect. In [8], using the methods introduced by Lilly [19] in the pure Ekman case ($\Lambda = 0$) we have computed the critical Reynolds number as a function of θ_0 and Λ for which linear instability occurs for the complete MHD problem.

The stabilizing effect of the magnetic field as well as the destabilizing effect of low latitudes can also be deduced from such an analysis.

2. The governing equations

Let Ω be a three-dimensional domain, with smooth boundaries (typically a ball, a half-space or region between two parallel planes), which will be called the core, Ω^c being the mantle to fit geophysical terminology.

In Ω, we consider the following MHD model, where we assume the fluid to be incompressible. We do not consider buoyancy effects here (see [16] for a discussion of the

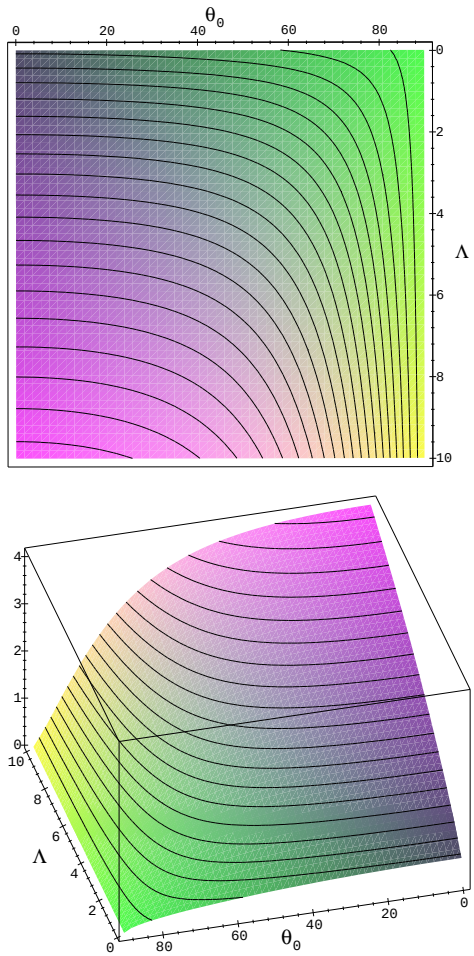

Figure 1. Re_s as a function of Elsasser Λ and colatitude θ_0. The stabilizing role of the normal component of the magnetic induction is clearly illustrated.

linear thermal Ekman layer). We neglect displacement currents in Maxwell's equations, and take into account the Coriolis effect

$$\begin{aligned}
&\rho(\partial_t \boldsymbol{u} + \boldsymbol{u}\cdot\nabla\boldsymbol{u}) - \mu\Delta\boldsymbol{u} + \nabla p + \rho\Omega_0 \boldsymbol{e}\times\boldsymbol{u} = \boldsymbol{j}\times\boldsymbol{B},\\
&\boldsymbol{j} = \mu_0^{-1}\mathrm{curl}\,\boldsymbol{B}, \quad \mathrm{curl}\,\boldsymbol{E} = -\partial_t\boldsymbol{B}, \quad \boldsymbol{j} = \sigma(\boldsymbol{E} + \boldsymbol{u}\times\boldsymbol{B}),\\
&\mathrm{div}\,\boldsymbol{B} = 0, \quad \mathrm{div}\,\boldsymbol{u} = 0.
\end{aligned} \tag{4}$$

$\boldsymbol{e}$ denotes a constant unit vector, direction of rotation, $\boldsymbol{j}$ denotes current density which is related through Ohm's law to the electric field $\boldsymbol{E}$ and the magnetic field $\boldsymbol{B}$. The electrical conductivity σ, the fluid dynamic viscosity μ and density ρ are positive constants. As a result, we can eliminate $\boldsymbol{j}$ and $\boldsymbol{E}$ in the above system and obtain

$$\begin{aligned}
&(\partial_t \boldsymbol{u} + \boldsymbol{u}.\nabla\boldsymbol{u}) - \nu\Delta\boldsymbol{u} + \frac{\nabla p}{\rho} + \Omega_0 \boldsymbol{e}\times\boldsymbol{u} = \frac{1}{\rho\mu_0}\mathrm{curl}\,\boldsymbol{B}\times\boldsymbol{B},\\
&\partial_t\boldsymbol{B} = \mathrm{curl}\,(\boldsymbol{u}\times\boldsymbol{B}) + \eta\Delta\boldsymbol{B},\\
&\mathrm{div}\,\boldsymbol{B} = 0, \quad \mathrm{div}\,\boldsymbol{u} = 0.
\end{aligned} \tag{5}$$

Where the magnetic diffusivity η is defined as $(\sigma\mu_0)^{-1}$ and the kinematic viscosity ν is defined as $\nu = \mu/\rho$.

Outside the shell, the mantle Ω^c is considered as an electrical insulator and the magnetic field is assumed to be harmonic:

$$\operatorname{curl} \boldsymbol{B} = 0, \quad \operatorname{curl} \boldsymbol{E} = -\partial_t \boldsymbol{B}, \quad \operatorname{div} \boldsymbol{E} = 0, \quad \operatorname{div} \boldsymbol{B} = 0. \tag{6}$$

At the core–mantle boundary $\partial\Omega$, we impose the velocity of the fluid to vanish and the normal component of the Poynting vector $\boldsymbol{E} \times \boldsymbol{B}$ to be continuous.

Introducing typical quantities

$$\boldsymbol{u} = U\boldsymbol{u}', \quad \boldsymbol{B} = \mathcal{B}\boldsymbol{B}', \quad \boldsymbol{E} = \mathcal{E}\boldsymbol{E}', \quad p = \pi p', \quad \boldsymbol{x} = L\boldsymbol{x}', \quad t = Tt',$$

and dropping the primes, we adimensionalize (5) as follows:

$$\begin{aligned} \frac{L}{UT}\partial_t \boldsymbol{u} + \boldsymbol{u}\cdot\nabla\boldsymbol{u} + \frac{\pi}{\rho U^2}\nabla p + \frac{\Omega_0 L}{U}\boldsymbol{e}\times\boldsymbol{u} - \frac{\nu}{UL}\Delta\boldsymbol{u} &= \frac{\mathcal{B}^2}{\rho\mu_0 U^2}\operatorname{curl}\boldsymbol{B}\times\boldsymbol{B}, \quad \frac{L}{UT}\partial_t\boldsymbol{B} \\ = \operatorname{curl}(\boldsymbol{u}\times\boldsymbol{B}) + \frac{\eta}{UL}\Delta\boldsymbol{B}, \qquad \operatorname{div}\boldsymbol{B} &= 0, \quad \operatorname{div}\boldsymbol{u} = 0. \end{aligned} \tag{7}$$

Taking

$$T = \frac{L}{U}, \quad \mathcal{E} = \mathcal{B}U, \quad \pi = \rho U\Omega_0 L, \quad \varepsilon = \frac{U}{\Omega_0 L}, \quad E = \frac{\nu}{\Omega_0 L^2}, \quad P_m = \frac{\nu}{\eta},$$

and

$$\Lambda = \frac{\mathcal{B}^2}{\rho\Omega_0\mu_0\eta}, \quad \theta = \frac{P_m\varepsilon}{E} = \frac{UL}{\eta},$$

we rewrite (7)

$$\begin{aligned} &\partial_t\boldsymbol{u} + \boldsymbol{u}.\nabla\boldsymbol{u} + \frac{\nabla p}{\varepsilon} + \frac{\boldsymbol{e}\times\boldsymbol{u}}{\varepsilon} - \frac{E}{\varepsilon}\Delta\boldsymbol{u} = \frac{\Lambda}{\varepsilon\theta}\operatorname{curl}\boldsymbol{B}\times\boldsymbol{B} \\ &\partial_t\boldsymbol{B} = \operatorname{curl}(\boldsymbol{u}\times\boldsymbol{B}) + \frac{1}{\theta}\Delta\boldsymbol{B}, \qquad \operatorname{div}\boldsymbol{B} = 0, \quad \operatorname{div}\boldsymbol{u} = 0, \end{aligned} \tag{8}$$

and in Ω^c, we have

$$\operatorname{curl}\boldsymbol{B} = 0, \quad \operatorname{curl}\boldsymbol{E} = -\partial_t\boldsymbol{B}, \quad \operatorname{div}\boldsymbol{E} = 0, \quad \operatorname{div}\boldsymbol{B} = 0. \tag{9}$$

The numbers ε, E, P_m, Λ, θ are respectively called Rossby, Ekman, magnetic Prandtl, Elsasser and magnetic Reynolds numbers.

Next, we split the magnetic field $\boldsymbol{B}$ into two parts a large-scale, time-independent field $\boldsymbol{B}_0 = \boldsymbol{e}'$ and a scaled perturbation $\boldsymbol{b}$ such that

$$\boldsymbol{B} = \boldsymbol{e}' + \theta\boldsymbol{b},$$

so that (8) becomes in Ω

$$\partial_t\boldsymbol{u} + \boldsymbol{u}\cdot\nabla\boldsymbol{u} + \frac{\nabla p}{\varepsilon} - \frac{E}{\varepsilon}\Delta\boldsymbol{u} + \frac{\boldsymbol{e}\times\boldsymbol{u}}{\varepsilon} = \frac{\Lambda}{\varepsilon}\operatorname{curl}\boldsymbol{b}\times\boldsymbol{e}' + \frac{\Lambda\theta}{\varepsilon}\operatorname{curl}\boldsymbol{b}\times\boldsymbol{b} \tag{10}$$

$$\partial_t\boldsymbol{b} + \boldsymbol{u}\cdot\nabla\boldsymbol{b} = \boldsymbol{b}\cdot\nabla\boldsymbol{u} + \frac{\operatorname{curl}(\boldsymbol{u}\times\boldsymbol{e}')}{\theta} + \frac{\Delta\boldsymbol{b}}{\theta}, \qquad \operatorname{div}\boldsymbol{b} = 0, \quad \operatorname{div}\boldsymbol{u} = 0, \tag{11}$$

and in Ω^c

$$\operatorname{curl}\boldsymbol{b} = 0, \quad \operatorname{curl}\boldsymbol{E} = -\theta\partial_t\boldsymbol{b}, \quad \operatorname{div}\boldsymbol{E} = 0, \quad \operatorname{div}\boldsymbol{b} = 0. \tag{12}$$

The boundary conditions with an insulator can be written as

$$\boldsymbol{u} = 0 \quad \text{and} \quad (\boldsymbol{E}\times\boldsymbol{b})\cdot\boldsymbol{n} \quad \text{is continuous.} \tag{13}$$

Notice in particular that on the fluid's side, we have $\operatorname{curl}\boldsymbol{b} = \boldsymbol{E}$.

We consider in the following the orderings for $E, \Lambda, \theta, \varepsilon$:

$$\varepsilon \to 0, \quad \Lambda = \mathcal{O}(1), \qquad \varepsilon\theta \to 0 E \sim \varepsilon^2. \tag{14}$$

Notice that this includes $\theta \to 0$, $\theta = \mathcal{O}(1)$ or $\theta \to +\infty$ with $\varepsilon\theta \to 0$.

These limits are relevant to the Earth's core [10, 11]. Typical values for the Earth's core are $\varepsilon \sim 10^{-7}$, $\Lambda = \mathcal{O}(1)$, $\varepsilon\theta \sim 10^{-4}$, $E \sim 10^{-15}$, which fit (14).

3. Statement of the results

Let us first consider the case $\Omega = \mathbb{R}^2 \times [0, +\infty[$ (half-plane $z \geqslant 0$) and let $\boldsymbol{e}$ and $\boldsymbol{e}'$ be the vectors given in (e_1, e_2, e_3) basis by

$$\boldsymbol{e} = (-\sin\theta_0, 0, \cos\theta_0)$$

and

$$\boldsymbol{e}' = \frac{e'}{\|e'\|} \qquad \text{with} \quad e' = (\sin\theta_0, 0, 2\cos\theta_0),$$

where we identify (e_1, e_2, e_3) with (e_θ, e_ϕ, e_r) at a given colatitude θ_0. The normalized imposed magnetic field $\boldsymbol{e}'$ is assumed to be dipolar, even though any other case could have been considered. Let $U_\infty = (u_{1,\infty}, u_{2,\infty})$ be a given velocity at infinity $z = +\infty$. Let $(\boldsymbol{u}_s(x, y, z), \boldsymbol{b}_s(x, y, z))$ be the Ekman–Hartmann layer (see section 4.2 for analytic expressions) which matches the boundary conditions at $z = 0$ and satisfies $(u_{s,1}, u_{s,2}) = U_\infty$ at $z = +\infty$.

Theorem 3.1. *The Ekman–Hartmann layers are stable provided*

$$\|U_\infty\| \frac{\varepsilon}{\sqrt{E}} \leqslant Re_s(\Lambda, \theta_0),$$

where Re_s is given analytically in section 4.4. More precisely, under this condition, if $(\boldsymbol{u}, \boldsymbol{b})$ is another solution of (10), (11)

$$\sup_{t \geqslant 0} \int \left(|\boldsymbol{u}(t) - \boldsymbol{u}_s|^2 + \frac{\Lambda\theta}{\varepsilon} |\boldsymbol{b}(t) - \boldsymbol{b}_s|^2 \right) \leqslant \int \left(|\boldsymbol{u}(0) - \boldsymbol{u}_s|^2 + \frac{\Lambda\theta}{\varepsilon} |\boldsymbol{b}(0) - \boldsymbol{b}_s|^2 \right).$$

Let us now turn to the mathematical approach of the problem. By mathematical approach, we mean partial differential equation (PDE) type mathematics. The aim is to describe the convergence of solutions of (10), (11) in the limit (14), dealing with all the nonlinearities and boundary conditions. We would like to emphasize here the differences between the approaches of PDE people and physicists: mathematicians try to prove convergence of *time dependent, fully nonlinear* solutions of (10), (11) to solutions of some reduced systems (without small parameters) on arbitrarly large time intervals (rarely globally in time), the limit system being also *fully nonlinear* (as complex as two-dimensional Euler's equations). On the other side, physicists are more interested in *global in time* stability of *time independent boundary-layer profiles* (the stability in Lyapunov or dynamical sense). Each theorem is followed by a small comment to make the link with physical concerns.

In what follows, $\Omega = \mathbb{R}^2 \times [0, 1]$, and to simplify the analysis, $\boldsymbol{e} = \boldsymbol{e}' = e_3$, perpendicular to the boundary of Ω (a similar analysis could probably be done for different vectors $\boldsymbol{e}$ and $\boldsymbol{e}'$ provided they are not tangent to $\partial\Omega$). In section 4 we make the formal analysis of the limit $\varepsilon \to 0$. As usual in antisymmetric perturbations of parabolic systems, we have to distinguish between well-prepared an ill-prepared initial data [6, 14]. We prove, for well-prepared initial

data, that $\boldsymbol{j}^\varepsilon = \operatorname{curl} \boldsymbol{b}^\varepsilon$ goes to 0 and that $\boldsymbol{u}^\varepsilon$ converges to a two-dimensional vector field $\boldsymbol{u}_0^{int}$ independent on z, satisfying a damped Euler equation

$$\partial_t \boldsymbol{u}_0^{int} + (\boldsymbol{u}_0^{int} \cdot \nabla)\boldsymbol{u}_0^{int} + \beta \boldsymbol{u}_0^{int} + \nabla p_0^{int} = 0, \tag{15}$$

$$\operatorname{div} \boldsymbol{u}_0^{int} = 0, \tag{16}$$

where $\beta \boldsymbol{u}_0^{int}$ is a damping term, the sum of a viscous Ekman type pumping and a magnetic effect.

$$\beta = \sqrt{\frac{2E}{\varepsilon^2 \tan \frac{\tau}{2}}}$$

with

$$\tan \frac{\tau}{2} = \frac{1}{\Lambda + \sqrt{1 + \Lambda^2}}.$$

In section 4.2 we construct the Ekman–Hartmann layer, following for instance [1], and in section 4.3 we construct an approximate solution $(\boldsymbol{u}_\varepsilon^{app}, \boldsymbol{j}_\varepsilon^{app})$ starting from $\boldsymbol{u}_0^{int}$, an approximate solution which satisfies (10), (11) up to very small (in ε) error terms. It is classical that for $\beta = 0$, Sobolev norms of solutions of (15), (16) have a double exponential behaviour in time. But for $\beta > 0$ we prove the following.

Theorem 3.2. *Let $\beta > 0$ and let $s \geqslant 2$. There exists a positive function Γ_s such that every solution $\boldsymbol{u}_0^{int}$ of (15), (16) satisfies*

$$|\boldsymbol{u}_0^{int}(t, .)|_{L^\infty(\mathbb{R}^2)} \leqslant \Gamma_s(|\boldsymbol{u}_0^{int}(0, .)|_{H^{s+1}(\mathbb{R}^2)})\mathrm{e}^{-\beta t}. \tag{17}$$

This theorem is just the mathematical expression of the damping effect of the Ekman–Hartmann pumping: if the limit flow is initially smooth, it remains smooth and decreases exponentially in time. This is an improvement with respect to [14], since we can now get convergence results which are *global* in time, which was not the case in [14].

Let us now introduce the function

$$\Xi(k) = \sqrt{1 + k^2}\sqrt{k} \int_0^{+\infty} z(|\cos(zk)| + |\sin(zk)|)\mathrm{e}^{-z}\, \mathrm{d}z, \tag{18}$$

the critical Reynolds number for stability

$$Re_s(\Lambda) = \frac{1}{\Xi\left(\frac{1}{\Lambda + \sqrt{1+\Lambda^2}}\right)} \tag{19}$$

and the boundary-layer Reynolds number of $\boldsymbol{u}_0^{int}$ at time t,

$$Re_{BL}(t) = |\boldsymbol{u}_0^{int}(t, \cdot)|_{L^\infty(\mathbb{R}^2)} \frac{\varepsilon}{\sqrt{E}}. \tag{20}$$

We prove in section 5 the following convergence results.

Theorem 3.3. *Let $\boldsymbol{u}_0^{int}(0, x, y)$ be a given $H^s(\mathbb{R}^2)$ function, with $s > 5$. Let $\boldsymbol{u}_0^{int}(t, x, y)$ be the global solution of (15), (16) with initial data $\boldsymbol{u}_0^{int}(0, x, y)$. Let $\boldsymbol{u}_0^\varepsilon$ and $\boldsymbol{b}_0^\varepsilon$ be given sequences of $L^2(\Omega)$ and $L^2(\mathbb{R}^3)$ functions, respectively, such that*

$$\|\boldsymbol{u}_0^\varepsilon(x, y, z) - \boldsymbol{u}_0^{int}(0, x, y)\|_{L^2(\Omega)}^2 + \frac{\Lambda\theta}{\varepsilon}\|\boldsymbol{b}_0^\varepsilon(x, y, z)\|_{L^2(\mathbb{R}^3)}^2 \to 0 \qquad \text{as} \quad \varepsilon \to 0,$$

and let $\boldsymbol{u}^\varepsilon$, $\boldsymbol{b}^\varepsilon$ be global weak solutions of (10), (11) with initial data $\boldsymbol{u}_0^\varepsilon$ and $\boldsymbol{b}_0^\varepsilon$. Then

$$\|\boldsymbol{u}^\varepsilon - \boldsymbol{u}_0^{int}\|_{L^\infty([0,T], L^2(\mathbb{R}^2))} + \frac{\Lambda\theta}{\varepsilon}\|\boldsymbol{b}^\varepsilon\|_{L^\infty([0,T], L^2(\mathbb{R}^2))} \to 0$$

for every T such that

$$\sup_{0 \leqslant t \leqslant T} Re_{BL}(t) < Re_s(\Lambda). \tag{21}$$

This is just the mathematical formulation of the stability of Ekman–Hartmann layers, expressed in a time dependent framework of theorem 3.1.

We emphasize the fact that we are only considering so-called 'well-prepared initial data' (that is sequences of initial data u_0^ε which converge to a z independent function $\boldsymbol{u}_0^{int}$ as $\varepsilon \to 0$).

Notice that the boundary layers do not appear in the L^2 norm: we require no control of $\boldsymbol{u}_0^\varepsilon$ near the boundaries. In particular, there is no need to impose $\boldsymbol{u}_0^\varepsilon$ to behave like Ekman–Hartmann layers as described in section 4.2 near $z = 0$ and $z = 1$. Using the decay result of section 5.1, condition (21) can be replaced by a condition on the initial data $\boldsymbol{u}_0^{int}$, which gives the following.

Theorem 3.4. *Let $\boldsymbol{u}_0^{int}(0, x, y)$ be a given $H^s(\mathbb{R}^2)$ function, with $s > 5$. Let $\boldsymbol{u}_0^{int}(t, x, y)$ be the global solution of (15), (16) with initial data $\boldsymbol{u}_0^{int}(0, x, y)$. Let $\boldsymbol{u}_0^\varepsilon$ and $\boldsymbol{b}_0^\varepsilon$ be given sequences of respectively $L^2(\Omega)$ and $L^2(\mathbb{R}^3)$ functions such that*

$$\|\boldsymbol{u}_0^\varepsilon(x, y, z) - \boldsymbol{u}_0^{int}(0, x, y)\|^2_{L^2(\Omega)} + \frac{\Lambda\theta}{\varepsilon}\|\boldsymbol{b}_0^\varepsilon(x, y, z)\|^2_{L^2(\mathbb{R}^3)} \to 0 \qquad \text{as} \quad \varepsilon \to 0,$$

and let $\boldsymbol{u}^\varepsilon$, $\boldsymbol{b}^\varepsilon$ be global weak solutions of (10), (11) with initial data $\boldsymbol{u}_0^\varepsilon$ and $\boldsymbol{b}_0^\varepsilon$. Then

$$\|\boldsymbol{u}^\varepsilon - \boldsymbol{u}_0^{int}\|_{L^\infty([0,+\infty[,L^2(\mathbb{R}^2))} + \frac{\Lambda\theta}{\varepsilon}\|\boldsymbol{b}^\varepsilon\|_{L^\infty([0,+\infty[,L^2(\mathbb{R}^2))} \to 0$$

provided

$$\Gamma_{s-1}(|\boldsymbol{u}_0^{int}(0, ., .)|_{H^s(\mathbb{R}^2)})\frac{\varepsilon}{\sqrt{E}} < Re_s(\Lambda). \tag{22}$$

Physically, this ensures the global stability of the solution using the exponential decreasing of the maximum norm of the limit velocities.

We complete this study by proving in the spirit of [4, 9] (in the particular case $b = 0$ to shorten the proof) that weak solutions of (10), (11) are in fact strong and unique for ε small enough.

Theorem 3.5. *Let $s > 5$. Let $\boldsymbol{u}_0^{int}(0, x, y)$ be a given $H^s(\mathbb{R}^2)$ function satisfying the stability criterion (22). Let $\boldsymbol{u}_0^{int}(t, x, y)$ be the corresponding global solution of (15), (16) and let us construct the sequence of approximate solutions $\boldsymbol{u}_\varepsilon^{app}$ as in section 4.3 up to order ε^2. There exists $\varepsilon_0 > 0$ and $C_0 > 0$ such that if $\varepsilon < \varepsilon_0$ and if $\boldsymbol{u}_0$ satisfies*

$$|\nabla(\boldsymbol{u}_0 - \boldsymbol{u}_\varepsilon^{app})(0, x, y, z)|_{L^2(\Omega)} + \frac{|\left(\boldsymbol{u}_0 - \boldsymbol{u}_\varepsilon^{app}\right)(0, x, y, z)|_{L^2(\Omega)}}{\varepsilon^2} \leqslant C_0 \tag{23}$$

then denoting by $\boldsymbol{u}$ the global weak solutions of the rotating Navier–Stokes equations with initial data $\boldsymbol{u}_0$, we have $D^2\boldsymbol{u} \in L^2((0, +\infty) \times \Omega)$ and $\nabla\boldsymbol{u} \in L^\infty(0, +\infty; L^2(\Omega))$. Moreover, $\boldsymbol{u}$ is unique.

This has important physical consequences, as it guarantees that if at $t = 0$ the velocity field is smooth, it remains smooth for all time.

A similar result (weak solutions are in fact strong) in the case of the quasigeostrophic system with periodic boundary conditions and for ill-prepared initial data has been proved by Chemin in [4]. Notice, however, that here we deal with vanishing viscosity and that the initial conditions have large gradients in the boundary layers. In particular, the condition of smallness of ε which arises in [4] is never fulfilled in our case and we have to replace it by a condition of type (23).

4. Asymptotic behaviour

4.1. The limit system

As usual when we have two parameters which go to 0 (namely ε and $\varepsilon\theta$), the asymptotic expansion depends on particular links between these two quantities, and leads to many cases. In order to avoid technicalities and to get a simple asymptotic expansion we will restricit ourselves to one particular case and assume that $\theta = \varepsilon$. The general case (no link between θ and ε) can be treated in a similar way, and leads to similar first order and similar boundary-layer behaviour.

As usual in boundary-layer theory, we look for approximate solutions of the form

$$\boldsymbol{u}^{\varepsilon,app} = \sum_{k\geqslant 0} \varepsilon^k \left(\boldsymbol{u}_k^{int}(t,x,y,z) + \boldsymbol{u}_k^{BL}\left(t,x,y,\frac{z}{\lambda}\right) + \boldsymbol{u}_k^{BL,upper}\left(t,x,y,\frac{1-z}{\lambda}\right)\right), \tag{24}$$

and similarly we introduce $\boldsymbol{b}_k^{int}$, $\boldsymbol{b}_k^{BL}$ and $\boldsymbol{b}_k^{BL,upper}$, $\boldsymbol{j}_k^{int}$ defined by $\boldsymbol{j}_k^{int} = \operatorname{curl} \boldsymbol{b}_k^{int}$ and similarly for $\boldsymbol{j}_k^{BL}$ and $\boldsymbol{j}_k^{BL,upper}$, where λ denotes the size of the boundary layer that will be precised later on. Let $\boldsymbol{u}_k^{int} = (u_k^{int}, v_k^{int}, w_k^{int})$ and similarly for $\boldsymbol{u}_k^{BL}$ and $\boldsymbol{u}_k^{BL,upper}$. In (24) we enforce $\boldsymbol{u}_k^{BL}$ and $\boldsymbol{u}_k^{BL,upper}$ to be rapidly decreasing in their last argument. Putting (24) in (10), (11) and identifying the terms in ε^{-1} and θ^{-1} in the interior of the domain we get

$$e_3 \times (\boldsymbol{u}_0^{int} + \Lambda \boldsymbol{j}_0^{int}) + \nabla p_0^{int} = 0, \tag{25}$$

$$\partial_z \boldsymbol{u}_0^{int} + \operatorname{curl} \boldsymbol{j}_0^{int} = 0, \tag{26}$$

which leads to

$$\boldsymbol{j}_0^{int} = 0 \tag{27}$$

and

$$w_0^{int} = 0, \qquad \boldsymbol{u}_0^{int} \quad \text{depends only on } x, y \tag{28}$$

('magnetostrophic flow'). Now equalling the terms in ε^{-1} and θ^{-1} in the boundary layers gives that

$$p_0^{BL} = 0, \qquad b_{3,0}^{BL} = 0 \tag{29}$$

as usual in fluid boundary layers (the pressure does not vary much in the layer).

Equalling the terms of order ε^0 in (10) we get

$$\partial_t \boldsymbol{u}_0^{int} + (\boldsymbol{u}_0^{int} \cdot \nabla)\boldsymbol{u}_0^{int} + e_3 \times (\boldsymbol{u}_1^{int} + \Lambda \boldsymbol{j}_1^{int}) + \nabla p_1^{int} = 0$$

and taking the 2D curl of it, with $\omega_0^{int} = \partial_1 v_0^{int} - \partial_2 u_0^{int}$ (which only depends on x and y), we have

$$\partial_t \omega_0^{int} + (\boldsymbol{u}_0^{int} \cdot \nabla)\omega_0^{int} = \partial_z w_1^{int} + \Lambda \partial_z j_{3,1}^{int} \tag{30}$$

which after a vertical integration, since ω_0^{int} and u_0 do not depend on z, gives the two-dimensional limit equation

$$\partial_t \omega_0^{int} + (\boldsymbol{u}_0^{int}.\nabla)\omega_0^{int} = w_1^{int}(x,y,1) - w_1^{int}(x,y,0) + \Lambda j_{3,1}^{int}(x,y,1) - \Lambda j_{3,1}^{int}(x,y,0). \tag{31}$$

For $\Lambda = 0$ we recover the case of Ekman layers [12], as studied in [14]. We have now to compute w_1^{int} and $j_{3,1}^{int}$ on $z = 0$ and $z = 1$. For this we will study the boundary layers which appear near $z = 0$ and $z = 1$. We will prove in the next section that

$$w_1^{int}(x,y,1) - w_1^{int}(x,y,0) + \Lambda j_{3,1}^{int}(x,y,1) - \Lambda j_{3,1}^{int}(x,y,0) = -\beta \omega_0^{int}$$

with

$$\beta = \sqrt{\frac{2E}{\varepsilon^2 \tan\frac{\tau}{2}}}$$

where

$$\tan\frac{\tau}{2} = \frac{1}{\Lambda + \sqrt{1+\Lambda^2}}.$$

This will lead to the limit system on $\omega_0^{int}(t, x, y)$

$$\partial_t \omega_0^{int} + (\boldsymbol{u}_0^{int} \cdot \nabla)\omega_0^{int} + \beta\omega_0^{int} = 0 \tag{32}$$

with $\operatorname{div} \boldsymbol{u}_0^{int} = 0$, $w_0^{int} = 0$, $\omega_0^{int} = \partial_1 v_0^{int} - \partial_2 u_0^{int}$ and $\boldsymbol{j}_0^{int} = 0$. Notice that (32) has global strong solutions for smooth initial data.

4.2. Boundary layers

Let us focus on the boundary layer near $z = 0$. Let $\zeta = z/\lambda$ and let $\boldsymbol{u}_0^{BL} = (u_0^{BL}, v_0^{BL}, w_0^{BL})$, $\boldsymbol{u}_1^{BL} = (u_1^{BL}, v_1^{BL}, w_1^{BL})$, $\boldsymbol{b}_0^{BL} = (b_{1,0}^{BL}, b_{2,0}^{BL}, b_{3,0}^{BL})$, $\boldsymbol{b}_1^{BL} = (b_{1,1}^{BL}, b_{2,1}^{BL}, b_{3,1}^{BL})$, $\boldsymbol{j}_1^{BL} = (j_{1,1}^{BL}, j_{2,1}^{BL}, j_{3,1}^{BL})$ with

$$\lim_{\zeta=+\infty} \boldsymbol{u}_0^{BL} = \lim_{\zeta=+\infty} \boldsymbol{u}_1^{BL} = \lim_{\zeta=+\infty} \boldsymbol{b}_0^{BL} = \lim_{\zeta=+\infty} \boldsymbol{b}_1^{BL} = \lim_{\zeta=+\infty} \boldsymbol{j}_1^{BL} = 0.$$

By incompressibility condition, $\partial_\zeta w_0^{BL} = 0$ hence

$$w_0^{BL} = 0.$$

Moreover, in the boundary layer, (10) and (11) give

$$-v_0^{BL} - \frac{E}{\lambda^2}\partial_\zeta^2 u_0^{BL} = \frac{\Lambda}{\lambda}\partial_\zeta b_{1,0}^{BL}, \qquad \partial_\zeta^2 b_{1,0}^{BL} + \lambda\partial_\zeta u_0^{BL} = 0, \tag{33}$$

and

$$u_0^{BL} - \frac{E}{\lambda^2}\partial_\zeta^2 v_0^{BL} = \frac{\Lambda}{\lambda}\partial_\zeta b_{2,0}^{BL}, \qquad \partial_\zeta^2 b_{2,0}^{BL} + \lambda\partial_\zeta v_0^{BL} = 0, \tag{34}$$

hence, eliminating $b_{1,0}^{BL}$ and $b_{2,0}^{BL}$, we obtain

$$-\partial_\zeta v_0^{BL} - \frac{E}{\lambda^2}\partial_\zeta^3 u_0^{BL} = -\Lambda\partial_\zeta u_0^{BL}, \tag{35}$$

$$\partial_\zeta u_0^{BL} - \frac{E}{\lambda^2}\partial_\zeta^3 v_0^{BL} = -\Lambda\partial_\zeta v_0^{BL}. \tag{36}$$

It follows $A = \partial_\zeta u_0^{BL} + \mathrm{i}\partial_\zeta v_0^{BL} \in \mathbb{C}$ is solution of

$$\partial_\zeta^2 A = A\frac{\lambda^2}{E}(\Lambda + \mathrm{i}). \tag{37}$$

Defining τ by

$$\cos\tau = \frac{\Lambda}{\sqrt{1+\Lambda^2}}, \qquad \text{and} \qquad \sin\tau = \frac{1}{\sqrt{1+\Lambda^2}},$$

recalling that $A \to 0$ when $\zeta \to +\infty$ and choosing

$$\lambda = \left(\frac{E}{\Lambda}\right)^{\frac{1}{2}} \frac{\sqrt{\cos\tau}}{\cos\frac{\tau}{2}} = \sqrt{2E\tan\frac{\tau}{2}}, \tag{38}$$

we obtain

$$A(t,x,y,\zeta) = A(t,x,y,0)\exp\left(-\zeta\left(1+\mathrm{i}\tan\frac{\tau}{2}\right)\right),$$
$$\tan\frac{\tau}{2} = \frac{1}{\Lambda+\sqrt{1+\Lambda^2}}, \tag{39}$$

and

$$u_0^{BL}(t,x,y,\zeta)+\mathrm{i}v_0^{BL}(t,x,y,\zeta)$$
$$= (u_0^{BL}(t,x,y,0)+\mathrm{i}v_0^{BL}(t,x,y,0))\exp\left(-\zeta\left(1+\mathrm{i}\tan\frac{\tau}{2}\right)\right). \tag{40}$$

As a result, using $\boldsymbol{u}_0^{BL}+\boldsymbol{u}_0^{int}=0$ at $\zeta=0$, we finally write

$$u_0^{BL}(t,x,y,\zeta) = \exp(-\zeta)\left\{-u_0^{int}(t,x,y,0)\cos\left(\zeta\tan\frac{\tau}{2}\right) - v_0^{int}(t,x,y,0)\sin\left(\zeta\tan\frac{\tau}{2}\right)\right\} \tag{41}$$

$$v_0^{BL}(t,x,y,\zeta) = \exp(-\zeta)\left\{u_0^{int}(t,x,y,0)\sin\left(\zeta\tan\frac{\tau}{2}\right) - v_0^{int}(t,x,y,0)\cos\left(\zeta\tan\frac{\tau}{2}\right)\right\}. \tag{42}$$

Using the incompressibility condition

$$\partial_x u_0^{BL} + \partial_y v_0^{BL} + \frac{\varepsilon}{\lambda}\partial_\zeta w_1^{BL} = 0$$

we deduce

$$w_1^{BL}(t,x,y,\zeta) = -\exp(-\zeta)\omega_0^{int}(t,x,y)\sin\left(\zeta\tan\frac{\tau}{2}+\frac{\tau}{2}\right)\sqrt{E\varepsilon^{-2}\sin\tau}. \tag{43}$$

As $w_1^{int}+w_1^{BL}=0$ at $\zeta=0$, we get the succion expression

$$w_1^{int}(x,y,0) = \omega_0^{int}(t,x,y)\sin\left(\frac{\tau}{2}\right)\sqrt{E\varepsilon^{-2}\sin\tau}. \tag{44}$$

Next, using (11), $\partial^2_{\zeta\zeta}\boldsymbol{b}_0^{BL}=0$ and hence

$$\boldsymbol{b}_0^{BL}=0.$$

Moreover, $D = b_{1,1}^{BL}+\mathrm{i}b_{2,1}^{BL}$ satisfies

$$\partial_\zeta^2 D = -\frac{\lambda}{\varepsilon}A,$$

hence

$$D = \frac{\lambda}{\varepsilon}\frac{(u_0^{BL}+\mathrm{i}v_0^{BL})}{1+\mathrm{i}\tan\frac{\tau}{2}}, \tag{45}$$

and

$$b_{1,1}^{BL} = \left(u_0^{BL}\cos\frac{\tau}{2}+v_0^{BL}\sin\frac{\tau}{2}\right)\sqrt{E\varepsilon^{-2}\sin\tau}, \tag{46}$$

$$b_{2,1}^{BL} = \left(-u_0^{BL}\sin\frac{\tau}{2}+v_0^{BL}\cos\frac{\tau}{2}\right)\sqrt{E\varepsilon^{-2}\sin\tau}. \tag{47}$$

In other words, we have

$$b_{1,1}^{BL}(t,x,y,\zeta) = \exp(-\zeta)\left\{-u_0^{int}(t,x,y,0)\cos\left(\frac{\tau}{2}+\zeta\tan\frac{\tau}{2}\right)\right.$$
$$\left. - v_0^{int}(t,x,y,0)\sin\left(\frac{\tau}{2}+\zeta\tan\frac{\tau}{2}\right)\right\}\sqrt{E\varepsilon^{-2}\sin\tau} \tag{48}$$

$$b_{2,1}^{BL}(t,x,y,\zeta) = \exp(-\zeta)\left\{u_0^{int}(t,x,y,0)\sin\left(\frac{\tau}{2}+\zeta\tan\frac{\tau}{2}\right)\right.$$
$$\left. - v_0^{int}(t,x,y,0)\cos\left(\frac{\tau}{2}+\zeta\tan\frac{\tau}{2}\right)\right\}\sqrt{E\varepsilon^{-2}\sin\tau}. \tag{49}$$

From (48), (49), we deduce that

$$j_{3,1}^{BL}(t,x,y,\zeta) = -\exp(-\zeta)\omega_0^{int}(t,x,y)\cos\left(\frac{\tau}{2}+\zeta\tan\frac{\tau}{2}\right)\sqrt{E\varepsilon^{-2}\sin\tau}, \tag{50}$$

and using $j_{3,1}^{BL} + j_{3,1}^{int} = 0$ for $\zeta = 0$, the currents entering the layer write

$$j_{3,1}^{int}(t,x,y,0) = \omega_0^{int}(t,x,y)\cos\left(\frac{\tau}{2}\right)\sqrt{E\varepsilon^{-2}\sin\tau}. \tag{51}$$

It follows that

$$(w_1^{int} + \Lambda j_{3,1}^{int})(t,x,y,0) = \omega_0^{int}(t,x,y)\sqrt{\frac{E}{2\varepsilon^2\tan\frac{\tau}{2}}}. \tag{52}$$

Let us observe that in the limit $\Lambda \to 0$, $\lambda = \sqrt{2E}$, $\beta = \sqrt{2E/\varepsilon^2}$ and we recover classical Ekman layers:

$\boldsymbol{b}_1^{BL} \equiv 0$,

$u_0^{BL}(t,x,y,\zeta) = \exp(-\zeta)\{u_0^{BL}(t,x,y,0)\cos\zeta + v_0^{BL}(t,x,y,0)\sin\zeta\}$

$v_0^{BL}(t,x,y,\zeta) = \exp(-\zeta)\{-u_0^{BL}(t,x,y,0)\sin\zeta - v_0^{BL}(t,x,y,0)\cos\zeta\}$.

On the other hand, in the limit when $\Lambda \to +\infty$, $\lambda^2 \sim E/\Lambda$ and one obtains Hartmann-type layers

$$u_0^{BL}(t,x,y,\zeta) = u_0^{BL}(t,x,y,0)\exp(-\zeta), \tag{53}$$

$$v_0^{BL}(t,x,y,\zeta) = v_0^{BL}(t,x,y,0)\exp(-\zeta), \tag{54}$$

$$b_{1,1}^{BL} = \frac{\lambda}{\varepsilon}u_0^{BL}, \qquad b_{2,1}^{BL} = \frac{\lambda}{\varepsilon}v_0^{BL}. \tag{55}$$

Observe that the Ekman succion (44) vanishes in this case, whereas the magnetic damping (51) tends to infinity.

4.3. Construction of approximate solutions

It is now routine work to construct an approximate solution u_ε^{app}, j_ε^{app}, b_ε^{app} starting from u_0^{int} and the boundary-layer terms constructed in the previous section (see for instance [14] for details in the case of pure Ekman layer, and [6]). By approximate solutions, we mean functions which match the boundary conditions, which satisfy the divergence free conditions, and which satisfy (10) up to small error terms $R_{1,\varepsilon}$, and (11) up to $R_{2,\varepsilon}$, and moreover for every $t \geqslant 0$, $s > 5$,

$$|R_{1,\varepsilon}|_{L^2(\Omega)} \leqslant C\varepsilon^{\frac{1}{2}}\|u_0^{int}\|_{H^s(\mathbb{R}^2)}, \tag{56}$$

$$|R_{2,\varepsilon}|_{L^2(\Omega)} \leqslant C\varepsilon^{\frac{3}{2}}\|u_0^{int}\|_{H^s(\mathbb{R}^2)}, \tag{57}$$

$$|\boldsymbol{u}_\varepsilon^{app}|_{L^\infty(\Omega)} + \varepsilon^{-1}|\boldsymbol{b}_\varepsilon^{app}|_{L^\infty(\Omega)} \leqslant C\|u_0^{int}\|_{L^\infty(\mathbb{R}^2)}, \tag{58}$$

$$|\partial_x\boldsymbol{u}_\varepsilon^{app}|_{L^\infty(\Omega)} + |\partial_y\boldsymbol{u}_\varepsilon^{app}|_{L^\infty(\Omega)} + |\partial_z w_\varepsilon^{app}|_{L^\infty(\Omega)} \leqslant C\|u_0^{int}\|_{L^\infty(\mathbb{R}^2)}. \tag{59}$$

We have to estimate

$$g(\Lambda) = \sup_{x,y}\left|\int_0^{1/2} z|\partial_z u_0^{BL}|\mathrm{d}z\right|$$

and similar integrals for $\frac{1}{2} \leqslant z \leqslant 1$, and with u_0^{BL} replaced by v_0^{BL}. Using (41) we get

$$\partial_z u_0^{BL} = \lambda^{-1}\left(u_0^{int} - v_0^{int}\tan\frac{\tau}{2}\right)\cos\left(\zeta\tan\frac{\tau}{2}\right)\mathrm{e}^{-\zeta}$$
$$+\lambda^{-1}\left(u_0^{int}\tan\frac{\tau}{2} + v_0^{int}\right)\sin\left(\zeta\tan\frac{\tau}{2}\right)\mathrm{e}^{-\zeta}$$

and therefore

$$g(\Lambda) \leqslant \lambda \left|u_0^{int} - v_0^{int} \tan\frac{\tau}{2}\right| \int_0^{+\infty} \zeta \left|\cos\left(\zeta \tan\frac{\tau}{2}\right)\right| \mathrm{e}^{-\zeta}\, \mathrm{d}\zeta$$
$$+\lambda \left|u_0^{int} \tan\frac{\tau}{2} + v_0^{int}\right| \int_0^{+\infty} \zeta \left|\sin\left(\zeta \tan\frac{\tau}{2}\right)\right| \mathrm{e}^{-\zeta}\, \mathrm{d}\zeta$$
$$\leqslant \sqrt{1+\tan^2\left(\frac{\tau}{2}\right)}\lambda \|\boldsymbol{u}_0^{int}\|_{L^\infty(\mathbb{R}^2)} \int_0^{+\infty} \zeta \left(\left|\cos\left(\zeta \tan\frac{\tau}{2}\right)\right|\right.$$
$$\left. + \left|\sin\left(\zeta \tan\frac{\tau}{2}\right)\right|\right) \mathrm{e}^{-\zeta}\, \mathrm{d}\zeta.$$

Hence, as $\lambda = \sqrt{2E\tan(\tau/2)}$,

$$\left|\int_0^{1/2} z|\partial_z u_0^{BL}|\, \mathrm{d}z\right| \leqslant \sqrt{2E}\|\boldsymbol{u}_0^{int}\|_{L^\infty(\mathbb{R}^2)}\, \Xi\left(\tan\frac{\tau}{2}\right). \tag{60}$$

4.4. Slanted magnetic field and rotation

Let us consider in this section Ekman–Hartmann layers in an half-space, at a colatitude θ_0, with a uniform velocity field at infinity. The angle between the outward normal of the plane and the rotation vector is therefore θ_0. Let ψ be the angle of the magnetic field with the normal of the plane. Provided $\theta_0 \neq \pi/2$ and $\psi \neq \pi/2$, the calculations of the boundary layers can be carried out and the results are very similar to those of section 4.2. Let us present them in the case $\theta \in [0, \pi/2)$: the size of the layer λ is now

$$\lambda = \sqrt{\frac{2E}{\cos\theta_0}\tan\frac{\tau'}{2}},$$

where

$$\tan\frac{\tau'}{2} = \frac{\cos\theta_0}{\Lambda\cos^2\psi + (\Lambda^2\cos^4\psi + \cos^2\theta_0)^{1/2}}.$$

Let

$$Re_s(\Lambda,\theta) = \frac{\sqrt{\cos\theta_0}}{\Xi\left(\tan\frac{\tau'}{2}\right)}.$$

If we assume that the static magnetic field $\boldsymbol{B}_0$ is a pure axial dipole with internal sources, one obtains

$$\cos\psi = \frac{2\cos\theta_0}{(1+3\cos^2\theta_0)^{\frac{1}{2}}},$$

since $\boldsymbol{B}_0$ is proportional to $2\cos\theta_0 \mathrm{e}_r + \sin\theta_0 \mathrm{e}_{\theta_0}$ in spherical coordinates. Up to the above parameter changes, the boundary-layer expressions (41), (42), (48), (49) still hold in suitably scaled coordinates.

Those expressions clearly degenerate at the equator. For $\theta_0 = \pi/2$ (see [12]) and $\psi = \pi/2$ (see [22]), we do not study this singularity here, and will restrict our work to the values of θ_0 such that the layer is well-defined by the above expressions (roughly $\theta_0 < \pi/2 - E^{1/3}$).

5. Stability of mixed Ekman–Hartmann boundary layers

5.1. Time decay of limit solutions

The aim of this section is to prove that the maximum norm of the interior velocity $\boldsymbol{u}^{int}$ which is known to exist for all time (by a small modification of Youdovich argument) decays

exponentially in time. In terms of the vorticity $\omega_0^{int} = \operatorname{curl} \boldsymbol{u}_0^{int}$, the limit system reads as a damped two-dimensional Euler equation

$$\partial_t \omega_0^{int} + (\boldsymbol{u}_0^{int} \cdot \nabla)\omega_0^{int} + \beta\omega_0^{int} = 0 \qquad \text{in} \quad \mathcal{D}'(\mathbb{R}_t^+ \times \mathbb{R}^2) \qquad \text{and} \quad \omega_{0|t=0}^{int} = \omega_{0,0}^{int}.$$

As u_0^{int} is divergence free, we have for all $p \in [1, +\infty]$

$$|\omega_0^{int}(t, .)|_{L^p(\mathbb{R}^2)} = |\omega_{0,0}^{int}|_{L^p(\mathbb{R}^2)} \mathrm{e}^{-\beta t}.$$

Using the following classical estimates on commutators [17]

$$|[D^\alpha, u\nabla]\omega|_{L^2} \leqslant C(|\omega|_{L^\infty}|u|_{H^{s+1}} + |\nabla u|_{L^\infty}|\omega|_{H^s})$$

for $|\alpha| = s \geqslant 2$, and assuming that $\operatorname{div} u = 0$ and $\omega = \operatorname{curl} u$,

$$|\nabla u|_{L^\infty} \leqslant C(|\omega|_{L^\infty} + |\omega|_{L^2}) + C_s|\omega|_{L^\infty} \log_+\left(\frac{|\omega|_{H^s}}{|\omega|_{L^\infty}}\right)$$

we deduce that for all fixed $s \in \mathbb{N}$, $s \geqslant 2$

$$\frac{1}{2}\frac{\mathrm{d}}{\mathrm{d}t}|\omega_0^{int}(t, .)|^2_{H^s(\mathbb{R}^2)} + \beta|\omega_0^{int}(t, .)|^2_{H^s(\mathbb{R}^2)} \leqslant C(|\omega_0^{int}(t, .)|_{L^\infty(\mathbb{R}^2)} + |\nabla \boldsymbol{u}_0^{int}|_{L^\infty(\mathbb{R}^2)})|\omega_0^{int}(t, .)|^2_{H^s(\mathbb{R}^2)}.$$

It follows that defining α by

$$\alpha(t) = |\omega_0^{int}(t, .)|_{H^s(\mathbb{R}^2)} \mathrm{e}^{\beta t}, \tag{61}$$

we observe that

$$\alpha(t) \leqslant \alpha(0) + C\int_0^t \mathrm{e}^{-\beta s}\alpha(s) \times \left(|\omega_{0,0}^{int}|_{L^\infty(\mathbb{R}^2)} \log_+\left(\frac{\alpha(s)}{|\omega_{0,0}^{int}|_{L^\infty(\mathbb{R}^2)}}\right) + |\omega_{0,0}^{int}|_{L^\infty(\mathbb{R}^2)} + |\omega_{0,0}^{int}|_{L^2(\mathbb{R}^2)}\right) \mathrm{d}s. \tag{62}$$

Let $A = |\omega_{0,0}^{int}|_{L^2(\mathbb{R}^2)}$, let $B = |\omega_{0,0}^{int}|_{L^\infty} + |\omega_{0,0}^{int}|_{L^2(\mathbb{R}^2)}$, and let $\psi(t)$ be the right-hand side of (62). We have

$$\dot{\psi}(t) \leqslant C\exp(-\beta t)\psi(t)\left(A\log_+\left(\frac{\psi(t)}{A}\right) + B\right)$$

therefore

$$\int_{\psi(0)/A}^{\psi(t)/A} \frac{\mathrm{d}u}{u(\log_+ u + BA^{-1})} \leqslant \int_0^t CA\exp(-\beta s) \leqslant CA\beta^{-1}. \tag{63}$$

But $u\log u$ is not integrable near $+\infty$, therefore (63) bounds $\psi(t)$ and therefore $\alpha(t)$ using (62) in terms of $|\omega_{0,0}^{int}|_{L^2(\mathbb{R}^2)}$ and $|\omega_{0,0}^{int}|_{L^\infty}$ which gives theorem 3.2.

5.2. Proof of the stability result

We will only prove theorem 3.4, the proof of theorem 3.3 being similar and easier. Denoting $\boldsymbol{v} = \boldsymbol{u}_\varepsilon - \boldsymbol{u}_\varepsilon^{app}$, $\mathrm{e} = \boldsymbol{E}_\varepsilon - \boldsymbol{E}_\varepsilon^{app}$, and $\boldsymbol{m} = \boldsymbol{b}_\varepsilon - \boldsymbol{b}_\varepsilon^{app}$, we obtain

$$\partial_t \boldsymbol{v} + \boldsymbol{u}_\varepsilon \cdot \nabla \boldsymbol{v} + \boldsymbol{v} \cdot \nabla \boldsymbol{u}_\varepsilon^{app} - \frac{E}{\varepsilon}\Delta \boldsymbol{v} + \nabla\pi + \frac{e_3 \times \boldsymbol{v}}{\varepsilon} = \frac{\Lambda}{\varepsilon}\operatorname{curl} \boldsymbol{m} \times e_3 + \frac{\Lambda\theta}{\varepsilon}\left(\boldsymbol{b}_\varepsilon.\nabla \boldsymbol{m} + \boldsymbol{m}.\nabla \boldsymbol{b}_\varepsilon^{app}\right) - R_{1,\varepsilon}, \tag{64}$$

$$\operatorname{div} \boldsymbol{v} = 0, \quad \operatorname{div} \boldsymbol{m} = 0, \quad \text{and} \quad \boldsymbol{v}_{|\partial\Omega} \equiv 0, \tag{65}$$

and

$$\partial_t \boldsymbol{m} + \boldsymbol{u}_\varepsilon.\nabla \boldsymbol{m} + \boldsymbol{v}\cdot\nabla \boldsymbol{b}_\varepsilon^{app} - \boldsymbol{b}_\varepsilon\cdot\nabla\boldsymbol{v} - \boldsymbol{m}\cdot\nabla\boldsymbol{u}_\varepsilon^{app} = \frac{1}{\theta}\Delta\boldsymbol{m} - \frac{1}{\theta}\mathrm{curl}\,(\boldsymbol{v}\times e_3) - R_{2,\varepsilon}, \quad (66)$$

whereas in Ω^c, we simply have

$$\mathrm{curl}\,\boldsymbol{m} = 0, \quad \mathrm{curl}\,\boldsymbol{e} = -\theta\partial_t\boldsymbol{m}, \quad \mathrm{div}\,\boldsymbol{m} = 0 \quad \text{and} \quad \mathrm{div}\,\boldsymbol{e} = 0. \quad (67)$$

We recall estimates (56)–(60) for all time $t \geqslant 0$. In order to obtain energy bounds, we multiply (64) by $\boldsymbol{v}$ and (66) by $\boldsymbol{m}\Lambda\theta/\varepsilon$ to get

$$\begin{aligned}\frac{\mathrm{d}}{\mathrm{d}t}\int_\Omega \frac{1}{2}\left(|\boldsymbol{v}|^2 + \frac{\Lambda\theta}{\varepsilon}|\boldsymbol{m}|^2\right)\mathrm{d}x + \frac{E}{\varepsilon}\int_\Omega |\nabla\boldsymbol{v}|^2\,\mathrm{d}x + \frac{\Lambda}{\varepsilon}\int_\Omega |\mathrm{curl}\,\boldsymbol{m}|^2\,\mathrm{d}x \\ + \frac{\Lambda}{\varepsilon}\int_{\partial\Omega}(\mathrm{curl}\,\boldsymbol{m}\times\boldsymbol{m})\cdot\boldsymbol{n} \leqslant |R_{1,\varepsilon}|_{L^2(\Omega)}|\boldsymbol{v}|_{L^2(\Omega)} + \frac{\Lambda\theta}{\varepsilon}|R_{2,\varepsilon}|_{L^2(\Omega)}|\boldsymbol{m}|_{L^2(\Omega)} \\ + \left|\int_\Omega\left(\frac{\Lambda\theta}{\varepsilon}\boldsymbol{m}_i\boldsymbol{m}_k + \boldsymbol{v}_i\boldsymbol{v}_k\right)\partial_i\boldsymbol{u}_{k,\varepsilon}^{app}\,\mathrm{d}x\right| + \left|\int_\Omega \frac{\Lambda\theta}{\varepsilon}\left(\boldsymbol{m}_i\boldsymbol{v}_k + \boldsymbol{m}_k\boldsymbol{v}_i\right)\partial_i\boldsymbol{b}_{k,\varepsilon}^{app}\,\mathrm{d}x\right|,\end{aligned}$$

where $\boldsymbol{n}$ denotes the outward normal to Ω. Next, we observe using the fact that $\boldsymbol{v}$ vanishes on $\partial\Omega$

$$\int_\Omega \boldsymbol{m}_i\boldsymbol{m}_k\partial_i\boldsymbol{u}_{k,\varepsilon}^{app}\,\mathrm{d}x = -\int_\Omega \boldsymbol{u}_{k,\varepsilon}^{app}\boldsymbol{m}_i(\partial_i\boldsymbol{m}_k - \partial_k\boldsymbol{m}_i)\,\mathrm{d}x,$$

hence

$$\begin{aligned}\left|\int_\Omega \frac{\Lambda\theta}{\varepsilon}\boldsymbol{m}_i\boldsymbol{m}_k\partial_i\boldsymbol{u}_{k,\varepsilon}^{app}\,\mathrm{d}x\right| &\leqslant C\frac{\Lambda\theta}{\varepsilon}|\mathrm{curl}\,\boldsymbol{m}|_{L^2(\Omega)}|\boldsymbol{m}|_{L^2(\Omega)}\Gamma_0\exp(-\beta t), \\ &\leqslant \kappa\frac{\Lambda}{\varepsilon}|\mathrm{curl}\,\boldsymbol{m}|^2_{L^2(\Omega)} + C_\kappa\Gamma_0^2\frac{\Lambda\theta^2}{\varepsilon}|\boldsymbol{m}|^2_{L^2(\Omega)}\exp(-2\beta t).\end{aligned}$$

Similarly, we have

$$\int_\Omega(\boldsymbol{m}_i\boldsymbol{v}_k + \boldsymbol{m}_k\boldsymbol{v}_i)\partial_i\boldsymbol{b}_{k,\varepsilon}^{app}\,\mathrm{d}x = \int_\Omega \boldsymbol{b}_{k,\varepsilon}^{app}(\boldsymbol{m}_i(\partial_k\boldsymbol{v}_i - \partial_i\boldsymbol{v}_k) + \boldsymbol{v}_i(\partial_k\boldsymbol{m}_i - \partial_i\boldsymbol{m}_k))\,\mathrm{d}x$$

hence

$$\begin{aligned}&\left|\int_\Omega \frac{\Lambda\theta}{\varepsilon}(\boldsymbol{m}_i\boldsymbol{v}_k + \boldsymbol{m}_k\boldsymbol{v}_i)\partial_i\boldsymbol{b}_{k,\varepsilon}^{app}\,\mathrm{d}x\right| \\ &\quad\leqslant \Lambda\theta(|\boldsymbol{m}|_{L^2(\Omega)}|\nabla\boldsymbol{v}|_{L^2(\Omega)} + |\boldsymbol{v}|_{L^2(\Omega)}|\mathrm{curl}\,\boldsymbol{m}|_{L^2(\Omega)})\exp(-\beta t), \\ &\quad\leqslant \frac{\kappa E}{\varepsilon}|\nabla\boldsymbol{v}|^2_{L^2(\Omega)} + \kappa\frac{\Lambda}{\varepsilon}|\mathrm{curl}\,\boldsymbol{m}|^2_{L^2(\Omega)} + C_\kappa\frac{\Lambda\theta}{\varepsilon}|\boldsymbol{m}|^2_{L^2(\Omega)}\Lambda\theta\frac{\varepsilon^2}{E}\exp(-2\beta t) \\ &\qquad + C_\kappa\varepsilon\Lambda\theta^2|\boldsymbol{v}|^2_{L^2(\Omega)}\exp(-2\beta t).\end{aligned}$$

The last term involving the velocity $\boldsymbol{v}$ is estimated as in [6, 14]. Namely, for $i = x, y$ and arbitrary k, and for $i = k = z$, using (58), (59),

$$\left|\int_\Omega \boldsymbol{v}_i\boldsymbol{v}_k\partial_i\boldsymbol{u}_{k,\varepsilon}^{app}\,\mathrm{d}x\right| \leqslant C\Gamma_s|\boldsymbol{v}|^2_{L^2(\Omega)}\exp(-\beta t).$$

It remains to handle the case $i = z$ and $k = x, y$. For this, we first remark that

$$\left|\int_\Omega \boldsymbol{v}_i\boldsymbol{v}_k\partial_i(\boldsymbol{u}_\varepsilon^{app} - \boldsymbol{u}_\varepsilon^{BL})\right| \leqslant C\Lambda_s\exp(-\beta t)|\boldsymbol{v}|^2_{L^2}.$$

Moreover,

$$\begin{aligned}
\left|\int_{\mathbb{R}^2\times[0,1/2]} v_3 v_1 \partial_z u_\varepsilon^{BL}\,\mathrm{d}x\,\mathrm{d}y\,\mathrm{d}z\right| &= \left|\int_{\mathbb{R}^2\times[0,1/2]}\left(\int_0^z \partial_z v_3(t,x,y,z')\,\mathrm{d}z'\right)\right.\\
&\quad\left.\times\left(\int_0^z \partial_z v_1(t,x,y,z')\,\mathrm{d}z'\right)\partial_z u_\varepsilon^{BL}\,\mathrm{d}x\,\mathrm{d}y\,\mathrm{d}z\right|\\
&\leqslant \sqrt{\int_0^{1/2}\int_{\mathbb{R}^2}|\partial_z v_3|^2\,\mathrm{d}x\,\mathrm{d}y\,\mathrm{d}z}\sqrt{\int_0^{1/2}\int_{\mathbb{R}^2}|\partial_z v_1|^2\,\mathrm{d}x\,\mathrm{d}y\,\mathrm{d}z}\sup_{(x,y)\in\mathbb{R}^2}\\
&\quad\times\left|\int_0^{1/2} z|\partial_z u_\varepsilon^{BL}|\,\mathrm{d}z\right|\\
&\leqslant \|\partial_z v_3\|_{L^2(\mathbb{R}^2\times[0,1/2])}\|\partial_z v_1\|_{L^2(\mathbb{R}^2\times[0,1/2])}\|\boldsymbol{u}_0^{int}\|_{L^\infty(\mathbb{R}^2)}\sqrt{2E}\,\Xi\left(\tan\frac{\tau}{2}\right)\\
&\leqslant \left(\frac{1}{2\sqrt{2}}\|\partial_z v_3\|^2_{L^2(\mathbb{R}^2\times[0,1/2])}+\frac{1}{\sqrt{2}}\|\partial_z v_1\|^2_{L^2(\mathbb{R}^2\times[0,1/2])}\right)\\
&\quad\times\|\boldsymbol{u}_0^{int}\|_{L^\infty(\mathbb{R}^2)}\sqrt{2E}\,\Xi\left(\tan\frac{\tau}{2}\right)
\end{aligned}$$

and similarly for $i=z$ and $k=y$. Therefore,

$$\begin{aligned}
&\left|\int_{\mathbb{R}^2\times[0,1]} v_3 v_1 \partial_z u_\varepsilon^{BL}\,\mathrm{d}x\,\mathrm{d}y\,\mathrm{d}z\right| + \left|\int_{\mathbb{R}^2\times[0,1]} v_3 v_2 \partial_z v_\varepsilon^{BL}\,\mathrm{d}x\,\mathrm{d}y\,\mathrm{d}z\right|\\
&\qquad\leqslant \|\nabla v\|^2_{L^2(\Omega)}\|\boldsymbol{u}_0^{int}\|_{L^\infty(\mathbb{R}^2)}\sqrt{E}\,\Xi\left(\tan\frac{\tau}{2}\right)\\
&\qquad\leqslant \sqrt{E}\,\Xi\left(\tan\frac{\tau}{2}\right)\|\nabla v\|^2_{L^2(\Omega)}\Gamma_s\exp(-\beta t)
\end{aligned}$$

where we used theorem 3.2. Thus, finally using the equations (67) in Ω^c, we obtain

$$\begin{aligned}
\frac{\Lambda\theta}{\varepsilon}\int_{\partial\Omega}(\mathrm{curl}\,\boldsymbol{m}\times\boldsymbol{m})\cdot\boldsymbol{n} &= \frac{\Lambda\theta}{\varepsilon}\int_{\partial\Omega}(\boldsymbol{e}\times\boldsymbol{m})\cdot\boldsymbol{n} = -\frac{\Lambda\theta}{\varepsilon}\int_{\Omega^c}\mathrm{div}\,(\boldsymbol{e}\times\boldsymbol{m})\,\mathrm{d}x\\
&= \frac{\Lambda\theta^2}{2\varepsilon}\frac{\mathrm{d}}{\mathrm{d}t}\int_{\Omega^c}|\boldsymbol{m}|^2\,\mathrm{d}x,
\end{aligned}$$

so that we can estimate the energy in the whole space $\mathbb{R}^3$

$$\begin{aligned}
&\frac{\mathrm{d}}{\mathrm{d}t}\left(\int_\Omega\frac{1}{2}|\boldsymbol{v}|^2+\frac{\Lambda\theta}{2\varepsilon}\int_\Omega|\boldsymbol{m}|^2\,\mathrm{d}x+\frac{\Lambda\theta^2}{2\varepsilon}\int_{\Omega^c}|\boldsymbol{m}|^2\,\mathrm{d}x\right)+\frac{E}{\varepsilon}\int_\Omega|\nabla\boldsymbol{v}|^2\,\mathrm{d}x\\
&\qquad+\frac{\Lambda}{\varepsilon}\int_\Omega|\mathrm{curl}\,\boldsymbol{m}|^2\,\mathrm{d}x\\
&\qquad\leqslant C\left(|\boldsymbol{v}|^2_{L^2(\Omega)}(1+\varepsilon\Lambda\theta^2)+\frac{\Lambda\theta}{\varepsilon}|\boldsymbol{m}|^2_{L^2(\Omega)}\theta\left(1+\Lambda\frac{\varepsilon^2}{E}\right)+\varepsilon\right)\exp(-\beta t)\\
&\qquad+\left(\Gamma_s\sqrt{E}\,\Xi\left(\tan\frac{\tau}{2}\right)+2\kappa\frac{E}{\varepsilon}\right)|\nabla\boldsymbol{v}|^2_{L^2(\Omega)}+2\kappa\frac{\Lambda}{\varepsilon}|\mathrm{curl}\,\boldsymbol{m}|^2_{L^2(\Omega)}.
\end{aligned}$$

Therefore, if (22) is satisfied, and for κ small enough we have the global estimate

$$\begin{aligned}
&\sup_{t\geqslant 0}\left(|\boldsymbol{v}(t,.)|^2_{L^2(\Omega)}+\frac{\Lambda\theta}{\varepsilon}|\boldsymbol{m}(t,.)|^2_{L^2(\Omega)}+\frac{\Lambda\theta^2}{\varepsilon}|\boldsymbol{m}(t,.)|^2_{L^2(\Omega^c)}\right)\\
&\qquad+\kappa'\frac{E}{\varepsilon}\int_0^{+\infty}|\nabla\boldsymbol{v}|^2_{L^2(\Omega)}\,\mathrm{d}s+\kappa'\frac{\Lambda}{\varepsilon}\int_0^{+\infty}|\mathrm{curl}\,\boldsymbol{m}|^2_{L^2(\Omega)}\,\mathrm{d}s\\
&\qquad\leqslant C_\beta\left(|\boldsymbol{v}(0,\dot{)}|^2_{L^2(\Omega)}+\frac{\Lambda\theta}{\varepsilon}|\boldsymbol{m}(0,.)|^2_{L^2(\Omega)}+\frac{\Lambda\theta^2}{\varepsilon}|\boldsymbol{m}(0,.)|^2_{L^2(\Omega^c)}+\varepsilon\right)
\end{aligned}$$

for some constant depending on β, and for κ' arbitrary close to 1.

5.3. Global strong solutions for the Navier–Stokes equations for small enough ε

Hereafter, we focus on the case when $\boldsymbol{b} \equiv 0$ which correspond to the rotating incompressible Navier–Stokes equations between two parallel plates. As proven in [2, 4] in the three-dimensional periodic case, large enough Rossby numbers ε yield global classical solutions for the Navier–Stokes equations for suitable initial conditions. We want here to prove that this result holds for the boundary-value problem.

As in the above section, we define $\boldsymbol{v} = \boldsymbol{u}_\varepsilon - \boldsymbol{u}_\varepsilon^{app}$ solution of

$$\partial_t \boldsymbol{v} + \boldsymbol{v} \cdot \nabla \boldsymbol{v} + \nabla \pi - \frac{1}{Re} \Delta \boldsymbol{v} = L_\varepsilon, \qquad \operatorname{div} \boldsymbol{v} = 0, \tag{68}$$

where

$$L_\varepsilon = -\frac{e_3 \times \boldsymbol{v}}{\varepsilon} - \boldsymbol{v} \cdot \nabla \boldsymbol{u}_\varepsilon^{app} - \boldsymbol{u}_\varepsilon^{app} \cdot \nabla \boldsymbol{v} + R_\varepsilon^N \tag{69}$$

with

$$|R_\varepsilon^N|_{L^2(\Omega)} \leqslant C \varepsilon^{N+\frac{1}{2}} \mathrm{e}^{-\beta t}, \tag{70}$$

where N is a given integer such that $N \geqslant 3$. If the stability criterion is satisfied, we obtain when $Re = \varepsilon^{-1} C_{Re}$ for some constant C_{Re},

$$\sup_{t \geqslant 0} |\boldsymbol{v}(t, .)|^2_{L^2(\Omega)} + \frac{1}{Re} \int_0^{+\infty} |\nabla \boldsymbol{v}|^2_{L^2(\Omega)} \, \mathrm{d}s \leqslant C |\boldsymbol{v}(0, .)|^2_{L^2(\Omega)} + C \varepsilon^{2N+1} = K_\varepsilon^0. \tag{71}$$

In order to prove that $\boldsymbol{u}_\varepsilon$ is smooth whenever ε is small enough, we proceed as in [9] in the context of two-dimensional multiphase MHD flows. First, we multiply (68) by $\partial_t \boldsymbol{v}$ and integrate by parts as follows

$$\begin{aligned} \int_0^t |\partial_t \boldsymbol{v}|^2_{L^2(\Omega)} \, \mathrm{d}s + \frac{1}{2Re} |\nabla \boldsymbol{v}(t, .)|^2_{L^2(\Omega)} &\leqslant \frac{1}{2Re} |\nabla \boldsymbol{v}(0, .)|^2_{L^2(\Omega)} + \frac{1}{2} \int_0^t |\partial_t \boldsymbol{v}|^2_{L^2} \, \mathrm{d}s \\ &\quad + C \int_0^t (|L_\varepsilon|^2_{L^2(\Omega)} + |\boldsymbol{v} \nabla \boldsymbol{v}|^2_{L^2}) \, \mathrm{d}s \end{aligned}$$

hence

$$\begin{aligned} \int_0^t |\partial_t \boldsymbol{v}|^2_{L^2(\Omega)} \, \mathrm{d}s + \frac{1}{Re} |\nabla \boldsymbol{v}(t, .)|^2_{L^2(\Omega)} &\leqslant \frac{1}{Re} |\nabla \boldsymbol{v}(0, .)|^2_{L^2(\Omega)} + C \int_0^t |L_\varepsilon|^2_{L^2(\Omega)} \, \mathrm{d}s \\ &\quad + C \int_0^t |\boldsymbol{v}|^2_{L^4(\Omega)} |\nabla \boldsymbol{v}|^2_{L^4(\Omega)} \, \mathrm{d}s. \end{aligned} \tag{72}$$

Rewriting (68) as a Stokes equation

$$-\frac{1}{Re} \Delta \boldsymbol{v} + \nabla \pi = L_\varepsilon - \boldsymbol{v}.\nabla \boldsymbol{v} - \partial_t \boldsymbol{v}, \quad \operatorname{div} \boldsymbol{v} = 0, \quad \text{and} \quad \boldsymbol{v} = 0 \quad \text{on} \quad \partial\Omega,$$

classical estimates yield

$$\frac{1}{Re^2} |D^2 \boldsymbol{v}|^2_{L^2(\Omega)} \leqslant C (|\partial_t \boldsymbol{v}|^2_{L^2(\Omega)} + |L_\varepsilon|^2_{L^2(\Omega)} + |\boldsymbol{v} \cdot \nabla \boldsymbol{v}|^2_{L^2(\Omega)}).$$

Combining with (72) we get

$$\begin{aligned} \int_0^t \left(|\partial_t \boldsymbol{v}|^2_{L^2} + \frac{|D^2 \boldsymbol{v}|^2_{L^2}}{Re^2} \right) \mathrm{d}s + \frac{1}{Re} |\nabla \boldsymbol{v}(t, .)|^2_{L^2} &\leqslant \frac{C}{Re} |\nabla \boldsymbol{v}(0, .)|^2_{L^2} \\ &\quad + C \int_0^t (|\boldsymbol{v}|^2_{L^4} |\nabla \boldsymbol{v}|^2_{L^4} + |L_\varepsilon|^2_{L^2}) \, \mathrm{d}s. \end{aligned} \tag{73}$$

Combining the following two Gagliardo–Nirenberg inequalities,

$$|\boldsymbol{v}|_{L^4}^2 \leqslant C|\boldsymbol{v}|_{L^2}^{1/2}|\nabla \boldsymbol{v}|_{L^2}^{3/2}$$

and

$$|\nabla \boldsymbol{v}|_{L^4}^2 \leqslant C|\nabla \boldsymbol{v}|_{L^2}^{1/2}(|\nabla \boldsymbol{v}|_{L^2} + |D^2\boldsymbol{v}|_{L^2})^{3/2}$$

we deduce that for all $\kappa > 0$

$$|\boldsymbol{v}|_{L^4(\Omega)}^2|\nabla \boldsymbol{v}|_{L^4(\Omega)}^2 \leqslant \frac{\kappa}{Re^2}(|D^2\boldsymbol{v}|_{L^2(\Omega)}^2 + |\nabla \boldsymbol{v}|_{L^2(\Omega)}^2) + C_\kappa Re^6|\boldsymbol{v}|_{L^2(\Omega)}^2|\nabla \boldsymbol{v}|_{L^2(\Omega)}^8.$$

Next, we observe that arguing as in the preceding section, we can estimate

$$|\boldsymbol{v}\cdot\nabla \boldsymbol{u}_\varepsilon^{app}|_{L^2(\Omega)}^2 + |\boldsymbol{u}_\varepsilon^{app}.\nabla \boldsymbol{v}|_{L^2(\Omega)}^2 \leqslant C|\nabla \boldsymbol{v}|_{L^2(\Omega)}^2 \exp(-2\beta t)$$

which leads to

$$|L_\varepsilon|_{L^2}^2 \leqslant C|\nabla \boldsymbol{v}|_{L^2}^2 \exp(-2\beta t) + C\frac{|\boldsymbol{v}|_{L^2}^2}{\varepsilon^2} + C\varepsilon^{2N+1}\exp(-2\beta t).$$

As a result, we obtain using the Poincaré lemma, for $\varepsilon \leqslant 1$,

$$\int_0^t \left(|\partial_t \boldsymbol{v}|_{L^2(\Omega)}^2 + \frac{1}{Re^2}|D^2\boldsymbol{v}|_{L^2(\Omega)}^2\right)\mathrm{d}s + \frac{1}{Re}|\nabla \boldsymbol{v}(t,.)|_{L^2(\Omega)}^2 \leqslant \frac{C}{Re}|\nabla \boldsymbol{v}(0,.)|_{L^2(\Omega)}^2$$
$$+\frac{C}{Re^6}\int_0^t |\boldsymbol{v}|_{L^2}^2|\nabla \boldsymbol{v}|_{L^2}^8\,\mathrm{d}s + C\int_0^t \frac{|\nabla \boldsymbol{v}|_{L^2}^2}{\varepsilon^2}\,\mathrm{d}s + C\varepsilon^{2N+1}.$$

Using the Poincaré lemma and $|\boldsymbol{v}(t,.)|_{L^2}^2 \leqslant K_\varepsilon^0$ we get

$$\int_0^t \left(|\partial_t \boldsymbol{v}|_{L^2(\Omega)}^2 + \frac{1}{Re^2}|D^2\boldsymbol{v}|_{L^2(\Omega)}^2\right)\mathrm{d}s + \frac{1}{Re}|\nabla \boldsymbol{v}(t,.)|_{L^2(\Omega)}^2 \leqslant \frac{C}{Re}|\nabla \boldsymbol{v}(0,.)|_{L^2}^2$$
$$+CRe^{10}K_0^\varepsilon\int_0^t \left(\frac{|\nabla \boldsymbol{v}|_{L^2}^2}{Re}\right)^4\mathrm{d}s + C\frac{Re}{\varepsilon^2}K_0^\varepsilon + C\varepsilon^{2N+1}$$
$$\leqslant C\frac{|\nabla \boldsymbol{v}(0,.)|_{L^2}^2}{Re} + \frac{CK_0^\varepsilon}{\varepsilon^{10}}\int_0^t \left(\frac{|\nabla \boldsymbol{v}|_{L^2}^2}{Re}\right)^4\mathrm{d}s + \frac{CK_0^\varepsilon}{\varepsilon^3}.$$

Let

$$\alpha(t) = \frac{|\nabla \boldsymbol{v}(t,.)|_{L^2}^2}{Re},$$
$$C_0 = C\frac{|\nabla \boldsymbol{v}(0,.)|_{L^2}^2}{Re} + \frac{CK_0^\varepsilon}{\varepsilon^3},$$
$$C_1 = \frac{CK_0^\varepsilon}{\varepsilon^{10}}$$

and

$$\psi(t) = C_0 + C_1\int_0^t \alpha^4\,\mathrm{d}s.$$

We have

$$\alpha \leqslant C_0 + C_1\int_0^t \alpha^4\,\mathrm{d}s$$

therefore,

$$\dot{\psi} \leqslant C_1\alpha\psi^3$$

hence

$$\psi(t) \leqslant \psi(0)\left(1 - 2\psi(0)^2 C_1 \int_0^{+\infty} \alpha \, \mathrm{d}s\right)^{-1/2}$$

which bounds $\psi(t)$ in terms of $\psi(0)$ provided

$$2\psi(0)^2 C_1 \int_0^{+\infty} \alpha \, \mathrm{d}s \leqslant 1/2$$

that is provided

$$\left(\frac{|\nabla \boldsymbol{v}(0,.)|_{L^2}^2}{Re} + \frac{K_0^\varepsilon}{\varepsilon^3}\right)^2 K_0^\varepsilon \frac{K_0^\varepsilon}{\varepsilon^{10}} \leqslant C_\infty$$

where C_∞ is some universal constant, or equivalently provided

$$|\nabla \boldsymbol{v}(0,.)|_{L^2}^2 + \frac{K_0^\varepsilon}{\varepsilon^4} \leqslant C_\infty$$

which ends the proof. Notice that the uniqueness property is a straightforward consequence of the above regularity. Besides, additional bounds can be obtained by deriving the equation in time and integrating by parts, but no further details will be given here.

5.4. Proof of theorem 3.1

To prove theorem 3.1 just follow section 5.2 and notice that the term $(\boldsymbol{v} \cdot \nabla)\boldsymbol{u}_s$ reduces to $v_3 \partial_z \boldsymbol{u}_s$ which can be absorbed in the viscosity exactly as in section 5.2 leading to the fact that $\int |\boldsymbol{v}|^2 + \frac{\Lambda\theta}{\varepsilon} \int |\boldsymbol{m}|^2$ is decreasing.

Acknowledgments

The authors would like to thank Y Brenier and D Jault for many fruitful discussions.

References

[1] Acheson D J and Hide R 1973 Hydromagnetics of rotating fluids *Rep. Prog. Phys.* **36** 159–221
[2] Babin A, Mahalov A and Nicolaenko B 1996 Global splitting, integrability and regularity of 3D Euler and Navier Stokes equations for uniformly rotating fluids *Eur. J. Mech.* **15** 291–300
[3] Beale J T, Kato T and Majda A 1984 Remarks on the breakdown of smooth solutions for the 3-D Euler equations *Commun. Math. Phys.* **94** 61–6
[4] Chemin J-Y 1995 A propos d'un problème de pénalisation de type antisymétrique *C. R. Acad. Sci., Paris* **321** 861–4
[5] Desjardins B, Dormy E and Grenier E Linear instability of Ekman Hartmann boundary layers, in preparation
[6] Desjardins B and Grenier E Derivation of the quasigeostrophic potential vorticity equations, *Adv. Diff. Eqns* to appear
[7] Desjardins B and Grenier E 1997 On the homogeneous model of wind driven ocean circulation *SIAM J. Appl. Math.* to appear
[8] Desjardins B and Grenier E 1998 Reynolds.m, a package to compute critical Reynolds numbers *Preprint* http://www.dmi.ens.fr/equipes/edp/Reynolds/reynolds.m
[9] Desjardins B and Le Bris C Remarks on a nonhomogeneous model of magnetohydrodynamics *Diff. Int. Eqns* to appear
[10] Dormy E *Thèse de Doctorat* Institut de Physique du Globe, place Jussieu, 75005 Paris, France
[11] Dormy E, Cardin P and Jault D MHD flow in a slightly differentially rotating spherical shell, with conducting inner core, in a dipolar magnetic field *Earth Planet. Sci. Lett.* to appear
[12] Greenspan H P 1969 The theory of rotating fluids *Cambridge Monographs on Mechanics and Applied Mathematics*

[13] Grenier E and Guès O 1998 On the inviscid limit of noncharacteristic nonlinear parabolic systems *J. Diff. Eqns* to appear
[14] Grenier E and Masmoudi N 1997 Ekman layers of rotating fluids, the case of well prepared initial data *Commun. Par. Diff. Eqns* **22** 953–75
[15] Jault D 1995 Model Z by computation and Taylor's condition *Geophys. Astrophys. Fluid Dyn.* **79** 99–124
[16] Julien K, Legg S, Mc Williams J and Werne J 1996 Rapidly rotating turbulent Rayleigh-Bénard convection *J. Fluid Mech.* **322** 243–73
[17] Kato T and Ponce G 1988 Commutator estimates and the Euler and Navier-Stokes equations *Commun. Pure Appl. Math.* **41** 891–907
[18] Kuang W and Bloxham J 1997 An Earth-like dynamo model *Nature* **389** 371–4
[19] Lilly D K1966 On the instability of the Ekman boundary layer *J. Atmos. Sci.*, **23** 481–94
[20] Poirier J-P 1994 Physical properties of the Earth's core *C. R. Acad. Sci., Paris* **318** 341–50
[21] Poirier J-P 1991 *Introduction to the Physics of the Earth's Interior* (Cambrdige: Cambridge University Press)
[22] Roberts P H 1967 Singularity of Hartmann layers *Proc. R. Soc.* **300** 94–107
[23] Taylor J B The magnetohydrodynamics of a rotating fluid and the Earth's dynamo problem *Proc. R. Soc.* **274** 274–84

Journal of Computational Physics **151,** 676–683 (1999)
Article ID jcph.1999.6213, available online at http://www.idealibrary.com on IDEAL®

An Accurate Compact Treatment of Pressure for Colocated Variables

Emmanuel Dormy

University of California at Los Angeles, I.G.P.P., 405 Hilgard Avenue, Los Angeles, California 90095-1567
E-mail: dormy@math.ucla.edu

Received August 12, 1998; revised January 20, 1999

We propose a new scheme for the pressure treatment in computations of incompressible flow using a colocated grid arrangement. To avoid oscillations associated with the sparse non-compact stencil, we introduce a compact fourth-order equivalent of this stencil and study its advantages over the classical second-order averaging procedure. © 1999 Academic Press

Key Words: compact differencing; incompressible Navier–Stokes equation; velocity-pressure decoupling.

1. INTRODUCTION

When computing incompressible Navier–Stokes equations on a non-staggered (colocated) grid, a Poisson equation is to be solved for the pressure (or pseudo pressure in the fractional step formalism). The numerical instability, often referred to as the "checkerboard problem" or "odd–even decoupling problem" then has to be addressed. This problem arises when second-order central difference approximations are implemented for both the pressure gradient operator in the momentum equation and the divergence operator in the continuity equation (or, with the cell centered finite volume formalism, if fluxes are obtained by central differencing), and when the discrete Poisson equation is defined, in a consistent and conservative manner, as the product of these two operators [1, 2]. This Poisson equation corresponds to a non-compact sparse stencil and produces an oscillatory pressure field. Various approaches have been used to overcome this difficulty. Van der Wijngaart [3] proposed to filter out the oscillations. To introduce a coupling term, Russel and Abdallah [4] increased the order of the divergence operator at the cost of an enlargement of the stencil for the discrete Laplace operator. The most common approach (here referred to as "compact averaged") involves the derivation of a non-conservative compact pressure Poisson equation [2, 5–7]. This modification is introduced differently depending on the way the pressure is treated in the time integration. It can be understood as a smoothing of the pressure field through

0021-9991/99 $30.00
Copyright © 1999 by Academic Press
All rights of reproduction in any form reserved.

an artificial dissipation. The energy conserving property of the scheme is destroyed in this process. The error thus introduced in the discrete continuity equation is proportional to the fourth-order derivatives of the pressure [8]. The idea of the present method is to introduce a fourth-order "compact equivalent" to the conservative discrete pressure equation.

2. GENERAL METHODOLOGY

In the following, we will present the method using the fractional step formalism (first-order accurate in time [9]), though it can probably be generalized to the pressure correction approach or other schemes. We will thus suppose a velocity field $\boldsymbol{u}^*$, which does not satisfy the continuity equation (for instance obtained by time-advancing the Navier–Stokes equations without invoking continuity) and we want to project it onto a divergence-free field by subtracting the gradient of a pressure-like variable ϕ so that

$$\boldsymbol{u} = \boldsymbol{u}^* - \nabla_h \phi. \tag{1}$$

Taking the divergence of this equation and requiring $\boldsymbol{u}$ to satisfy the continuity equation gives

$$\Delta_{2h}\phi = \nabla_h \cdot \boldsymbol{u}^*, \tag{2}$$

where Δ_{2h} stands for the second-order centered approximation of the Laplacian skipping the neighboring points (as represented on Fig. 1a). The sparse nature of this operator leads to pressure oscillations. A possible remedy to this problem is to interpolate variables linearly, which leads to a second-order approximation of (2)

$$\Delta_h \phi = \nabla_h \cdot \boldsymbol{u}^*. \tag{3}$$

We will refer to this in the sequel as the "compact averaged" scheme. This scheme can be interpreted as adding a second-order dissipative term to the pressure in order to damp the oscillations. In the following we will derive fourth-order compact equivalents of (2).

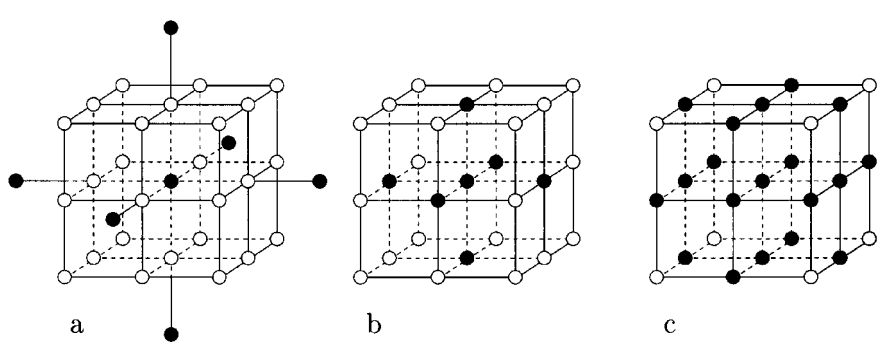

FIG. 1. Computational molecules for the three-dimensional pressure equation; only the black points are used for the computation. (a) The Δ_{2h} operator, being defined as the product of numerical divergence of the gradient, accurate but oscillating. (b) The 7 points compact operator obtained by interpolation. (c) The 19 points fourth-order compact equivalent operator.

2.1. One Dimension Compact Derivation

Using the expression of truncation error for the second-order finite difference scheme

$$\Delta_h \phi = \frac{\partial^2 \phi}{\partial x^2} + \frac{h^2}{12}\frac{\partial^4 \phi}{\partial x^4} + \mathcal{O}(h^4), \tag{4}$$

one easily derives the second-order error introduced in replacing (2) with (3):

$$\Delta_h \phi = \Delta_{2h}\phi - \frac{h^2}{4}\frac{\partial^4 \phi}{\partial x^4} + \mathcal{O}(h^4). \tag{5}$$

The error thus introduced is of the same order as the one for the discretization scheme (see [2, 4]). However, the discrete Laplacian is only a second-order estimate of the discrete divergence of the gradient. Using the fractional step procedure described above (see [10, 11, 9]) thus leads to a modified velocity field in which numerical errors in the divergence are significantly higher than roundoff error.

The consistent derivation of the pressure-like equation gives

$$\Delta_{2h}\phi = \nabla_h \cdot \boldsymbol{u}^*, \tag{6}$$

$$\frac{\partial^2 \phi}{\partial x^2} + \frac{h^2}{3}\frac{\partial^4 \phi}{\partial x^4} = \nabla_h \cdot \boldsymbol{u}^* + \mathcal{O}(h^4). \tag{7}$$

Using a Hermitian compact expression one can derive a fourth-order approximation of Eq. (7),

$$\Delta_h \phi + \frac{h^2}{4}\frac{\partial^4 \phi}{\partial x^4} = \nabla_h \cdot \boldsymbol{u}^* + \mathcal{O}(h^4), \tag{8}$$

$$\Delta_h \phi = \left[I - \frac{h^2}{4}\Delta_h\right](\nabla_h \cdot \boldsymbol{u}^*) + \mathcal{O}(h^4), \tag{9}$$

where I stand for the identity operator.

Note that this compact scheme was not derived to increase the accuracy of the continuous operator approximation as is the case for other compact formulations [12–18]. Instead it is derived to approximate to a higher accuracy the conservative non-compact stencil. The compact scheme we propose (9) is still second-order accurate, but has the same second-order behavior as the conservative sparse stencil (6). The overall accuracy of the discretization is thus second-order in space and first-order in time, but the dilatation effects associated with the non-conservative treatment of the pressure are reduced to a fourth order. Note that this approach also shares some similarity with what is refered to as "improving the order of approximation" in the Support Operator formalism [19].

2.2. Three-Dimensions Generalization

The idea of the previous paragraph can be adapted to three-dimensional problems, though this is not straightforward. The original non-compact formulation can be written as

$$\frac{\partial^2 \phi}{\partial x^2} + \frac{h_x^2}{3}\frac{\partial^4 \phi}{\partial x^4} + \mathcal{O}\left(h_x^4\right) + \frac{\partial^2 \phi}{\partial y^2} + \frac{h_y^2}{3}\frac{\partial^4 \phi}{\partial y^4} + \mathcal{O}\left(h_y^4\right) + \frac{\partial^2 \phi}{\partial z^2} + \frac{h_z^2}{3}\frac{\partial^4 \phi}{\partial z^4} + \mathcal{O}\left(h_z^4\right) = \nabla_h \cdot \boldsymbol{u}^*. \tag{10}$$

Note that the second-order terms cannot be easily expressed in terms of $\nabla_h \cdot \boldsymbol{u}^*$.

2.2.1. *Single Step Procedure*

Following the method used by Spotz and Carey [15] (but with a non-uniform grid) a compact fourth-order approximation to (10) can be derived in the form

$$\Delta_x\phi + \Delta_y\phi + \Delta_z\phi - \frac{1}{4}\Delta_x\left[h_y^2\Delta_y\phi + h_z^2\Delta_z\phi\right] - \frac{1}{4}\Delta_y\left[h_x^2\Delta_x\phi + h_z^2\Delta_z\phi\right]$$
$$- \frac{1}{4}\Delta_z\left[h_x^2\Delta_x\phi + h_y^2\Delta_y\phi\right] \simeq \left[I - \frac{h_x^2}{4}\Delta_x - \frac{h_y^2}{4}\Delta_y - \frac{h_z^2}{4}\Delta_z\right](\nabla_h \cdot \boldsymbol{u}^*), \qquad (11)$$

where Δ_x, Δ_y, Δ_z stand for the h-discrete three point Laplace scheme respectively in the x, y, and z directions. Notice that this expression not only involves a modification of the right-hand side (rhs), but also a modification of the operator on the left-hand side (lhs), with the addition of extra diagonal terms. The corresponding 19 points *computational molecule* is displayed in Fig. 1c.

2.2.2. *Two Step Procedure*

The previous approach corresponds to a direct adaptation of the one-dimensional idea to the three-dimensional case. It achieves fourth-order accuracy, but only at the cost of a modification of the lhs itself for the treatment of cross derivatives. In two spatial dimensions this would only increase the stencil from five to nine points. In three space dimensions however this increase is much more important as the standard seven-points stencil has to be modified to a nineteen-points molecule. This significantly increases the computational time required. It was found (see Subsection 3.1) that the number of iterations to resolve this problem with a CGSTAB algorithm [20] is about three times that required by the nine-points scheme.

We propose here an alternative two-step approach that allows fourth-order accuracy at twice the computational cost of the second-order interpolated scheme. Equation (10) can be approximated with fourth-order accuracy using a two-step procedure. The first step is a second order approximation to the second-order truncation terms written as

$$\Delta_h\psi = \left(h_x^2\frac{\partial^4}{\partial x^4} + h_y^2\frac{\partial^4}{\partial y^4} + h_z^2\frac{\partial^4}{\partial z^4}\right)\nabla_h \cdot \boldsymbol{u}^*. \qquad (12)$$

Technically, evaluation of the rhs of (12) involves higher order derivatives of $\nabla_h \cdot \boldsymbol{u}^*$ which implicates larger stencils (five-point stencils in 1D).

A second step uses ψ as a correction term:

$$\Delta_h\phi = \nabla_h \cdot \boldsymbol{u}^* - \frac{1}{4}\psi. \qquad (13)$$

Note that ψ scales as $\mathcal{O}(h^2)$ and that (13) is thus consistent with (2).

The pressure thus defined satisfies (2) to the fourth-order (as with the previous method) and the computational cost is exactly twice the cost of the second order scheme as each of the steps requires the resolution of a seven-points compact Laplace operator (of the form displayed in Fig. 1b).

Though the lhs stencils are simple and compact, the rhs of the first step involves a non-compact stencil. However, this does not increase the numerical cost as this term does not need to be inverted.

3. NUMERICAL EXAMPLES

3.1. *One-Dimensional Function*

Though incompressible flow in one dimension of space is a rather limited notion, we want to test the ability of the scheme on a simple problem. Let us assume a velocity field $\boldsymbol{u}^*$ of the form

$$\boldsymbol{u}^* = \sin(4\pi x), \qquad x \in [0, 1]. \tag{14}$$

Application of the procedure described in Subsection 2.1 to this one-dimensional function should obviously lead to

$$\boldsymbol{u} = \boldsymbol{u}^* - \nabla_h \phi \equiv \mathbf{0}. \tag{15}$$

The compact fourth-order scheme used here (9) is defined implicitly as

$$\frac{1}{h^2}(\phi_{i-1} - 2\phi_i + \phi_{i+1}) = \frac{1}{4}(\nabla_h \cdot \boldsymbol{u}^*)_{i-1} + \frac{1}{2}(\nabla_h \cdot \boldsymbol{u}^*)_i + \frac{1}{4}(\nabla_h \cdot \boldsymbol{u}^*)_{i+1}. \tag{16}$$

We report in Table I the errors (defined as the maximum of the absolute value of $\nabla_h \cdot \boldsymbol{u}$) with varying discretizations, solutions are represented in Fig. 2. The orders of the various schemes are vindicated.

It should be noted that, in one dimension, the compact scheme only requires an additional multiplication by a tridiagonal matrix on the rhs (as compared with the compact averaged scheme). The computational cost of the compact equivalent scheme is thus very similar to that of the compact averaged approach.

3.2. *Three-Dimensional Flow*

We have constructed a code for the purpose of studying three-dimensional rapidly rotating magnetohydrodynamic buoyancy-driven turbulence. It is known [24] that buoyancy-affected flows require a fine pressure-velocity coupling. Furthermore, in the physical problem that motivated this work, we expect from previous studies [21] plate-like shear zones. It is important to compute gradients in these regions accurately. This motivated the choice of

TABLE I
Errors (Maximum of the Absolute Value) in the Numerical Divergence with Varying Grid Sizes (N)

N	C.A.	C.E.
20	1.12	0.11
40	0.30	$7.4 \cdot 10^{-3}$
80	$7.70 \cdot 10^{-2}$	$4.74 \cdot 10^{-4}$
160	$1.93 \cdot 10^{-2}$	$2.98 \cdot 10^{-5}$
320	$4.84 \cdot 10^{-3}$	$1.86 \cdot 10^{-6}$

Note. As expected, the compact averaged scheme's error (C.A.) evolves as $1/N^2$, while the fourth-order compact equivalent scheme's error (C.E.) evolves as $1/N^4$. The solution derived using the sparse non-compact scheme is of the order of the numerical zero (about 10^{-13}).

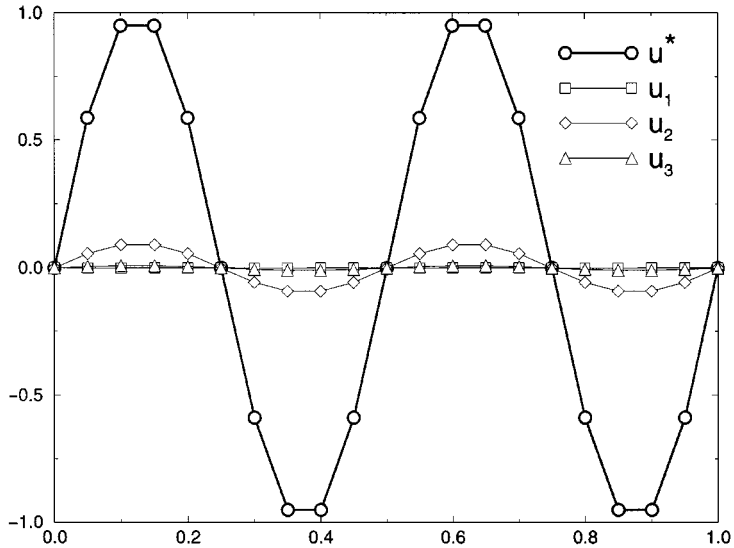

FIG. 2. Starting with a velocity field $\boldsymbol{u}^*$, which does not satisfy the continuity condition, we want to compute the velocity field $\boldsymbol{u}$ by subtracting the gradient of a pseudo-pressure. This is done by solving a discrete Poisson equation, using for $\boldsymbol{u}_1$ the natural expression Δ_{2h} (accurate but leading to oscillations); for $\boldsymbol{u}_2$ the compact averaged scheme Δ_h; for $\boldsymbol{u}_3$ the fourth-order compact equivalent of Δ_{2h}. Errors when varying the discretization are reported in Table I.

colocated variables though the geometry is rather simple. In a work in preparation, we test adaptations of the ENO scheme [22, 23] for advective transport on incompressible flows. This also motivated the development of the present equivalent scheme for the pressure gradient.

We use here our code with no magnetic field and no rotation and we study a simple laminar buoyancy-driven flow of a Boussinesq fluid in a fully periodic domain. Time integration is performed using the optimal second-order TVD (total variation diminishing) Runge–Kutta method [23] (see also [11]). We report here some results obtained with the above described scheme.

Figure 3 displays the time evolution of the divergence after each full time step. The single step compact equivalent approach is found to give accurate results in three dimensions. The single step procedure leads with a $50 \times 50 \times 25$ grid to a decrease of the error in the numerical divergence of a coefficient about 14. This method led to a significant increase of the required CPU time (about a factor three with the compact averaged scheme). The two-step algorithm is found to give slightly better and more regular results (probably because we achieve a better resolution of the seven-point stencil with our iterative solver). As expected it requires twice the computational time of the compact averaged method, although it was found numerically that ψ does not need to be computed with as great an accuracy as ϕ. Relaxing the precision constraint on ψ we were able to obtain a fourth-order accurate solution with only 50% more time than the second-order averaged computation.

4. CONCLUSION

We introduced a compact fourth-order equivalent of the pressure equation for the discrete resolution of the incompressible Navier–Stokes equation. This approach suppresses the

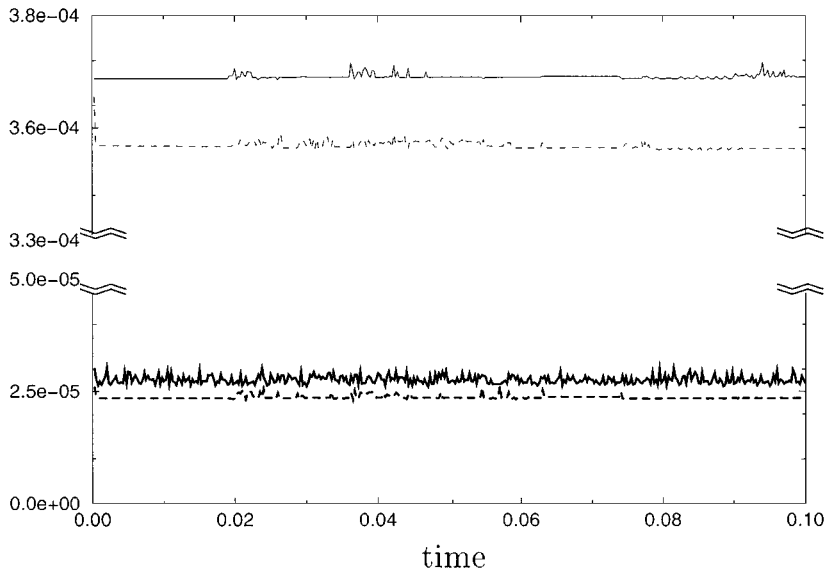

FIG. 3. Time evolution of the numerical divergence in three-dimensional simulations of a buoyancy driven convective flow (resolution is $50 \times 50 \times 25$). The computation starts with a flow computed using the C.A. method. Integration with the C.A. method gives the solid line curve. Introduction of the mass matrix of the single step fourth-order compact equivalent scheme improves the solution a little, though the overall accuracy is still second order (dashed curve). Modification of the operator to obtain fourth-order accuracy requires a stronger computational effort but yields much better results (bold curve). Finally the two-step method (dashed bold) gives as good (if not better) results for a lower computational effort. None of these simulations is oscillating because of the compact nature of the operators used.

spatial odd–even decoupling of the pressure field without adding a second-order damping term (as was previously the case). This significantly reduces the residual errors in the discrete continuity equation.

Three-dimensional simulations have been performed and this approach has been shown to give satisfactory results at a reasonable computational cost (using a two-step algorithm) for the fully periodic buoyancy driven flow that motivated this study.

Further important issues remain to be addressed about the scheme introduced here, such as the treatment of boundary conditions (e.g., see [25]) as well as the generalization of this technique to unstructured grids.

ACKNOWLEDGMENTS

The author is grateful to Professor Paul H. Roberts for his interest and advice as well as for reading this manuscript and to Rob Van der Wijngaart for kindly providing a copy of [3]. He also thanks Professor Stanley Osher for useful comments. This research was supported by the N.S.F. under Grant EAR 97-25627 and by the French *Ministère des Affaires Etrangères* under Lavoisier Grant 4403 STR/FE. Computations were carried at the San Diego Supercomputer Center.

REFERENCES

1. S. Patankar, A calculation procedure for two-dimensional elliptic situations, *Numer. Heat Transfer* **4**, 409 (1981).

2. J. Ferziger and M. Perić, *Computational Methods for Fluid Dynamics* (Springer-Verlag, New York/Berlin, 1996).
3. R. Van der Wijngaart, *Composite Grid Techniques and Adaptative Mesh Refinement in Computational Fluid Dynamics*, Ph.D. thesis, Stanford University, 1990.
4. P. A. Russell and S. Abdallah, Dilatation-free solutions for the incompressible flow equations on nonstaggered grids, *AIAA J.* **35**, 585 (1997).
5. M. Perić, R. Kessler, and G. Scheuerer, Comparison of finite-volume numerical methods with staggered and colocated grids, *Comput. & Fluids* **16**(4), 389 (1988).
6. S. Abdallah, Numerical solutions of the pressure Poisson equation with Neumann boundary conditions using a non-staggered grid, *J. Comput. Phys.* **70**, 182, 193 (1987).
7. C. M. Rhie and W. L. Chow, Numerical study of the turbulent flow past an airfoil with trailing edge separation, *AIAA J.* **21**(11), 1525 (1983).
8. F. Sotiropoulos and S. Abdallah, The discrete continuity equation in primitive variable solutions of incompressible flow, *J. Comput. Phys.* **95**, 212 (1991).
9. J. B. Perot, An analysis of the fractional step method, *J. Comput. Phys.* **108**, 51 (1993).
10. J. Kim and P. Moin, Application of a fractional-step method to incompressible Navier–Stokes equations, *J. Comput. Phys.* **59**, 308 (1985).
11. H. Le and P. Moin, An improvement of fractional-step methods for the incompressible Navier–Stokes equations, *J. Comput. Phys.* **92**, 369 (1991).
12. R. Hirsh, Higher order accurate difference solutions of fluid mechanics problems by a compact differencing technique, *J. Comput. Phys.* **19**, 90 (1975).
13. M. Gupta, High accuracy solutions of incompressible Navier–Stokes equations, *J. Comput. Phys.* **93**, 343 (1991).
14. S. Lele, Compact finite-difference schemes with spectral-like resolution, *J. Comput. Phys.* **103**, 16 (1992).
15. W. Spotz and G. Carey, A high-order compact formulation for the 3D Poisson equation, *Numer. Methods Partial Differentiel Equations* **12**, 235 (1996).
16. W. E and J.-G. Liu, Essentially compact schemes for unsteady viscous incompressible flows, *J. Comput. Phys.* **126**, 122 (1996).
17. W. E and J.-G. Liu, Finite difference methods for 3D viscous incompressible flows in the vorticity-vector potential formulation on non-staggered grids, *J. Comput. Phys.* **138**, 57 (1997).
18. J. Strikwerda, High-order-accurate schemes for incompressible viscous flow, *Int. J. Numer. Methods Fluids* **24**, 715 (1997).
19. M. Shashkov, *Conservative Finite-Difference Methods on General Grids* (CRC Press, Boca Raton, FL, 1996).
20. H. A. Van den Vorst, BI-GCSTAB: A fast and smoothly converging variant of BI-CG for the solution of non-symmetric linear systems, *SIAM J. Sci. Stat. Comput.* **13**, 631 (1992).
21. M. G. StPierre, On the local nature of turbulence in Earth's outer core, *Geophys. Astrophys. Fluid Dynam.* **83**, 293 (1996).
22. A. Harten, B. Engquist, S. Osher, and C. Shakravarthy, Uniformly high order essentially non-oscillatory schemes, III, *J. Comput. Phys.* **71**, 231 (1987).
23. C. W. Shu, *Essentially Non-oscillatory and Weighted Essentially Non-oscillatory Schemes for Hyperbolic Conservation Laws*, ICASE Report No. 97-65, NASA/CR-97-206253, 1997.
24. P. Johansson and L. Davidson, Modified collocated simplec algorithm applied to buoyancy-affected turbulent flow using a multigrid solution procedure, *Numer. Heat Transfer B* **28**, 39 (1995).
25. M. H. Carpenter, D. Gottlieb, and S. Abarbanel, The stability of numerical boundary treatments for compact high-order finite-difference schemes, *J. Comput. Phys.* **108**, 272 (1993).

Geochemistry Geophysics Geosystems G3
AN ELECTRONIC JOURNAL OF THE EARTH SCIENCES
Published by AGU and the Geochemical Society

Article
Volume 1
Published October 18, 2000
Paper number 2000GC000062
ISSN: 1525-2027

Numerical models of the geodynamo and observational constraints

Emmanuel Dormy, Jean-Pierre Valet, and Vincent Courtillot
Institut de Physique du Globe de Paris,Laboratoire de Géomagnétisme et Paléomagnétisme, 4, place Jussieu, 75252 Paris cedex 05, France (dormy@ipgp.jussieu.fr; valet@ipgp.jussieu.fr; courtillot@ipgp.jussieu.fr)

[1]0 **Abstract:** The past few years have seen the emergence of a large number of numerical simulations of the geodynamo. In parallel, both new and old geomagnetic, archeomagnetic, and paleomagnetic observations have been interpreted as actual geomagnetic features and used as constraints for dynamo models. Naturally, model predictions should be tested against actual characteristics of the geomagnetic field. Despite huge differences (sometimes in excess of a billion) between the values of parameters used in the simulations and those estimated for the Earth, it is intriguing that many available simulations succeed in producing largely axial dipolar magnetic fields with weaker nondipolar structures, in agreement with the first-order characteristics of the geomagnetic field. Yet, when considering finer characteristics, there are significant differences, and failures to actually produce a number of fundamental characteristic features. In this presentation, we first review numerical results obtained to date, then we attempt to summarize which field characteristics derived from observational data sets can be considered robust. On the basis of simple criteria used to evaluate the degree of confidence that can be placed in each datum, we sort presumably characteristic geomagnetic features into three categories (robust, controversial, and unlikely). We conclude that numerical models should be illustrated with a number of key "predictions," averaged over at least 10 dipole diffusion times. These predictions should be tested against the subset of robust observations only. Controversial observations should await additional confirmation.

Keywords: Geodynamo; Earth core; geomagnetic field; magnetic records.

Index terms: Dynamo theory; time variation-secular and long term; paleomagnetic secular variation.

Received March 1, 2000; **Revised** July 21, 2000; **Accepted** August 18, 2000; **Published** October 18, 2000.

Dormy, E., J.-P. Valet, and V. Courtillot, 2000. Numerical models of the geodynamo and observational constraints, *Geochem. Geophys. Geosyst.*, vol. 1, Paper number 2000GC000062 [23,981 words, 2 figures, 2 tables]. Published October 18, 2000.

1. Introduction

[2]0 After decades of work generally performed in parallel but with rather little interaction, specialists of magnetic field observation, on one hand, and modeling, on the other hand, have come to interact much more recently. Papers coauthored by dynamo specialists and geophysicists observing the field over timescales ranging from real time to geological time have appeared [*Gubbins and Coe*, 1993; *Ultré-Guérard et al.*, 1998; *Glatzmaier et al.*, 1999; *Coe et al.*, 2000]. Acceleration of both theoretical and numerical work has produced a num-

Copyright 2000 by the American Geophysical Union

ber of numerical dynamo models that may have some geophysical relevance. Remarkably, most if not all of these numerical simulations share characteristics with the present or past Earth's field as it is now known to us: this includes the dominance of the axial dipolar component, weak nondipolar structures, and, in some cases, full polarity reversal. In order to validate these codes a benchmark comparison is being coordinated by Ulrich Christensen from Göttingen University.

[3] Yet some of the main parameters that control dynamo equations, such as the Ekman number (E) or the magnetic Prandtl number (Pm), that are used in the numerical calculations are extremely far from their estimated values for the Earth. It has even been shown in the case of simplified problems [*Dormy et al.*, 1998] that the numerical values commonly used for modeling do not lead to the equilibria that are appropriate for the Earth.

[4] For instance, the Ekman number is defined as the ratio of the rotation timescale (for the Earth, that is the day) and the viscous diffusion timescale. The day is a terribly short timescale compared to any other relevant timescale that applies to the Earth's core: the Ekman number is believed to be as small as 10^{-15} for the Earth [*Poirier*, 1994; *De Wijs et al.*, 1998]. Yet it is impossible with present computers to attain E values smaller than 10^{-6} for the dynamo problem. This implies that the viscous diffusion term in numerical models is too strong by a coefficient of the order of one billion. Viscous effects decrease very slowly with decreasing values of the Ekman number: as $E^{1/2}$ for boundary layers, as $E^{1/3}$ for axial shear. Thus the Ekman number must be extremely small for viscous effects to be negligible. When viscous effects are restricted to very small regions of shear, it is referred to as the "asymptotic regime" of small E. This regime is relevant to the Earth's core. Ekman numbers that can be achieved in current numerical simulations are not small enough to allow viscous effects to be neglected in the main flow (viscosity actually being used to ensure numerical stability). One may therefore expect the flows computed in numerical models to be of a large scale because of the important viscous dissipation of the small-scale flow.

[5] The magnetic Prandtl number is a measure of the ratio of two other characteristic timescales: the timescale for dissipation of electrical currents with respect to viscous diffusion timescale. The magnetic Prandtl number is estimated at about 10^{-6} for the Earth's core [see *Poirier*, 1994; *Braginsky and Roberts*, 1995] when in practice, it is always chosen to be of the order of or larger than 1 in numerical models (to allow dynamo action). For more Earth-like values, electrical current dissipation and thus field diffusion are very efficient and make it more difficult to achieve self-excited dynamo action. Also, this implies that the field will dominantly be of a large scale (independent of the scale of the flow) in the Earth's core itself as well as at its boundary (an important argument when downward continuing the field at the core-mantle boundary (CMB)).

[6] The numerical values of two essential parameters in dynamo equations are therefore off from their actual Earth values by factors in excess of one million! Yet increasing numbers of authors point out "Earth-like" features in their numerical models. Quoted features include a dominant dipolar axial component, so-called flux patches, westward drift, and in some cases polarity reversal. Most of these characteristics are validated with instantaneous snapshots of the models.

[7] Field observations are becoming simultaneously available at timescales ranging over at least 6 orders of magnitude (from annual to

millions of years) and a more modest spatial scale range (from global to spherical harmonic degree of order 10, i.e., "wavelengths" from 20,000 to 2000 km). However, these "observational constraints" may not be equally robust, and all groups of geomagnetists and paleomagnetists may not agree on their significance. Proper knowledge of all the pitfalls and sources of uncertainties in data acquisition (from magnetic observatory or satellite observations to sampling of rocks for paleomagnetic analysis, laboratory procedures, statistical treatment of raw data, and extraction of descriptive mean field models) is requested before these data can safely be used as constraints and guidelines by theoreticians and dynamo numericists.

[8] In section 2, we briefly summarize published dynamo models and recall the numerical values they use for characteristic parameters and the "Earth-like" features they are reporting. Section 3 is a critical review of field features uncovered from observations, organized in order of increasing timescale. The features we describe are sorted into three categories: robust, controversial, and rejected. In section 4, we confront the class of what we believe to be robust observations versus numerical predictions.

2. Status of Numerical Dynamo Models

[9] Modeling of magnetic induction in the Earth's core is a complex problem that involves the equations of magnetohydrodynamics in a rotating frame. It can be written using various approximations (compressible, Boussinesq, anelastic, etc.), heating, boundary conditions, and nondimensionalizations. In order to give a coherent picture of the models available so far, we have chosen to present them here using a common convention for nondimensionalization (we will use the core radius r_c as the length scale and define the Ekman number as $\nu/\Omega r_c^2$, where ν is the kinematic viscosity and Ω the Earth's angular velocity). When presenting these models, we will try to highlight the differences in the parameters they use (see Table 1), as well as in the approximations they apply. We point out in particular any Earth-like behavior they feature. We first introduce a few notions that are necessary to describe these models. The Ekman and magnetic Prandtl numbers have already been introduced. The Prandtl number is the ratio of the thermal versus kinematic diffusive timescales and is of the order of one or less than one in the Earth (between 0.01 and 1; or slightly above one if chemical diffusion is used instead of thermal diffusion). The ratio of the magnetic Prandtl number versus the Prandtl number is defined as the Roberts number; for the Earth's core it is of a magnitude comparable to that of the magnetic Prandtl number (about 10^{-6}). We will concentrate here on convection driven dynamos as this is the case in the papers presented here. It should be noted that other possible sources of energy are proposed for the geodynamos; these include chemical convection (with a shorter diffusive timescales) and precession. The Rayleigh number is a measure of the energy input to the system: the higher its value, the more vigorous motions will be. This parameter is defined using different conventions in numerical works (depending on the heating mode selected and on the normalizing quantity); it is very poorly known as far as the Earth's core is concerned [*Braginsky and Roberts*, 1995], but we know it must be high enough for motions to be able to sustain a magnetic field. Finally, we want to define what is meant by "strong field" and "weak field" dynamos. These notions were first introduced in asymptotic studies, with a meaning that is different from that used in numerical studies. Following *Roberts* [1978], for very rapidly rotating bodies like the Earth's core and when the magnetic Prandtl number is small, there would be two

Table 1. Parameter Values, Model Specifications, and Model Outputs for Numerical Three-Dimensional Dynamos

	Parameters			Model			Outputs				
	E ($\nu/\Omega r^2$)	Pr (ν/κ)	Pm (ν/η)	Equations	Boundary Conditions	Integration Time	Dipolar Field	Λ (F_B/F_Ω)	Reversals	Westward Drift	Others
Glatzmaier and Roberts [1995a, 1995b]	$\ell = 1$, 1.8×10^{-6} $\ell = 10$, 1.3×10^{-4} $\ell = 20$, 1.0×10^{-3}	5000	500	Boussinesq, no inertia	conducting I.C., Ins. M., rigid, with enhanced viscosity near boundaries	$3\tau_d$	yes	500	yes	yes	spectrum, I.C. super-rot.
Glatzmaier and Roberts [1996a]	$\ell = 1$, 1.8×10^{-6} $\ell = 10$, 1.3×10^{-4} $\ell = 20$, 1.0×10^{-3}	5000	500	Boussinesq, axial-inertia	conducting I.C., Ins. mantle, rigid	$0.8\tau_d$	yes		not yet	yes	spectrum, I.C. super-rot.
Glatzmaier and Roberts [1996b] and following	$\ell = 1$, 1.8×10^{-6} $\ell = 10$, 6.5×10^{-5} $\ell = 20$, 5.1×10^{-4}	725	725	anelastic, axial-inertia	conducting I.C., Ins. mantle, rigid	$15\tau_d$	yes	100	yes	yes	spectrum, I.C. super-rot.
Kuang-Bloxham	$\ell = 1$, 4.0×10^{-5} $\ell = 10$, 9.0×10^{-5} $\ell = 20$, 4.9×10^{-4}	1	1	Boussinesq, axial-inertia	conducting I.C., Ins. M.+conducting layer, stress free	$2\tau_d$	yes	$\mathcal{O}(1)$	not yet	yes	flux expulsion, Pacific window, spectrum
Busse et al.	5.1×10^{-4}–7.2×10^{-4}	5–20	100	Boussinesq, full-inertia	Ins. M. & I.C., stress free	$1.4\tau_d$	yes	2–20	not yet		
Kageyama et al.	4.0×10^{-4}	1	10.6–15	compressible, full-inertia	$B \wedge r = 0$, rigid	$50\tau_d$	yes	7×10^{-4}	yes		patches, sawtooth?
Christensen et al.	4.2×10^{-5}–4.2×10^{-4}	1	0.5–5	Boussinesq, full-inertia	Ins. M. & I.C., rigid or stress free	$3\tau_d$ to $10\tau_d$	yes	0.14–14	not yet	yes	patches
Kitauchi-Kida	5.6×10^{-3}	1	8.3–14.2	Boussinesq, full-inertia	vacuum, rigid	$100\tau_d$	yes	60	yes	yes	quasi threefold symmetry
Sakuraba-Kono	$\ell = 1$, 6.3×10^{-5} $\ell = 10$, 7.1×10^{-5} $\ell = 20$, 1.3×10^{-4}	1	20	Boussinesq, full-inertia	conducting I.C., Ins. mantle, rigid	$3\tau_d$	yes	0.1–10	not yet		Archean paleointensity
Katayama et al.	7.2×10^{-3}–7.2×10^{-2}	1	35	Boussinesq, full-inertia	Ins. M. & I.C., stress free	$6\tau_d$	yes	6×10^{-4}	not yet	yes	
Earth	10^{-15}	1/7	10^{-6}					$\mathcal{O}(1)$?			

Each row from the left corresponds to one model as described in a paper or series of papers. The last row recalls parameter estimates for the Earth's core. The first three columns display the parameters described in the text: the Ekman number, the Prandtl number, and the magnetic Prandtl number. The next three columns present the model used in the computations: equations, boundary conditions, and integration times (scaled with respect to the dipole free decay time $\tau_d \simeq 20$ kyr). Finally, the last five columns state the character of the generated field found in each model through the answer to the following questions: "Is the field dipolar?", "What is its strength?" (measured by the Elsasser number, defined as the ratio of the Lorentz force to the Coriolis term), "Did it reverse during the simulations?", "Does it drift westward?", etc. Ins., insulating; I.C., inner core; M, mantle; rot., rotation.

branches of dynamo solutions (i.e., two kinds of solutions): the weak field branch and the strong field branch. Let us start from a nonmagnetic state and let the Rayleigh number increase (starting from zero). At first the fluid is at rest, then, beyond a first critical value of this parameter, convection starts (this appearance of a new kind of solution is referred to as a "bifurcation"). The amplitude of convection increases as the Rayleigh number is further increased (the nature of this bifurcation is characterized by the asymptotic study of *Soward* [1977]). Beyond a second critical value, motions become energetic enough to maintain a magnetic field (starting with a perturbation): this is the dynamo bifurcation. This second bifurcation produces a weak field dynamo, in the sense that the amplitude of the field is controlled by viscous effects (though viscosity is very small). If the Rayleigh number is further increased, this branch disappears beyond a third critical value, and the solution quickly evolves to another branch (through runaway growth of the magnetic field intensity). On this new branch, viscous effects are negligible and the amplitude of the field is now controlled by magnetostrophic equilibrium (between Lorentz and Coriolis forces). The nondimensional number measuring the ratio of the Lorentz force to the Coriolis acceleration, namely the Elsasser number, is then close to unity [*Soward*, 1979]. This second solution is referred to as the strong field branch. Given the strength of the measured geomagnetic field, it is clear that the Earth's dynamo corresponds to that kind of solution. The geometry of the solution on that branch should significantly differ from the previous one. In fact, once on that strong field branch, the magnetic field has relaxed the constraints imposed by rapid rotation on the flow, and dynamo action is expected to exist even if the Rayleigh number is now decreased below its first critical value (onset of convection). It is worth noting that such behavior (subcritical dynamo action) has not been observed so far in any numerical models with a spherical geometry.

[10] This whole scenario has been established for small magnetic Prandtl numbers and in the limit of small Ekman numbers or vanishing viscosity (relevant to the Earth), and it is only relevant to that regime. For numerical work one refers to a strong field dynamo if the magnetic field term is on the same order of magnitude, or even much larger than the Coriolis term (the Elsasser number is then equal or larger than unity); this, of course, does not imply that viscosity is negligible (as would be needed with the original definition). Viscosity is never negligible in current three-dimensional numerical models, whose stability always rely on the viscous term. The strong field notion used to discuss numerical models must therefore not be confused with the well-defined one used in the asymptotic regime (see *Childress and Soward* [1972] for a rigorous definition between parallel planes). Indeed, studies of simplified problems strongly suggested that in the asymptotic regime, the Elsasser number should settle to values very close to unity on the strong field branch (see *Eltayeb and Roberts* [1970], *Eltayeb and Kumar* [1977], *Fearn* [1979a, 1979b], and *Soward* [1979], and for a review, see *Soward* [1998]). We will see that such is not always the case for numerically strong field dynamos.

[11] It is important to note here that molecular values were used to evaluate all diffusivities (i.e., viscosity as well as thermal and magnetic diffusivities). It can be argued that small-scale turbulent flow will lead to equivalent large-scale diffusivities that could be several orders of magnitude larger than molecular values. Through a study of the small-scale thermal instability of the core, *Braginsky and Meytlis* [1990] obtained a qualitative picture of the anisotropic turbulent motions and field. They expect that the effects of small-scale turbulence

on the large-scale flow will be highly anisotropic and that the equivalent thermal diffusivity tensor could compare in magnitude with magnetic diffusivity. If this is true and if one neglects the important anisotropy, then the equivalent Roberts number at large scale would be close to one. It is also often argued that vigorous convective models lead to order one values for the equivalent Prandtl number. A simplified argument would then be that all equivalent diffusivities are of the same order, which would imply order one Roberts, Prandtl, and magnetic Prandtl numbers and an Ekman number close to 10^{-9}. The "turbulent" Ekman number evaluated this way would still be several orders of magnitude smaller than can be achieved so far numerically. For ratios of diffusivities (especially the Roberts number and the magnetic Prandtl number), the turbulent estimates are much easier to use than the values based on molecular diffusivities.

[12] This turbulent modification of the parameters can be justified with the qualitative picture described above, but it is not theoretically established. It does not take into account the strong anisotropy of the small-scale flow. Also, experimental studies show that setting a turbulent Prandtl number to unity is an oversimplification, even for nonrotating and nonmagnetic low Prandtl number turbulent convection [*Cioni et al.*, 1997].

[13] Of course, the present goal of numerical simulations cannot yet be to achieve geophysical values of the parameters based on molecular diffusivities! Only the asymptotic behavior, and a well-approximated large-scale solution, constitute a realistic objective. One can then wonder whether this aim can be better achieved using magnetic Prandtl numbers based on either isotropic turbulent diffusivities (i.e., magnetic Prandtl number of order 1) or molecular values (i.e., 10^{-6}). This remains an open question. However, part of the difficulty clearly is to understand how dynamo action is maintained despite the very efficient magnetic diffusivity (compared with other ones). Assuming an order 1 magnetic Prandtl number is a way to get around this issue.

2.1. Zhang and Busse

[14] In 1988 and 1989, Zhang and Busse presented magnetic field generation results in a rotating spherical shell with imposed symmetry with respect to the equator and imposed periodicity in longitude (this is therefore not fully three dimensional). They studied magnetic Prandtl numbers above which they obtained steady or oscillatory dynamos with either quadrupolar or dipolar fields [see also *Zhang et al.*, 1989]. Their approach (later extended by *Hirshing and Busse* [1995]) consisted in following the consecutive bifurcations, starting from the nonmagnetic solution. Being close to the mathematical/physical understanding described above, this approach should allow one to describe solutions on the weak field branch and to safely establish the strong field branch (after runaway growth of the field intensity). This seems to be a safe approach to ensure that parameters different from Earth values indeed lead to the appropriate equilibria (e.g., magnetostrophic balance). The numerical scheme used for resolving the nonlinearity (Galerkin) required moderate values of the Rayleigh number; also in order to study the dynamo bifurcation (starting with arbitrarily small magnetic field), a very high resolution would be needed for the convective regime at high values of the Rayleigh number. When trying to increase the Rayleigh number and/or decrease the Ekman number, authors noted [*Zhang et al.*, 1989] that magnetic fields tend to decay. In these earlier studies, little attempt was made to compare numerical solutions with geomagnetic features. They only concerned westward drift of the nondipole part

of the field [*Zhang et al.*, 1989] and suggestions that reversal maybe due to the close competition observed between dipolar and quadrupolar field geometries.

2.2. Glatzmaier and Roberts

[15] In a series of papers, Glatzmaier and Roberts showed that chaotic dynamos exhibiting features similar to those of the geomagnetic field can be simulated with current computers. Their approach was different from that of Zhang and Busse. Instead of following successive bifurcations (or modifications) of the solution as the Rayleigh number was increased, starting with a nonmagnetic solution, they fixed the Rayleigh number and exhibited a dynamo solution starting with large initial magnetic fields. The Elsasser number (defined on the maximum value of the field) was found to be larger than one.

[16] They successively used two approaches to model the liquid outer core. The first approach [*Glatzmaier and Roberts*, 1995a, 1995b, 1996a] relied on the Boussinesq approximation. Essentially, all density variations were neglected, except for the buoyancy effect. This approximation has been used in most subsequent numerical models. It is not quite appropriate for the Earth, since density varies with depth in the core, but it is a reasonable approximation. The second approach [*Glatzmaier and Roberts*, 1996b and following] relied on the more appropriate anelastic approximation, allowing for varying properties of the Earth with depth. This approximation and its application to the Earth's core had been fully introduced by *Braginsky and Roberts* [1995]. It was not found to yield drastic changes on the solution.

[17] The first model [*Glatzmaier and Roberts*, 1995a, 1995b] was the first to exhibit reversals in a configuration trying to mimic the Earth's core. This model is very sophisticated and incorporates many different features (hyperviscosity, rotation of the inner core, thin conducting layer at the base of the mantle, etc.). Numerical integration of the model was performed over some three dipole diffusion times (to attest dynamo action). Inertia was dropped in this integration, because of the low value (10^{-6}) of the coefficient scaling it (for geophysically realistic values of parameters). This term was discarded, whereas numerical reasons imposed that a 10^9 times smaller term (viscous effects) be retained. The model incorporated enhanced viscosity in boundary layers. The authors later noted [*Glatzmaier and Roberts*, 1996a, 1997b] that this feature was at least partly responsible for destabilizing the solution (which led to the reversal) and significantly altered the field spectrum. When removing this additional enhanced turbulent viscosity in boundary layers, *Glatzmaier and Roberts* [1996a] noted that the solution got more strongly dipolar and did not reverse for the remainder of their simulation. Other modifications included reintroduction of inertia for the zonal axisymmetric components of the flow and a significant reduction of the electrical conductivity of the lower mantle [see *Glatzmaier and Roberts*, 1996a]. It was integrated further over less than one dipole diffusion time. They observed flux patches in these models and noted that the nondipolar part of the simulated field at the outer boundary (CMB) was qualitatively similar in structure to that on Earth and had westward drifting features [*Glatzmaier and Roberts*, 1997b].

[18] The second model [*Glatzmaier and Roberts*, 1996b, 1996c] was similar to the first one (in its 1996a version), but it used an inhomogeneous (or anelastic) approximation. This approximation is based on the assumption that velocities in the fluid flow are small compared with acoustic velocities. The temperature gradient at the outer sphere was superadiabatic and uniform. The associated

heat loss generated thermal and compositional sources at the inner sphere boundary by cooling the whole domain. Both thermal and compositional driving mechanisms were considered, and model parameters were slightly modified, the hyperdiffusivity was reduced. The field generated by this model again showed a tendency to drift westward. For both models the behavior was very different inside and outside the tangent cylinder (the cylinder having the same axis as the axis of rotation and the same radius as the inner core). The most intense magnetic activity was confined to the interior of this cylinder (in contrast with most other models reported below). This second model was also studied in different configurations [see *Glatzmaier and Roberts*, 1997a]: heterogeneous heat flux at the outer sphere (inspired by lower mantle tomography), subadiabatic model, and subadiabatic model with varying heat flux.

[19] Important ingredients of all these simulations were assumptions concerning the way the small-scale turbulent flow, which could not be numerically resolved, affected the large-scale flow and field. Crucial to the success of the numerical work was the introduction of enhanced dissipation of the higher spectral components, a procedure described as using "hyperviscosity." The same was also applied to magnetic and thermal diffusivity, and referred to as using "hyperdiffusivity." This procedure, though essential for the numerical work, is difficult to justify on physical grounds. In very approximate terms we might say that the simulations introduce enhanced turbulent diffusivities in the horizontal directions, rather than in the directions given by the rotation axis and the large-scale magnetic field, as identified by *Braginsky and Meytlis* [1990]. The effective Ekman number varies with the spherical harmonic degree of the field. The effect of hyperviscosity on the large-scale solution is unknown, though *Zhang and Jones* [1997] showed that the introduction of hyperviscosity in convection simulations not only has some impact on the effective Ekman number (see Table 1 for the Ekman number at various degree l) but also modifies the force balance in the momentum equation and thus the asymptotic behavior itself (see the discussion by *Sarson and Jones* [1999]). This issue was recently addressed in the dynamo regime by *Grote et al.* [2000b] (see section 2.4). They found that the effects of hyperdiffusivities increased as the Ekman number was decreased.

[20] In both models the authors observed that the solid core rotates faster than the mantle. There is an ongoing debate in the seismological community to determine whether such superrotation of the inner core is actually observed in the Earth [*Song and Richards*, 1996; *Su et al.*, 1996; *Souriau et al.*, 1997; *Souriau*, 1998a, 1998b; *Poupinet et al.*, 2000]. Magnetic observations of a polar vortex were recently reported [*Pais and Hulot*, 1997, 2000; *Olson and Aurnou*, 1999]. These observations appear to be compatible with a thermally driven rotation of the inner core [*Aurnou et al.*, 1996; *Pais and Hulot*, 2000] but also with a nonrotating inner core [*Olson and Aurnou*, 1999]. *Kuang* [1999] argued that this effect could be an artefact, due to excessive viscous coupling in numerical models. The issue of a possible rotation of the Earth's inner core is therefore not yet resolved.

[21] *Glatzmaier et al.* [1999] studied reversals with this model and various patterns of heat flux at the core-mantle boundary. They extended time integration over some 15 dipole diffusion times. Surprisingly, they found that the case with uniform heat flux at the core-mantle boundary appeared the most Earth-like. The simulation using a prescribed heat flux inferred from seismic velocity anomalies (tomography) in the lowermost mantle did not

produce a very realistic field (a reversal lasted more than one dipole diffusion time), plus the excursion frequency appeared much too high. The authors suggested that variations in heat flux at the core-mantle boundary could thus be smaller than previously thought. Interestingly, varying numerical resolutions, they noted that the field strength depended on the resolution used. The dipole moment, on average lower than that stimated for the Earth, was found to be greater or similar when numerical resolution was increased. Very recently, *Coe et al.* [2000] performed a detailed comparison of reversals in these numerical simulations. Both homogeneous and heterogeneous heat fluxes at the outer boundary were found to feature low intensities during reversals, with longer-term intensity variation resembling sawtooth behavior. Statistical studies of virtual geomagnetic pole (VGP) paths, i.e., paths followed by the poles of a dipole that would produce the observed directions at a given site, were performed during reversals. In the case of the heterogeneous model it was suggested that VGP paths seem to correlate with high heat flux areas, though only two reversals were available.

[22] Parameters used for these models are presented in Table 1. The choice of these parameters is of course not unique and other parameters could be added (e.g., the Roberts number, introduced in section 2). An interesting number is the ratio of the Ekman to the magnetic Prandtl number, sometimes referred to as the magnetic Ekman number, and representing the ratio of the rotation timescale (the day) to the magnetic timescale. This number is important when comparing numerical with actual time units (as will be discussed in section 3). It is close to 10^{-9} for the Earth. Parameters used in the Glatzmaier and Roberts models were set to approach this value (using nominal coefficients, i.e., neglecting hyperdiffusivities). It is useful to recall that viscosity does not enter the definition of this number.

2.3. Kuang and Bloxham

[23] *Kuang and Bloxham* [1997] presented another model that they called "an Earth-like numerical dynamo model." They studied a Boussinesq model including a conducting inner core. They assumed a conductive layer above the core-mantle boundary and used hyperviscosity, only axial inertia was retained. Reported integration times range over four dipole diffusion times. Their solution differs greatly from the Glatzmaier and Roberts models: convection and induction occur mainly outside the tangent cylinder. Many differences exist between both models (definition of hyperviscosity, heat flux, rotation rate, boundary conditions, etc.). *Kuang and Bloxham* [1997] attributed most of the differences in the numerical results to the kinematic boundary conditions. Moreover, they produced a solution comparable to the Glatzmaier and Roberts model when using the same kinematic boundary conditions. Glatzmaier and Roberts used a no-slip (or rigid) kinematic boundary condition: this condition is physically realistic (motion of a fluid near a solid wall should vanish). Kuang and Bloxham, on the other hand, used free-slip (or stress-free) boundary conditions (no penetration but also no tangential stress). This condition has the convenient property of suppressing sharp boundary layers (numerically difficult to resolve). The authors claimed that since viscosity is very small in the Earth's core, the effects of these layers could be neglected, and thus the layers be suppressed from the computations. They suggested that viscous effects (associated with high Ekman number values) in the Glatzmaier-Roberts dynamo models were especially important near boundaries (in boundary layers). They claimed that by using stress-free boundary conditions, hence suppressing strong viscous effects at the boundary, they would reduce viscosity effects in their model to an almost negligible level, bringing it closer to expected Earth behavior [*Kuang and Bloxham*, 1997].

The possibility of boundary layer instabilities in the parameter regime thought to be valid for the Earth [*Desjardins et al.,* 1999, also Instability of Ekman-Hartmann boundary layers, with application to the fluid flow near the core-mantle boundary, submitted to *Physics of the Earth and Planetary Interiors*, 2000] however raises questions on the validity of this simplification.

[24] *Kuang and Bloxham* [1998] next presented a comparison of their results with the actual Earth's magnetic field. They proposed an interpretation in terms of physical quantities, under the assumption that viscous effects were negligible in their computation (this scaling is comparable to the one used by Glatzmaier and Roberts). They focused their comparison on westward drift, episodes of flux expulsion, and behavior similar to the so-called "Pacific dipole window" (i.e., low secular variation in the Pacific hemisphere, see below). They compared the spectrum of the field generated by their dynamo with that based on historical measurements of the Earth's magnetic field. While other groups generally compared the spectrum of their dynamo fields with the Earth's field for 1980 (well known because of MAGSAT data), Kuang and Bloxham used the *Bloxham and Jackson* [1992] reconstruction of the mean field over the last 300 years (this field model incorporates some additional assumptions, including damping of higher degree terms). They also noted that flow at the core surface was similar to that inferred from secular variation. However, they did not report any polarity reversal. The full description of their numerical model was recently published [*Kuang and Bloxham*, 1999].

[25] *Kuang* [1999] investigated the role of boundary conditions in this dynamo model. He presented two computations, one with stress-free boundaries and the other with no-slip boundaries. His main concern was to show that when viscous couplings at the boundaries are eliminated (free-slip conditions), the axial Lorentz torque acting on cylindrical surfaces (coaxial with the axis of rotation) almost balances fluid inertia, leading to the suggestion that viscosity had little effect on the solution. Kuang showed that with free-slip boundary conditions the viscous torque was smaller than the Lorentz torque (by a factor of 2) on most of these cylinders. Using free-slip boundary conditions led to an oscillating (rather than rotating) inner core. Note finally that the Elsasser number was measured using averaged field values.

2.4. Busse and Coworkers

[26] *Wicht and Busse* [1997] presented the study of numerical dynamos, using a Boussinesq approximation with full inertia, as well as stress-free and insulating boundary conditions. Their study was limited to even azimuthal wave numbers (implying symmetry of the solution about a meridional plane). The authors concentrated on numerical resolution and sequences of bifurcations (see the discussion of the model by Zhang and Busse above) at low Prandtl number values ($Pr \simeq 0.1$). They showed that the subcritical dynamo effect disappeared when numerical resolution was increased. Thus they could not produce numerical dynamos for Rayleigh numbers below the critical value for convection (except when restricting their comparison to the dominant azimuthal wave number). Later, *Busse et al.* [1998] used a Chebychev (instead of Fourier) radial scheme and studied the influence of the Prandtl number. They investigated chaotic dynamos and noted a strong dependence of the mean zonal flow on the Prandtl number. More strikingly, they noted that the ratio of magnetic to kinetic energy density is proportional to the Prandtl number (after nondimensional reasoning and confirmation by their numerical results). Because the inertial term scales as the inverse of the Prandtl number, magnetic energy density would necessarily be larger than kinetic energy density in models where the inertial term is dropped (e.g.,

Glatzmaier and Roberts' first model, Jones et al.) or partly dropped (e.g., Glatzmaier and Roberts' following models, Kuang and Bloxham). This emphasizes how the popular distinction between weak and strong field dynamos in numerical models can be very misleading (see also the nontrivial definitions of these notions in the beginning of this section). The authors also noted that the ratio of magnetic energies of the axisymmetric to nonaxisymmetric components of the induced field increased strongly with the Prandtl number. *Busse et al.*, [1998, p. 212] stressed that "the impression currently en vogue in parts of the scientific community that the problem of the origin of the Earth's magnetic field has been solved is overly optimistic" and insisted on the need for numerical dynamos with magnetic Prandtl numbers lower than unity (not yet achieved so far). *Grote et al.* [1999] showed that for (1) Prandtl number unity, (2) magnetic Prandtl numbers in the neighborhood of unity, and (3) with Ekman numbers ranging from 6×10^{-5} to 2.4×10^{-4}, the field generated by dynamo action is dominantly axial quadrupolar. They argue that this preference is related to the suppression of convection in polar regions observed at lower Ekman numbers. *Grote et al.*, [2000a, p. 270] present a more detailed parameter space and distinguish between regular and chaotic dipolar dynamos, quadrupolar dynamos, and hemispherical dynamos (where the magnetic field nearly vanishes in one hemisphere due to "roughly equal contributions from the axial quadrupolar and dipolar fields"). The type of solution is found to depend mainly on the magnetic Prandtl number and on the Rayleigh number. Dipolar dynamos were only reported for magnetic Prandtl numbers above 10 [see *Grote et al.*, 2000a, Figure 1]. *Grote et al.* [2000a, p. 271] insisted that in such simulations "the magnetic field does not seem to influence the convection velocity very much." *Grote et al.* [2000b] investigated the role of hyperviscosity on their dynamo model and noted that unrealistic dynamical effects could be introduced. The ratio between axisymmetric and nonaxisymmetric components of the magnetic energies was also found to be larger in hyperdiffusive simulations (by a factor 4). The authors note that the differences between hyperdiffusive and regular dynamos increase when the Ekman number is decreased and the Rayleigh number increased.

2.5. Kageyama and Sato

[27] *Kageyama and Sato* [1997a, 1997b, 1997c] presented a dynamo model in a rotating spherical shell filled with a conductive ideal gas; thus they solved equations in the compressible case. They used rigid kinematic boundary conditions and included full inertia. Magnetic boundary conditions in their model were not very geophysical: only the radial component of the field was allowed to be nonzero at the boundary (the authors argue that this ensures that the Poynting vector flux through the boundaries is zero). They first [*Kageyama and Sato*, 1997a] concentrated on the linear growth phase (before saturation) and described how the field was increased by convective columns. They next [*Kageyama and Sato*, 1997b] studied a (numerical) strong field dynamo, in which the magnetic field was found to be strongly dipolar, the second largest multipole being the octupole (representing 77% of the dipole in terms of energy). Kageyama and Sato concluded that dipolar fields were a natural consequence of columnar convection in a rotating spherical geometry. *Kageyama and Sato* [1997c] focused on the magnetic field distribution at the CMB and in the equatorial plane. Recently, *Kageyama et al.* [1999] extended integration time from some 15 to about 50 dipole diffusion times and presented a numerical polarity reversal in their model (the magnetic Prandtl number was here increased to 15). They observed that the dipole reversal was followed by a sequence of octupole reversals,

each one correlated with energy jumps, and suggested that paleomagnetists should look for such features in data.

2.6. Christensen-Olson-Glatzmaier

[28] *Christensen et al.* [1998] published a dynamo model without hyperdiffusivity, retaining full inertia and using no-slip boundary conditions. Boundary conditions were rigid and insulating (including the inner core). The authors noted that their model qualitatively reproduced several structural characteristics of the present-day geomagnetic field: a dipole-dominated magnetic field, with distinct bundles of strong radial flux at high latitudes, low flux over the poles, and paired spots of reversed flux near the equator. The magnetic flux contribution to the dipole moment was concentrated in distinct patches at about 60° latitude. The field generated appeared to be more dipolar than the present geomagnetic field. Its structure appeared to be comparable to that found in the work of Kuang and Bloxham's model.

[29] In a later study, *Olson et al.* [1999] exhibited two regimes for dynamo action, which depend on the Rayleigh number (energy input). The first one (low Rayleigh number) corresponds to a strongly columnar regime (comparable to laminar convection with no magnetic field). The dipole-dominated external field then appears to be formed from a superposition of flux bundles. The authors observed a pattern of reversed flux patches that propagated in the westward direction at low latitudes. At higher Rayleigh numbers they observed the development of convection inside the tangent cylinder, characterized by polar upwelling and azimuthal winds. This second regime reproduced some of the features thought to be typical of the present magnetic field: concentrated flux patches, polar minima in field intensity, and episodes of westward drift (this regime contains some elements of similarity with the Glatzmaier and Roberts dynamo).

[30] Recently, *Christensen et al.* [1999] published a systematic parameter study of their dynamo model and varied the kinematic boundary conditions. Again, they obtained mainly axial dipolar fields (with a few quadrupolar exceptions). Interestingly, they found little influence of the kinematic boundary conditions (no-slip versus free-slip) in their model, contrary to what Kuang and Bloxham observed. They suggest this discrepancy is due to the use of an insulating inner core, which suppresses magnetic torque on the inner core. They studied various magnetic Prandtl numbers (they decreased, for the first time, this parameter slightly below one and presented dynamos at $Pm = 0.5$). As the magnetic Prandtl number was decreased below a critical value for a given Ekman number, the authors observed that no self-sustained dynamo action could occur. This is an important result, because the minimum critical values they obtained are about one million times larger than the magnetic Prandtl number relevant to the Earth's core. They observed, however, by decreasing the Ekman number by a factor of 10, that the critical value decreased as well. By computing the exponent for the evolution of this parameter (over a rather short range), they estimated that an Ekman number as small as 10^{-12} would be necessary to sustain dynamo action in the regime of small magnetic Prandtl number (10^{-6}). This confirms the need to study high rotation rates (i.e., small Ekman numbers) to observe dynamo action in a medium with efficient magnetic field diffusion (small magnetic Prandtl number), as is the case for the Earth's core.

[31] The magnetic fields they obtained at the outer boundary for two of their dynamo models were of smaller scale, with flux spots stretched in a meridional direction. The authors sug-

gested that the field at the Earth's core-mantle boundary could be small scale as well (despite the much larger magnetic diffusivity) but would appear large scale because of the limited resolution used to represent the core field (largely because of difficulties in removing crustal effects). Broad features (such as patches) in a low-pass filtered representation of their results compared well with those observed in the 1980 field model. No reversal nor significant excursion was observed in any of these studies.

[32] *Kutzner and Christensen* [2000] studied the influence of different driving mechanisms on this model. They reported dipolar dynamos when modeling chemical convection or thermal convection with an imposed temperature difference between the ICB and the CMB. When using purely internal heating (e.g., radioactive heat sources in the core), they only reported dynamos producing quadrupolar (or more complex) fields (see also, in section 2.4, quadrupolar dynamos reported by Grote et al.).

2.7. Kitauchi and Kida

[33] *Kitauchi and Kida* [1998] presented numerical simulations with a Boussinesq model with full inertia. Boundary conditions were somewhat ungeophysical: vacuum was assumed outside the shell. Their solution took the form of a weak field dynamo with periodic reversals of the dipole moment. The flow consisted in convection columns (with a fivefold symmetry); they observed that the magnetic field did not share the same symmetry and studied the mechanism of field intensification. Kitauchi and Kida noted that the structure of the external magnetic field they obtained bore some similarities with the Earth's field: the pattern of the magnetic field was antisymmetric with respect to the equatorial plane and strong magnetic flux in the middle latitudes drifted westward. *Kida and Kitauchi* [1998] increased the magnetic Prandtl number and reported chaotic polarity reversals of their solution. Four observational constraints were considered in this article: dominance of the dipole component, chaotic nature of dipole reversals, quasi-threefold symmetry around the rotation axis, and westward drift of the magnetic field. They noted that these features were all well reproduced by their model except for the quasi-threefold symmetry. Using the reported magnetic energy, one can estimate the Elsasser number to be close to 60.

2.8. Sakuraba and Kono

[34] *Sakuraba and Kono* [1999] presented the study of a numerical dynamo model in a spherical shell and in a full-sphere simulation. They used a Boussinesq model and retained full inertia. The authors used hyperviscosity (see definition section 2.2). The aim of their work was to study the effect of the conducting and free-to-rotate inner core on field generation. They observed that field induction was particularly important near the zone of strong shear associated with boundary layers (precisely those boundary layers suppressed in models using free-slip kinematic boundary conditions). They reported an "Earth like dipole field" and concluded that the thin boundary layers were important in the magnetic field generation process. They observed the stabilizing effect of the inner core on the magnetic field and suggested that growth of the inner core could help interpret the low paleointensity records from the Archean.

2.9. Katayama and Coworkers

[35] *Katayama et al.* [1999] presented a Boussinesq dynamo model with full inertia and an insulating inner core. Stress-free (or free-slip) boundary conditions were used (suppressing boundary layers). The authors examined the magnetic field generation mechanism of their solutions. The magnetic field appeared to be confined in cyclonic convection columns (in a

manner comparable to the models of Zhang and Busse or Kageyama and Sato presented above). They describe the "numerical weak field" regime (the Elsasser number can be estimated, based on the magnetic energy, to be less than 10^{-3}). In this regime, and with Ekman number of 0.07, they still obtained a dominantly dipolar axial field. They also noted that patterns of velocity and magnetic field drift westward in their simulation, although they did not observe any reversal (so far) in the parameter range they studied.

2.10. Jones and Coworkers

[36] We also would like to briefly report some results obtained with a mean field approximation model introduced by *Jones et al.* [1995]. In this approach, only an arbitrary azimuthal component was considered in addition to the mean axisymmetric component. The authors used a two-mode approximation, which is self-consistent and is referred to as a 2.5-dimensional model. Although this model is not a full three-dimensional solution to the MHD equations, some of the results they reported have Earth-like behavior and can shed some light on the behavior of fully 3-D models. The main advantage of their approach is to make numerical integration lighter, thus allowing the extention of the range of studied parameter values. *Jones et al.* [1995] studied different parameter regimes and found a (numerical) "weak field" regime as well as a (numerical) "strong field" regime. The fields were largely axial and dipolar but had an axisymmetric dipolar component about twice as large as in the Earth and a larger value of the nonaxisymmetric components. *Jones et al.* [1995] also studied a model in which a stable layer was introduced at the top of the core in order to decrease these discrepancies.

[37] *Sarson et al.* [1998] presented a systematic study of the 2.5-D model, using hyperdiffusivity for some simulations only. This model produced solutions very similar to some of the previously published 3-D numerical dynamos, yet at much lower cost. At the higher values of the Ekman and Roberts numbers and moderately supercritical Rayleigh numbers, results were very similar to the *Zhang and Busse* [1988, 1989] solutions. At lower values of these parameters (with hyperviscosity) the solution reproduced most of the characteristics of the *Glatzmaier and Roberts* [1995a, 1995b, 1996a, 1996b] model. *Sarson and Jones* [1999] studied magnetic field reversals in more detail in the latter parameter regime. The origin of reversals was interpreted in terms of "buoyancy surges" occurring inside the tangent cylinder. It was demonstrated that suppressing the Lorentz force did not significantly alter the basic form of the flow, again showing that viscosity has a very important effect on numerical solutions and that the magnetic field exerts a relatively minor influence on the solution (despite the dynamo being a "numerically" strong field).

2.11. Conclusions on Geodynamo Models

[38] We summarize the results presented above in Table 1. The first three columns of Table 1 recall parameter values used in the models (using the common nondimensionalizations introduced above); the next three columns summarize the differences in the model definitions and integration times; the last five columns summarize the outputs from these models. All models succeed in producing dipolar fields. Most of them are strong field models according to the definition used by numericists (i.e., Elsasser number above unity). Note that the Elsasser numbers reported here are those given by the authors (or derived from values of magnetic energy). They are based in most cases on the mean value of the magnetic field throughout the core, although some authors prefer to use its maximum value (e.g., Glatzmaier and Roberts). Actually, most models produce Elsasser num-

bers much larger than unity, opposed to what is expected in the asymptotic regime (see discussion at the beginning of this section). Also, several authors [*Grote et al.*, 2000a; *Sarson et al.*, 1998] have pointed out that the Lorentz force could be suppressed from numerical integration without affecting much the geometry of their solutions. Reversals were observed in some models but relatively short integration times (below 5 dipole diffusion times for most models) do not allow a significant distinction between models. Most models are found to have westward drifting features, and a few other Earth-like features have also been noted in the last column.

[39] We wish to stress that the most fundamental point to have emerged from numerical simulations within the last few years is probably that most of the available numerical models, even with Ekman numbers close to 0.1 [see *Katayama et al.*, 1999] succeed in producing an external magnetic field largely dominated by an axial dipole component (with a few quadrupolar exceptions, see *Grote et al.* [1999, 2000a] and *Kutzner and Christensen* [2000]), with weaker nondipolar structures and in some cases even polarity reversal of the dipole. With perhaps exaggerated optimism one could argue that despite drastic differences in the parameter regimes, numerical dynamos capture the essential features of the Earth's magnetic field generation mechanism. Somewhat puzzling, though, are the discrepancies on the generation mechanisms involved in these models. Some models generate the magnetic field by chaotic motions mainly inside the cylinder tangent to the inner core (e.g., Glatzmaier and Roberts), others by chaotic motions mainly outside this cylinder (e.g., Kuang and Bloxham); some propose a giant alpha effect in columnar structures comparable to nonmagnetic convection rolls (e.g., Christensen et al. or Kitauchi and Kida); some stress the role of boundary layers in the field generation mechanism (e.g., Sakuraba and Kono), whereas others artificially suppress these layers (e.g., Kuang and Bloxham, Busse et al., or Katayama et al.). This stresses the need for robust yet detailed constraints to describe what an Earth-like magnetic field actually should be and hopefully establish whether any of the available models fulfills these constraints. This is the object of the following two sections.

3. Evaluation of Observational Constraints

[40] A picture of the present-day geomagnetic field would, of course, not be sufficient to describe the Earth's magnetic field, much in the same way it would be impossible to determine the climate of a region with only a snapshot of the weather at an arbitrary time. We therefore present here a short review of observational facts established with geomagnetism, archeomagnetism, and paleomagnetism, and attempt to find objective criteria that allow one to propose which observations can be considered as robust and can (should) be used in order to efficiently constrain numerical models. Data provided by geomagnetism, archeomagnetism, and paleomagnetism are based on instrumental and interpolation methods whose heterogeneity must be taken into account; their accuracy and time constants vary over a very large range. Some simple criteria must be sought to provide an objective basis to decide which of these observations are indeed robust and relevant. There is not much worry regarding present-day and historical field determinations over the last centuries, although improving accuracy and spatial coverage are of course important. *Bloxham and Gubbins* [1985] have considerably extended our knowledge of the geomagnetic field over the last three centuries, using ancient ship logs. Confidence in the results is a function of irregular data distribution and, for instance, lack of intensity

measurements prior to 1830. Most controversies or ambiguous observations occur for older periods and longer timescales, when magnetic measurements are linked to acquisition of magnetization by artefacts or rocks. This is due to uncertainties in dating and in the complex process of magnetization acquisition.

[41] For this reason, global geomagnetic features must be properly documented by multiple records from different locations (and different materials whenever possible). It is also important that additional testing be provided by different approaches or alternative parameters. Converging observations reached independently by various teams should be considered as a prerequisite to the evaluation of the records. It is obviously difficult to reach any conclusion about the actual interpretation of the records, as long as there is controversy going on about the validity of the observations or the relevance of the interpretations. It cannot be excluded that in the near future, new data or theories could invalidate some features that we presently retain as actual characteristics of the field. Conversely, some ongoing controversies could be settled by new data. On the basis of these ideas we will attempt to sort observations in three categories: A, the most robust ones that are supported by multiple locations/analyses/authors; B, those that are still at the center of live ongoing controversies, and C, those that have at some time been proposed but are now considered most unlikely. We believe there is overall agreement within the community on the first (A) category.

[42] Analyses based on present or historical field data are useful to document most variations with time constants of a few hundred years, which seem to characterize the evolution of the main part of nondipole terms. The mean archeomagnetic field documents longer field changes and appears to resemble the paleomagnetic field [e.g., *Carlut et al.*, 1999]. Its geometry is also much simpler (i.e., lower harmonic degrees prevail) than the complex historical field. As recalled above, such timescale-dependent magnetic behavior, with complex short-term secular variation opposed to longer-term smoother changes, is reminisent of the contrast between the complexity of weather patterns and longer-term evolution of the climate [see *Cox*, 1975]. At all timescales, one seeks to characterize the steady and transient parts of the field, to describe their amplitude and space variations, and to relate one timescale to the next. For instance, *Hulot and Le Mouël* [1994] and *Carlut et al.* [1999] have attempted to identify the typical time constants of individual spherical harmonic components of the field; these components are noted g_n^m and h_n^m and are respectively defined as the cosine and sine terms in the spherical harmonic expansion of the magnetic potential in the mantle (assumed to be an insulator). These timescales are of the order of 500 years for the equatorial dipole (g_1^1,h_1^1) and less for other higher-order terms, whereas the axial dipole (g_1^0) changes much slower. In the following, we summarize our analysis of available data and observations based on their characteristic duration, starting with the shortest ones.

3.1. From 0.1 Year to 1 kyr

3.1.1. Secular Variation Impulses

[43] Many summaries of the present-day and historical field time variations are available [e.g., *Merrill et al.*, 1996; *Courtillot and Le Mouël*, 1988]. It is now generally accepted that the conductive mantle efficiently attenuates and therefore screens out variations with internal origin with a time constant shorter than a few months. The shortest phenomena of unquestionable internal origin are the so-called geomagnetic secular variation impulses or jerks [*Courtillot and Le Mouël*, 1984], which have occurred (irregularly) some seven times in the

last 150 years [*Alexandrescu et al.*, 1995, 1996a, 1996b, 1997; *Mandea-Alexandrescu et al.*, 1999; *McMillan*, 1996]. These worldwide events have a total duration of the order of, or possibly less than, 1 year. They possibly propagate and are attributed to brief, major changes in the large-scale flow in the core [*Hulot et al.*, 1993]. They are well established and thus fully satisfy category A requirements. Although the sequence of identified jerks is very short, their occurrence appears to be quite irregular, with seven events between the present and 1870, and none in the preceding 150 years [*Alexandrescu et al.*, 1997; *Mandea-Alexandrescu et al.*, 1999]. The impulses, which are separated by quieter intervals, shape much of recent secular variation. This is found to correlate well with predictions based on time-dependent models of flow in the core, and with observed length of day changes, implying core-mantle coupling with exchange of angular momentum, as was first shown for the 1969–1985 period by *Jault et al.* [1988] and extended to the 1840–1990 period by *Jackson et al.* [1993], then developed in more detail by *Pais and Hulot* [2000].

[44] Interestingly, the fastest impulses have been inferred not from geomagnetic but from paleomagnetic observations: they are those associated with the polarity transition recorded 16 Myr ago at the Steens Mountain in Oregon. In a series of papers [e.g., *Coe and Prévot*, 1989; *Coe et al.*, 1995], a French-U.S. team investigated the origin of a puzzling progressive evolution of paleomagnetic directions in the interiors of two transitional lava flows. Each lava unit recorded a complete sequence of directions going all the way from that of the underlying flow to the direction of the overlying flow. In the absence of any clear evidence for anomalous rock magnetic properties [*Camps et al.*, 1999] these features have been interpreted in terms of very fast geomagnetic changes, which would have reached 10° and 1000 nT per day. For comparison, values typical of the present-day secular variation are of the order of 0.1° and 50 nT per year, i.e., some 10^4 times slower. Such paleomagnetic impulses would thus have been even larger and sharper than geomagnetic jerks.

[45] These geomagnetic time constants could be constrained by estimates of the cooling times of individual flows. However, such rapid changes do not seem to be compatible with accepted values of mantle conductivity [see *Ultré-Guérard and Achache*, 1995]. Additional detailed investigations have therefore been conducted in order to see whether this situation could not have arisen because of remagnetization of the flows. Remagnetizations of lava flows, yielding complex or unusual directions, have been detected at several localities where reversals have been recorded. A first interesting example on Oligocene basaltic rocks was given by *Hoffman* [1984]. Recently, *Valet et al.* [1998] observed the coexistence of both polarities within flows marking the last reversal boundary (0.78 Ma) and also in a lava flow associated with the onset of the upper Réunion subchron (2.13 Ma) in Ethiopia. In these cases a purely geomagnetic interpretation would imply that a full reversal took place in only a few days. As in the Steens Mountain case, there is no striking difference between the rock magnetic properties of these units and the rest of the sequence, but a scenario involving thermochemical remagnetization in the early stages of magnetization is not incompatible with the results. Thermochemical magnetic overprinting can be particularly serious when it affects a flow emplaced at a time of very low field intensity, sandwiched between flows emplaced at a time of full (stable polarity) intensity. The same effects may as well unfortunately alter features of secular variation recorded in lava flows. Although difficult to demonstrate, such remagnetization events are far more likely to be identified when a reversal has occurred than during a period of constant polarity. A recent investigation of additional

flows at Steens by members of the original study team casts doubt on the geomagnetic significance of the paleomagnetic directions [*Camps et al.*, 1999]. Therefore the existence of very large and rapid changes that have been documented from a single site by a unique team remain controversial and thus cannot be retained as a robust characteristic of reversals (category C). The occurrence of complex and hardly detectable remagnetization effects remains the most reasonable assumption.

3.1.2. Westward Drift and Flux Patches (Decades to Millenia)

[46] Among the first observations that have been made over the longer time range of decades to millenia are the decrease in geomagnetic axial dipole intensity (of the order of 5% per century) and the famous westward drift of the nondipole field [see, e.g., *Merrill et al.*, 1996]. This drift of isoporic lines and foci was discovered by Halley in 1692 and quantified by *Bullard et al.* [1950], who evaluated its global rate at 0.18°/yr. *Bloxham and Jackson* [1992] [see also *Bloxham and Gubbins*, 1985, 1986] have emphasized the fact that over three centuries, westward drift has been far from uniform. The observations that the most intense westward drift was found over the Atlantic hemisphere and that the historical nondipole field had been small in the Pacific Ocean have been made by a number of authors [e.g., *Bloxham and Gubbins*, 1985; *Walker and Backus*, 1996; *McElhinny et al.*, 1996; *Johnson and Constable*, 1998]. *Le Mouël* [1984] showed that the large-scale geometry of flow at the surface of the core, under the geostrophic approximation, could account in a rather simple way for this apparent discrepancy between both hemispheres. Since there is controversy regarding its interpretation this observation has been ranked in category B.

[47] *Gire et al.* [1984] tried to estimate the "instantaneous" rate of westward drift and its time changes based on separate individual field components. They showed that this was an ill-posed problem, without a unique solution. Drift estimates are significantly larger when the Y (east) component is used and smaller when X (north) is used. Drift estimates also vary with time, with values at the time of the 1970 secular variation impulse being a minimum. If this is attributed to bodily drift of core fluid, then the drift rate in 1980 was about twice as large as that before. More importantly, *Yukutake* [1967] showed that drift estimates also depended strongly on latitude (see also the more recent analysis of *Jault et al.* [1988]). Under the frozen flux and geostrophic approximations, *Jault et al.* [1988] were able to show that this could be due to differential rotation of core fluid with time constants of the order of 10 years and overall symmetry with respect to the equator. The characteristic latitudinal patterns of drift estimates based on components X, Y, and Z can be interpreted in terms of rigid rotation of axial cylindrical annuli about the Earth's rotation axis. The corresponding zonal flow model has those annuli intersecting the CMB at latitudes less than 40° rotating westward at about 0.1°/yr, whereas annuli at higher latitudes rotate at a similar velocity but eastward. As a result, the overall changes in the angular momentum of these core annuli roughly balance changes in the angular momentum of the mantle (or length of day). The various results reported, i.e., the large variability of estimates as a function of geophysical area (Pacific versus non-Pacific hemispheres), latitude, geomagnetic component, and time, cast serious doubt on the physical reality and meaning of a (bodily) westward drift of geomagnetic features. A recent investigation of torsional oscillations [*Pais and Hulot*, 2000] illustrates this issue: the variation of angular velocities with latitude is far from constant, neither is the time variation of the sign of the component of the flow corresponding to an axial rotation (T_1^0). A systematic and

global westward drift certainly enters the category C.

[48] Evidence for drift has been sought in archeomagnetic data. Relevant references and discussions can be found in the work of *Merrill et al.* [1996]. On the basis of 2000 years of archeomagnetic data, *Evans* [1987] argued that they demonstrated westward drift at some 0.3°/yr, but this was shown to be a highly nonunique interpretation [*Merrill et al.*, 1996].

[49] The most intriguing feature that emerged from the historical compilations of *Gubbins and Bloxham* [1987] was a concentration of magnetic flux at high latitudes in both hemispheres. These are particularly prominent in the Northern Hemisphere near 120° (both east and west) longitudes and 60° latitude and obviously fit category A. They have been attributed to convection columns in the fluid core, parallel to the rotation axis and tangent to the (solid) inner core. A third patch near 0° longitude, which would be required to complete some form of (threefold) symmetry, and the corresponding mirror images in the Southern Hemisphere are either missing or not well developed. In the Southern Hemisphere this could partly be due to relatively sparse data coverage.

3.1.3. Dipole Versus Nondipole Field

[50] A number of authors have tried to identify persistent features in archeomagnetic field models, which extend beyond the range of historical data. Naturally, this entails less detailed representations of the field, with much lower spatial resolution: in general, the mean amplitudes and variations of the lower degree spherical harmonic components are evaluated and tested against a priori statistical models of the field. Such a model has been proposed (actually based on paleomagnetic data) by *Constable and Parker* [1988] and extended by *Hulot and Le Mouël* [1994]. Spherical harmonic components of the field are supposed to be independent stationary central random Gaussian variables with known correlation functions, zero mean (except g_1^0 and g_2^0) and variances depending only of degree n. This approach allows one to evaluate the time intervals over which the time series become uncorrelated. On the basis of historical and archeomagnetic data, *Hulot and Le Mouël* [1994] and *Hongre et al.* [1998] have shown that the correlation times for terms with degree 2 or higher were less than 150 years; correlation times for the equatorial and axial dipoles are respectively thought to be of the order of 500 years and much larger. *Hongre et al.* [1998] (see also *Carlut et al.*, 1999] show that historical and archeomagnetic data are compatible with zero long-term averages for the equatorial dipole and for the quadrupole and octupole. When the field is averaged over, say, 2000 years or more, only the axial dipole remains. As no study exists to the contrary, we assign an A rating to the persistence of an axial dipolar field over times over 2000 years.

3.2. From 1 to 10 kyr

[51] As one attempts to jump from scales of thousands to tens of thousands of years, one crosses the boundary where archeomagnetism and artefacts are replaced by paleomagnetism and natural rocks. Yet finding rocks that record field changes with a ~10 kyr resolution is very difficult. The most limiting factor is the general difficulty in correlating records in time over large distances. This is typically the case for secular variation records covering the past 10 kyr. Sediments with high deposition rates are required to document nondipole field changes with sufficient resolution. As a consequence the corresponding database has been mostly obtained from lake sediments. A large number of records has been published from western Europe, North America, Australia, and Japan (see *Opdyke and Channel* [1996] for a more de-

tailed account). Correlation of individual records even over short distances requires very accurate dating. The better dated data sets from Britain have been merged together into a well-dated "master curve" of directional changes for the past 10 kyr. The variations seem to match over distances of up to 2000 km, from western Europe to Iceland, but are incompatible with the record from the Sea of Galilee. Secular variation from Australia is more difficult to correlate because of the lower amplitude of directional changes. The general lack of similarity of records from Argentina, Australia, and the North American Great Lakes confirms that patterns of secular variation cannot be correlated over large distances. In summary, when considered together, these paleomagnetic records display large-amplitude variations, up to 60° in declination and 30° in inclination and suggest the possibility that secular variation waveforms could be recurrent at some sites [*Lund et al.*, 1988].

3.2.1. Westward Drift

[52] *Runcorn* [1959] championed the use of (*D*,*I*) or Bauer diagrams to relate anticlockwise looping to westward drift of nonaxial dipolar sources (see also *Thompson and Barraclough* [1982]). However, *Dodson* [1979] showed that this Runcorn's rule suffered a number of violations. Work on lake sediments on the 10,000 to 30,000 year timescale [e.g., *Denham*, 1975; *Thouveny et al.*, 1990] has suggested alternating periods of clockwise and anticlockwise rotation in Bauer diagrams, which would correspond to alternate periods of eastward and westward drift. These have been sometimes interpreted as evidence for propagating dynamo waves [e.g., *Parker*, 1979; *Hagee and Olson*, 1989]. However, none of these studies have been clear or systematic. In any case, the significance of westward drift, which was emphasized in the 1950s and until the 1970s, has decreased. It is no longer considered as a characteristic feature of the field and its secular variation, and thus enters category C. It is not a robust feature that can be imposed on dynamo models, despite the fact that it seems to have remained ingrained in some recent presentations of geomagnetic field behavior.

3.2.2. Excursions and Reversals

[53] In contrast to reversals, which correspond to a full polarity change, excursions reflect deviations from the geocentric axial dipole (GAD) that are only considered to be "larger than normal" paleosecular variation. The meaning of such deviations remained controversial for a long time because they were mostly observed at a single location and associated with a large reduction in magnetization intensity, which could be indicative of remagnetization. It became clear that excursions of the geomagnetic field did exist when the same events could be detected at distinct locations, and in some cases in different materials, i.e., volcanics and sediments [*Verosub and Benerjee*, 1977; *Verosub*, 1982; *Champion et al.*, 1988; *Quidelleur and Valet*, 1994]. Excursions and reversals share several common characteristics, which suggest that they can be treated as manisfestations of similar processes within the core. Alternatively, excursions are regarded by some authors as an intrinsic part of secular variation, whereas reversals would involve longer time and larger spatial scales [*Lund*, 1997]. The main question is thus to know whether paleomagnetic records are detailed and accurate enough to make a clear distinction between these two possibilities.

3.2.3. Apparent Duration of Excursions and Reversals

[54] Excursions and reversals are, geologically speaking, rapid phenomena and thus their exact duration is extremely delicate to evaluate. In their recent review on polarity transitions, *Merrill and McFadden* [1999] have summarized

four distinct approaches to estimate the duration of reversals. Estimates derived from cooling of intrusive igneous rocks are not very reliable because of uncertainties in cooling rates. Statistical approaches involving the number of occurrences of intermediate directions are also not very meaningful. Indeed, in many cases, records have been obtained from single lava flows so that it is impossible to distinguish intermediate directions associated with excursions from transitional directions during reversals. Actually, it is common to encounter lava flows with directions pointing farther away from the geographic pole than expected for usual secular variation during periods without reversals. Direct absolute dating of long sequences with well-identified events is the most reliable approach with volcanics. However, most records are incomplete owing to the episodic nature of volcanic activity. Oversampling of particular field directions is frequent, as is the absence of recording during other periods. Above all, the uncertainties inherent to dating techniques are at least equivalent to the duration of the event. Combining and averaging datings of parallel records does not reduce uncertainties and thus does not solve the problem.

[55] An interesting case is the Laschamp event, which was initially detected in several lava flows from the French Massif central at Laschamp, Olby, and Louchardière [*Bonhommet and Babkine*, 1967]. The Laschamp event is by far the most extensively dated excursion. Three sets of measurements performed at three laboratories on the same sample sites [*Gillot et al.*, 1979] indicate that absolute ages of the Laschamp and Olby flows lie between 38 and 50 ka with a mean estimate of 46.6 ± 2.4 ka [*Levi et al.*, 1990]. However, there is strong overlap of the determinations when dispersion is taken into account. This conclusion is reinforced when adding results from Icelandic lava flows, which very likely recorded the same event with a mean age of 42.9 ± 7.8 ka obtained from 19 determinations [*Levi et al.*, 1990]. Thus, despite the existence of detailed records, it is impossible to obtain better estimates for the duration of this event.

[56] Records from sediments could be more appropriate. The best and most detailed records of the Laschamp event have been published recently by S. Lund et al. (Deep sea sediment records of the Laschamp geomagnetic field excursion (~40,000 14C years BP), submitted to *Geophysical Journal International*, 2000) based on marine sediments with very high deposition rates. The results indicate a duration of 2000 years for the period with low intensity and a shorter one for directional changes. The fact that intensity changes would last longer than directional changes is readily understood [*Mary and Courtillot*, 1993], if one accepts that the (axial) dipole plays a special role among other field components [*Courtillot et al.*, 1992]. Indeed, the intensity of the (axial) dipole needs to be reduced by a very significant factor (of the order of 3 to 5), compared to its "normal" values, before dipolar dominance in field geometry at the Earth's surface is significantly affected (and field directions or VGPs start departing strongly from a dipole-dominated field).

[57] These estimates obviously require that the mean deposition rate was high enough and more or less constant and also that smoothing resulting from postdepositional reorientations can be neglected. Actually, whereas records with very high deposition rates are supposed to provide the best estimates, in such cases, there is an increased probability that the deposition rate was highly variable. It is often claimed that field reversals last longer than excursions because excursional directions are rare in sediments while transitional directions are more frequent, which would explain also why there are so few estimates of their duration. However, several factors can affect the sediment thick-

ness over which the magnetic event has been recorded. Significant delay in the acquisition of magnetization can generate smoothing of non-antipodal pre- and posttransitional directions and thus create artificial intermediate directions [*Rochette*, 1990; *Langereis et al.*, 1992]. This smoothing effect is more pronounced for reversals than for excursions for which the pre- and postevent directions are close and not antipodal [*Quidelleur and Valet*, 1994]. In the same vein, complications can arise from early diagenetic processes [*Van Hoof*, 1993], with particular intervals being affected by dissolution and/or precipitation of minerals, resulting in the obliteration of an excursion or alternatively in a longer apparent duration.

[58] Not only are there differences between the apparent duration of different events but also for the same event recorded at different locations. This is particularly well documented for the last reversal. Such variability could reflect the fact that the apparent duration of reversals or excursions actually depends on site location. Indeed, the intensity of the axial dipole decreases during reversals and excursions and higher-order terms become more prominent or may even dominate field geometry. Because they fluctuate with a much shorter spatial wavelength, the duration of directional changes can be strikingly different at different locations [*Quidelleur and Valet*, 1996; *Carlut et al.*, 1999]. This would explain why very different durations (from a few years to 10 kyr) have been published for the Brunhes-Matuyama reversal and also why excursions are so difficult to observe.

[59] In summary, we do not find convincing evidence for significant differences between durations of excursions and reversals. In most cases, directional changes would take place in less than 5 kyr, which justify that this upper limit actually fits category A. However, durations as short as 1 kyr or even less have been proposed based on high-resolution records [*Love and Mazaud*, 1997; *Merrill and McFadden*, 1999] and cannot be totally excluded. There are also longer durations such as for the Gauss-Matuyama [*Glen et al.*, 1999]. *Gubbins* [1999] suggested recently that the field would reverse in the liquid outer core during excursions but not in the inner core, whereas reversals would involve the entire core. A similar suggestion, based on 3-D simulations of these events, was discussed by *Glatzmaier et al.* [1999]. In fact, Gubbins divides the field into the outer core field and the inner core field, whereas Glatzmaier et al. simulations show that the two different field polarities tend to divide along the tangent cylinder (that is, the field outside the tangent cylinder can reverse its polarity without the field inside the tangent cylinder reversing). These appealing suggestions are not yet testable, since the overall variability of the duration of reversals still does not allow one to argue that they would last significantly longer than excursions. The first critical parameter that should be explored is the apparent duration of a same event at different sites, which depends on details of field morphology.

3.2.4. Field Intensity During Excursions

[60] The absence of records with sufficiently good geographic coverage implies that the documentation of the "excursional" field is relatively limited and thus prevents us from drawing firm conclusions. There is no systematic feature emerging from the present excursion database. Virtual geomagnetic poles (VGP) are often used as a simple way to characterize field geometry during excursions and reversals. The compilation of excursional VGPs does not show any preference for a particular sector of longitude [*Quidelleur and Valet*, 1994]. In fact, the present data set remains fully compatible with the simplest hypothesis, which links excursions to amplified directional secular variation directly related with a large decrease in the geocentric axial dipole (GAD) [*Courtillot et*

al., 1992; *Mary and Courtillot*, 1993; *Courtillot and Valet*, 1995].

[61] Further indications about the origin of excursions come from relative paleointensity records, which demonstrate that most acknowledged excursional events are coeval with a large decrease in the GAD. Recent papers [*Langereis et al.*, 1997; *Lund*, 1997; *Lund et al.*, 1998] report compilations of excursions in the most recent Brunhes (0–780 ka) normal chron. Six excursions can now be reliably considered as worldwide events, whereas five others have not been globally correlated [*Langereis et al.*, 1997]. The six global events are associated with the major intensity lows in the composite paleointensity record of *Guyodo and Valet* [1999]. This is consistent with the observation that nondipole components did not emerge everywhere in the five cases with a larger GAD and also that the apparent duration of each excursion is significantly different at each site [*Quidelleur et al.*, 1999]. Thus the frequency of excursions in the last Myr appears to be much higher and to yield a much more unstable image of the field than was assumed before. Several results indicate that the same characteristics prevailed during periods older than 1 Myr, and it appears likely that excursions punctuated the entire history of the geomagnetic field. We therefore believe that excursions, and their frequency of occurrence, is a major field characteristic that must be considered as an actual constraint for dynamo modeling (category A).

[62] Very few detailed records of absolute paleointensity have been obtained across excursions [*Roperch et al.*, 1988; *Chauvin et al.*, 1991; *Carlut et al.*, 1999]. A noticeable feature is the absence of field recovery (during the excursional period) before the field returns to initial polarity. This is also the case in the sedimentary records. However, we are well aware that the brevity of the event in comparison with the resolution of the records prevents any strong inferences. One can speculate that the absence of recovery could be a sufficient condition for a rapid return to initial polarity; conversely, intense recovery following a geomagnetic instability could be a necessary condition to induce a stable polarity. However, if excursions and reversals are primarily linked with strong decreases in (axial) dipole intensity with little changes in the amplitudes of other (nondipolar) terms, a whole spectrum of excursions will simply be due to fluctuations in dipole intensity. The smaller the fluctuation, the more evasive the excursion. In that case the notion of field recovery is part of the description and definition of the excursion, with no other special physical causal link. Given the very few detailed records obtained so far, it is premature to consider such observations as systematic and hence to give them too much weight in dynamo modeling (thus C rating).

3.2.5. Field Intensity Variations Across Reversals

[63] A large number of paleomagnetic studies have been carried out for about 20 years in order to document field variations during reversals. It is now relatively well established, on the basis of sedimentary as well as volcanic records, that field intensity drops significantly and that these changes last longer than directional changes (see *Merrill and McFadden* [1999] for a complete review). Again, this is simply because a large decrease in dipole intensity is necessary before directions depart significantly from dipolar ones [*Mary and Courtillot*, 1993]. There are also indications that recovery following a transition is short and culminates in higher values than before the decay phase. Indeed, the four detailed volcanic records including determinations of absolute paleointensity provide support for such an asymmetry. Strong posttransitional field values have been reported in a Pliocene

reversal recorded at Kauai [*Bogue and Paul*, 1993] and in the upper Jaramillo subchron recorded from Tahiti [*Chauvin et al.*, 1990]. The comparable characteristics emerge also from the 15 Ma old Steens Mountain reversal [*Prévot et al.*, 1985] and the Matuyama-Brunhes transition recorded from La Palma in the Canary islands [*Valet et al.*, 1999]. Similar observations have been drawn from sediments but over much longer periods (we will return to this later). In the present situation we are only dealing with relatively short time periods preceeding and following the reversals. In this case the present database shows asymmetrical field changes. Since additional records are still needed on this matter, this observation has been classified in category B.

3.2.6. Field Morphology During Reversals

[64] Many reversal studies have attempted to constrain field geometry on the basis of the configuration of VGP paths. After early publications of a few sparse records from volcanic flows, most attention was focused on sedimentary records. It was rapidly accepted that the field was not dipolar during reversals [*Dagley and Lawley*, 1974; *Hillhouse and Cox*, 1976]. Despite still ongoing discussions the nondipolar character of the transitional field is more and more widely recognized and seen as a direct consequence of the overall and systematic drop of dipole intensity. We consider that this is an A level constraint that must be produced by numerical simulations of reversals. Syntheses of paleomagnetic records published about 10 years ago yielded several very interesting and still controversial observations [*Clement*, 1991; *Tric et al.*, 1991; *Laj et al.*, 1992; *Gubbins*, 1994; *Gubbins and Love*, 1998], such as the existence of preferred longitudinal bands for VGP paths, over the Americas and eastern Asia, possibly in relation with the cold circum-Pacific regions in the lower mantle (outlined by seismic tomography). It was shown subsequently [*Valet et al.*, 1992; *McFadden et al.*, 1993] that this coincidence cannot be interpreted without taking into account the poor distribution of paleomagnetic sites, which lie mostly 90° away from the preferred bands. Actually, many factors related to acquisition of magnetization in sediments in the case of low field intensity can generate VGP paths 90° away from the observation sites [*Quidelleur and Valet*, 1994; *Quidelleur et al.*, 1995; *Barton and McFadden*, 1996; *Langereis et al.*, 1992; *Rochette*, 1990]. *Prévot and Camps* [1993] observed also that there is no preferred longitudinal band emerging from the database of volcanic records. Recently, *Love* [1998] questioned this interpretation, arguing that similar directions from successive flows should not be averaged, because they do not necessarily result from a very rapid succession of eruptions. Instead, he treated each individual flow as a single time event (implying no correlation between successive flows, or identically that the duration between flows was longer than the typical correlation times of secular variation; see above). This is a drastic assumption and a violation of the Occam's razor principle. The most extensively dated flows from Hawaii show evidence that such is not the case [*Holcomb*, 1987] and a recent study of the same reversals [*Herrero-Bervera and Valet*, 1999] recorded in three parallel sections show that identical successive transitional directions are not reproduced between parallel sections. This is clear evidence of fast sampling of geomagnetic changes by irregular and spatially limited volcanic flows. Actually, both analyses are limited by the number of sites and by the identification of actual transitional directions. Because VGPs obtained from volcanics can reach latitudes as low as 45–50° during episodes of large secular changes (and of course excursions), one should restrain reversal analyses to "actual" transitional directions, i.e., corresponding to VGP latitudes less than 45° in order to support a more robust analysis. There

is actually no clear distinction between excursional and transitional VGPs; *Love*'s [1998] subset of data shows significant scatter when restrained to "pure" transitional VGPs. Would we wish to rely on VGP positions lower than 45° (and not 60°), the number of points would become far too small to perform any robust analysis. An answer to this question should rely exclusively on volcanic records with well-defined pre- and posttransitional directions and a sufficient number of intermediate directions. Only those records have some significance in terms of transitional field characteristics, without generating unacceptable uncertainties about the origin of the directions and their stratigraphic relationship. The distribution of poles extracted from this very limited database does not display any preferred location nor does it show any evidence for systematics in the reversal process. For these reasons the hypothesis of preferred longitudinal VGP paths fits category B.

[65] Using another selection of records, *Hoffman* [1991, 1992, 1996] pointed out the existence of VGP clusters in the vicinity of south America and above western Australia, which could be due to persistent inclined dipolar field configurations during the reversal process. This suggestion would establish some link between sedimentary and volcanic records. Such features could imply some form of indirect control of the reversal processes by the mantle, generating heterogeneous flow at the CMB. Such heterogeneous constraints at the CMB are not taken into account in most present dynamos. However, VGP clusters could simply indicate that a series of volcanic flows were emitted over a short interval of time compared to the time constants of secular variation (years rather than centuries or millenia). As described above, clusters of directions are not reproduced between nearby sections of the same reversals in Hawaii [*Herrero-Bervera and Valet*, 1999] and are therefore most likely due to a brief spurt of volcanic activity. These cannot be considered as statistically uncorrelated data for the kind of analyses we wish to perform. The apparent concentration of VGPs close to south America and western Australia could therefore still be considered as a coincidence (or a sampling artefact). Thus it cannot be considered as certain yet that long-lived transitional states represent an actual characteristic of the reversing field, and this leads us to rank this observation within category B.

[66] A dominant feature emerging from the most detailed sedimentary [*Valet et al.*, 1986; *Tric et al.*, 1991; *Channell and Lehman*, 1997) and volcanic (*Mankinen et al.*, 1985; *Chauvin et al.*, 1990; *Herrero-Bervera and Valet*, 1999] records is their complex structure, with large directional variations (particularly in inclination) preceeding and/or following the transition. The presence of such large loops shows similarity with secular variation of the present nondipole field. This observation reinforces the concept of a rather complex transitional field that would be dominated by nondipole components, subsequent to the large decrease of intensity that has been observed in all records of reversals. Therefore the simple model that considers the field variations during reversals as identical to historical secular variaton [*Dagley and Lawley*, 1974; *Valet et al.*, 1989; *Courtillot et al.*, 1992] remains in our view the most plausible. The large loops are easily modeled as soon as the drop in (axial) dipole field intensity is large enough to let the typical pattern of secular variation of nondipole terms emerge. This observational fact should in our view be considered as an actual characteristic of transitional field morphology, and could be a useful constraint for numerical dynamos (category A).

3.3. From 10 to 100 kyr

3.3.1. Oscillations of Dipole Moment

[67] In principle, field intensity changes should not be decoupled from directional

changes and the magnetic field vector should be studied as a whole. Unfortunately, paleointensity studies were only developed extensively during the past decade. Except for the past 40 kyr, which are well documented by a large number of full vector data, not much information has been gained from records of absolute paleointensity. Recent development in the measurement of relative paleointensity from sediments has significantly changed this picture. Thirty-two records from different locations around the globe have now been integrated into the Sint-800 composite curve, which describes the variations of the GAD field intensity up to 800 kyr [*Guyodo and Valet*, 1999]. The resolution of the curve is limited by the subset of records with the poorest resolution and is not better than a few thousand years. Directional variations mostly reflect changes in dipole field intensity. The geomagnetic nature of the signal is strongly supported by its agreement with an independent estimate derived from the variation in ^{10}Be production during the past 200 kyr [*Frank et al.*, 1997; *Frank*, 2000].

[68] Several features inherent to these records can thus be considered as actual geomagnetic characteristics and thus fit category A. The first one is the very variable overall character of the field, which depicts a succession of large 20–60 kyr long oscillations and changes in amplitude, that can exceed a factor of 5. Within the limits imposed by the low resolution of the curve to document short-term variations we could not identify any periodicity in any time interval (long enough to allow proper spectral analysis). Thus dipolar field intensity has varied in a nonperiodical, erratic manner (periodicity would enter category C). Another interesting observation (see above) is that the weakest intensities always correspond with geomagnetic excursions.

3.3.2. Average Dipole Moment

[69] Another aspect is the time-averaged value of the dipole moment. Between 50 and 15 ka B.P. the number of volcanic records is large enough to average out nondipole components within 5 kyr windows. For this period the dipole moment has an average value of $(4.5 \pm 0.6) \times 10^{22}$ Am^2, nearly half the $(8.7 \pm 1.6) \times 10^{22}$ Am^2 value found over the past 10 kyr.

3.4. From 0.1 to 5 Myr

3.4.1. Average Dipole Moment

[70] For older periods, temporal coverage of the volcanic database is much poorer than with sediments. The calibration of Sint-800 has been performed by adjusting the younger part of the curve with the volcanic data set. Since Sint-800 incorporates a very large number of records, it is reasonable to consider that the differences in amplitude between distinct records have been averaged out. Thus the mean value of 6.0×10^{22} Am^2 with a standard deviation (s.d.) of 1.5 obtained for the past 800 kyr can be considered with good confidence. Unfortunately, this calculation cannot be extended as yet over a longer period by using sediments because of the absence of worldwide records. The number of volcanic records is also far too sparse and poorly constrained in time. In addition, a typical problem inherent in the volcanic data set is that dispersion increases with the number of results within each temporal window. Overall averages performed from volcanics tend to indicate higher values than those derived from calibrated sedimentary records. The 4 Myr long record from the Pacific ocean [*Valet and Meynadier*, 1993] has an average value of 4.0×10^{22} Am^2 (s.d. 1.9). This is almost half the 7.4×10^{22} Am^2 value (s.d. 4.3), which is often quoted [*Merrill et al.*, 1996] and in satisfactory agreement with the determination of 5.49×10^{22} Am^2 (s.d. 2.36) recently pub-

lished by *Juarez and Tauxe* [2000] after careful data selection. Note, however, that the volcanic database derived from this subset has very poor temporal coverage and large dispersion. Sedimentary records calibrated with volcanic data remain at the present time the most promising approach to extract the field mean intensity over a long period of time.

[71] In summary, it is likely that the average field intensity was about 6×10^{22} Am^2 during the past 0.8 Myr, which is 30% lower than the present-day field. Despite large uncertainties and poor geographical and temporal coverage of the existing data, there is no evidence as yet for any substantial long-term decrease (or increase) of mean field intensity for, say, the past 10 Myr. Of course, there is no reason why present-day field intensity should be considered as representative of the long-term average. One can thus consider that the mean intensity varies between 4 and 6×10^{22} Am^2 on this timescale (category A). This is reasonably well established for the past 1 Myr and is likely to hold also the past few million years.

3.4.2. Sawtooth Pattern of Intensity Variations

[72] No attention could be paid to field intensity changes across reversals until the recent emergence of long and well-dated sedimentary sequences. It is essential to detect whether specific conditions prevail before the field reverses and if there is any influence of reversals on dynamo operation. The most intriguing feature is the sawtooth shape of the records that features a long-term decrease of the field intensity during periods of stable polarity and a large and rapid increase immediately after the reversals. Such characteristics have been observed in several records from the Pacific and Indian Oceans [*Valet and Meynadier*, 1993; *Valet et al.*, 1994; *Thibal et al.*, 1995; *Verosub et al.*, 1996]. However, there are also records that do not exhibit such asymmetry between the pre- and postreversal periods [*Laj et al.*, 1996]. *Raisbeck et al.* [1994] attempted to observe the changes in ^{10}Be production that are modulated by the screening effect of the geomagnetic field against penetration of cosmic rays. However, the results were inconclusive, since they did not reveal any variation accompanying the large-intensity changes that prevail during reversals. Several alternative nongeomagnetic explanations have also been proposed [*Meynadier and Valet*, 1995; *Mazaud*, 1996; *Meynadier and Valet*, 1996; *Kok and Tauxe*, 1996a, 1996b], but they have not been convincingly demonstrated so far [*Meynadier and Valet*, 1996; *Meynadier et al.*, 1998]. Of course, this does not validate the geomagnetic origin of the sawtooth shape of relative paleointensity, which has thus been ranked among the B level observations. Detailed records of ^{10}Be production for this period would certainly be extremely useful. Another promising approach may be provided by detailed study of young marine magnetic anomalies: recent studies [*Gee et al.*, 1996; G. Pouliquen et al., A geomagnetic record over the last 4 million years from deep-tow magnetic anomaly profiles across the Central Indian Ridge, submitted to *Journal of Geophysical Research*, 2000] have shown that the oceanic crust formed at ridges can provide a reliable record of field intensity changes. The 4 Myr records obtained so far from sediments depict a field evolution dominated by a succession of highs and lows, similar to the past 800 kyr. The intensity lows coincide either with reversals or with excursions and/or short events. Thus it appears that the major characteristics of variations in field intensity (time constants, amplitude, averaged value) remained unchanged during the past four million years. In other words, no drastic changes in field intensity variations need to be expected in numerical dynamos over periods of a few million years.

3.4.3. The Last 5 Myr (Very Long Term Averages of Spherical Harmonic Coefficients)

[73] Paleomagnetists have assembled large directional databases from sediments and lava flows to search for persistent features in the geomagnetic field in the time window from hundreds of thousands to millions of years. Recent analyses [e.g., *Johnson and Constable*, 1997; *Kelly and Gubbins*, 1997; *Carlut and Courtillot*, 1998] of some of these bases using diverse inverse techniques come to somewhat different conclusions. All agree on the presence and robustness of a long-term axial quadrupole g_2^0, on the order of 5% of g_1^0. *Carlut and Courtillot* [1998] estimate that all other terms have long-term zero averages, compatible with the *Constable and Parker* [1988] Gaussian process. *Carlut et al.* [1999] find that the persistent axial quadrupole emerges from noise when the length of the available time series exceeds about 6 kyr. This would be why archeomagnetic data are not sufficient to isolate it. *Johnson and Constable* [1997] and *Kelly and Gubbins* [1997] find flux concentrations at the core surface under Canada and Siberia, similar to those observed over historical times and possibly related to columns parallel to the rotation axis in the core. They propose that the present pattern of secular variation is typical of the past millions of years. *Johnson and Constable* [1997] find significantly smaller higher-order and nonzonal terms than *Kelly and Gubbins* [1997], yet they do believe that they are significant. Therefore, given ongoing debates, in addition to g_1^0, only a small persistent g_2^0 (about 5% of g_1^0) can be considered as a robust constraint on the 10^5 to 10^6 year timescale for modeling purposes (category A). Values of other g_n^m and h_n^m remain controversial. However, they can all be safely considered to be below 1 μT (a rather weak category A constraint).

3.5. Beyond 5 Myr

3.5.1. Changes in Reversal Frequency

[74] There have been many studies dealing with statistics of the reversal sequence, some claiming that reversals form a Poissonian process, whereas others favor some form of determinism. The distinction is sometimes subtle. The succession of polarity intervals is closely approximated by a Poisson process or at least by a gamma process [*McFadden*, 1984; *McFadden and Merrill*, 1984, 1986, 1993; *McFadden et al.*, 1987; *Lutz and Watson*, 1988], assuming that short events have been missed in the reversal sequence. This implies that subsequent refinement of the magnetic polarity timescale could bring different conclusions. Thus the distribution of the length of polarity intervals cannot be considered as a major constraint to build an Earth-like dynamo.

[75] However, reversal frequency slowly changes between well-defined values. The long-term (hundreds of Myr) average is of the order of 1 reversal per million years, and the maximum value when averaged over a few million year does not seem to exceed 6 reversals per million years (category A).

3.5.2. Superchrons

[76] It could be tempting to take into consideration the occurrence of very long periods without reversals, such as the Cretaceous or Kiaman superchrons. These are periods when the field apparently did not reverse for tens of millons of years (though, see *Tarduno et al.* [1992], on the presence of events within the Cretaceous superchron). There is no doubt that these are extreme occurrences in the time series of geomagnetic chrons (category A). However, there is no agreement on how extreme they are. They might correspond to possible values with low probabilities; the small total number of available reversals precludes a firm statistical con-

clusion. They might correspond to times when the process responsible for geomagnetic reversals passed below a certain critical threshold, and reversals could start again only when that threshold was exceeded again. Various other analyses [e.g., *McFadden and Merrill*, 1995] suggested that these intervals would reflect cessation of the reversal process. In other words, the geodynamo would have a reversing and a nonreversing state. Alternatively, *Gallet and Hulot* [1997] proposed an explanation in terms of perturbations of the reversal process. Such changes may depend on factors directly connected with boundary conditions that affect the flow pattern within the core (such as the distribution of heterogeneities within the D″ zone of the lower mantle) and therefore may not be related to the intrinsic time constants of the geodynamo. Consequently, we feel that taking these superchrons as constraints for dynamo modeling is not yet warranted, particularly in the case of homogeneous conditions at the CMB.

[77] The same remark also holds for the hypothesis that there would be a long period of low dipole intensity between 120 and 180 Ma [*Perrin et al.*, 1991; *Courtillot and Besse*, 1987]. Note that the accumulation of new results suggests that the duration of this period (if ever it existed) has been considerably overestimated, so that no reliable estimate can be derived as long as a large independent set of data has not been obtained (category B).

[78] The observational constraints summarized in this section are listed in Table 2, together with what we estimate to be their robustness and reliability and whether they can actually be used in constraining numerical dynamo models.

4. Discussion and Conclusion

[79] A comparison between characteristics of numerical models and observations requires additional care, both when interpreting results from numerical models and when selecting relevant constraints. In this section, we first try to highlight the difficulties of such an exercise; we then attempt a comparison based on previously published models (when relevant data, i.e., numerical results, are available, which is far from being the general situation); finally, we propose a short list of the features that we feel should be presented with each numerical model in the future to allow a more efficient comparison with observational constraints.

[80] The scaling of quantities extracted from numerical models requires some attention before they can be compared with Earth values. Equations are usually solved in nondimensional form (to broaden potential use of the solutions and reduce the number of parameters involved). If all nondimensional numbers used in the computations were equal to their geophysical values, an obvious transformation would then allow one to scale numerical results and compare them with actual observations. It is clear at this point that this is not the case and that parameters used in the numerical simulations may significantly differ from geophysical estimates. In this case, the "scaling" needed to compare results with observations is not straightforward anymore and one can interpret the discrepancies in the nondimensional numbers in terms of different physical quantities. For example, if the Ekman number ($\nu/\Omega r_c^2$) used in the numerical model is larger than the Earth value, this could be interpreted as either due to a higher value of viscosity or to a smaller size of the core or to slower rotation of the Earth.

[81] Moreover, interpretations need to be consistent with the definition of all other nondimensional numbers relevant to the system. For instance, we may want to scale the results of a computation to compare the intensity of the

Table 2. Major Characteristics of the Geomagnetic Field

Timescale	*F*	*D, I*	Field Characteristic	Multiple Sites	Volcanics and Sediments	Different Authors	Controversy	Status
0.1–1 kyr	x	x	geomagnetic impulses	y	n.a.	y		A
		x	geomagnetic impulses during reversals	n	y?	n	y	C
	x	x	Pacific dipole window	y	n.a.	y	y	B
	x	x	global and systematic westward drift	n	n.a.		y	C
			columns and patches	y	n.a.	y		A
			dipole dominates	y	n.a.	y		A
1–10 kyr		x	global and systematic westward drift	n	n.a.	y	y	C
			excursions and reversals have similar durations shorter than 5 kyr	y	y	y		A
	x	x	excursions associated with intensity lows	y	y	y		A
	x	x	reversals dominated by nondipole components	y	y	y		A
	x	x	asymmetrical decay and recovery immediately before and after reversal	y	y	y		B
		x	preferred longitudes of transitional VGPs	y	n	y	y	B
		x	long-lived transitional states	y	n	y	y	B
10–100 kyr	x	x	20 to 60 kyr long oscillations of dipole moment	y	y	y		A
	x	x	periodic variations of dipole moment	n	n.a.	n	y	C
	x	x	dipole dominates	y	y	y		A
0.1–5 Myr	x		long-term decrease (saw-tooth) during stable polarity	y	y	y	y	B
	x		average dipole moment between 4 and 6×10^{22} A.m^2	y	y	y		A
		x	columns and patches	y	y	y	y	B
	x	x	dipole dominates	y	y	y		A
		x	$1000 < g_2^0 < 2000$ nT	y	y	y		A
		x	$g_n^m h_n^m < 1000$nT	y	y	y		A
>5 Myr		x	reversal frequency < 6/Myr	y	y	y		A
		x	superchrons	y	y	y		A
		x	Mezosoïc dipole low	y		y	y	B

Each line corresponds to a proposed characteristic feature of the field. These are arranged (as in the text) in the order of increasing timescales (first column). Next two columns indicate whether these involve measurements of field intensity (*F*) and/or direction (*D*,*I*). The characteristic feature (next column) is then evaluated through the answer to the following questions (four next columns): "Was it observed at multiple sites?", "Was it observed both in volcanics and sediments?", "Was it reported by different authors?", "Is it an ongoing controversy?". The last column is a direct consequence of the preceeding ones and suggests a classification of field characteristics into three categories: A (established), B (still discussed), and C (unlikely). Only category A will be retained for comparison with numerical models. (Abbreviations used are as follows: n.a., not applicable; y, yes; n, no.)

induced magnetic field with that observed for the Earth. Field intensity is usually based on rotation rate and magnetic diffusivity. If we want to interpret our results using Earth values for both quantities, we must consider all nondimensional numbers using these values. Let us assume that we describe our system with three nondimensional numbers: the Ekman, Prandtl, and magnetic Prandtl numbers. Because rotation is now fixed, viscosity is given by the value of the Ekman number used in the computation. Because magnetic diffusivity is also fixed (to determine field intensity), thermal diffusivity is given by the value of the magnetic Prandtl number used in the computation. As a consequence, because viscosity and thermal diffusivity are given, there is only one consistent (imposed) value for the Prandtl number. When inertia is dropped from the computation, the Prandtl number is "free" (although it should be kept small to justify the simplification); but if such is not the case, its value is already independently fixed in the computation, leading to a possible inconsistency in interpreting the results (see discussions by *Glatzmaier and Roberts* [1995a, 1995b] and *Kuang and Bloxham* [1998]).

[82] Timescale constraints are particularly difficult to take into account with numerical models. The reason for this difficulty is again a consequence of the parameters used in the simulations (that can be readily interpreted as ratios of characteristic timescales). Numerical results are often published using "year" as unit of time. By year, authors generally mean "magnetic year," i.e., the timescale constructed using the dipole decay time, or magnetic diffusion timescale in the Earth's core (roughly 20 kyr). A consequence is that the ratio of the rotation timescale (the day) to the magnetic timescale (directly proportional to the magnetic Ekman number defined above) is much larger than it should be. One can count much less than a day per year in most models.

[83] The fact that numerical models use parameters far from geophysical estimates must be taken into account when establishing which observational constraints can effectively be used for comparison with numerical predictions. For example, it is difficult to directly incorporate constraints based on timescales in numerical results, for the reasons stated above, and we will therefore prefer to present them in terms of ratios of characteristic times or scale them using the dipole diffusion time.

[84] In section 2 on generally accepted facts versus ongoing controversies, we propose a classification of magnetic features (i.e., geomagnetic and paleomagnetic "observations"; see Table 2) in three main categories: those that are established independently by different teams and essentially agreed on by most authors and that can safely be considered as robust constraints for numerical dynamo modeling (A); those for which the extent of controversy or disagreement is such that they should not be used pending confirmation (B); and those that are most unlikely (C). Some features that had been proposed in the past can clearly now be rejected. The decision to place data into one category should be as objective as possible, and we have outlined a few criteria that we believe should be prerequisites. However, there is clearly room left for ambiguity and personal bias (or preference), and we do not claim to be free of such limitations.

[85] A sensible choice appears to be to retain only the first category of observations (A) as constraints for numerical models. We believe features placed in this category to be free of controversies. Following the presentation adopted in Table 2 and starting with the 0.1–1 kyr scale, the existence of geomagnetic impulses should clearly be retained as a strong and well-established constraint. Features such as the Pacific dipole window low, columns and patches, or even the ratio g_2^0/g_1^0 (as estimated

over this timescale) need confirmation from longer timescale observations. On the 1–10 kyr scale the existence of excursions and reversals and the fact that both have similar durations (shorter than half of the dipole decay time) clearly is a robust and efficient constraint and so are as well the existence of intensity lows associated with excursions and the nondipolar character of the field during reversals. On the 10–100 kyr scale, oscillations of dipole intensity with time constants of the order of 1 to 3 dipole decay times is a robust constraint. On the 0.1–5 Myr scale the average intensity of the field between 4×10^{22} and 6×10^{22} Am^2 is well established as well as the ratio g_2^0/g_1^0, close to 5%. From longer scales the only robust observations are the maximum reversal frequency ($\sim$5 Myr^{-1}) and the existence of superchrons. Because such timescales are comparable with the characteristic timescales of mantle convection and evolution, there is a possibility that superchrons are not only due to some internal mechanism of the dynamo but are linked to boundary conditions imposed by the mantle on the CMB. This issue is still the focus of an ongoing debate, and it should not, at this stage, be retained as a robust constraint. This prevents us from establishing a meaningful minimum reversal frequency.

[86] In summary, according to the above discussion, there appear to be currently 10 and only 10 well-established, robust constraints for dynamo models: (1) Dipolar character of the field; (2) existence of geomagnetic impulses or jerks with a short time scale (less than 10^{-4} times of the dipole decay time); (3) existence of excursions on timescales of the order of one tenth to one half the dipole decay time; (4) excursions associated with intensity lows; (5) existence of reversals, with a duration comparable to that of excursions, and occurring at a rate of at most 1 per 10 dipole decay times; (6) nondipolar character of the field during reversals; (7) nonperiodic long-term oscillations of dipole intensity (1 to 3 dipole decay times) with maximum amplitude 5×10^{22} Am^2; (8) long-term average dipole intensity between 4×10^{22} and 6×10^{22} Am^2 (when averaged over more than ten dipole decay times); (9) long-term average value of g_2^0 between 1 and 2 μT (i.e., close to 5% of that of g_1^0), when averaged over more than 10 dipole decay times; and (10) long-term average values of all higher-degree terms lower than 1 μT, when averaged over more than 10 dipole decay times.

[87] Clearly, there is no proof that any magnetic field satisfying all these requirement will necessarily correspond to the same generation mechanism as that actually operating within the Earth's core; comparisons with asymptotic studies constitute the only robust confirmation. Also, one could imagine a numerical dynamo model could be based on the correct physical processes occurring in the Earth's core but not satisfy some constraints, simply because some parameter values would not be appropriate (and as a result, some outputs would not scale properly). Nevertheless, this appears to be a minimal set of well-established necessary conditions for a numerical model to claim Earth-like behavior.

[88] Most numerical models were integrated over a few dipole diffusion times (about 3) to attest self-sustained dynamo action. However, it is clear from section 2 that to test for Earth-like behavior, relevant features and numerical predictions should be averaged over at least 10 dipole diffusion times.

[89] Comparing the above list with Table 1, it is striking that apart from dipole dominancy, not many features are common to both. Many numerical models appear to concentrate on rather controversial features that cannot be considered as indisputably Earth-like (such as westward drift of the field) but also outputs from these models were not formatted in a way that would allow direct comparison with ob-

servational constraints. No impulses (jerks) seem to have been uncovered in numerical models. Excursions have only been reported by the recent work of *Glatzmaier et al.* [1999]. When models presented reversals (e.g., Glatzmaier and Roberts; Kageyama et al.; Kitauchi and Kida), the maximum reversal frequency of about 1 per 10 dipole diffusion times (τ_d) can be used directly as a constraint. Clearly, the *Glatzmaier and Roberts* [1995a, 1995b] model (one reversal in $\sim$3 τ_d) is not testable, because it is available over too short a time period. *Glatzmaier et al.* [1999] (two reversals in $\sim$15 τ_d) and *Kageyama et al.* [1999] (one reversal in $\sim$50 τ_d) are on the right side according to this test, although time integration is obviously too short to establish a reversal frequency. *Kitauchi and Kida* [1998] presented a polarity time series with some 30 reversals in $\sim$100 τ_d, long enough to suggest that the frequency value is significantly above the requirement for Earth-like behavior.

[90] Figure 1e presents dipole moment fluctuations as observed over the last 3 million years, i.e., approximately 150 dipole decay times [*Valet and Meynadier*, 1993] together with the SINT-800 paleointensity stack over the last 800 kyr [*Guyodo and Valet*, 1999]. These are compared to the numerical results published by three groups: *Kida and Kitauchi* [1998], *Kageyama et al.* [1999], and *Glatzmaier et al.* [1999]. These results cover a long enough time interval to allow comparison with the Earth observations. In addition, a histogram of the dipole moment values in the corresponding time series is shown (normalized to unit area, except for Figure 1c and the red part of 1e (SINT-800) for which it was normalized to one half). Direct inspection of Figure 1 shows that the *Kida and Kitauchi* [1998] curve (Figure 1d) does not feature the alternance of polarities that characterizes chrons (i.e., fails to predict a symmetric bimodal histogram). The *Glatzmaier et al.* [1999] tomographic model (Figure 1b) has too much high frequency oscillations, i.e., secular variation and excursions (as noted by the authors), leading to a "flatter" histogram. The results of *Kageyama et al.* [1999] (Figure 1c) are closer to traditional ideas of what bimodal fluctuations should be like. However, there is a lack of lower dipole moment values, which is not observed in the case of Earth, and more importantly the large contribution of the octupole (not shown in Figure 1) is not at all Earth-like. Finally, only the results from the *Glatzmaier et al.* [1999] homogeneous model (Figure 1a) appear acceptable. Indeed, they look very much like a portion of the observed record near 90–120 τ_d, but, of course, the integration time (15 τ_d) is still too short to allow a robust comparison.

[91] Checking constraints concerning the duration of reversals would require comparison of plots of paleomagnetic directions with numerical results. Only *Glatzmaier et al.* [1999] provide such plots for reversals. Both reversals reported for the homogeneous model were appropriately fast; however, the second reversal in the tomographic model was apparently too long. It would be useful if other models provided such information. The nondipolar character of the field during reversals would also need documentation (such as field spectra during reversals, only provided by *Glatzmaier and Roberts* [1995a, 1995b]).

[92] Finally, when trying to constrain the g_n^m, h_n^m coefficients, it is clear that much relevant information is usually absent from most papers presenting numerical dynamos. These constraints are readily converted into constraints on the energy spectrum of the average field ($W_n = (n+1)\sum_{m=0}^{n}(g_n^{m2} + h_n^{m2})$; [*Lowes*, 1974]) at the core-mantle boundary over a long enough period of time (above 10 τ_d). Spectra have been published for a few numerical models. Unfortunately, these spectra were often instantaneous or averaged over only a short period of time (the

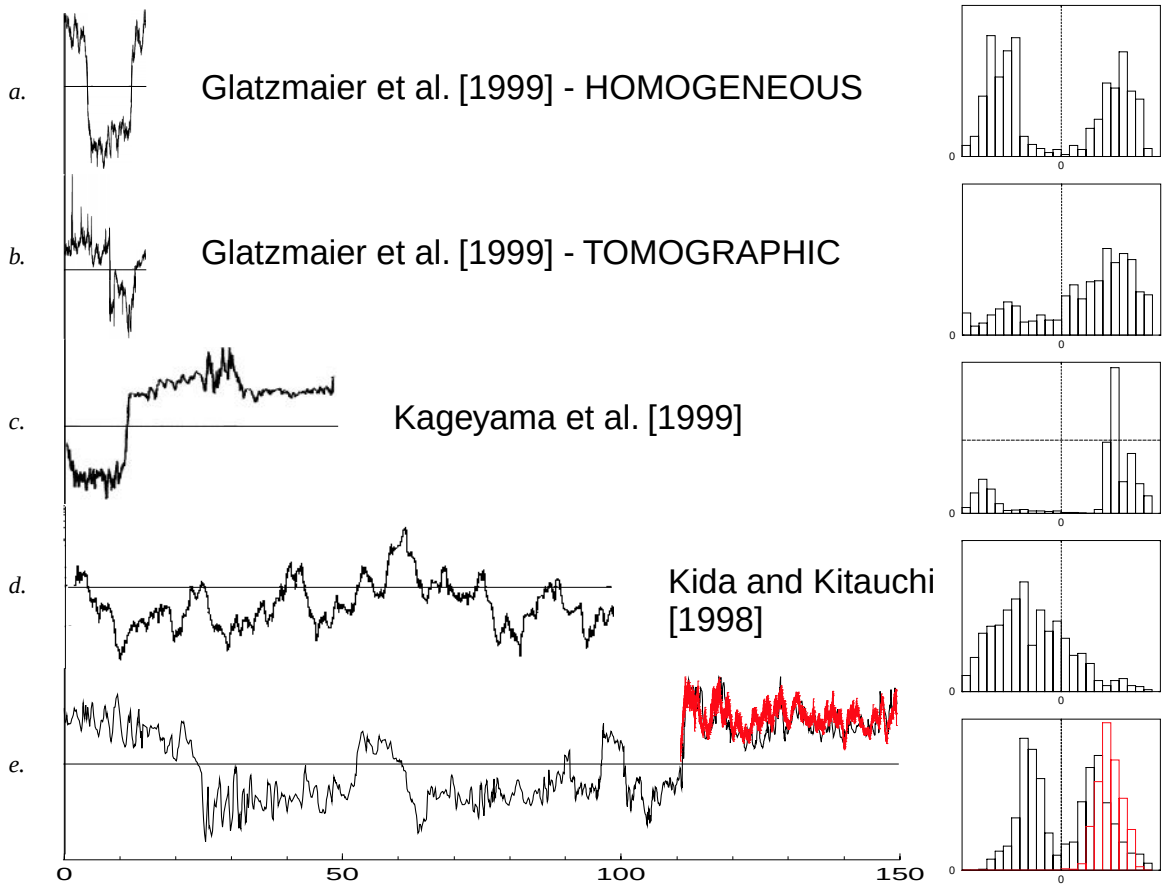

Figure 1. Time evolution of the dipole moment (relative values) for numerical dynamo models with integration times longer than 10 dipole diffusion times (base lines correspond to zero). The x coordinate has been scaled using dipole diffusion time τ_d as unit. (a, b) time evolution of the dipole moment as published by *Glatzmaier et al.* [1999]; (c) same for *Kageyama et al.* [1999]; and (d) same for Kida and Kitauchi, [1998]. It should be stressed that the length of time integration does not reflect the amount of modeling and computational work, since the parameter regime is very different from one model to the other (see Table 1). (e) Dipole moment measured for the Earth over the last 3 Myr [*Valet and Meynadier*, 1993] using the same convention for time (present is at the far right), the red graph corresponding to the SINT-800 paleointensity stack over the last 800 kyr [*Guyodo and Valet*, 1999]. The histograms on the right show the distribution of the dipole moments for each simulation and for the observations (see text).

only exception being the model of Glatzmaier and Roberts in the work of *Coe et al.* [2000]); also, these spectra have been plotted at different elevations (Earth surface, core-mantle boundary, or depth corresponding to a flat spectrum).

[93] We show all available spectra from those papers, reduced to a common elevation (outer bounding sphere, corresponding to the core-mantle boundary) on Figure 2. Spectra from Glatzmaier and Roberts (GR95-1995b; GR96b-1996b) correspond to instantaneous spectra (three spectra for GR95, one for GR96b). The spectra from Glatzmaier and Roberts (GR96a-1996a) correspond to a series of values over 300 year (the green bars correspond to the intervals

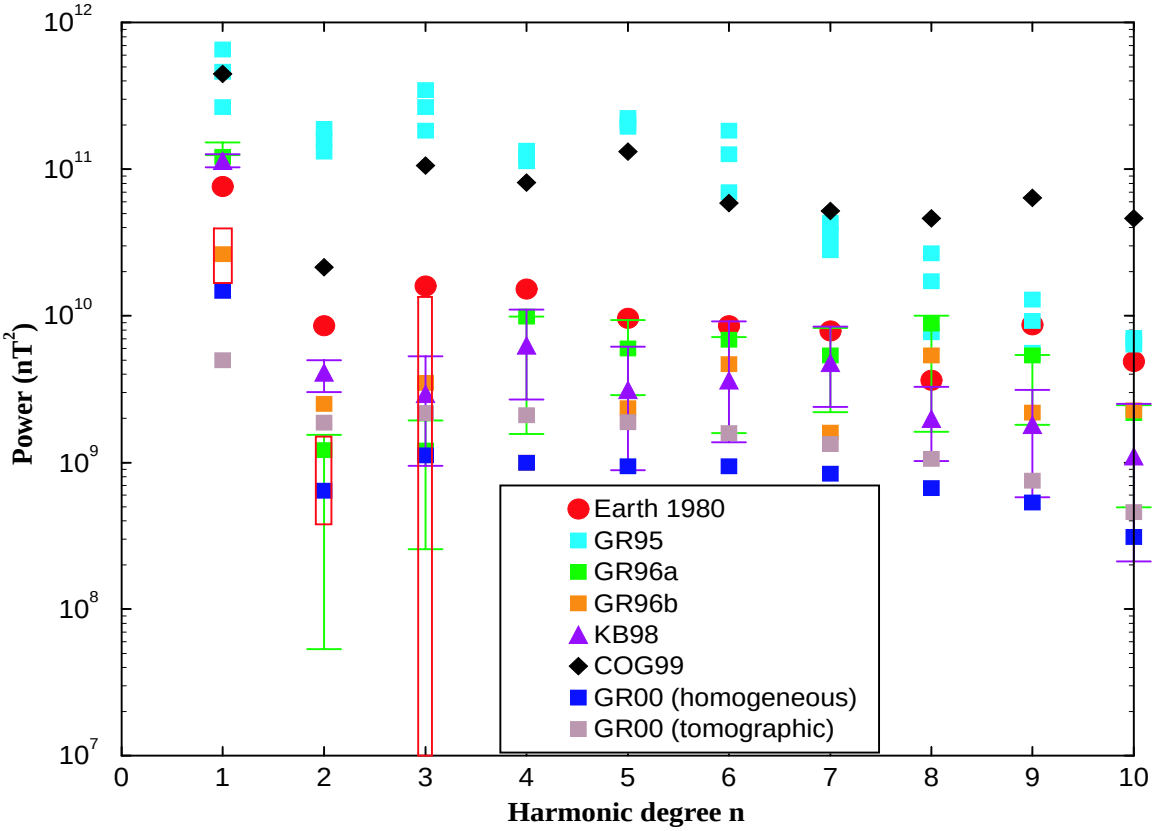

Figure 2. Published power spectra ($w_n=(n+1)\sum_{m=1}^{n}(g_n^{m2}+h_n^{m2})$ [after *Lowes*, 1974] for numerical dynamo models. Spectra have been converted to a common unit and reduced to a common depth (core-mantle boundary). Red dots represent the 1980 instantaneous spectrum for the Earth; red boxes represent the intervals for the average field as inferred from paleomagnetic data (see text). Symbols for numerical models are given in the inset; codes and references are given in the text (Note that not all model spectra are averaged over the same length of time; see text).

over which these range). Kuang and Bloxham (KB98-1998) display a spectrum averaged over 1500 years shown with its variance (bars). They have, unfortunately, not published a spectrum averaged over the total duration ($\sim$2 τ_d) of their simulation. COG98 is a time average (probably over 3 τ_d) spectrum from *Christensen et al.* [1998]. Two spectra from *Coe et al.* [2000] were averaged over 15 τ_d. They correspond to the Glatzmaier and Roberts model (GR00; one with homogeneous thermal boundary conditions, the other with an imposed heat flux inspired by tomographic seismological studies). The 1980 field model (constructed with MAGSAT data and observatories) is shown as red dots. This spectrum is used for comparison by most authors (with the exception of *Kuang and Bloxham* [1998], who used the *Bloxham and Jackson* [1992] model for comparison). It is clear from section 2 that the field spectrum of the Earth in 1980 or over 300 years cannot be used as a valid constraint. On the other hand, the first three components of the spectrum are well constrained when averaged over more than 10 τ_d (using the knowledge of the corresponding g_n^m, h_n^m coefficients; see Figure 2). The corresponding bounds are also indicated, for information, on Figure 2. Clearly, one should not use

these bounds to test all spectra displayed on Figure 2, as they do not correspond to fields averaged over more than 10 τ_d. The only exceptions are the two spectra presented by *Coe et al.* [2000] that correspond to the Glatzmaier and Roberts model.

[94] Figure 2 allows us to conclude that models such as GR95 and COG99, though averaged over only a limited duration, are far more energetic at all degrees than the actual geomagnetic field. On the other hand, the "homogeneous" model (GR00) of *Coe et al.* [2000], averaged over 15 τ_d, is rather close to the best information we have about the paleomagnetic field spectrum, whereas the "tomographic" model has a much too weak dipole. The GR00 homogeneous model [*Glatzmaier et al.*, 1999; *Coe et al.*, 2000] appears to fit rather well the contraints summarized in Figure 1 and 2, and it is the only one so far to come close to such success (the Kuang and Bloxham KB98, though possibly promising, is averaged over only a fraction of τ_d, which is too short for a robust conclusion). However, we recall that the GR00 model suffers, like the other models, from unrealistic values of the Ekman and magnetic Prandtl numbers. Puzzling features include a large Elsasser number ($\sim$100), contrary to expected (but not demonstrated) Earth values which are on the order of one. Also, magnetic induction and fluid motion is localized mostly within the inner part of the cylinder tangent to the solid inner core, whereas models based on secular variation have most of the motion outside of this cylinder. Finally, the value of the mean dipole term in the spectrum could be ill resolved, since the authors state that their high-resolution tests produce field intensities that can be greater than Earth values [*Glatzmaier et al.*, 1999].

[95] We may conclude this review with some perspectives for forthcoming studies. We suggest that future numerical models wanting to test for Earth-like behavior should clearly present quantities averaged over the full integration time, which should (if possible) be at least 10 τ_d. From the observational side it would, of course, be most useful to establish the validity of some observations in category B, to propose additional constraints for dynamo models. Indeed, *Carlut et al.* [2000] propose that the mean values derived from paleomagnetic data over half a million years and more could be attained for timescales only slightly in excess of archeomagnetic values, of the order of 10 kyr, i.e., not 10 but only one half a dipole diffusion time.

Acknowledgments

[96] E.D. is grateful to Dominique Jault for enlightening discussions and for correcting preliminary versions of this manuscript. The authors wish to thank Stuart Gilder and Yves Gallet for useful comments.

References

Alexandrescu, M., D. Gibert, G. Hulot, J.-L. Le Mouël, and G. Saracco, Detection of geomagnetic jerks using wavelet analysis, *J. Geophys. Res.*, *100*(B7), 12,557–12,572, 1995.

Alexandrescu, M., V. Courtillot, and J.-L. Le Mouël, Geomagnetic field direction in Paris since the mid-sixteenth century, *Phys. Earth Planet. Inter.*, *98*, 321–360, 1996a.

Alexandrescu, M., D. Gibert, G. Hulot, J.-L. Le Mouël, and G. Saracco, Worldwide wavelet analysis of geomagnetic jerks, *J. Geophys. Res.*, *101*(B10), 21,975–21,994, 1996b.

Alexandrescu, M., V. Courtillot, and J.-L. Le Mouël, High-resolution secular variation of the geomagnetic field in western Europe over the last 4 centuries: Comparison and integration of historical data from Paris and London, *J. Geophys. Res.*, *102*(B9), 20,245–20,258, 1997.

Aurnou, J., D. Brito, and P. Olson, Mechanics of inner core super-rotation, *Geophys. Res. Lett.*, *23*, 3401–3404, 1996.

Barton, C. E., and P. L. McFadden, Inclination shallowing and preferred transitional VGP paths, *Earth Planet. Sci. Lett.*, *140*, 147–157, 1996.

Bloxham, J., and D. Gubbins, The secular variation of the Earth's magnetic field, *Nature*, *317*, 777–781, 1985.

Bloxham, J., and D. Gubbins, Geomagnetic field analysis, VI, Testing the frozen-flux hypothesis, *Geophys. J. R. Astron. Soc.*, *84*, 139–152, 1986.

Bloxham, J., and A. Jackson, Time-dependant mapping of the magnetic field at the core-mantle boundary, *J. Geophys. Res.*, *97*, 19,537–19,563, 1992.

Bogue, S. W., and H. A. Paul, Distinctive field behaviour following geomagnetic reversals, *Geophys. Res. Lett.*, *20*, 2399–2402, 1993.

Bonhommet, N., and J. Babkine, Sur la présence d'aimantations inversées dans la Chaîne des Puys, *C. R. Acad. Sci. Paris*, *264*, 92–94, 1967.

Braginsky, S., and V. P. Meytlis, Local turbulence in the Earth's core, *Geophys. Astrophys. Fluid. Dyn.*, *55*(2), 71–87, 1990.

Braginsky, S., and P. H. Roberts, Equations governing convection in Earth's core and the geodynamo, *Geophys. Astrophys. Fluid. Dynam.*, *79*, 1–97, 1995.

Bullard, E. C., C. Freedman, H. Gellman, and J. Nixon, The westward drift of the Earth's magnetic field, *Philos. Trans. R. Soc. London*, *A243*, 67–92, 1950.

Busse, F. H., E. Grote, and A. Tilgner, On convection driven dynamos in rotating spherical shells, *Stud. Geophys. Geod.*, *42*, 211–223, 1998.

Camps, P., R. S. Coe, and M. Prévot, The transitional geomagnetic impulses hypothesis: Geomagnetic fact or rock-magnetic artifact?, *J. Geophys. Res.*, *104*, 17,747–17,758, 1999.

Carlut, J., and V. Courtillot, How complex is the time-averaged geomagnetic field over the past 5 Myr?, *Geophys. J. Int.*, *134*, 527–544, 1998.

Carlut, J., J.-P. Valet, X. Quidelleur, V. Courtillot, T. Kidane, Y. Gallet, and P.-Y. Gillot, Paleointensity across the Réunion event in Ethiopia, *Earth Planet. Sci. Lett.*, *170*, 17–34, 1999.

Carlut, J., V. Courtillot, and G. Hulot, Over how much time should the geomagnetic field be averaged to obtain the mean paleomagnetic field?, *Terra Nova*, *11*(5), 239–243, 2000.

Champion, D. E., M. A. Lanphere, and M. A. Kuntz, Evidence for a new geomagnetic reversal from lava flows in Idaho: Discussion of short polarity reversals in the Brunhes and late Matuyama polarity chrons, *J. Geophys. Res.*, *93*, 11,667–11,680, 1988.

Channell, J. E. T., and B. Lehman, The last two geomagnetic polarity reversals recorded in high deposition-rate sediments drifts, *Nature*, *389*, 712–715, 1997.

Chauvin, A., P. Roperch, and R. A. Duncan, Records of geomagnetic reversals from volcanic islands of french Polynesia, *J. Geophys. Res.*, *95*, 2727–2752, 1990.

Chauvin, A., P.-Y. Gillot, and N. Bonhommet, Paleointensity of the Earth's magnetic field recorded by two late quaternary volcanic sequences at the island of La Réunion (Indian Ocean), *J. Geophys. Res.*, *96*, 1981–2006, 1991.

Childress, S., and A. M. Soward, Convection-driven hydromagnetic dynamos, *Phys. Rev. Lett.*, *29*, 837–839, 1972.

Christensen, U., P. Olson, and G. Glatzmaier, A dynamo model interpretation of geomagnetic field structures, *Geophys. Res. Lett.*, *25*, 10, 1998.

Christensen, U., P. Olson, and G. Glatzmaier, Numerical modeling of the geodynamo: A systematic parameter study, *Geophys. J. Int.*, *138*, 393–409, 1999.

Cioni, S., S. Ciliberto, and J. Sommeria, Strongly turbulent Rayleigh-Bénard convection in mercury: Comparison with results at moderate Prandtl number, *J. Fluid Mech.*, *335*, 111–140, 1997.

Clement, B. M., Geographical distribution of transitional VGPs: Evidence for non zonal equatorial symmetry during the Matuyama-Brunhes geomagnetic reversal, *Earth Planet. Sci. Lett.*, *104*, 48–58, 1991.

Coe, R. S., and M. Prévot, Evidence suggesting extremely rapid field variation during a geomagnetic reversal, *Earth Planet. Sci. Lett.*, *92*, 292–298, 1989.

Coe, R. S., M. Prévot, and P. Camps, New evidence for extraordinarily rapid change of the geomagnetic field during a reversal, *Nature*, *374*, 687–692, 1995.

Coe, R. S., L. Hongre, and G. Glatzmaier, An examination of simulated geomagnetic polarity reversals, *Proc. R. Soc. London*, *358*(1768), 1141–1170, 2000.

Constable, S. R., and R. L. Parker, Statistics of the geomagnetic secular variation for the past 5 Myr, *J. Geophys. Res.*, *93*, 11,569–11,581, 1988.

Courtillot, V., and J. Besse, Magnetic field reversals, polar wander, and core-mantle coupling, *Science*, *237*, 1140–1147, 1987.

Courtillot, V., and J.-L. Le Mouël, Geomagnetic secular variation impulses, *Nature*, *311*, 709–716, 1984.

Courtillot, V., and J.-L. Le Mouël, Time variations of the Earth's magnetic field: From daily to secular, *Annu. Rev. Earth Planet. Sci.*, *16*, 389, 1988.

Courtillot, V., and J.-P. Valet, Secular variation of the Earth magnetic field; from jerks to reversals, *C. R. Acad. Sci. Paris, Ser. IIa*, *320*, 903–922, 1995.

Courtillot, V., J.-P. Valet, G. Hulot, and J.-L. Le Mouël, The Earth's magnetic field: Which geometry?, *Eos Trans. AGU*, *73*(32), 337, 1992.

Cox, A., The frequency of geomagnetic reversals and the symmetry of the nondipole field, *Rev. Geophys.*, *13*, 3, 1975.

Dagley, P., and E. Lawley, Paleomagnetic evidence for the transitional behaviour of the geomagnetic field, *Geophys. J. R. Astron. Soc.*, *36*, 577–598, 1974.

Denham, C. R., Spectral analysis of paleomagnetic time series, *J. Geophys. Res.*, *80*, 1897–1901, 1975.

Desjardins, B., E. Dormy, and E. Grenier, Stability of mixed Ekman-Hartmann boundary layers, *Nonlinearity*, *12*(2), 181, 1999.

De Wijs, G., et al., The viscosity of liquid iron at the physical conditions of the Earth's core, *Nature*, *392*(6678), 239–243, 1998.

Dodson, R. E., Counterclockwise precession of the geomagnetic field vector and westward drift of the non dipole field, *J. Geophys. Res.*, *84*, 637–644, 1979.

Dormy, E., P. Cardin, and D. Jault, MHD flow in a slightly differentially rotating spherical shell, with conducting inner core, in a dipolar magnetic field, *Earth Planet. Sci. Lett.*, *160*, 15–30, 1998.

Eltayeb, I. A., and S. Kumar, Hydromagnetic convective instabilities of a rotating self-gravitating fluid sphere containing a uniform distribution of heat sources, *Proc. R. Soc. London, Ser. A*, *353*, 145–162, 1977.

Eltayeb, I. A., and P. H. Roberts, On the hydromagnetics of rotating fluids, *Astrophys. J.*, *162*, 688–701, 1970.

Evans, M. E., New archeomagnetic evidence for the persistence of the geomagnetic westward drift, *J. Geomagn. Geoelectr.*, *39*, 769–772, 1987.

Fearn, D., Thermally driven hydromagnetic convection in a rapidly rotating sphere, *Proc. R. Soc. London, Ser. A*, *369*, 227–242, 1979a.

Fearn, D., Thermal and magnetic instabilities in a rotating fluid sphere, *Geophys. Astrophys. Fluid Dyn.*, *14*, 103–126, 1979b.

Frank, M., Comparison of cosmogenic radionuclide production and geomagnetic field intensity over the last 200 000 years, *Philos. Trans. R. Soc.*, *358*, 1089–1107, 2000.

Frank, M., B. Schwarz, S. Baumann, P. Kubik, M. Suter, and A. Mangini, A 200 kyr record of cosmogenic radionuclide production rate and geomagnetic field intensity from ^{10}Be in globally stacked deep-sea sediments, *Earth Planet. Sci. Lett.*, *149*, 121–129, 1997.

Gallet, Y., and G. Hulot, Stationary and nonstationary behaviour within the geomagnetic polarity timescale, *Geophys. Res. Lett.*, *24*(15), 1875–1878, 1997.

Gee, J., L. Tauxe, and E. Barg, Lower Jaramillo transition records from the equatorial Atlantic and Indian Oceans, *Proc. ODP Sci. Results*, *121*, 1990.

Gee, J., D. A. Schneider, and D. V. Kent, Marine magnetic anomalies as recorders of geomagnetic intensity variations, *Earth Planet. Sci. Lett.*, *144*, 327–335, 1996.

Gillot, P.-Y., J. Labeyrie, C. Laj, G. Valladas, G. Guerin, G. Poupeau, and G. Delibrias, Age of the Laschamp paleomagnetic excursion revisited, *Earth Planet. Sci. Lett.*, *42*, 444–450, 1979.

Gire, C., J.-L. Le Mouël, and T. Madden, The recent westward drift rate of the geomagnetic field and the body drift of external layers of the core, *Ann. Geophys.*, *2*(1), 37–45, 1984.

Glatzmaier, G., and P. H. Roberts, A three-dimensional convective dynamo solution with rotating and finitely conducting inner core and mantle, *Phys. Earth Planet. Inter.*, *91*, 63–75, 1995a.

Glatzmaier, G., and P. H. Roberts, A three-dimensional self-consistent computer simulation of a geomagnetic field reversal, *Nature*, *377*, 203–209, 1995b.

Glatzmaier, G., and P. H. Roberts, On the magnetic sounding of planetary interiors, *Phys. Earth Planet. Inter.*, *98*, 207–220, 1996a.

Glatzmaier, G., and P. H. Roberts, An anelastic evolutionary geodynamo simulation driven by compositional and thermal convection, *Physica D*, *97*, 81–94, 1996b.

Glatzmaier, G., and P. H. Roberts, Rotation and magnetism of Earth's inner core, *Science*, *274*, 1887–1891, 1996c.

Glatzmaier, G., and P. H. Roberts, Simulating the geodynamo, *Contemp. Phys.*, *38*, 1997a.

Glatzmaier, G., and P. H. Roberts, Numerical simulation of the geodynamo, *Acta Astron. Geophys. Univ. Comenianae*, *XIX*, 1997b.

Glatzmaier, G., R. Coe, L. Hongre, and P. H. Roberts, The role of the Earth's mantle in controlling the frequency of geomagnetic reversals, *Nature*, *401*, 885–890, 1999.

Glen, J., R. Coe, and J. Liddicoat, A detailed record of paleomagnetic field change from Searles Lake, California, 2, The Gauss/Matuyama polarity reversal, *J. Geophys. Res.*, *104*, 12,883–12,894, 1999.

Grote, E., F. H. Busse, and A. Tilgner, Convection-driven quadrupolar dynamos in rotating spherical shells, *Phys. Rev. E*, *60*(5), 5025–5028, 1999.

Grote, E., F. H. Busse, and A. Tilgner, Regular and chaotic spherical dynamos, *Phys. Earth Planet. Inter.*, *117*, 259–272, 2000a.

Grote, E., F. H. Busse, and A. Tilgner, Effects of hyperdiffusivities on dynamo simulations, *Geophys. Res. Lett.*, *27*, 2001–2004, 2000b.

Gubbins, D., Geomagnetic polarity reversals: A connection with secular variation and core-mantle interaction, *Rev. Geophys.*, *32*(1), 61–83, 1994.

Gubbins, D., The distinction between geomagnetic excursions and reversals, *Geophys. J. Int.*, *137*, F1–F3, 1999.

Gubbins, D., and J. Bloxham, Morphology of the geomagnetic field and implications for the geodynamo, *Nature*, *325*, 509–511, 1987.

Gubbins, D., and R. S. Coe, Longitudinally confined geomagnetic reversal paths from nondipolar transition fields, *Nature*, *362*, 51–53, 1993.

Gubbins, D., and J. J. Love, Preferred VGP paths during geomagnetic polarity reversals: Symmetry considerations, *Geophys. Res. Lett.*, *25*(7), 1079–1082, 1998.

Guyodo, Y., and J.-P. Valet, Global changes in geomagnetic intensity during the past 800 thousand years, *Nature*, *399*, 249–252, 1999.

Hagee, V. L., and P. Olson, An analysis of paleomagnetic secular variation in the Holocene, *Phys. Earth Planet. Inter.*, *56*, 266–284, 1989.

Herrero-Bervera, E., and J.-P. Valet, Paleosecular variation during sequential geomagnetic reversals from Hawaii, *Earth Planet. Sci. Lett.*, *171*, 139–148, 1999.

Hillhouse, J., and A. Cox, Brunhes-Matuyama polarity transition, *Earth Planet. Sci. Lett.*, *29*, 51–64, 1976.

Hirshing, W., and F. Busse, Stationary and chaotic dynamos in rotating spherical shells, *Phys. Earth Planet. Inter.*, *90*, 243–254, 1995.

Hoffman, K. A., Late acquisition of "primary" remanence in some fresh basalts: A case of spurious paleomagnetic results, *Geophys. Res. Lett.*, *11*, 681–684, 1984.

Hoffman, K. A., Long-lived transitional states of the geomagnetic field and the two dynamo families, *Nature*, *354*, 273–277, 1991.

Hoffman, K. A., Dipolar reversal states of the geomagnetic field and core-mantle dynamics, *Nature*, *359*, 789–794, 1992.

Hoffman, K. A., Transitional paleomagnetic field behavior: Preferred paths or patches?, *Surv. Geophys.*, *17*, 207–211, 1996.

Holcomb, R. T., Eruptive history and long-term behaviour of Kilauea volcano, Hawaii, in *Volcanism in Hawaii*, edited by R. W. Decker, T. L. Wright, and P. H. Stauffer,*U.S. Geol. Surv. Prof. Pap.*, *1350*, 261–350, 1987.

Hongre, L., G. Hulot, and A. Khokhlov, An analysis of the geomagnetic field over the past 2000 years, *Phys. Earth Planet. Int.*, *106*, 311–335, 1998.

Hulot, G., and J.-L. Le Mouël, A statistical approach to the Earth's main magnetic field, *Phys. Earth Planet. Int.*, *82*, 167–183, 1994.

Hulot, G., M. Le Huy, and J.-L. Le Mouël, Secousses (jerks) de la variation séculaire et mouvements dans le noyau terrestre, *C. R. Acad. Sci. Paris, Ser. II*, *317*, 333–341, 1993.

Jackson, A., J. Bloxham, and D. Gubbins, Time-dependent flow at the core surface and conservation of angular momentum in the coupled core-mantle system, in *Dynamics of the Earth's Deep Interior and Earth Rotation, Geophys. Monogr. Ser.*, vol. 72, edited by J.-L. Mouël et al., pp. 97–107,AGU, Washington, D. C., 1993.

Jault, D., C. Gire, and J.-L. Le Mouël, Westward drift, core motions and exchanges of angular momentum between core and mantle, *Nature*, *333*, 353–356, 1988.

Johnson, C. L., and C. G. Constable, The time averaged geomagnetic field: Global and regional biases for 0–5Ma, *Geophys. J. Int.*, *131*, 643–666, 1997.

Johnson, C. L., and C. G. Constable, Persistently anomalous Pacific geomagnetic fields, *Geophys. Res. Lett.*, *25*, 1011–1014, 1998.

Jones, C., A. Longbottom, and R. Hollerbach, A self-consistent convection driven geodynamo model, using a mean field approximation, *Physics Earth Planet. Int.*, *92*, 119–141, 1995.

Juarez, M. T., and L. Tauxe, The intensity of the time averaged geomagnetic field: The last 5 Myr, *Earth Planet. Sci. Lett.*, *175*, 169–180, 2000.

Kageyama, A., and T. Sato, Velocity and magnetic field structures in magnetohydrodynamic dynamo, *Phys. Plasma*, *4*(5), 1569–1575, 1997a.

Kageyama, A., and T. Sato, Generation mechanism of a dipole field by a magnetohydrodynamic dynamo, *Phys. Rev. E*, *55*, 4, 1997b.

Kageyama, A., and T. Sato, Dipole field generation by an MHD dynamo, *Plasma Phys. Controlled Fusion*, *39*, A83–A91, 1997c.

Kageyama, A., M. Ochi, and T. Sato, Flip-flop transitions of the magnetic intensity and polarity reversals in the magnetohydrodynamic dynamo, *Phys. Rev. Lett.*, *82*(26), 5409–5412, 1999.

Katayama, J., M. Matsushima, and Y. Honkura, Some characteristics of magnetic field behavior in a model of MHD dynamo thermally driven in a rotating spherical shell, *Phys. Earth Planet. Int.*, *111*, 141–159, 1999.

Kelly, P., and D. Gubbins, The geomagnetic field over the past 5 million years, *Geophys. J. Int.*, *128*, 1–16, 1997.

Kida, S., and H. Kitauchi, Thermally driven MHD dynamo in a rotating spherical shell, *Prog. Theoret. Phys. Suppl.*, *130*, 121–136, 1998.

Kitauchi, H., and S. Kida, Intensification of magnetic field by concentrate-and-stretch of magnetic flux lines, *Phys. Fluids*, *10*(2), 457–468, 1998.

Kok, Y. S., and L. Tauxe, Saw-tooth pattern of relative paleointensity records and cumulative viscous remanence, *Earth Planet. Sci. Lett.*, *137*, 95–99, 1996a.

Kok, Y. S., and L. Tauxe, Saw-tooth pattern of sedimentary paleointensity records explained by cumulative viscous remanence, *Earth Planet. Sci. Lett.*, *144*, E9–E14, 1996b.

Kuang, W., and J. Bloxham, An Earth-like numerical dynamo model, *Nature*, *389*, 371–374, 1997.

Kuang, W., and J. Bloxham, Numerical dynamo modeling: Comparison with the Earth's magnetic field, in *The Core-Mantle Boundary Region, Geodyn. Ser.*, vol. 28,edited by M. Gurnis et al., pp. 197–208, AGU, Washington, D. C., 1998.

Kuang, W., and J. Bloxham, Numerical modeling of magnetohydrodynamic convection in a rapidly rotating

spherical shell: Weak and strong field dynamo action, *J. Comput. Phys.*, *153*, 51–81, 1999.

Kuang, W., Force balances and convective state in the Earth's core, *Phys. Earth Planet. Int.*, *116*, 65–79, 1999.

Kutzner, C., and U. Christensen, Effects of driving mechanisms in geodynamo models, *Geophys. Res. Lett.*, *27*, 29–32, 2000.

Laj, C., A. Mazaud, R. Weeks, M. Fuller, and E. Herrero-Bervera, Geomagnetic reversal paths, *Nature*, *351*, 447, 1992.

Laj, C., C. Kissel, and F. Garnier, Relative geomagnetic field intensity and reversals for the last 1.8 My from a central equatorial Pacific core, *Geophys. Res. Lett.*, *23*(23), 3393–3396, 1996.

Langereis, C. G., A. A. M. van Hoof, and P. Rochette, Longitudinal confinement of geomagnetic reversal paths: Sedimentary artefact or true field behavior?, *Nature*, *358*, 226–230, 1992.

Langereis, C. G., M. J. Dekkers, G. J. DeLange, M. Paterne, and P. J. M. vanSantvoort, Magnetostratigraphy and astronomical calibration of the last 1.1 Myr from an eastern Mediterranean piston core and dating of short events in the Brunhes, *Geophys. J. Int.*, *129*, 75–94, 1997.

Le Mouël, J.-L., Outer core geostrophic flow and secular variation of Earth's geomagnetic field, *Nature*, *311*, 734–735, 1984.

Levi, S., H. Audunsson, R. A. Duncan, L. Kristansson, P.-Y. Gillot, and S. P. Jakobsson, Late Pleistocene geomagnetic excursion in Icelandic lavas: Confirmation of the Laschamp excursion, *Earth Planet. Sci. Lett.*, *96*, 443–457, 1990.

Love, J. J., Paleomagnetic volcanic data and geometric regularity of reversals and excursions, *J. Geophys. Res.*, *103*(B6), 12,435–12,452, 1998.

Love, J. J., and A. Mazaud, A database for the Matuyama-Brunhes magnetic reversal, *Phys. Earth Planet. Inter.*, *103*, 207–245, 1997.

Lowes, F. J., Spatial power spectrum of the main geomagnetic field, and extrapolation to the core, *Geophys. J. R. Astron. Soc.*, *36*, 717–730, 1974.

Lund, S. P., Initial paleomagnetic results from ODP leg 172 — Evidence for at least 14 geomagnetic excursions during the Brunhes epoch (abstract), *Eos Trans. AGU*, *78*, Fall Meet. Suppl., F181, 1997.

Lund, S. P., J. C. Liddicoat, K. R. Lajoie, T. L. Henyey, and S. W. Robinson, Paleomagnetic evidence for longer term (10^4 year) memory and periodic behavior in the Earth's core dynamic process, *Geophys. Res. Lett.*, *15*, 1101–1104, 1988.

Lund, S. P., G. Acton, B. Clement, M. Hastedt, M. Okada, T. Williams, and the ODP Leg 172 Scientific Party, Geomagnetic field excursions occurred often during the last million years, *Eos Trans. AGU*, *79*, 178–179, 1998.

Lutz, T. M., and G. S. Watson, Effects of long-term variation on the frequency spectrum of the geomagnetic reversal record, *Nature*, *334*, 240–242, 1988.

Mandea-Alexandrescu, M., D. Gibert, G. Hulot, J.-L. Le Mouël, and G. Saracco, An estimate of average lower mantle conductivity by wavelet analysis of geomagnetic jerks, *J. Geophys. Res.*, *104*(B8), 17,735–17,745, 1999.

Mankinen, E. A., M. Prévot, C. S. Grommé, and R. S. Coe, The Steens Mountain (Oregon) geomagnetic polarity transition 1, Directional history, duration of episodes and rock magnetism, *J. Geophys. Res.*, *90*, 10,393–10,416, 1985.

Mary, C., and V. Courtillot, 3-D representation of geomagnetic reversal records, *J. Geophys. Res.*, *98*, 22,461–22,476, 1993.

Mazaud, A., Saw-tooth variation in magnetic intensity profiles and delayed acquisition of magnetization in deep sea cores, *Earth Planet. Sci. Lett.*, *139*, 379–386, 1996.

McElhinny, M. W., and W. E. Senanayake, Variations in the geomagnetic dipole. I. The past 50,000 years, *J. Geomagn. Geoelectr.*, *34*, 39–51, 1982.

McElhinny, M. W., P. L. McFadden, and R. T. Merrill, The myth of the Pacific dipole window, *Earth Planet. Sci. Lett.*, *143*, 13–22, 1996.

McFadden, P. L., Statistical tools for the analysis of geomagnetic reversal sequences, *J. Geophys. Res.*, *89*, 3363–3372, 1984.

McFadden, P. L., and R. T. Merrill, Lower mantle convection and geomagnetism, *J. Geophys. Res.*, *89*, 3354–3362, 1984.

McFadden, P. L., and R. T. Merrill, Geodynamo energy source constraints from paleomagnetic data, *Phys. Earth Planet. Inter.*, *43*, 22–33, 1986.

McFadden, P. L., and R. T. Merrill, Inhibition and geomagnetic field reversals, *J. Geophys. Res.*, *98*, 6189–6199, 1993.

McFadden, P. L., R. T. Merrill, W. Lowrie, and D. V. Kent, The relative stabilities of the reverse and normal polarity states of the Earth's magnetic field, *Earth Planet. Sci. Lett.*, *82*, 372–383, 1987.

McFadden, P. L., R. T. Merrill, and C. E. Barton, Do virtual geomagnetic poles follow preferred path during geomagnetic reversals?, *Nature*, *361*, 342–344, 1993.

McMillan, S., A geomagnetic jerk for the early 1990's, *Earth Planet. Sci. Lett.*, *137*, 189–192, 1996.

Merrill, R. T., and P. L. McFadden, Geomagnetic polarity transitions, *Rev. Geophys.*, *37*, 201–226, 1999.

Merrill, R. T., M. W. McElhinny, and P. L. McFadden, *The Magnetic Field of the Earth: Paleomagnetism, The Core and the Deep Mantle*, Academic, San Diego, Calif., 1996.

Meynadier, L., and J.-P. Valet, Relative paleointensity in sediments: What should we believe?, paper presented at IUGG XXI General Assembly, Boulder, Colo., 1995.

Meynadier, L., and J.-P. Valet, Post-depositional realignment of magnetic grains and asymmetrical saw-toothed pattern of magnetization intensity, *Earth Planet. Sci. Lett.*, *140*, 123–132, 1996.

Meynadier, L., J.-P. Valet, Y. Guyodo, and C. Richter, Saw-toothed variations of relative paleointensity and cumulative viscous remanence: Testing the records and the model, *J. Geophys. Res.*, *103*, 7095–7105, 1998.

Olson, P., and J. Aurnou, A polar vortex in the Earth's core, *Nature*, *402*, 170–173, 1999.

Olson, P., U. Christensen, and G. Glatzmaier, Numerical modeling of the geodynamo: Mechanisms of field generation and equilibration, *J. Geophys. Res.*, *104*, 10,383–10,404, 1999.

Opdyke, D., and E. T. Channel, Magneto stratigraphy, in *Int. Geophys. Ser.*, 346 pp., Academic, San Diego, Calif., 1996.

Pais, A., and G. Hulot, Could some axial differential rotation at the core surface be detected by geomagnetic observations?, in *IAGA Abstract Volume*, p. 11,Uppsala, Sweden, 1997.

Pais, A., and G. Hulot, Length of day decade variations, torsional oscillations and inner core superrotation: Evidence from recovered core surface zonal flows, *Phys. Earth Planet. Inter.*, *118*, 291–316, 2000.

Parker, E. N., *Cosmical Magnetic Fields*, Clarendon Press, Oxford, England, 1979.

Perrin, M., M. Prévot, and E. Mankinen, Low intensity of the geomagnetic field in Early Jurassic time, *J. Geophys. Res.*, *96*, 14,197–14,210, 1991.

Poirier, J.-P., Physical properties of the Earth's core, *C. R. Acad. Sci. Paris*, *318*, 341–350, 1994.

Poupinet, G., A. Souriau, and O. Coutant, The existence of an inner core super-rotation questioned by teleseismic doublets, *Phys. Earth Planet. Inter.*, *118*(1–2), 77–88, 2000.

Prévot, M., and P. Camps, Absence of longitudinal confinement of poles in volcanic records of geomagnetic reversals, *Nature*, *366*, 53–57, 1993.

Prévot, M., Mankinen, R. S. Coe, C. S. Grommé, The Steens Mountain (Oregon) geomagnetic polarity transition. Field intensity variations and discussion of reversal models, *J. Geophys. Res.*, *90*, 10,417–10,448, 1985.

Quidelleur, X., and J.-P. Valet, Paleomagnetic records of excursions and reversals: Possible biases caused by magnetization artefacts?, *Phys. Earth Planet. Inter.*, *82*, 27–48, 1994.

Quidelleur, X., and J.-P. Valet, Geomagnetic changes across the last reversal recorded in lava flows from La Palma (Canaries islands), *J. Geophys. Res.*, *101*, 13,755–13,774, 1996.

Quidelleur, X., J.-P. Valet, M. LeGoff, and X. Bouldoire, Field dependence on magnetization of laboratory redeposited deep-sea sediments: First results, *Earth Planet. Sci. Lett.*, *133*, 311–325, 1995.

Quidelleur, X., P.-Y. Gillot, J. Carlut, and V. Courtillot, Link between excursions and paleointensity inferred from abnormal field directions recorded at La Palma around 600 ka, *Earth Planet. Sci. Lett.*, *168*, 233–242, 1999.

Raisbeck, G. M., F. Yiou, and S. Z. Zhou, Paleointensity puzzle, *Nature*, *371*, 207–208, 1994.

Roberts, P. H., Magnetoconvection in a rapidly rotating fluid, in *Rotating Fluids in Geophysics*, edited by P. H. Roberts and A. M. Soward, p. 421,Academic, San Diego, Calif., 1978.

Rochette, P., Rationale of geomagnetic reversal versus remanence recording process in rocks: A critical review, *Earth Planet. Sci. Lett.*, *98*, 33–39, 1990.

Roperch, P., N. Bonhommet, and S. Levi, Paleointensity of the Earth's magnetic field during the Laschamp excursion and its geomagnetic implications, *Earth Planet. Sci. Lett.*, *88*, 209–219, 1988.

Runcorn, S. K., On the theory of the geomagnetic secular variation, *Ann. Geophys.*, *15*, 87–92, 1959.

Sakuraba, A., and M. Kono, Effect of the inner core on the numerical solution of the magnetohydrodynamic dynamo, *Phys. Earth Planet. Inter.*, *111*, 105–121, 1999.

Sarson, G., and C. Jones, A convection driven geodynamo reversal model, *Phys. Earth Planet. Inter.*, *111*, 3–20, 1999.

Sarson, G., C. Jones, and A. Longbottom, Convection driven geodynamo models of varying Ekman number, *Geophys. Astrophys. Fluid Dyn.*, *88*, 225–259, 1998.

Schneider, D. A., and D. V. Kent, The paleomagnetic field from equatorial deep-sea sediments: Axial symmetry and polarity asymmetry, *Science*, *242*, 252–256, 1988.

Song, X., and P. Richards, Seismological evidence for differential rotation of the Earth's inner core, *Nature*, *382*, 221–224, 1996.

Souriau, A., Earth's inner core — Is the rotation real?, *Science*, *281*(5373), 55–56, 1998a.

Souriau, A., New seismological constraints on differential rotation of the inner core from Novaya Zemlya events recorded at DRV *Antarctica*, *Geophys. J. Int.*, *134*, 1–5, 1998b.

Souriau, A., P. Roudil, and B. Moynot, Inner core differential rotation: Facts and artefacts, *Geophys. Research Lett.*, *24*(16), 2103–2106, 1997.

Soward, A. M., On the finite amplitude thermal instability of a rapidly rotating fluid sphere, *Geophys. Astrophys. Fluid Dyn.*, *9*, 19–74, 1977.

Soward, A. M., Convection driven dynamos, *Phys. Earth Planet. Inter.*, *20*, 134–151, 1979.

Soward, A. M., The Earth's dynamo, In *Recent Advances in Fluid Mechanics*, pp. 249–268,P. L. Sachdev and M. Venkatachalppa, Gordon and Breach, New York, 1998.

Su, W., A. Dziewonski, and R. Jeanloz, Planet within a planet — Rotation of the inner-core of Earth, *Science*, *274*, 1883–1887, 1996.

Tarduno, J. A., W. Lowrie, W. Sliter, T. Bralower, and F. Heller, Reversed polarity characteristics magnetizations in the Albian Contessa Section, Umbrian Apennines, Italy: Implications for the existence of a mid-cretaceous mixed polarity interval, *J. Geophys. Res.*, *97*, 241–271, 1992.

Thibal, J., J. P. Pozzi, V. Barthès, and G. Dubuisson, Continuous record of geomagnetic field intensity between 4.7 and 2.7 Ma from downhole measurements, *Earth. Planet. Sci. Lett.*, *136*, 541–550, 1995.

Thompson, R., and D. R. Barraclough, Geomagnetic secular variation based on spherical harmonic and cross validation analyses of historical and archeomagnetic data, *J. Geomagn. Geoelectr.*, *34*, 245–263, 1982.

Thouveny, N., K. M. Créer, and I. Blunk, Extension of the lac du Bouchet paleomagnetic record over the last 120,000 years, *Earth Planet. Sci. Lett.*, *97*, 140–161, 1990.

Tric, E., C. Laj, C. Jehanno, J.-P. Valet, A. Mazaud, C. Kissel, and S. Iaccarino, A detailed record of the upper Olduvai polarity transition from high sedimentation rate marine deposits of the Po valley, *Phys. Earth Planet. Inter.*, *65*, 319–336, 1991.

Ultré-Guérard, P., and J. Achache, Core flow instabilities and geomagnetic storms during reversals: The Steens mountain impulsive field variation revisited, *Earth Planet. Sci. Lett.*, *139*, 91–99, 1995.

Ultré-Guérard, P., D. Jault, M. Alexandrescu, and J. Achache, Improving geomagnetic field models for the period 1980–1999 using Oersted data, *Earth Planet. Space*, *50*, 635–640, 1998.

Valet, J.-P., and L. Meynadier, Geomagnetic field intensity and reversals during the last four million years, *Nature*, *366*, 234–238, 1993.

Valet, J.-P., C. Laj, and P. Tucholka, High resolution sedimentary record of a geomagnetic reversal, *Nature*, *322*, 27–32, 1986.

Valet, J.-P., L. Tauxe, and D. Clark, The Matuyama-Brunhes polarity transition recorded from Lake Tecopa sediments (Calif.), *Earth Planet. Sci. Lett.*, *87*, 463–472, 1988.

Valet, J.-P., L. Tauxe, and B. M. Clement, Equatorial and mid-latitudes records of the last geomagnetic reversal from the Atlantic Ocean, *Earth Planet. Sci. Lett.*, *94*, 371–384, 1989.

Valet, J.-P., P. Tucholka, V. Courtillot, and L. Meynadier, Paleomagnetic constraints on the geometry of the geomagnetic field during reversals, *Nature*, *356*, 400–407, 1992.

Valet, J.-P., L. Meynadier, F. Bassinot, and F. Garnier, Relative paleointensity across the last geomagnetic reversal from sediments of the Atlantic, Indian and Pacific oceans, *Geophys. Res. Lett.*, *21*(6), 485–488, 1994.

Valet, J.-P., T. Kidane, V. Soler, J. Brassart, V. Courtillot, and L. Meynadier, Remagnetization in lava flows recording pretransitional directions, *J. Geophys. Res.*, *103*, 9755–9775, 1998.

Valet, J.-P., J. Brassart, X. Quidelleur, V. Soler, P.-Y. Gillot, and L. Hongre, Paleointensity variations across the last geomagnetic reversal at La Palma (Canary Islands, Spain), *J. Geophys. Res.*, *104*, 7577–7598, 1999.

Van Hoof, The Gilbert/Gauss sedimentary geomagnetic reversal record from southern Sicily, *Geophys. Res. Lett.*, *20*, 835–838, 1993.

Verosub K. L., Geomagnetic excursions: A critical assessment of the evidence as recorded in sediments of the Brunhes epoch, *Philos. Trans. R. Soc. London, Ser. A*, *306*, 161–168, 1982.

Verosub, K. L., and S. K. Benerjee, Geomagnetic excursions and their paleomagnetic record, *Rev. Geophys.*, *15*, 145–155, 1977.

Verosub, K. L., E. Herrero-Bervera, and A. P. Roberts, Relative geomagnetic paleointensity across the Jaramillo subchron and the Matuyama/Brunhes boundary, *Geophys. Res. Lett.*, *23*, 467–470, 1996.

Walker, A., and G. E. Backus, On the difference between the average values of Br2in the Atlantic and Pacific hemispheres, *Geophys. Res. Lett.*, *23*, 1965–1968, 1996.

Wicht, J., and F. H. Busse, Magnetohydrodynamic dynamos in rotating spherical shells, *Geophys. Astrophys. Fluid Dyn.*, *86*, 103–129, 1997.

Yukutake, T., The westward drift of the Earth's magnetic field in historic times, *J. Geomagn. Geoelectr.*, *19*, 103–116, 1967.

Zhang, K., and F. H. Busse, Finite amplitude convection and magnetic field generation in a rotating spherical shell, *Geophys. Astrophys. Fluid Dyn.*, *44*, 33–53, 1988.

Zhang, K., and F. H. Busse, Convection driven magnetohydrodynamic dynamos in rotating spherical shells, *Geophys. Astrophys. Fluid Dyn.*, *49*, 97–116, 1989.

Zhang, K., and C. Jones, The effect of hyperviscosity on geodynamo models, *Geophys. Res. Lett.*, *24*, 2869–2872, 1997.

Zhang, K., F. H. Busse, and W. Hirsching, Numerical models in the theory of geomagnetism, in *Geomagnetism and Paleomagnetism*, pp. 347–358,edited by F. J. Lowes et al., Kluwer Acad., Norwell, Mass., 1989.

ELSEVIER

Physics of the Earth and Planetary Interiors 124 (2001) 283–294

PHYSICS OF THE EARTH AND PLANETARY INTERIORS

www.elsevier.com/locate/pepi

Instability of Ekman–Hartmann boundary layers, with application to the fluid flow near the core–mantle boundary

Benoît Desjardins [a], Emmanuel Dormy [b,c,*], Emmanuel Grenier [d]

[a] C.E.A/D.I.F., B.P. 12, 91680 Bruyères le Châtel, France
[b] I.P.G.P., 4 place Jussieu, 75252 Paris Cedex 05, France
[c] C.N.R.S., Paris, France
[d] U.M.P.A., E.N.S. Lyon, 46 allée d'Italie, 69364 Lyon Cedex 07, France

Received 26 June 2000; accepted 6 October 2000

Abstract

Our aim is to investigate the instability of mixed Ekman–Hartmann boundary layers arising in rotating incompressible magnetohydrodynamics flows in a parameter regime relevant to the Earth liquid core. We perform a local study in a half space at a given co-latitude $\theta \neq \pi/2$, and assume a mean dipolar axial magnetic field with internal sources. Instabilities are driven, for high enough Reynolds number, by the quadratic term in the momentum equation. Following the work of Lilly [J. Atmos. Sci. 23 (1966) 481], we restrict our analysis to the linearized growth phase. We describe the dependence of the critical Reynolds number in terms of θ and Elsasser number (measuring the relative strength of Lorentz and Coriolis terms). It is found that no matter how large the Elsasser number is, there exists a critical band centered on the equator in which instabilities can occur. For geophysically relevant values of parameters, this band extends over some 45° away from the equator. This study establishes the possibility of boundary layer instabilities near the core–mantle boundary. © 2001 Elsevier Science B.V. All rights reserved.

Keywords: Core–mantle boundary; Ekman–Hartmann layers; Earth core dynamics

1. Introduction

The magnetohydrodynamic flow in the Earth's core is believed to support a self excited dynamo process responsible for the Earth's magnetic field. Though one has very few means of access to the deep interior of our planet, most of the parameters characterizing the dynamics in the core are relatively well known (Poirier, 1991, 1994). One can model the Earth's core by a spherical shell, filled with a conducting fluid of density ρ, kinematic viscosity ν, conductivity σ, which rotates rapidly with angular velocity Ω. We will only consider here phenomena occurring close to the outer bounding sphere. Important parameters are the Ekman number E, the Rossby number ε, the Elsasser number Λ and the magnetic Reynolds number $\mathcal{R}_{\mathrm{m}}$. These are defined introducing the magnetic diffusivity $\eta = (\sigma\mu_0)^{-1}$, a typical velocity U, length scale $\mathcal{L}$ and magnetic field $\mathcal{B}$ as

$$E = \frac{\nu}{2\Omega\mathcal{L}^2}, \qquad \varepsilon = \frac{U}{2\Omega\mathcal{L}},$$
$$\Lambda = \frac{\mathcal{B}^2}{2\Omega\rho\mu_0\eta}, \qquad R_{\mathrm{m}} = \frac{U\mathcal{L}}{\eta}. \tag{1}$$

The role of boundary layers on the dynamics of the core and on the geodynamo is usually thought to be

* Corresponding author.
E-mail address: dormy@ipgp.jussieu.fr (E. Dormy).

0031-9201/01/$ – see front matter © 2001 Elsevier Science B.V. All rights reserved.
PII: S0031-9201(01)00210-2

small. The laminar Ekman layer effect on the main flow, through the Ekman suction, scales as $E^{1/2}$. The Ekman suction is even reduced by magnetic effects (Acheson and Hide, 1973). This would of course be very different if the boundary layers happened to be unstable (they could then extend over a larger domain and would most probably affect the main flow). Recent studies showed that pure Ekman layer instabilities could indeed produce field generation and act as a dynamo (Ponty et al., 2000). In the last few years, numerous numerical models of self excited dynamos have been proposed (see Dormy et al. (2000) for a review). Among these models, some suppressed boundary layers using stress-free boundary conditions (Busse et al., 1999; Christensen et al., 1999; Katayama et al., 1999; Kuang and Bloxham, 1997, 1999). This was proven to strongly modify the moderate Ekman number solutions with a conducting inner core (Kuang and Bloxham, 1997; Christensen et al., 1999). Suppression of these boundary layers is based on the assumption that they are stable, and thus, small and negligible. Other numerical models retained the Ekman layers and observed a large field induction in laminar layers near the core–mantle boundary (CMB) for moderate values of the Ekman number (Sakuraba and Kono, 1999). The evidence of instabilities of these layers would shed some new light on the flow near the CMB, but also on numerical models for the dynamo.

We present a linearized study for instability of the mixed Ekman–Hartmann boundary layers in rotating incompressible magnetohydrodynamic flows. It is known (Gilman, 1971) that Ekman–Hartmann layer (as the Ekman layer and the Hartmann layer) are unstable to two-dimensional rolls for sufficiently high Reynolds numbers. The purpose of this work is to extend previous instability studies (Leibovich and Lele, 1985; Lilly, 1966; Gilman, 1971), to incompressible MHD flows near a spherical boundary at a given co-latitude $\theta \in [0, \pi/2)$ for dipolar static magnetic field. The Reynolds number at which these instabilities occur, as well as the details of these instabilities, are the subject of this article. The possibility for such instabilities to occur near the CMB will then be discussed.

2. Model description

2.1. Laminar Ekman–Hartmann boundary layer

We focus in this study to the parameter range relevant for the Earth's core, and in particular small value of the magnetic Prandtl number ($E\mathcal{R}_{\mathrm{m}}\varepsilon^{-1}$). We perform a local analysis at a given co-latitude, assuming a dipolar axial mean magnetic field with internal sources. More precisely, we consider a half space $\mathcal{D}$ filed with an incompressible conducting fluid governed by the Navier–Stokes equations coupled with the induction equation

$$\begin{cases} \partial_t \boldsymbol{u} + \boldsymbol{u}\cdot\nabla\boldsymbol{u} + \dfrac{\nabla p}{\varepsilon} + \dfrac{\boldsymbol{e}_\Omega \times \boldsymbol{u}}{\varepsilon} - \dfrac{E}{\varepsilon}\Delta\boldsymbol{u} = \dfrac{\Lambda}{\varepsilon R_{\mathrm{m}}}\operatorname{curl}\boldsymbol{B}\times\boldsymbol{B} \\ \partial_t \boldsymbol{B} = \operatorname{curl}(\boldsymbol{u}\times\boldsymbol{B}) + \dfrac{1}{\mathcal{R}_{\mathrm{m}}}\Delta\boldsymbol{B}, \quad \operatorname{div}\boldsymbol{B} = 0, \qquad \operatorname{div}\boldsymbol{u} = 0 \end{cases} \tag{2}$$

where $\boldsymbol{e}_\Omega$ denotes the constant unit vector in the direction of rotation, $\boldsymbol{B}$ the magnetic field, and $\boldsymbol{E} = (\operatorname{curl}\boldsymbol{B})/\mathcal{R}_{\mathrm{m}} - \boldsymbol{u}\times\boldsymbol{B}$ the electric field.

Outside the shell ($\mathcal{D}^c$), the mantle is considered to be an electrical insulator and the magnetic field is thus assumed to be harmonic

$$\begin{aligned} &\operatorname{curl}\boldsymbol{B} = 0, \qquad \operatorname{curl}\boldsymbol{E} = -\partial_t\boldsymbol{B}, \\ &\operatorname{div}\boldsymbol{E} = 0, \qquad \operatorname{div}\boldsymbol{B} = 0. \end{aligned} \tag{3}$$

At the CMB $\partial\mathcal{D}$, we require the velocity of the fluid to vanish and the tangential component of the electric field and magnetic field to be continuous.

We consider in the sequel the following orderings for ε, Λ, $\mathcal{R}_{\mathrm{m}}$, E

$$\varepsilon \to 0, \quad \Lambda \sim \mathcal{O}(1), \quad \varepsilon\mathcal{R}_{\mathrm{m}} \to 0, \quad E \sim \varepsilon^2. \tag{4}$$

These limits are relevant to the Earth's core (Dormy et al., 1998; Desjardins et al., 1999).

We define our frame of reference (x, y, z) with x in the $\boldsymbol{e}_1$ direction (co-latitude), y in the $\boldsymbol{e}_2$ direction (longitude) and z in the $\boldsymbol{e}_3$ direction (radial direction) (see Fig. 1).

We also assume that the direction of the static magnetic field $\boldsymbol{B}_0$ varies in latitude as a pure axial

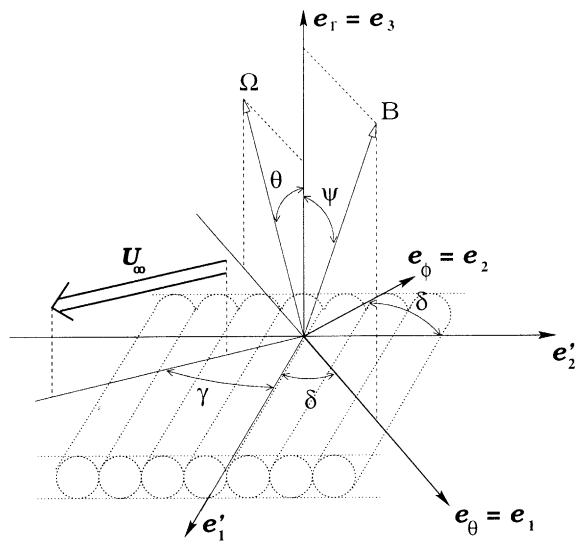

Fig. 1. Geometry of the local study. Rotation vector and magnetic field, respectively, make an angle θ and ψ with the normal to the boundary. Traveling wave solutions are sought for an external velocity $\boldsymbol{U}_\infty$. These quantities, respectively, make an angle δ and $\gamma_0 = \delta + \gamma$ with the plane ($\boldsymbol{\Omega}$, $\boldsymbol{B}$).

dipole with internal sources, so that we can write $\boldsymbol{e}_\Omega = (-\sin\theta, 0, \cos\theta)$, $\boldsymbol{e}_B = e'/||e'||$ with $e' = (\sin\theta, 0, 2\cos\theta)$ and hence

$$\cos\psi = \frac{2\cos\theta}{(1+3\cos^2\theta)^{1/2}} \quad \text{is the vertical component of } \boldsymbol{B}_0. \tag{5}$$

Note that the polarity of the field can be reversed through a modification of ψ in $\pi + \psi$, what does not affect the rest of the study.

Note also that the first assumption here is that the static magnetic field $\boldsymbol{B}_0$ has only two non-zero coordinates b_1 and b_3. If such was not the case, a second angle (say ψ_{H}) would need to be introduced at this stage. The dipolar variation of the field's direction (i.e. the precise relation between θ and ψ), however, becomes important only in Section 2.5 and following.

Introducing the normal Elsasser number $\Lambda_\perp = \Lambda\cos^2\psi(\cos\theta)^{-1}$, it is convenient to define τ such that $\tan\tau = \Lambda_\perp^{-1}$. With this definition, the width of the laminar Ekman–Hartmann boundary layer $\lambda\mathcal{L}$ varies (see Acheson and Hide, 1973; Desjardins et al., 1999) as

$$\lambda = \sqrt{\frac{2E\tan(\tau/2)}{\cos\theta}}, \tag{6}$$

where

$$\tan(\tau/2) = \frac{\cos\theta}{\Lambda\cos^2\psi + (\Lambda^2\cos^4\psi + \cos^2\theta)^{1/2}}. \tag{7}$$

The boundary layers are obtained by introducing the scaled vertical coordinate $z' = z/\lambda$. Assuming that the limit flow at $z' = \infty$ has the form $\boldsymbol{U}_\infty = (\cos\gamma_0, -\sin\gamma_0, 0)$ and that the magnetic field vanishes at infinity, one obtains (Acheson and Hide, 1973; Benton and Loper, 1969, 1970; Gilman and Benton, 1968; Loper, 1970a,b) a stationary velocity profile (U, V, $W = 0$) and magnetic profile (B_1, B_2, $B_3 = 0$),

$$\begin{aligned}
U(z') &= \cos\gamma_0 - \mathrm{e}^{-z'}\cos\left(z'\tan(\tau/2) + \gamma_0\right),\\
V(z') &= -\sin\gamma_0 + \mathrm{e}^{-z'}\sin\left(z'\tan(\tau/2) + \gamma_0\right),\\
B_1(z') &= -\sqrt{\frac{E\sin\tau}{\cos\theta}}\,\mathrm{e}^{-z'}\\
&\qquad \cos\left(\frac{\tau}{2} + z'\tan(\tau/2) + \gamma_0\right)\cos\psi,\\
B_2(z') &= \sqrt{\frac{E\sin\tau}{\cos\theta}}\,\mathrm{e}^{-z'}\\
&\qquad \sin\left(\frac{\tau}{2} + z'\tan(\tau/2) + \gamma_0\right)\cos\psi.
\end{aligned} \tag{8}$$

So that the velocity at infinity makes an angle $-\gamma_0$ with the x direction (i.e. $\boldsymbol{e}_\theta$).

It should be noted that Loper (1970a,b) demonstrated that this profile does not depend on the conductivity of the outer domain ($\mathcal{D}^c$). This result, however, does not extend to the following sections (instability).

2.2. Ekman–Hartrnann boundary layer instabilities

The laminar Ekman–Hartmann boundary layer profile (8) is known (Gilman, 1971) to be unstable to two-dimensional disturbances for sufficiently high Reynolds number. The relevant number here is the boundary layer Reynolds number, it is defined as the classical Reynolds number ($u\ell/\nu$), but using a typical length scale ℓ based on the boundary layer width, rather than the problem size.

For the Ekman layer at the pole, it is expressed as

$$Re_0 = \varepsilon\sqrt{\frac{2}{E}}. \tag{9}$$

If we now define the local boundary layer Reynolds number Re on the scale λ, we can write

$$Re = \frac{\lambda\varepsilon}{E}. \tag{10}$$

This quantity is constructed on the width of the Ekman–Hartmann boundary layer which varies with θ and Λ. It is, thus, the relevant physical quantity. However, it needs to be compared with the local boundary Reynolds number for the Earth (which depends on latitude). The quantity Re_0 (9) used in Desjardins et al. (1999) is scaled with respect to an arbitrary length: the width of the pure Ekman layer at the poles and can thus be compared with the same quantity for the Earth's core.

In a previous work (Desjardins et al., 1999), we derived analytically a range of Reynolds number for which nonlinear stability holds. More precisely, defining the function Ξ by

$$\Xi(k)=\sqrt{1+k^2}\int_0^{+\infty} z(|\cos(kz)|+|\sin(kz)|)\,\mathrm{e}^{-z}\,\mathrm{d}z, \tag{11}$$

it was shown that if the Reynolds number Re attached to the boundary layer satisfies

$$Re = Re_0\sqrt{\frac{\tan(\tau/2)}{\cos\theta}} < Re_s = \frac{1}{\Xi(\tan(\tau/2))}, \tag{12}$$

the corresponding MHD flow is nonlinearly stable (see Eq. (7) for the definition of $\tan(\tau/2)$ and Fig. 2). Note that $\Xi(k)$ is not defined here as in Desjardins et al. (1999), since we consider the local value of the Reynolds number Re instead of a global estimate Re_0. In our previous study, we concluded that assuming an order one Reynolds number Re_0 for the boundary layer near the CMB, stability could only be demonstrated locally near the poles if the Elsasser number was above unity. Re_s is probably a poor bound on Re. We will now study the linearized problem to establish with accuracy the boundary layer Reynolds number for instability.

Numerical simulations will yield upper bounds Re_i such that if

$$Re > Re_i(\Lambda, \theta), \tag{13}$$

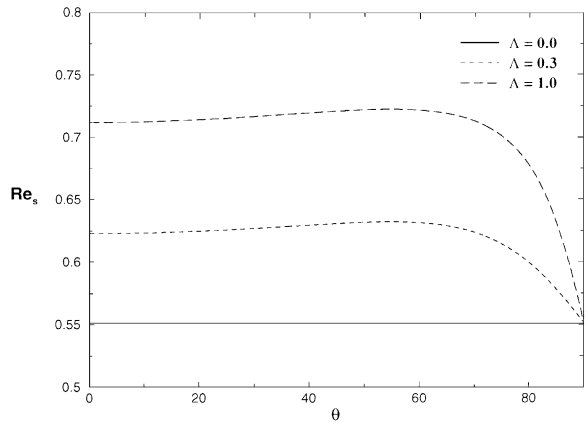

Fig. 2. Representation of an analytical result from our previous study (Re_s), here using present conventions. If the Reynolds number Re attached to the boundary layer is lower than Re_s, non-linear stability is demonstrated. We concentrate in the sequel on boundary layer Reynolds number above Re_s.

the Ekman–Hartmann flow is linearly unstable. We establish that the flow is then unstable in the following sense: there exists arbitrarily small initial perturbations which grow exponentially in time in the linear phase and reach a non negligible size (i.e. the supremum of the difference between the velocities of the perturbed flow and the unperturbed one does not go to 0 as ε goes to 0). However, we do not demonstrate mathematically that the energy of the perturbation grows significantly. The corresponding non-linear analysis is postponed to further study.

In the absence of electromagnetic coupling and for the co-latitude $\theta = 0$, Lilly (1966) showed that the pure Ekman flow is linearly unstable to two-dimensional disturbances when the boundary layer Reynolds number exceeds a critical value ($Re_i \simeq 54.16$). This study was extended to the Ekman–Hartmann profile by Gilman (1971) (still for a horizontal boundary). Leibovich and Lele (1985) extended this approach in the pure Ekman case to a spherical boundary and demonstrated the importance of the horizontal component of $\boldsymbol{\Omega}$. The case of the Ekman–Hartmann layer near a spherical boundary (in the sense $\boldsymbol{\Omega}$ and $\boldsymbol{B}_0$ vary with θ) is addressed in the present work.

A finer estimate than (4) can be achieved for geophysical parameters (Poirier, 1991, 1994; Hulot et al.,

1990). We use the radius of the core as length $\mathcal{L}$ and the following values: $||B_d|| \simeq 5 \times 10^5$ nT, $\rho \simeq 10^4\,\mathrm{kg\,m^{-3}}$, $\mu_0 \simeq 4\pi \times 10^{-7}\,\mathrm{T\,m\,A^{-1}}$, $\eta \simeq 1.1\,\mathrm{m^2\,s^{-1}}$, $\nu \simeq 10^{-6}\,\mathrm{m^2\,s^{-1}}$, $\Omega \simeq 7.3 \times 10^{-5}\,\mathrm{rad\,s^{-1}}$ and $||\boldsymbol{u}|| \simeq 10\,\mathrm{km}$ per year $\simeq 3 \times 10^{-4}\,\mathrm{m\,s^{-1}}$.

This yields the following values for non-dimensional numbers

$$\Lambda \simeq 0.13, \quad \varepsilon \simeq 6 \times 10^{-7}, \quad E \simeq 5.5 \times 10^{-16}, \\ \mathcal{R}_\mathrm{m} \simeq 9.5 \times 10^2, \quad Re_0 \simeq 35.6. \tag{14}$$

A few words on two important simplifications are needed. First, we will neglect large scale electrical currents (corresponding to curl $\boldsymbol{B}_0$) in their interactions with the induced field and second we only consider the dipolar component of the magnetic field (B_d) when constructing $\boldsymbol{B}_0$ and evaluating Λ.

The interaction of small scale currents curl $\boldsymbol{b}$ with large scale field $\boldsymbol{B}_0$ is of order $1/\lambda$. The interaction of large scale currents curl $\boldsymbol{B}_0$ with $\boldsymbol{b}$, however, does not enter this order. Physically, this last term is scaled as $1/L$, where L is based on magnetic diffusion. Clearly for the limits considered here (4) the ratio of viscosity to magnetic diffusivity ($\mathcal{R}_\mathrm{m} E\varepsilon^{-1}$) tends to zero and this effect can be neglected.

The toroidal component of the field can indeed be neglected here, as it needs to vanish near the insulating mantle. Writing the magnetostrophic equilibrium near the core mantle boundary would yield

$$\frac{\partial B_\mathrm{tor}}{\partial r} \sim \mu_0 \rho \frac{2\Omega u}{B_d} \simeq 4 \times 10^{-7}\,\mathrm{T\,m^{-1}}. \tag{15}$$

It is clear that B_tor would remain much smaller than B_d in the area of interest for our study (a few meters thick).

The Elsasser number thus evaluated is lower than unity and the Reynolds number Re_0 greater than 1, it is then reasonable to study precisely the onset of instability, since non-linear stability was not established in Desjardins et al. (1999) for this parameter régime.

2.3. Linearized system

Let us consider linearized perturbations ($\boldsymbol{u}$, p, $\boldsymbol{b}$) of the stationary profile (8). Magnetic perturbations are scaled according to $\boldsymbol{B} = \boldsymbol{e}_B + \mathcal{R}_\mathrm{m}\boldsymbol{b}$. Coordinates are scaled as $x' = \lambda^{-1}x$, $t' = \lambda^{-1}t$. Then, dropping the primes, we obtain

$$\frac{\varepsilon}{\lambda}(\partial_t \boldsymbol{u} + \boldsymbol{U}\cdot\nabla\boldsymbol{u} + \boldsymbol{u}\cdot\nabla\boldsymbol{U}) - \frac{E}{\lambda^2}\Delta\boldsymbol{u} + \frac{\nabla p}{\lambda} \\ = \frac{\Lambda}{\lambda}\mathrm{curl}\,\boldsymbol{b}\times\boldsymbol{e}_B - \boldsymbol{e}_\Omega\times\boldsymbol{u} \\ + \frac{\Lambda\mathcal{R}_\mathrm{m}}{\lambda}(\mathrm{curl}\,\boldsymbol{B}\times\boldsymbol{b} + \mathrm{curl}\,\boldsymbol{b}\times\boldsymbol{B}), \quad \mathrm{div}\,\boldsymbol{u} = 0, \tag{16}$$

$$\frac{R_\mathrm{m}}{\lambda}(\partial_t\boldsymbol{b} + \boldsymbol{U}\cdot\nabla\boldsymbol{b} + \boldsymbol{u}\cdot\nabla\boldsymbol{B} - \boldsymbol{b}\cdot\nabla\boldsymbol{U} - \boldsymbol{B}\nabla\boldsymbol{u}) \\ = \frac{1}{\lambda}\mathrm{curl}(\boldsymbol{u}\times\boldsymbol{e}_B) + \frac{1}{\lambda^2}\Delta\boldsymbol{b}, \quad \mathrm{div}\,\boldsymbol{b} = 0. \tag{17}$$

We will consider perturbations which are plane traveling waves (see Fig. 1) and we will change the reference frame (x, y, z) to (x', y', z) such that x' derivatives of ($\boldsymbol{u}$, p, $\boldsymbol{b}$) vanish. We, therefore, introduce the angle δ between the intersection of the plane of the waves and the plane (x, y) and the projection of e and e' on the plane (x, y).

We then rotate coordinates (x, y) by an angle δ to get (x', y'). In the sequel, the primes of x' and y' are dropped. In this new frame, ($\boldsymbol{u}$, p, $\boldsymbol{b}$) are independent of x, and

$$\boldsymbol{e}_\Omega = (-\sin\theta\cos\delta,\ -\sin\theta\sin\delta,\ \cos\theta),$$

$$\boldsymbol{e}_B = (\sin\psi\cos\delta, \sin\psi\sin\delta, \cos\psi).$$

We use the velocity components u along $\boldsymbol{e}_1'$, the field component b_1 along the same axis scaled as $\tilde{\beta} = b_1/(\lambda\cos\psi)$ and stream function $\tilde{\phi}$ with vector potential $\tilde{\mathcal{X}}$ in the normal plane.

We now take traveling wave type perturbations $\tilde{\phi}$, $\tilde{\mathcal{X}}$, u and $\tilde{\beta}$ as follows:

$$\tilde{\phi}(t, y, z) = \phi(z)\,\mathrm{e}^{i\alpha(y-ct)}, \\ \tilde{\mathcal{X}}(t, y, z) = \mathcal{X}(z)\,\mathrm{e}^{i\alpha(y-ct)}, \\ u(t, y, z) = \mu(z)\,\mathrm{e}^{i\alpha(y-ct)}, \\ \tilde{\beta}(t, y, z) = \beta(z)\,\mathrm{e}^{i\alpha(y-ct)}. \tag{18}$$

The set of differential equations governing these perturbations (demonstration is given in the Appendix A)

can be written as

$$\begin{aligned} & ci\alpha\, Re(\phi'' - \alpha^2\phi) \\ & \quad = -(\phi'''' - 2\alpha^2\phi'' + \alpha^4\phi) \\ & \qquad +2\tan\frac{\tau}{2}(-\mu' + i\alpha\tan\theta\sin\delta\,\mu) \\ & \qquad +i\alpha V\, Re(\phi'' - \alpha^2\phi) - i\alpha\, Re\, V''\phi \\ & \qquad -\left(1-\tan^2\frac{\tau}{2}\right)(\mathcal{X}''' - \alpha^2\mathcal{X}' \\ & \qquad +i\alpha\tan\psi\sin\delta\,(\mathcal{X}'' - \alpha^2\mathcal{X})), \end{aligned} \tag{19}$$

$$\begin{aligned} & ci\alpha\, Re\,\mu \\ & \quad = -(\mu'' - \alpha^2\mu) \\ & \quad +2\tan\frac{\tau}{2}(\phi' - i\alpha\tan\theta\sin\delta\,\phi) \\ & \quad +i\alpha\, Re(V\mu + U'\phi) \\ & \quad -\left(1-\tan^2\frac{\tau}{2}\right)(\beta' + i\alpha\tan\psi\sin\delta\,\beta), \end{aligned} \tag{20}$$

$$i\alpha\tan\psi\sin\delta\mu + \mu' + \beta'' - \alpha^2\beta = 0, \tag{21}$$

$$\begin{aligned} & i\alpha\tan\psi\sin\delta(\phi'' - \alpha^2\phi) \\ & \quad +\phi''' - \alpha^2\phi' + \mathcal{X}'''' - 2\alpha^2\mathcal{X}'' + \alpha^4\mathcal{X} = 0. \end{aligned} \tag{22}$$

The coefficients U and V vary with z, what makes numerical computations necessary. They also depend on γ_0, minimization over γ_0 is, thus, required to get the most unstable configuration.

2.4. Boundary conditions

The system of differential equations expressed above requires 12 boundary conditions. We first state that velocity vanishes at $z = 0$, so that

$$\phi = 0, \qquad \phi' = 0, \qquad \mu = 0 \text{ at } z = 0.$$

Moreover, we assume that the tangential component of the electric field and the magnetic field are continuous across the interface (Roberts, 1967b). In the insulator, we can use the x invariance to write the magnetic field $\boldsymbol{b}$ in terms of $\tilde{\beta}$ and vector potential $\tilde{\mathcal{X}}$, as in Section 2.3, which leads to

$$\begin{aligned} & \Delta_{y,z}\tilde{\mathcal{X}} = 0, \qquad \partial_z\tilde{\beta} = \partial_y\tilde{\beta} = 0, \\ & \partial_z E_1 = \mathcal{R}_{\mathrm{m}}\partial_t\partial_z\tilde{\mathcal{X}}, \qquad \partial_y E_1 = \mathcal{R}_{\mathrm{m}}\partial_t\partial_y\tilde{\mathcal{X}}. \end{aligned}$$

Hence, taking $\boldsymbol{E}$ and $\boldsymbol{b}$ in the insulator as in (18), we deduce

$$E_1 = -i\alpha c\mathcal{R}_{\mathrm{m}}\mathcal{X}, \text{ and } \mathcal{X}'' - \alpha^2\mathcal{X} = 0.$$

In particular, $\mathcal{X}'(0^-) = \alpha\mathcal{X}(0^-)$, and the continuity of E_1 across the interface reduces to

$$\mathcal{X}''(0^+) = \alpha\mathcal{X}(0)(\alpha - ic\mathcal{R}_{\mathrm{m}}).$$

At infinity, we assume, as in Lilly (1966), that $\partial_z u$, $\partial_z v$, w, and $\partial_z^2 b_1$, $\partial_z^2 b_2$, $\partial_z b_3$ vanish, and write

$$\begin{aligned} & \phi = 0, \quad \phi'' = 0, \quad \mu' = 0, \text{ and } \beta'' = 0, \\ & \mathcal{X}' = 0, \quad \mathcal{X}''' = 0 \text{ at infinity.} \end{aligned}$$

Thus, the 12 conditions needed are expressed.

2.5. Relevant equilibria

As stressed in Leibovich and Lele (1985), in the pure Ekman case ($\Lambda = 0$), the θ and δ dependence of system (19–22) only relies on the parameter

$$\xi = \tan\theta\sin\delta.$$

First, it is useful to note that this parameter vanishes in the horizontal plane case. This highlights that though the laminar layer only depends on the normal component of $\boldsymbol{\Omega}$, the instabilities are affected by its horizontal component as well (Leibovich and Lele, 1985). The parameter ξ accounts for this effect.

It should be noted that changing δ into $\pi - \delta$ does not modify ξ, and thus does not affect the Reynolds number. This implies that if $\delta \neq \pi/2$, two instabilities with angles δ and $\pi - \delta$ occur for the same critical Reynolds number.

The minimizing value ξ^* of ξ is obtained in Leibovich and Lele (1985). For $\xi = \xi^*$, the boundary layer Reynolds number for instability (Re_i) is minimal. At low values of θ, $\xi = \xi^*$ cannot be realized and $\delta = \pi/2$ is required to have large values of ξ, as close as possible to ξ^*. Past a critical co-latitude $\theta^* = \mathrm{atan}(\xi^*) \simeq 63.8°$, the value of ξ, and thus, the Reynolds number for instability, can be maintained constant ($\xi = \xi^*$) through a proper variation of the angle δ

$$\delta = \delta_1 = \mathrm{asin}\left(\frac{\xi^*}{\tan\theta}\right),$$

or

$$\delta = \pi - \delta_1.$$

Near the equator, as $\tan\theta$ increases, δ_1 tends to zero, and the rolls get aligned with $\boldsymbol{e}_1$ (north–south).

In the mixed Ekman–Hartmann régime ($\Lambda \neq 0$), relevant to the Earth core, for an arbitrary imposed magnetic field, a similar reasoning leads to introducing

$$\xi' = \tan\psi \sin\delta.$$

The boundary layer Reynolds number for instability is then a function of both ξ and ξ', and the two parameters describe the full θ, ψ, δ dependence. Note that both ξ and ξ' vanish for $\theta = \psi = 0$. The terms, respectively, reflect the role of the horizontal component of $\boldsymbol{\Omega}$ and $\boldsymbol{B}_0$ on the instabilities.

If the imposed field varies in latitude as an axial dipole, ψ and θ are related through (5), so that constant values for ξ and ξ' cannot be maintained through a simple variation of δ, and thus, the critical Reynolds number will not be constant at low latitudes once $\Lambda \neq 0$. Note that neither ξ nor ξ' is affected by a, modification of θ in $\pi + \theta$, however, the profiles (8) are modified and we arbitrarily chose to restrict, our study to one hemisphere: $\theta \in [0, \pi/2]$.

Note also that neither ξ nor ξ' is affected by a modification of δ in $\pi - \delta$. This modification, therefore, leaves the Reynolds number unaffected, as was the case previously in the non-magnetic régime (both angles are unstable for the same boundary layer Reynolds number).

Because we assumed a perfectly dipolar variation of the static magnetic field (Eq. (5)), the value $\theta = \pi/2$ is singular both for the Ekman layer Greenspan (1969) and the Hartmann layer (Roberts, 1967a). As the value of θ increases toward the equator, the stable mixed Ekman–Hartmann boundary layer, however, degenerates to an Ekman layer. Indeed for $(\pi/2 - \theta) < \Lambda^{-1}$ rotation dominates. As a consequence, the equatorial singularity relevant to our study is the Ekman layer singularity. It scales as $E^{1/5}$ in the axial direction and as $E^{2/5}$ in the radial direction (e.g. Kleeorin et al., 1997). Our study is limited by the size of this singularity (which we do not intend to describe here), and thus, to values of θ smaller than $\pi/2 - E^{1/5}$. For geophysically realistic values of E, a thin strip of width 10^{-3} rad near the equator is to be excluded.

The instability Eqs. (19)–(22) in the magnetic régime ($\Lambda \neq 0$) still differ from the simple Ekman equations (i.e. $\Lambda = 0$) near the equator, because of the term associated with the horizontal component of the imposed magnetic field. But, as in the non-magnetic régime, δ must tend to zero (in order to maintain ξ and ξ' finite), also for the field we consider $\tan(\tau/2)$ tends to unity. As a consequence, all magnetic effects vanish near the equator, and the instability itself evolves toward the pure Ekman layer instability. Physically, this is related to the invariance of the pure Ekman layer instability with respect to the direction $\boldsymbol{e}_1$, the horizontal component of the imposed magnetic field lies precisely along this direction near the equator ($\delta = 0$) and does not affect the instability.

3. Numerical results

3.1. Validation

We developed a Fortran-90 code to compute the critical Reynolds number Re above which instabilities appear, resolving Eqs. (19)–(22). Eigenvalues of complex matrices were computed using the EISPACK library from Netlib (http://netlib.bell-labs.com/netlib/eispack). The gradient algorithm was parallelized using the MPI library. Results were tested successfully against previous studies: in the non-magnetic régime (Leibovich and Lele, 1985; Lilly, 1966), as well as in a horizontal plane in the pure Hartmann limit (Roberts, 1967b) and in the mixed Ekman–Hartmann régime (Gilman, 1971).

3.2. Results

We find that the layer is linearly unstable if $Re_0 > Re_i(\Lambda, \theta)$. We represent in Fig. 3 the critical Reynolds number Re_i versus the co-latitude θ, for different values of the Elsasser number $\Lambda \in \{0, 0.3, 1\}$. One can note on this figure that the critical Reynolds number for instability is no longer independent of θ at low latitudes once $\Lambda \neq 0$ as expected from the discussion in Section 2.5.

We can then construct an approximate estimate for the local boundary layer Reynolds number at the CMB

$$Re_{\mathrm{BL}} = \varepsilon\sqrt{\frac{2}{E}}\sqrt{\frac{\tan(\tau/2)}{\cos\theta}}. \tag{23}$$

Note, however, that this estimate is proportional to the estimation on ε, and thus, $\|\boldsymbol{u}\|$. The estimation (14) is based on secular variation studies (Bloxham and Jackson, 1992; Hulot et al., 1990) and represent a

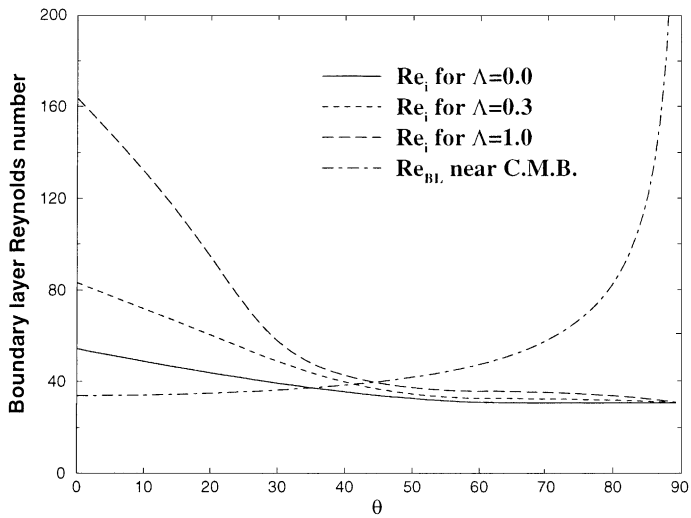

Fig. 3. Boundary layer Reynolds number for instability for three different values of the Elsasser number vs. co-latitude θ. An estimation of the boundary layer Reynolds number near the core–mantle boundary is also represented for comparison.

typical velocity near the CMB. It is clear, however, that the velocity could locally be at least twice as large and could also be several order smaller at other places; the value of Re_{BL} would then undergo the same variations. It is, thus, important to consider Re_{BL} as an estimate only. Re_{BL} computed from (14) and (23) is also represented on Fig. 3.

For the parameter range (14) relevant to the Earth core, there exists a critical co-latitude θ_{c} below which the Ekman–Hartmann boundary layer can be linearly unstable. From the estimated Re_{BL}, one would get $\theta_{\mathrm{c}} \simeq 45°$.

We would like to stress that, we previously established in Desjardins et al. (1999) the value below which non-linear stability could be proven (Re_s). This value being estimated analytically, it probably represents a poor estimate. However, comparing this value (see Fig. 2) with the present results (Re_i), a coefficient close to 50 is obtained for $\Lambda = 0.3$. This much lower value of Re_s could suggest, a possible subcritical bifurcation of the Ekman–Hartmann layer.

Let us now describe physically the instability (for $Re = Re_i$). The angle δ at which the instability grows is represented versus co-latitude θ on Fig. 4. The instability is aligned with the $\boldsymbol{e}_\phi$, direction near the pole for the three Elsasser numbers considered here. Past a critical co-latitude two branches of solution exist, corresponding to δ and $\pi - \delta$, as described in Section 2.5. This critical value of the co-latitude (noted θ^* in the non-magnetic case) decreases with Λ, as the horizontal component of the imposed magnetic field lies in the $\boldsymbol{e}_\theta$ direction and magnetic effects reduce shear in this direction (maximum when $\delta = 90°$). Near the equator, the instability is aligned with $\boldsymbol{e}_\theta$ in the magnetic régime as in the $\Lambda = 0$ case.

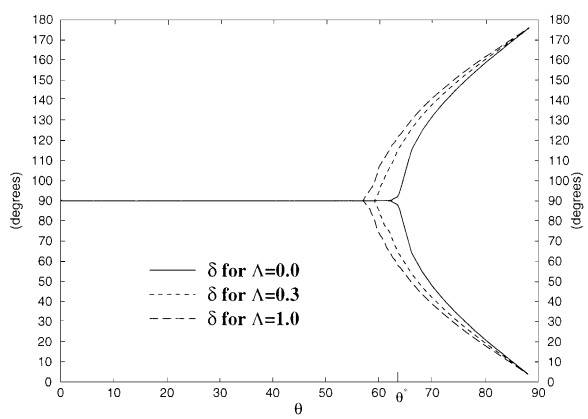

Fig. 4. Angles δ for instability with respect to $\boldsymbol{e}_\theta$ represented vs. the co-latitude θ. The instability develops in the $\boldsymbol{e}_\phi$ direction near the poles. Past a critical co-latitude (decreasing with Λ) two branches of solutions exist. The instability is aligned with $\boldsymbol{e}_\theta$ near the equator.

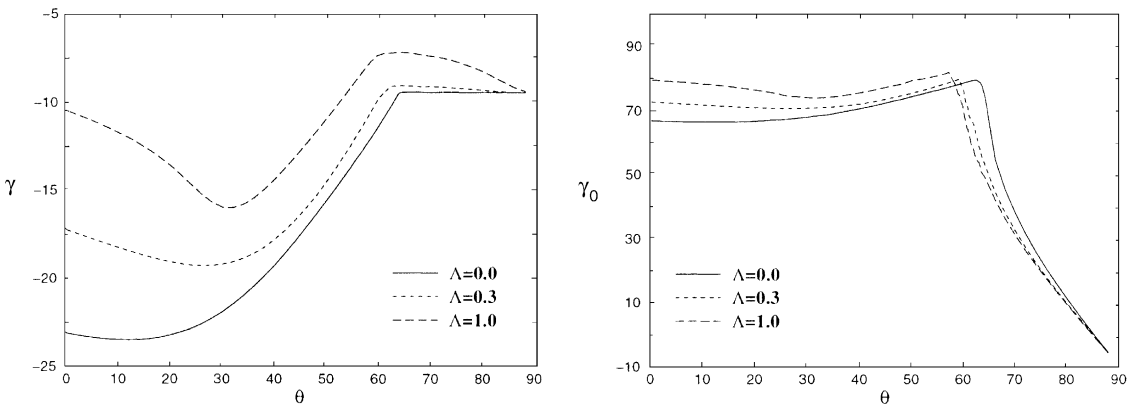

Fig. 5. Angles γ on the left and $\gamma_0 = \delta + \gamma$ (between the $\boldsymbol{e}_\theta$ direction and $\boldsymbol{U}_\infty$) on the right, both represented vs. co-latitude θ.

Angles γ between $\boldsymbol{e}_1'$ and the $\boldsymbol{U}_\infty$ flow corresponding to these instabilities (which enters Eqs. (19)–(22) through the expressions of U and V) are represented in Fig. 5, together with $\gamma_0 = \delta + \gamma$ corresponding to the angle between the $\boldsymbol{e}_\theta$ direction and $\boldsymbol{U}_\infty$ (see also Fig. 1, for angles construction).

The wave number α and the corresponding phase velocity $\alpha \times c_r$ are represented on Fig. 6. The solution propagates in the azimuthal direction in the equatorial region and towards the poles away from the equator.

3.3. Geophysical discussion

When trying to develop an intuitive understanding of the stability of the boundary layer near the Earth's CMB (an Ekman–Hartmann type of boundary layer), one can hesitate between two main lines of thinking. The first one states that the Reynolds number in the core is so high (around 10^8) that, one can hardly imagine anything laminar in the flow. The other lines that the layer is so thin ($\mathcal{L}E^{1/2}$ would represent less than a meter) that instabilities are unlikely to develop there. Probably the first geophysically relevant result of our work is to show how these two effects compensate and how the boundary layer near the core mantle boundary is extremely close to instability.

For geophysically realistic values of the control parameters, a critical band is found to extend over some 45° away from the equator (see Fig. 3). It is, however, useful to recall that Re_{BL} is only an estimate based on

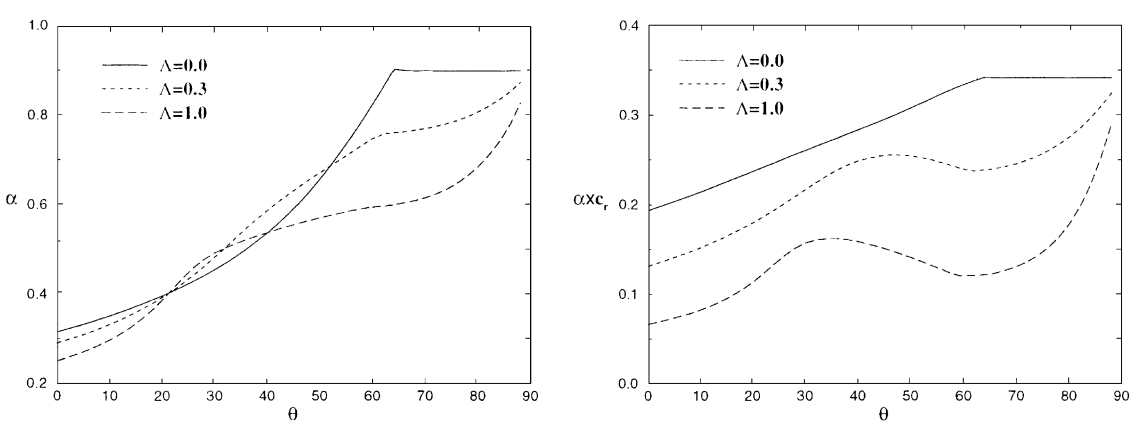

Fig. 6. Wave number α on the left and the corresponding phase velocity $\alpha \times c_r$ on the right, both represented vs. co-latitude θ.

a typical value of $\|\boldsymbol{u}\|$ and that its value is, therefore indicative.

The critical value for instability being so close to geophysical estimates, it appears useful to discuss with additional care the limitations of our study. We computed here the minimal Reynolds number after minimizing on γ (measuring the direction of $\boldsymbol{U}_\infty$). This direction could, in the Earth, be far from optimum. For example, an optimal Re_i, was obtained near the equator for $\gamma_0 = \delta + \gamma \simeq -10^\circ$ whereas in the Earth, flows near the CMB inferred from variations of the magnetic field (Bloxham and Jackson, 1992) are rather found to be aligned in the longitudinal direction near the equator ($\gamma_0 = \delta + \gamma \simeq \pm 90^\circ$). Also, we assumed a perfectly spherical boundary. This, however, seems reasonable as bumps at the CMB are known to be small about 4 km for wavelength larger than 300 km (Garcia and Sourian, 2000) and they would only slightly modify the results. We assumed that the static field varies in latitude as a perfect dipole, this certainly is not the case in the Earth. In particular, as the geographic equator and the magnetic equator would differ almost everywhere the normal component of the field may stabilize the flow near the geographic equator. This effect is, however, expected to be small. We assumed a perfectly insulating mantle. This is a reasonable assumption, as conductivity of the lower mantle is known to be very small (Alexandrescu et al., 1999) and the existence of a thin conductive layer appears most unlikely (Poirier et al., 1998). There are also some physical effects, not included in our model, that could alter the critical boundary layer Reynolds number. In particular effects of density perturbations were neglected. Buoyancy effects could modify the stability of the layer (see Braginsky (1999) for geophysical discussion of density profile near the CMB). Thermal effects could also possibly be associated with current sheets near the insulating mantle, this could help destabilize the layer. Also we insist again that, when comparing results with the estimated boundary Reynolds number near the CMB (Re_{BL}), only an order of magnitude was used for a $\|\boldsymbol{u}\|$. The problem of possible boundary layer instabilities near the CMB clearly deserves further study (especially concerning more complicated large scale fields and the effects of the direction of $\boldsymbol{U}_\infty$ and of the non dipolar component of the field), such study could rely on field map at the CMB and core flows derived from the secular variation of the field. This could also allow to test a possible relation between boundary layer instabilities and rapid geomagnetic impulses (or jerks) observed some eight times in the last century (Alexandrescu et al., 1995, 1996; Courtillot and Le Mouël, 1984; Mac Millan, 1996).

Acknowledgements

We acknowledge extremely useful discussions with Jean-Louis Le Mouël, that helped significantly to improve the manuscript. Authors have also benefited from fruitful discussions with Yann Brenier, Dominique Jault and Gauthier Hulot. E.D. is very grateful to Professor Andrew Soward for enlightening discussions about boundary layers and their singularities. The authors wish to remind that any error in this work would be their responsibility only. Numerical computations were performed on the Alphaservers' Cluster at the D.M.P.N. of Institute de Physique du Globe de Paris.

Appendix A. Mathematical construction of instability equations

Let us first recall that we have assumed in (4) that

$$\varepsilon \to 0, \quad \Lambda \sim \mathcal{O}(1), \quad \varepsilon \mathcal{R}_{\mathrm{m}} \to 0, \quad E \sim \varepsilon^2.$$

and that the magnetic field $\boldsymbol{B}$ was expended as $\boldsymbol{B} = \boldsymbol{e}_B + \mathcal{R}_{\mathrm{m}}\boldsymbol{b}$.

We consider perturbations of the stationary profile (8). However, B_1 and B_2 being of order $E^{1/2}$, only $\boldsymbol{e}_B$ is relevant here.

As $\boldsymbol{b}$ is of order ε, we can rewrite (16)–(17) as

$$Re\left(\partial_t \boldsymbol{u} + V\partial_y \boldsymbol{u} + w\frac{\mathrm{d}U}{\mathrm{d}z}\right) + \frac{\lambda^2}{E}\begin{vmatrix} -v\cos\theta - w\sin\theta\sin\delta \\ u\cos + w\sin\theta\cos\delta \\ -v\sin\theta\cos\delta + u\sin\theta\sin\delta \end{vmatrix} + \frac{\lambda}{E}\begin{vmatrix} 0 \\ \partial_y p - \Delta_{y,z}\boldsymbol{u} \\ \partial_{\boldsymbol{z}} p \end{vmatrix} = \frac{\Lambda\lambda}{E}\begin{vmatrix} \partial_z b_1\cos\psi + \partial_y b_1\sin\psi\sin\delta \\ -\partial_y b_1\sin\psi\cos\delta - j_1\cos\psi \\ -\partial_z b_1\sin\psi\cos\delta + j_1\sin\psi\sin\delta \end{vmatrix} \quad \text{(A.1)}$$

where $j_1 = \partial_y b_3 - \partial_z b_2$, and

$$\lambda(\sin\psi\sin\delta\,\partial_y\boldsymbol{u} + \cos\psi\,\partial_z\boldsymbol{u}) + \Delta_{y,z}\boldsymbol{b} = 0 \quad \text{(A.2)}$$

We will now use the velocity and field components along the axis of instability; in the normal plane, the divergence free condition on $\boldsymbol{u}$ and $\boldsymbol{b}$ yield the existence of a stream function $\tilde{\phi}$ and a vector potential $\tilde{\mathcal{X}}$ such that

$$v = -\partial_z \tilde{\phi}, \qquad w = \partial_y \tilde{\phi},$$
$$b_2 = -\lambda \cos\psi\, \partial_z \tilde{\mathcal{X}}, \qquad b_3 = \lambda \cos\psi\, \partial_y \tilde{\mathcal{X}}.$$

Denoting $\tilde{\beta} = b_1/(\lambda\cos\psi)$, $\tilde{\zeta} = \Delta_{y,z}\tilde{\phi}$ and $\tilde{\eta} = \Delta_{y,z,}\tilde{\mathcal{X}}$ and taking the first component of the curl of Eqs. (A.1) and (A.2), we deduce

$$\begin{aligned} &Re(D_t\tilde{\zeta} + V\partial_y\tilde{\zeta} - V''\partial_y\tilde{\phi}) \\ &\quad + \frac{\lambda^2}{E}(-\cos\theta\,\partial_z u + \sin\theta\sin\delta\,\partial_y u) - \Delta_{y,z}\tilde{\zeta} \\ &= \frac{\lambda^2 \Lambda\cos\psi}{E}(\cos\psi\,\partial_z\tilde{\eta} + \sin\psi\sin\delta\,\partial_y\tilde{\eta}), \end{aligned} \tag{A.3}$$

$$\begin{aligned} &Re(\partial_t u + V\partial_y u + U'\partial_y\tilde{\phi}) \\ &\quad + \frac{\lambda^2}{E}(\cos\theta\,\partial_z\tilde{\phi} - \sin\theta\sin\delta\,\partial_y\tilde{\phi}) - \Delta_{y,z}u \\ &= \frac{\lambda^2 \Lambda\cos\psi}{E}(\cos\psi\,\partial_z\tilde{\beta} + \sin\psi\sin\delta\,\partial_y\tilde{\beta}), \end{aligned} \tag{A.4}$$

$$\sin\psi\sin\delta\,\partial_y u + \cos\psi\,\partial_z u + \cos\psi\,\Delta_{y,z}\tilde{\beta} = 0, \tag{A.5}$$

$$\sin\psi\sin\delta\,\partial_y\tilde{\zeta} + \cos\psi\,\partial_z\tilde{\zeta} + \cos\psi\,\Delta_{y,z}\tilde{\eta} = 0. \tag{A.6}$$

We now take traveling wave type perturbations $\tilde{\phi}$, $\tilde{\mathcal{X}}$, u and $\tilde{\beta}$ as follows:

$$\begin{aligned} &\tilde{\phi}(t,y,z) = \phi(z)\,\mathrm{e}^{i\alpha(y-ct)}, \\ &\tilde{\mathcal{X}}(t,y,z) = \mathcal{X}(z)\,\mathrm{e}^{i\alpha(y-ct)}, \\ &u(t,y,z) = \mu(z)\,\mathrm{e}^{i\alpha(y-ct)}, \\ &\tilde{\beta}(t,y,z) = \beta(z)\,\mathrm{e}^{i\alpha(y-ct)}, \end{aligned} \tag{A.7}$$

and obtain an eigenvalue problem expressed in terms of a system of four ordinary differential equations:

$$\begin{aligned} &ci\alpha\, Re(\phi'' - \alpha^2\phi) \\ &\quad = -(\phi'''' - 2\alpha^2\phi'' + \alpha^4\phi) \\ &\qquad + \frac{\lambda^2}{E}(-\cos\theta\,\mu' + i\alpha\sin\theta\sin\delta\,\mu) \\ &\qquad + i\alpha V\, Re(\phi'' - \alpha^2\phi) - i\alpha\, Re\, V''\phi \\ &\qquad - \frac{\Lambda\lambda^2\cos\psi}{E}(\cos\psi(\mathcal{X}''' - \alpha^2\mathcal{X}') \\ &\qquad + i\alpha\sin\psi\sin\delta(\mathcal{X}'' - \alpha^2\mathcal{X})) \end{aligned} \tag{A.8}$$

$$\begin{aligned} ci\alpha\, Re\,\mu = &-(\mu'' - \alpha^2\mu) \\ &+ \frac{\lambda^2}{E}(\cos\theta\,\phi' - i\alpha\sin\theta\sin\delta\,\phi) \\ &+ i\alpha\, Re(V\mu + U'\phi) \\ &- \frac{\Lambda\lambda^2\cos\psi}{E}(\cos\psi\,\beta' + i\alpha\sin\psi\sin\delta\,\beta), \end{aligned} \tag{A.9}$$

$$i\alpha\sin\psi\sin\delta\,\mu + \cos\psi\,\mu' + \cos\psi(\beta'' - \alpha^2\beta) = 0, \tag{A.10}$$

$$\begin{aligned} &i\alpha\sin\psi\sin\delta(\phi'' - \alpha^2\phi) + \cos\psi(\phi''' - \alpha^2\phi') \\ &\quad + \cos\psi(\chi'''' - 2\alpha^2\chi'' + \alpha^4\chi) = 0 \end{aligned} \tag{A.11}$$

where the expressions $V = V(z)$, $V'' = V''(z)$, $U' = U'(z)$ in the reference frame (e_1', e_2', e_3') are obtained replacing γ_0 by $\gamma = \gamma_0 - \delta$ in (8).

Using the expression $\tan\tau = \cos\theta(\Lambda\cos^2\psi)^{-1} = \Lambda_\perp^{-1}$, the system (A.8)–(A.11) can be rewritten as

$$\begin{aligned} &ci\alpha\, Re(\phi'' - \alpha^2\phi) \\ &\quad = -(\phi'''' - 2\alpha^2\phi'' + \alpha^4\phi) \\ &\qquad + 2\tan\frac{\tau}{2}(-\mu' + i\alpha\tan\theta\sin\delta\,\mu) \\ &\qquad + i\alpha V\, Re(\phi'' - \alpha^2\phi) - i\alpha\, Re\, V''\phi \\ &\qquad - \left(1 - \tan^2\frac{\tau}{2}\right)(\mathcal{X}''' - \alpha^2\mathcal{X}' \\ &\qquad + i\alpha\tan\psi\sin\delta\,(\mathcal{X}'' - \alpha^2\mathcal{X})) \end{aligned} \tag{A.12}$$

$$\begin{aligned} &ci\alpha\, Re\,\mu \\ &\quad = -(\mu'' - \alpha^2\mu) + 2\tan\frac{\tau}{2}(\phi' - i\alpha\tan\theta\sin\delta\,\phi) \\ &\qquad + i\alpha\, Re(V\mu + U'\phi) - \left(1 - \tan^2\frac{\tau}{2}\right) \\ &\qquad \times(\beta' + i\alpha\tan\psi\sin\delta\,\beta) \end{aligned} \tag{A.13}$$

$$i\alpha \tan\psi \sin\delta\mu + \mu' + \beta'' - \alpha^2\beta = 0, \tag{A.14}$$

$$i\alpha \tan\psi \sin\delta(\phi'' - \alpha^2\phi) + \phi''' - \alpha^2\phi' + \mathcal{X}'''' - 2\alpha^2\mathcal{X}'' + \alpha^4\mathcal{X} = 0 \tag{A.15}$$

References

Acheson, D.J., Hide, R., 1973. Hydromagnetics of rotating fluids. Rep. Prog. Phys. 36, 159–221.

Alexandrescu, M., Gibert, D., Hulot, G., Le Mouël, J.-L., Saracco, G., 1995. Detection of geomagnetic jerks using wavelet analysis. J. Geophys. Res. 100 (B7), 12557–12572.

Alexandrescu, M., Gibert, D., Hulot, G., Le Mouël, J.-L., Saracco, G., 1996. Worldwide wavelet analysis of geomagnetic jerks. J. Geophys. Res. 101 (B10), 21975–21994.

Alexandrescu, M., Gibert, D., Le Mouël, J.-L., Hulot, G., Saracco, G., 1999. An estimate of average lower mantle conductivity by wavelet analysis of geomagnetic jerks. J. Geophys. Res. 104 (B8), 17735–17745.

Benton, E., Loper, D., 1969. On the spin-up of an electrically conducting fluid, Part 1. J. Fluid Mech. 39 (3), 561–586.

Benton, E., Loper, D., 1970. On the spin-up of an electrically conducting fluid, Part 2. J. Fluid Mech. 43 (4), 785–799.

Bloxham, J., Jackson, A., 1992. Time-dependent mapping of the magnetic field at the core–mantle boundary. J. Geophys. Res. 97, 19536–19563.

Braginsky, S.I., 1999. Dynamics of the stably stratified ocean at the top of the core. Phys. Earth Planet. Interiors 11 (1/2), 21–34.

Busse, F., Grote, E., Tilgner, A., 1999. On convection driven dynamos in rotating spherical shells. Studia Geophys. Geodyn. 42, 211–223.

Christensen, U., Olson, P., Glatzmaier, G., 1999. Numerical modelling of the geodynamo: a systematic parameter study. Geophys. J. Interiors 138, 393–409.

Courtillot, V., Le Mouël, J.-L., 1984. Geomagnetic secular variation impulses. Nature 311, 709–716.

Desjardins, B., Dormy, E., Grenier, E., 1999. Stability of mixed Ekman–Hartmann boundary layers. Nonlinearity 12, 181–199.

Dormy, E., Cardin, P., Jault, D., 1998. MHD flow in a slightly differentially rotating spherical shell, with conducting inner core, in a dipolar magnetic field. Earth Planet. Sci. Lett. 160, 15–30.

Dormy, E., Valet, J.-P., Courtillot, V., 2000. Numerical models of the Geodynamo and observational constraints. Geochem.-Geophys.-Geosyst. 1, 62.

Garcia, R., Souriau, A., 2000. Amplitude of the core–mantle boundary topography estimated by stochastic analysis of core phases. Phys. Earth and Planet. Interiors 117 (1/4), 345–359.

Gilman, P., Benton, E., 1968. Influence of an axial magnetic field on the steady linear Ekman boundary layer. Phys. Fluids 11, 2397–2401.

Gilman, P., 1971. Instabilities of the Ekman–Hartmann boundary layer. Phys. Fluids 14, 7–12.

Greenspan, H.P., 1969. The Theory of Rotating Fluids. Cambridge Monographs on Mechanics and Applied Mathematics, Cambridge.

Hulot, G., Le Mouël, J.-L., Jault, D., 1990. The flow at the core–mantle boundary: symmetry properties. J. Geomagn. Geoelectr. 42, 857–974.

Katayama, J., Matsushima, M., Honkura, Y., 1999. Some characteristics of magnetic field behavior in a model of MHD dynamo thermally driven in a rotating spherical shell. Phys. Earth Planet. Interiors 111, 141–159.

Kleeorin, N., Rogachevskii, I., Ruzmaikin, A., Soward, A.M., Starchenko, S., 1997. Axisymmetric flow between differentially rotating spheres in a dipole magnetic field. J. Fluid Mech. 344, 213–244.

Kuang, W., Bloxham, J., 1997. An Earth-like numerical dynamo model. Nature 389, 371–374.

Kuang, W., Bloxham, J., 1999. Numerical modeling of magnetohydrodynamic convection in a rapidly rotating spherical shell: weak and strong field dynamo action. J. Comput. Phys. 153, 51–81.

Leibovich, S., Lele, S.K., 1985. The influence of the horizontal component of the Earth's angular velocity on the instability of the Ekman layer. J. Fluid Mech. 150, 41–87.

Lilly, D.K., 1966. On the instability of the Ekman boundary layer. J. Atmos. Sci. 23, 481–494.

Loper, D., 1970a. General solution for the linearized Ekman–Hartmann layer on a spherical boundary. Phys. Fluids 13, 2995–2998.

Loper, D., 1970b. Steady hydromagnetic boundary layer near a rotating, electrically conducting plate. Phys. Fluids 13, 2999–3002.

Mac Millan, S., 1996. A geomagnetic jerk for the early 1990's. Earth Planet. Sci. Lett. 137, 189–192.

Poirier, J.-P., 1991. Introduction to the Physics of the Earth's Interior. Cambridge University Press, Cambridge.

Poirier, J.-P., 1994. Physical properties of the Earth's core. C. R. Acad. Sci. Paris 318, 341–350.

Poirier, J.-P., Malavergue, V., Le Mouël, J.-L., 1998. Is there a thin electrically conducting layer at the base of the mantle? In: The Core–Mantle Boundary Region, Vol. 28. AGU Geodynamics, pp. 131–137.

Ponty, Y., Gilbert, A.D., Soward, A.M., 2000. Kinematic dynamo action in flows driven by shear and convection. J. Fluid Mech., submitted for publication.

Roberts, P.H., 1967a. Singularity of Hartmann layers. Proc. R. Soc. A 300, 94–107.

Roberts, P.H., 1967b. An Introduction to Magnetohydrodynamics. Elsevier, Amsterdam.

Sakuraba, A., Kono, M., 1999. Effect of the inner core on the numerical solution of the magnetohydrodynamic dynamo. Phys. Earth Planet. Interiors 111, 105–121.

ELSEVIER

Physics of the Earth and Planetary Interiors 128 (2001) 25–34

PHYSICS OF THE EARTH AND PLANETARY INTERIORS

www.elsevier.com/locate/pepi

A numerical dynamo benchmark

U.R. Christensen [a,*], J. Aubert [b], P. Cardin [b], E. Dormy [c], S. Gibbons [d], G.A. Glatzmaier [e], E. Grote [f], Y. Honkura [g], C. Jones [d], M. Kono [h], M. Matsushima [g], A. Sakuraba [i], F. Takahashi [g], A. Tilgner [f], J. Wicht [a], K. Zhang [d]

[a] *Institut für Geophysik, Universität Göttingen, Herzberger Landstrasse 180, 37075 Göttingen, Germany*
[b] *LGIT, Observatoire des Sciences de l'Univers de Grenoble, B.P. 53, 38041 Grenoble Cedex 09, France*
[c] *Institut de Physique du Globe de Paris, 4 Place Jussieu, 75252 Paris Cedex 05, France*
[d] *Department of Mathematics, University of Exeter, Exeter EX4 4QE, UK*
[e] *Earth Sciences Department, University of California, Santa Cruz, CA 95064, USA*
[f] *Theoretische Physik IV, Universität Bayreuth, 95440 Bayreuth, Germany*
[g] *Department of Earth and Planetary Sciences, Tokyo Institute of Technology, 2-12-1 Ookayama, Meguro-ku, Tokyo 152-8551, Japan*
[h] *Institute for Study of the Earth's Interior, Okayama University, Yamada 827, Misasa, Tottori-ken 682-0193, Japan*
[i] *Department of Earth and Planetary Physics, University of Tokyo, Hongo 7-3-1, Bunkyo-ku, Tokyo 113-0033, Japan*

Received 31 December 2000; accepted 14 August 2001

Abstract

We present the results of a benchmark study for a convection-driven magnetohydrodynamic dynamo problem in a rotating spherical shell. The solutions are stationary aside from azimuthal drift. One case of non-magnetic convection and two dynamos that differ in the assumptions concerning the inner core are studied. Six groups contributed numerical solutions which show good agreement. This provides an accurate reference standard with high confidence. © 2001 Elsevier Science B.V. All rights reserved.

Keywords: Geodynamo; Numerical modeling

1. Introduction

In recent years, three-dimensional simulations of convection-driven magnetohydrodynamic dynamos in rotating spherical shells have become possible and are progressively employed to develop an understanding for the origin of the Earth's magnetic field and its spatial and temporal structure. The first models employed hyperdiffusivities and either neglected inertia or included only the axisymmetric part (Glatzmaier and Roberts, 1995; Kuang and Bloxham, 1997) or they assumed somewhat artificial boundary conditions for the magnetic field Kageyama and Sato (1995). Later models with more moderate values of the control parameters did not use these approximations (for example, Christensen et al., 1998; Busse et al., 1998; Christensen et al., 1999; Katayama et al., 1999; Grote et al., 2000). Several numerical codes for dynamo modelling have been developed independently by various groups, although they usually follow similar principles. The velocity and magnetic fields are represented by poloidal and toroidal scalar potentials and all the unknowns are expanded in spherical harmonic functions in the angular coordinates. Diffusive

* Corresponding author. Tel.: +49-551-39-7451; fax: +49-551-39-7459.
E-mail address: urc@uni-geophys.gwdg.de (U.R. Christensen).

0031-9201/01/$ – see front matter © 2001 Elsevier Science B.V. All rights reserved.
PII: S0031-9201(01)00275-8

terms in the equations are treated implicitly during time-stepping, while the non-linear terms are evaluated on grid points, which requires transformations between spectral and grid space (spectral transform method). The codes differ mainly in their treatment of the radial dependence and in the way the arising boundary value problems for each harmonic mode are solved. Some expand the variables in Chebyshev polynomials and use collocation methods, while others use finite differencing and grid representation. An exception is the method by Kageyama and Sato (1995), who have used finite differences throughout. Other codes that employ only local representations of the variables, for example by finite elements, are currently under development.

The verification of newly developed codes for complex nonlinear problems is not a simple task. Rigorous testing with analytical solutions is not possible for the fully non-linear problem. Comparison with other published solutions is difficult because they usually show chaotic time-dependence and because they make specific assumptions (for example, on boundary conditions or neglected terms), which are not implemented in other codes. The concept of a benchmark is to set up a simple, well defined and easily reproduced standard solution, which is confirmed by several independent codes and which is converged to great accuracy. It serves several purposes: (i) to increase the confidence in the correctness of the codes that contribute to the benchmark, (ii) to assess the accuracy and possibly the run-time performance of existing methods, and (iii) to assist future code developments by providing a well-established standard solution for verification.

The present benchmark was proposed at the study of the Earth's deep interior (SEDI) meeting of 1998 in Tours and has been expanded and modified as a result of discussions among the participants. Its basis is one of the few quasi-stationary dynamo solutions that have been reported in the literature (Christensen et al., 1999). The stationarity allows the comparison of well-defined numbers. Parameter values are moderate, so that high resolution is not required to reproduce the dynamo. The full inertia term is kept in the momentum equation and the concept of hyperdiffusivity is not used. In addition to the originally proposed dynamo with an insulating inner core co-rotating with the outer boundary (case 1), the cases of rotating non-magnetic convection (case 0) and that of a dynamo with a conducting and freely rotating inner core (case 2) have been added. Aside from global properties, such as kinetic and magnetic energies, where small inaccuracies may average out, some local values of the solution are also reported.

2. Definition of the benchmark cases

Thermal convection and magnetic field generation in a rotating spherical shell filled with an electrically conducting fluid are considered. The ratio of inner radius r_i to outer radius r_o is set to 0.35. Temperature is fixed to T_o and $T_\mathrm{o} + \Delta T$ on the outer and inner boundaries, respectively. The Boussinesq approximation is used and gravity varies linearly with radius. The equations are scaled with $D = r_\mathrm{o} - r_\mathrm{i}$ as the fundamental length scale, which makes the dimensionless radii equal to $r_\mathrm{o} = 20/13$ and $r_\mathrm{i} = 7/13$. The time scale is D^2/ν, with ν the kinematic viscosity, ν/D is the scale for velocity $\boldsymbol{u}$, and ΔT for temperature T. The scaled temperature on the outer boundary is zero. Magnetic induction $\boldsymbol{B}$ is scaled by $(\rho\mu\eta\Omega)^{1/2}$, where ρ is the density, μ the magnetic permeability, η the magnetic diffusivity, and Ω is the basic rotation rate about the z-axis. The non-hydrostatic pressure P is scaled by $\rho\nu\Omega$. The scaled equations are

$$E\left(\frac{\partial \boldsymbol{u}}{\partial t} + \boldsymbol{u}\cdot\nabla\boldsymbol{u} - \nabla^2\boldsymbol{u}\right) + 2\hat{z}\times\boldsymbol{u} + \nabla P = Ra\frac{\boldsymbol{r}}{r_\mathrm{o}}T + \frac{1}{Pm}(\nabla\times\boldsymbol{B})\times\boldsymbol{B} \tag{1}$$

$$\frac{\partial \boldsymbol{B}}{\partial t} = \nabla\times(\boldsymbol{u}\times\boldsymbol{B}) + \frac{1}{Pm}\nabla^2\boldsymbol{B} \tag{2}$$

$$\frac{\partial T}{\partial t} + \boldsymbol{u}\cdot\nabla T = \frac{1}{Pr}\nabla^2 T \tag{3}$$

$$\nabla\cdot\boldsymbol{u} = 0, \quad \nabla\cdot\boldsymbol{B} = 0 \tag{4}$$

Non-dimensional control parameters are the modified Rayleigh number

$$Ra = \frac{\alpha g_\mathrm{o}\,\Delta T\,D}{\nu\Omega} \tag{5}$$

where α is the thermal expansion coefficient and g_o gravity at the outer radius, the Ekman

number

$$E = \frac{\nu}{\Omega D^2}, \tag{6}$$

the Prandtl number

$$Pr = \frac{\nu}{\kappa}, \tag{7}$$

where κ is thermal diffusivity, and the magnetic Prandtl number

$$Pm = \frac{\nu}{\eta}. \tag{8}$$

The velocity vanishes on the rigid boundaries, relative to the state of rotation of the respective boundary. In cases 0 and 1, the inner and outer boundaries co-rotate. In case 1, the regions outside the fluid shell are electrical insulators and the magnetic field on the boundaries matches with appropriate potential fields in the exterior that imply no external sources of the field.

In case 2, the inner core is treated as an electrically conducting rigid sphere that can rotate around the z-axis relative to the outer boundary, which provides the frame of reference. Its moment of inertia is determined assuming the same density as in the liquid shell, and its angular acceleration results from viscous and magnetic torques. The moment of inertia is irrelevant for the final uniform rotation of the inner core, but influences the transient spinup. In the inner core Eq. (2) applies with the velocity field of rigid-body rotation and the same magnetic Prandtl number, i.e. the same electrical conductivity and magnetic permeability as in the fluid shell. At the boundary between inner core and fluid shell the magnetic field and the horizontal component of the electrical field are continuous.

The Ekman number is $E = 10^{-3}$ and the Prandtl number is $Pr = 1$ in all cases. In cases 0 and 1, we set the Rayleigh number to $Ra = 100$. In case 2, it is $Ra = 110$, which is approximately two times supercritical. The magnetic Prandtl number is zero in case 0 (non-magnetic convection) and is $Pm = 5$ in cases 1 and 2.

Because only the final quasi-stationary solutions are compared, the initial condition is, strictly speaking, not part of the benchmark definition. However, because non-magnetic convection is found stable against small magnetic perturbations at these parameters and because the dynamo solutions seem to have only a small basin of attraction, the initial state is of some concern. Also the existence of multiple dynamo solutions, for example with different azimuthal symmetry, cannot be ruled out. Here, we recommend a set of initial conditions, but any other conditions that lead to the desired solutions are also permissible. In all cases the initial velocity is zero and the initial temperature is

$$T = \frac{r_o r_i}{r} - r_i + \frac{210A}{\sqrt{17920\pi}} \times (1 - 3x^2 + 3x^4 - x^6)\sin^4\theta\cos 4\phi \tag{9}$$

where θ is the colatitude, ϕ the longitude, and $x = 2r - r_i - r_o$. This describes a conductive state with a perturbation of harmonic degree and order four superimposed. The amplitude is set to $A = 0.1$. In case 1, the initial magnetic field is for $r_i \le r \le r_o$:

$$B_r = \frac{5}{8}\left(8r_o - 6r - 2\frac{r_i^4}{r^3}\right)\cos\theta \tag{10}$$

$$B_\theta = \frac{5}{8}\left(9r - 8r_o - \frac{r_i^4}{r^3}\right)\sin\theta \tag{11}$$

$$B_\phi = 5\sin(\pi(r - r_i))\sin 2\theta. \tag{12}$$

This corresponds to a dipolar poloidal field created by a current density in the ϕ-direction which is uniform in radius and a superimposed toroidal field of harmonic degree two. The maximum value of both B_r and B_ϕ is 5. In case 2, the initial magnetic field is for $0 \le r \le r_o$:

$$B_r = 5\frac{4r_o - 3r}{3 + r_o}\cos\theta \tag{13}$$

$$B_\theta = 5\frac{9r - 8r_o}{2r_o + 6}\sin\theta \tag{14}$$

$$B_\phi = 5\sin\left(\pi\frac{r}{r_o}\right)\sin 2\theta. \tag{15}$$

3. Character of the solution

Starting from the recommended initial condition, a quasi-stationary solution is reached within approximately 15 time units in cases 1 and 2 and within 1.2 time units in case 0. The solution can be expressed by a vector function of the form

$$(\boldsymbol{u}, \boldsymbol{B}, T) = \boldsymbol{f}(r, \theta, \phi - \omega t) \tag{16}$$

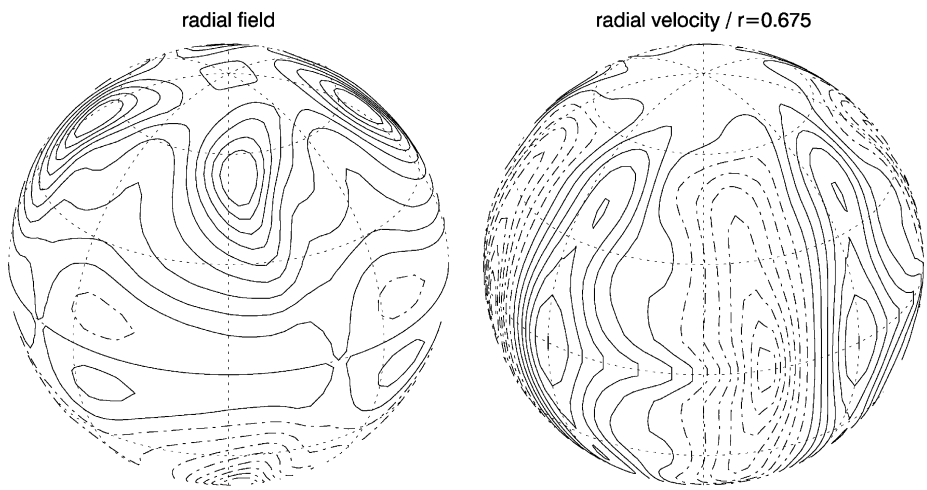

Fig. 1. Case 1: left, contours of B_r on outer boundary in steps of 0.25; right, contours of u_r at mid-depth in the shell, interval 2. Positive and zero contours solid lines, negative contours dash-dotted.

with ω being the drift frequency. In case 2, the inner core rotates at a uniform rate $\omega_{\rm ic}$ with respect to the outer boundary after the initial transient. The solutions are symmetric about the equator (dipole parity) and have fourfold symmetry in longitude. In order to reduce computer time, in some calculations this symmetry has been exploited by restricting the spherical harmonic expansions accordingly. This is safe because tests show that the solution is stable against small symmetry-breaking perturbations. Some aspects of the solution for case 1 are visualised in Fig. 1. Convection is columnar and the magnetic field on the outer boundary is strongly dipolar and dominated by four flux lobes. The figure shows a result obtained with moderate resolution and is meant for illustrative purposes only. The presence of a conducting and rotating inner core in case 2 has no strong effect of the overall pattern of the solution.

4. Requested data

Global averages as well as local data at a specific point are compared in this benchmark. In all cases, the drift frequency ω and the mean kinetic energy density in the fluid have been calculated as

$$E_{\rm kin} = \frac{1}{2V_{\rm s}}\int_{V_{\rm s}} \boldsymbol{u}^2\,{\rm d}V \tag{17}$$

where $V_{\rm s}$ refers to the volume of the fluid shell. In cases 1 and 2, the mean magnetic energy density in the shell is calculated as

$$E_{\rm mag} = \frac{1}{2V_{\rm s}EPm}\int_{V_{\rm s}} \boldsymbol{B}^2\,{\rm d}V. \tag{18}$$

In case 2, also the magnetic energy density $E^{\rm ic}_{\rm mag}$ in the inner core, defined equivalently to Eq. (18) for the inner core volume $V_{\rm ic}$, and the angular frequency $\omega_{\rm ic}$ of differential rotation of the inner core are requested. When participants compared preliminary results in the course of the benchmark study, the torque acting on the inner core turned out to be useful to identify errors. Therefore we also list the values of the Lorentz torque $\Gamma_{\rm L}$ scaled by $\rho D\nu^2$.

Defining a point where local data are to be taken is not trivial because it must be fixed in the drifting frame of reference. We take a point at mid-depth ($r = (r_{\rm i} + r_{\rm o})/2$) in the equatorial plane ($\theta = \pi/2$) whose ϕ-coordinate is given by the conditions $u_r = 0$ and $(\partial u_r/\partial\phi) > 0$. For this point we request in cases 0 and 1 the values of T and u_ϕ and additionally in case 1 the value of B_θ.

5. Methods

Six groups have contributed results to some or all of the benchmark cases. Here, each code is described briefly by some keywords. A more complete description can be found in the supplied references.

Aubert, Cardin and Dormy (ACD): Spherical harmonic expansion, finite differences in the radial direction (Dormy et al., 1998). The radial mesh interval decreases in geometrical progression towards the boundaries. Three-point stencil for second-order derivatives and five-point stencil for biharmonic operators (second-order accurate). Symmetry in longitude can be imposed.

Christensen, Wicht and Glatzmaier (CWG): Spherical harmonic expansion, Chebyshev polynomials in radial direction, alias-free transform (Glatzmaier, 1984; Christensen et al., 1999); the basic numerical method was also used in (Glatzmaier and Roberts, 1995). Symmetry in longitude assumed in most cases. Time step dynamically controlled, typically 1.5×10^{-4} at low spatial resolution and 0.75×10^{-4} at high resolution. Different versions of this code have been run on the benchmark problems by Christensen and Wicht and by Glatzmaier, respectively. Results obtained by Glatzmaier are marked by an asterisk (*).

Gibbons, Jones and Zhang (GJZ): Spherical harmonic expansion, finite-differencing in radial direction with non-equidistant grid using the Chebyshev zeros as grid points and a seven-point stencil for all derivatives.

Kono and Sakuraba (KS): Spherical harmonic expansion, Chebyshev tau method (Canuto et al., 1987) for radial coordinate (Sakuraba and Kono, 1999).

Tilgner and Grote (TG): Spherical harmonic expansion, Chebyshev polynomials in radial direction (Busse et al., 1998; Tilgner, 1999).

Takahashi, Matsushima and Honkura (TMH): Spherical harmonic expansion, finite difference with option for equidistant or non-uniform grid (Chebyshev points) in radial direction. Pressure defined on staggered grid points. Three-point stencil used for second-order derivatives and four-point stencil for derivatives at staggered grid points. Longitudinal symmetry exploited.

The three codes which use an expansion in Chebyshev polynomials in the radial direction (CWG, KS and TG) are structured very similarly. The three codes using finite differences in the radial direction (ACD, GJZ and TMH) differ for example in the order of the difference scheme and the structuring of the radial grid.

Most groups provide results at different resolution. All use 8-byte words (double precision). The spherical harmonic expansion is truncated at degree $\ell_{\max}$ and order $m_{\max}$. Most contributors include all terms with harmonic order $m \le \ell \le \ell_{\max}$ ($m_{\max} = \ell_{\max}$, triangular truncation), except GJZ, who truncate in most cases at $m \le \min(\ell, m_{\max})$ with $m_{\max} < \ell_{\max}$ (trapezoidal truncation). The minimum necessary number of grid points in θ-direction (Gauss points), on which non-linear products are calculated, is $\ell_{\max} + 1$, but some authors use a larger number of points N_θ to reduce aliasing effects (similarly in ϕ-direction). For alias-free computations of the non-linear terms N_θ needs to be equal or greater than $(3\ell_{\max} + 1)/2$ and for triangular truncation of the spherical harmonics the number of grid points in longitude needs to be twice this. In those codes which use a spectral representation in the radial direction, the number of radial grid points N_r may exceed the number of Chebyshev modes N_c, although in the present cases $N_r \simeq N_c$ has been used.

6. Results

At a qualitative level, all contributors obtain the same generic solutions, which is the prerequisite for a quantitative comparison and a convergence test. In order to compare specific numbers obtained with different codes at different resolution and in order to monitor convergence, we define as resolution R the third root of the number of degrees of freedom for each scalar variable:

$$R = N_r^{1/3}(\ell_{\max}[2m_{\max} + 1] - m_{\max}^2 + m_{\max} + 1)^{1/3}. \tag{19}$$

For $m_{\max} = \ell_{\max}$ this reduces to $R = N_r^{1/3}(\ell_{\max} + 1)^{2/3}$. In case 2, N_r refers to the combined number of radial points in the fluid shell and in the inner core.

6.1. Non-magnetic convection (case 0)

All results for case 0 are listed in Table 1. In Fig. 2, we compare most of the results as functions of R. Note that for each quantity except ω the range in the diagram is less than 2% of the absolute value. That is, all results that fall into the diagram agree within better than 2%. All results seem to converge towards the same point. The convergence is clearest for the fully spectral code by CWG (circles), where results at comparatively low resolution differ only marginally from those with high

Table 1
Results for benchmark case 0[a]

Group	N_r	N_θ	ℓ_{max}	E_{kin}	T	u_ϕ	ω
ACD	50	46	44	58.970	0.4259	−10.058	0.0602
ACD	100	46	44	58.515	0.4276	−10.134	0.1509
ACD	150	46	44	58.426	0.4279	−10.147	0.1686
ACD	250	92	44	58.379	0.4280	−10.153	0.1775
CWG	25	48	32	58.3499	0.42812	−10.1570	0.18283
CWG	33	80	53	58.3481	0.42811	−10.1571	0.18241
CWG*	49	96	63	58.3488	0.42811	−10.1570	0.18241
CWG	65	128	84	58.3480	0.42812	−10.1571	0.18241
GJZ	40	38	36 (20)	58.2208	0.42808	−10.1547	0.19198
GJZ	60	42	40 (28)	58.2955	0.42813	−10.1560	0.19010
GJZ	100	42	40 (28)	58.3348	0.42816	−10.1558	0.18289
TMH	40		36	58.5874	0.4271	−10.0823	0.1228
TMH	100		36	58.4028	0.4279	−10.1421	0.1670
TMH	100*e*		36	58.5471	0.4281	−10.1585	0.1560

[a] Notation: *e*, equidistant radial grid; m_{max} given in parentheses after ℓ_{max} when different.

resolution. Also the contributions by ACD (diamonds), GJZ (squares) and TMH (crosses) with radial finite differencing converge satisfactorily towards the same values at high R. For the finite difference methods the radial resolution has been found to be critical, and in fact the angular resolution has been kept constant or varied little in these calculations. ACD and GJZ report that results for a uniform radial grid (not shown in this paper) are much worse than for the non-uniform grids used here. The comparison supplied by TMH for $N_r = 100$ confirms this for E_{kin} and ω, although the differences are rather moderate. A non-uniform grid provides better resolution in the boundary layers, and even though the Ekman layer is not very thin at the moderate value of the Ekman number, good resolution of this layer seems to be essential.

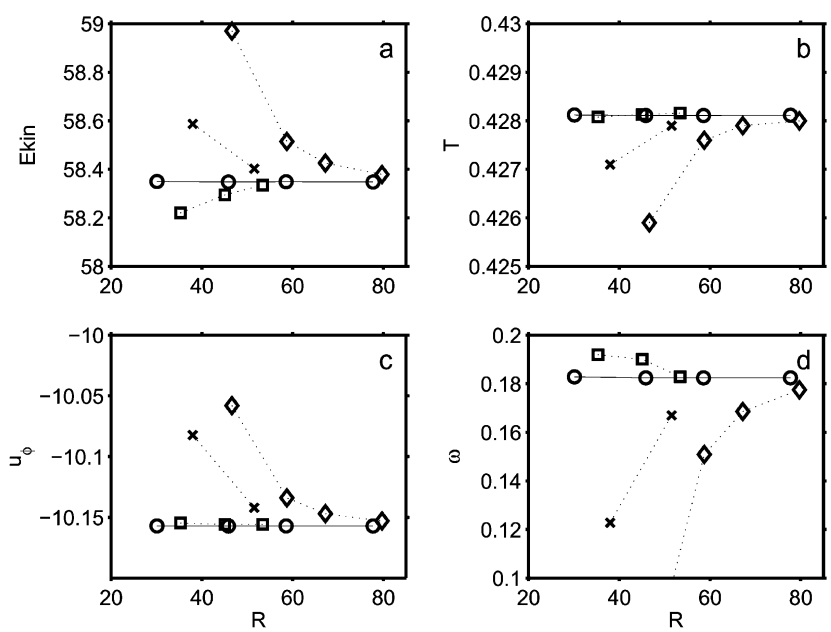

Fig. 2. Convergence of results for case 0: diamonds, ACD; circles, CWG; squares, GJZ; crosses, TMH. (a) Kinetic energy, (b) local temperature, (c) local azimuthal velocity, (d) drift frequency.

Table 2
Results for benchmark case 1[a]

Group	N_r	N_θ	ℓ_{max}	E_{kin}	E_{mag}	T	u_ϕ	B_θ	ω
ACD	48	46	44	29.965	601.912	0.3730	−7.864	−4.779	−3.038
ACD	90	46	44	30.637	623.204	0.3729	−7.669	−4.912	−3.102
ACD	150	46	44	30.732	625.681	0.3730	−7.634	−4.929	−3.105
ACD	200	92	44	30.758	626.284	0.3730	−7.626	−4.933	−3.105
CWG	21	40	26	30.5015	616.085	0.36281	−7.2228	−4.8456	−3.0926
CWG	25	48	32	30.7214	626.572	0.37373	−7.5941	−4.9023	−3.0852
CWG	33	64	42	30.7686	626.420	0.37390	−7.6427	−4.9358	−3.1011
CWG	33	80	53	30.7714	626.406	0.37325	−7.6211	−4.9285	−3.1016
CWG	41	96	64	30.7715	626.416	0.37337	−7.6250	−4.9288	−3.1016
CWG*	49	96	63	30.7716	626.413	0.37337	−7.6255	−4.9284	−3.1016
CWG	65	128	85	30.7734	626.409	0.37338	−7.6250	−4.9289	−3.1017
GJZ	40	38	36 (20)	30.1263	617.462	0.36226	−7.0899	−4.8972	−2.992
GJZ	40	52	50 (44)	30.5724	622.558	0.37314	−7.6201	−4.9101	−3.083
GJZ	80	52	50 (44)	30.7541	625.656	0.37325	−7.6203	−4.9301	−3.100
GJZ	100	54	52 (52)	30.7605	626.020	0.37336	−7.6308	−4.9232	−3.101
GJZ	150	78	50 (44)	30.7677	626.282	0.37328	−7.6210	−4.9333	−3.101
KS	48	64	42	30.7709	626.434	0.37376	−7.6376	−4.9333	−3.1009
TG	33	64	42	30.7695	626.402	0.37378	−7.6387	−4.9340	−3.0997
TMH	70*e*		26	31.0298	623.092	0.3679	−7.3525	−4.9220	−3.0949
TMH	70		26	30.7901	627.607	0.3675	−7.3330	−4.9190	−3.0735

[a] Notation: *e*, equidistant radial grid; m_{max} in parentheses after ℓ_{max} when different.

6.2. Dynamo with insulating inner core (case 1)

Results for case 1 are listed in Table 2 and some of them are plotted against resolution in Fig. 3. Again the agreement among the various contributions is very satisfactory; the range covered in each of the diagrams is only 1% of the total value. The general agreement is particularly good between the three codes using

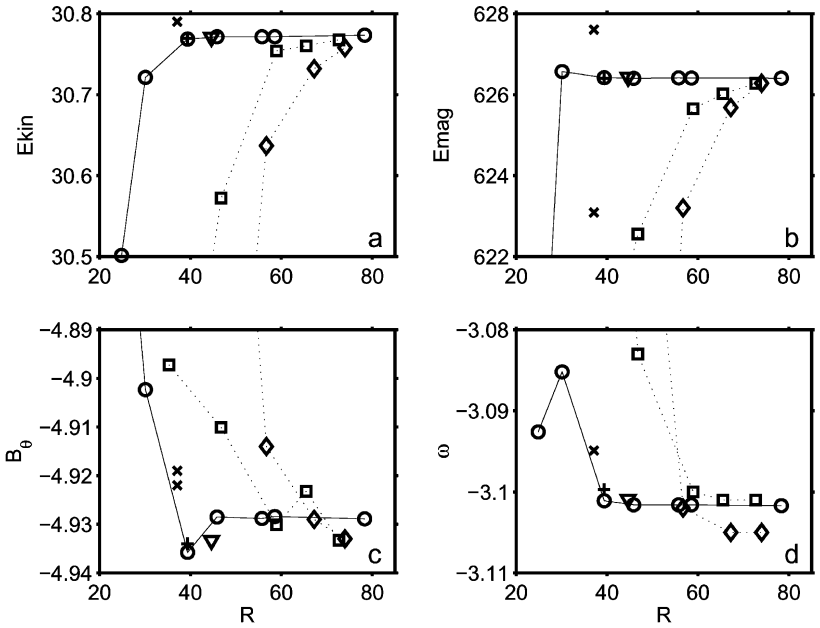

Fig. 3. Convergence of results for case 1: diamonds, ACD; circles, CWG; squares, GJZ; plus sign, TG; triangle, KS; crosses, TMH (uniform and non-uniform radial grid). (a) Kinetic energy, (b) magnetic energy, (c) local magnetic field component, (d) drift frequency.

Table 3
Results for benchmark case 2

Group	N_r	N_r^{ic}	N_θ	ℓ_{max}	E_{kin}	E_{mag}	E_{mag}^{ic}	ω	ω_{ic}	Γ_L
ACD	90	25	46	44	42.311	844.400	822.522	−3.834	−2.521	−91.023
ACD	150	40	46	44	42.392	845.400	821.855	−3.821	−2.598	−91.910
ACD	200	60	46	44	42.405	845.604	821.833	−3.816	−2.619	−92.212
ACD	250	70	46	44	42.409	845.694	821.885	−3.815	−2.630	−92.381
CWG	33	16	48	32	42.3295	849.003	824.255	−3.7584	−2.7393	−94.407
CWG	49	16	64	41	42.3713	845.932	823.162	−3.7984	−2.6706	−93.105
CWG	49	16	96	63	42.3882	845.605	822.667	−3.8027	−2.6594	−92.979
CWG*	49	16	96	63	42.3878	845.604	822.672	−3.8027	−2.6593	−92.978
CWG	49	20	96	63	42.3888	845.602	822.649	−3.8027	−2.6593	−92.978
CWG	49	16	128	84	42.3881	845.606	822.673	−3.8027	−2.6595	−92.979

Chebyshev expansion (circles, triangle and plus sign in Fig. 3), which is not surprising given that the codes are based on the same principles. For this method, only CWG (circles) provide results at variable resolution, but two codes with radial finite differencing seem to converge against the same values for the kinetic and magnetic energy, respectively. For the local values and the drift frequency convergence against a common point is less clear than for the energies, but the best resolved results agree within a quarter of a percent. For the local values the need to interpolate the respective fields between grid points is an additional source of error, which might explain the less systematic convergence behaviour.

CWG studied the influence of changing the time-step for two different spatial grids. Reducing the step by a factor of two lead to differences in the sixth decimal place. Therefore, a time-step which is smaller than what stability requires does not improve the solution significantly, at least in the weakly time-dependent regime of the benchmark dynamo.

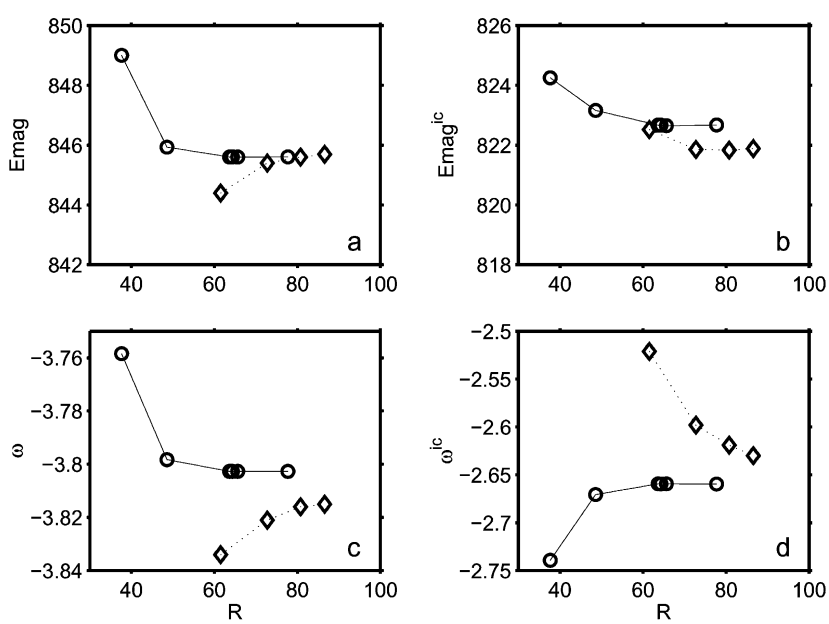

Fig. 4. Convergence of results for case 2: diamonds, ACD; circles, CWG. (a) Magnetic energy density in fluid shell, (b) magnetic energy density in inner core, (c) drift frequency, (d) rotation frequency of inner core.

6.3. Dynamo with conducting and rotating inner core (case 2)

Results for case 2 have only been reported by two contributors. The validity of the results is somewhat reinforced by the use of two different code versions by CWG (labelled with and without an asterisk). The basis for both versions is the fully spectral dynamo code by Glatzmaier (1984), but the additions for treating a conducting and rotating inner core have been implemented independently and overall the codes differ in some details. The two solutions agree within better than 4×10^{-5} for all requested properties. The results by ACD, who use a finite difference method in the radial direction, are in reasonable agreement with those by CWG (Table 3 and Fig. 4). The deviation is largest for the inner core rotation rate, about 1% at the highest resolution, but a quadratic extrapolation of ACD's results suggest that they converge against those by CWG.

The sum of the viscous and magnetic torques on the solid inner core is obviously zero because its rotation rate is steady. The viscous torque is positive (prograde) while the magnetic torque is negative (Table 3). GAG reports that the viscous torque on the stationary inner core of case 1 is also positive and cancels the negative viscous torque on the outer boundary so that the net torque on the fluid shell still vanishes, as it has to in steady state. It is interesting that the signs of the viscous torques on the two boundaries in the non-magnetic case 0 are opposite to what they are in case 1 and that the sign of the drift frequency ω differs between cases 0 and 1.

7. Discussion and conclusions

The comparison of codes that use finite differences in the radial direction with fully spectral methods suggests that the latter are more advantageous when high accuracy is required. In case of the partial finite difference methods, the radial resolution is clearly the accuracy-limiting factor. The exponential convergence behaviour of fully spectral methods is very helpful to pin down the solution to several significant digits, which is one aim of the benchmark study. Furthermore, an asset of the Chebyshev representation is that it allows one to calculate radial derivatives of the dependent variables on grid points with great accuracy. Because most computer time is used for the transformation in the angular coordinates, the additional time required for the Chebyshev transforms is far outweighed by the smaller number of radial grid levels that is needed to achieve a given accuracy. However, one must also keep in mind that the benchmark cases are simple in the sense that the spatial spectra drop off rapidly with wavenumber and time-dependence is weak, which makes them ideally suited for spectral methods. For chaotic dynamos at higher Rayleigh numbers and lower Ekman numbers, which require much higher spatial resolution, the spectral method becomes very expensive and may be less suited than other techniques for massively parallel computers. Unfortunately, a comparison study at such parameters would be far more difficult.

The overall level of agreement between different methods is remarkable when the resolution is sufficiently high. This allows us to define with great confidence a standard solution within narrow error

Table 4
Suggested standard solution with uncertainties

	Case 0	Case 1	Case 2
E_{kin}	58.348 ± 0.050	30.733 ± 0.020	42.388 ± 0.050
E_{mag}		626.41 ± 0.40	845.60 ± 0.40
$E_{\mathrm{mag}}^{\mathrm{ic}}$			822.67 ± 1.60
T	0.42812 ± 0.00012	0.37338 ± 0.00040	
u_ϕ	-10.1571 ± 0.0020	-7.6250 ± 0.0060	
B_θ		-4.9289 ± 0.0060	
ω	0.1824 ± 0.0050	-3.1017 ± 0.0040	-3.8027 ± 0.0250
ω_{ic}			-2.6595 ± 0.0600
Γ_{L}			-92.979 ± 1.200

limits for cases 0 and 1. We suggest that the best result from CWG be considered the standard. To estimate the range of uncertainty we require that the best-resolved results of two more codes (those by ACD and GJZ) fall into this range (Table 4). Because of the slower convergence of the latter two codes, the exact solution may be much closer to the suggested value than what the quoted accuracy suggests.

With only two completely independent contributions to case 2 we cannot claim the same level of confidence as in the other cases, but the convergence of the CWG results and the satisfactory agreement with the ACD solution justifies the selection of the best resolved result by CWG as a standard also in this case. Here, the uncertainty has been fixed to twice the difference between the best results by CWG and ACD, but not less than the uncertainty determined in case 1 for the same property (where applicable).

References

Busse, F.H., Grote, E., Tilgner, A., 1998. On convection driven dynamos in rotating spherical shells. Stud. Geophys. et Geod. 42, 1–6.

Canuto, C., Hussani, M.Y., Quateroni, A., Zhang, T.A., 1987. Spectral Methods in Fluid Dynamics. Springer, Berlin.

Christensen, U., Olson, P., Glatzmaier, G.A., 1998. A dynamo model interpretation of geomagnetic field structures. Geophys. Res. Lett. 25, 1565–1568.

Christensen, U., Olson, P., Glatzmaier, G.A., 1999. Numerical modelling of the geodynamo: a systematic parameter study. Geophys. J. Int. 138, 393–409.

Dormy, E., Cardin, P., Jault, D., 1998. MHD flow in a slightly differentially rotating spherical shell, with conducting inner core, in a dipolar magnetic field. Earth Planet. Sci. Lett. 160, 15–30.

Glatzmaier, G.A., 1984. Numerical simulations of stellar convective dynamos. I. The model and method. J. Comput. Phys. 55, 461–484.

Glatzmaier, G.A., Roberts, P.H., 1995. A three-dimensional convective dynamo solution with rotating and finitely conducting inner core and mantle. Phys. Earth Planet. Inter. 91, 63–75.

Grote, E., Busse, F.H., Tilgner, A., 2000. Regular and chaotic spherical dynamos. Phys. Earth Planet. Inter. 117, 259–272.

Kageyama, A., Sato, T., 1995. The complexity simulation group, computer simulation of a magnetohydrodynamic dynamo. Phys. Plasma 2, 1421–1431.

Katayama, J.S., Matsushima, M., Honkura, Y., 1999. Some characteristics of magnetic field behavior in a model of MHD dynamo thermally driven in a rotating spherical shell. Phys. Earth Planet. Inter. 111, 141–159.

Kuang, W., Bloxham, J., 1997. An Earth-like numerical dynamo model. Nature 389, 371–374.

Sakuraba, A., Kono, M., 1999. Effect of the inner core on the numerical solution of the magnetohydrodynamic dynamo. Phys. Earth Planet. Inter. 111, 105–121.

Tilgner, A., 1999. Spectral methods for the simulation of incompressible flow in spherical shells. Int. J. Num. Meth. Fluids 30, 713–724.

J. Fluid Mech. (2002), *vol.* 452, *pp.* 263–291. © 2002 Cambridge University Press
DOI: 10.1017/S0022112001006711 Printed in the United Kingdom

A super-rotating shear layer in magnetohydrodynamic spherical Couette flow

By E. DORMY[1], D. JAULT[2] AND A. M. SOWARD[3]

[1]Institut de Physique du Globe de Paris/CNRS, 4 place Jussieu, 75252 Paris Cedex 05, France
[2]LGIT/CNRS, Université Joseph Fourier BP53, 38041 Grenoble Cedex 9, France
[3]School of Mathematical Sciences, University of Exeter, Exeter EX4 4QE, UK

(Received 19 February 2001 and in revised form 12 July 2001)

We consider axisymmetric magnetohydrodynamic motion in a spherical shell driven by rotating the inner boundary relative to the stationary outer boundary – spherical Couette flow. The inner solid sphere is rigid with the same electrical conductivity as the surrounding fluid; the outer rigid boundary is an insulator. A force-free dipole magnetic field is maintained by a dipole source at the centre. For strong imposed fields (as measured by the Hartmann number M), the numerical simulations of Dormy *et al.* (1998) showed that a super-rotating shear layer (with angular velocity about 50% above the angular velocity of the inner core) is attached to the magnetic field line $\mathscr{C}$ tangent to the outer boundary at the equatorial plane of symmetry. At large M, we obtain analytically the mainstream solution valid outside all boundary layers by application of Hartmann jump conditions across the inner- and outer-sphere boundary layers. We formulate the large-M boundary layer problem for the free shear layer of width $M^{-1/2}$ containing $\mathscr{C}$ and solve it numerically. The super-rotation can be understood in terms of the nature of the meridional electric current flow in the shear layer, which is fed by the outer-sphere Hartmann layer. Importantly, a large fraction of the current entering the shear layer is tightly focused and effectively released from a point source at the equator triggered by the tangency of the $\mathscr{C}$-line. The current injected by the source follows the $\mathscr{C}$-line closely but spreads laterally due to diffusion. In consequence, a strong azimuthal Lorentz force is produced, which takes opposite signs either side of the $\mathscr{C}$-line; order-unity super-rotation results on the equatorial side. In fact, the point source is the small equatorial Hartmann layer of radial width $M^{-2/3}$ ($\ll M^{-1/2}$) and latitudinal extent $M^{-1/3}$. We construct its analytic solution and so determine an inward displacement width $O(M^{-2/3})$ of the free shear layer. We compare our numerical solution of the free shear layer problem with our numerical solution of the full governing equations for M in excess of 10^4. We obtain excellent agreement. Some of our more testing comparisons are significantly improved by incorporating the shear layer displacement caused by the equatorial Hartmann layer.

1. Introduction

The steady flow of viscous fluid confined inside a spherical shell, which results when the inner (radius r_i^*) and outer (radius r_o^*) boundaries rotate at different angular velocities Ω_i^* and Ω_o^* respectively about a common axis, is referred to as spherical Couette flow. When the spheres almost corotate rapidly, the motion measured in a frame corotating with (say) the outer sphere is slow and satisfies linear equations. The determination of the resulting steady flow is a classical problem in the theory of

rotating fluids. Proudman (1956) showed that the mainstream flow outside boundary layers is predominantly geostrophic, while its magnitude is determined by the Ekman suction into and out of the Ekman layers attached to the inner and outer spherical boundaries. The Ekman layer is singular on the equator of the inner sphere; this feature is linked to the existence of a free shear layer on the tangent cylinder to the inner sphere extending from its equator to the intersection with the outer sphere. The nature of the flow in this tangent-cylinder shear layer was resolved by Stewartson (1966), while the extension of this shear layer analysis to more general geometries was undertaken by Moore & Saffman (1969). The strong shear at the tangent cylinder was reproduced numerically by Hollerbach (1994) down to small Ekman number $E = 5 \times 10^{-6}$. Decreasing E further to $E = 10^{-8}$, Dormy, Cardin & Jault (1998) recovered the structure of the free shear layer found by Stewartson (1966).

In the case of electrically conducting fluid, the magnetohydrodynamic flow that results in the presence of an applied axisymmetric meridional (poloidal) magnetic field is considerably more complicated. The MHD extension to the Proudman–Stewartson problem described above was first investigated numerically by Hollerbach (1994), who considered an axial dipole magnetic field. The inner solid sphere ($r^* \leqslant r_i^*$) was assumed to be an insulator (unlike the case of a solid sphere with the same electrical conductivity as the fluid, which we will consider) as was the solid outer region ($r^* \geqslant r_o^*$). When the applied dipole magnetic field is sufficiently weak that the Lorentz force, as measured by the Hartmann number M, remains small compared to the Coriolis force (specifically small Elsasser number EM^2), he found that a free shear layer remained on the tangent cylinder; the structure of this layer was determined by Kleeorin *et al.* (1997). When the Coriolis and Lorentz forces are comparable, $EM^2 = O(1)$, the inner and outer boundary layers are of mixed Ekman–Hartmann type, whereas the free shear layer evaporates. Nevertheless, when the applied magnetic field is strong, $EM^2 \gg 1$, a free shear layer reappears but now aligned with the magnetic field lines which graze either the inner or the outer boundary; elsewhere on these boundaries the boundary layers are predominantly Hartmann in character. Models of this type were developed by Starchenko (1997). In the case of the dipole field, the grazing field line is the one which touches the outer spherical boundary at its equator. The strong dipole field is the limit that interests us here and below we will expand in greater detail on the background to our chosen model.

The rapid rotation limit $E \ll 1$ with $EM^2 = O(1)$ has geophysical applications. The numerical geodynamo simulations of Glatzmaier & Roberts (1995) have revealed the importance of detached shear layers in rotating MHD systems. Indeed a liquid sodium prototype of a dynamo experiment based on fluid instabilities riding on these layers is now being built in Grenoble: a spherical cavity filled with sodium will be enclosed between a permanent magnet and an outer container made of inox; measurement of the electrical potential will give insight into the dynamics inside the cavity because the outer boundary is poorly conducting. Recently there has been much discussion about a possible differential rotation between the solid inner core and the mantle of the Earth. There is now some evidence indicating that the speed of the inner core surface relative to the mantle is no larger than the fluid velocity at the core surface, as inferred from the secular variation of the Earth's magnetic field (Vidale, Dodge & Earle 2000). The differential rotation between the inner solid core and the outer solid mantle, together with the detached shear layers occurring in the numerical dynamo experiments, points to the importance of the idealized model of spherical Couette flow in the presence of an applied magnetic field, as described above. Kleeorin *et al.* (1997) adopted an applied dipole field because it is meridional and as such interacts

strongly with the predominantly azimuthal flow driven by the differential rotation of the boundaries. Another attractive feature of a dipole magnetic field is that it is force free and so by itself drives no motion. Of course, in the Earth that differential rotation may well be caused by the angular momentum transport resulting from asymmetric convection; such complications are outside the scope of the simplified models driven by differential rotation described above.

In order to understand processes that are predominantly magnetic in character, we concern ourselves with the strong field limit $EM^2 \gg 1$. This is outside the geophysically relevant parameter range, but may be pertinent to certain slowly rotating planetary objects with strong magnetic fields. Then the Coriolis force is relatively small and whether or not the system is in rapid rotation ceases to be a significant issue (Starchenko 1997). Much of the dynamics in that limit is captured by the simpler problem in which the outer sphere is at rest ($\Omega_o^* = 0$). We will study that problem in the case of small differential rotation and so will require that the inner sphere rotates slowly. Motivated by planetary applications, we assume that the inner sphere is electrically conducting having the same conductivity as the fluid, while the outer boundary is an electrical insulator. Though, of course, for laboratory applications other electrical boundary conditions are of interest too. The typical strength B_0^* of the force-free applied dipole magnetic field and the importance of advection are measured by the Hartmann and magnetic Reynolds numbers

$$M = \frac{L^* B_0^*}{\sqrt{\mu_o \rho \nu \eta}} \quad \text{and} \quad R_M = \frac{L^{*2} \Omega_i^*}{\eta} \quad (L^* = r_o^* - r_i^*) \tag{1.1a, b}$$

respectively, where ρ is the density, ν is the viscosity, μ_o is the magnetic permeability and η is the magnetic diffusivity. We restrict attention to strong magnetic fields and slow steady flow which correspond to the limits

$$M \gg 1 \quad \text{and} \quad R_M \ll 1. \tag{1.2a, b}$$

The later assumption ensures that the magnetic field perturbations are small and is essentially the basis on which we linearize our equations.

In our large Hartmann number limit, various boundary layers can be isolated. Hartmann layers of width $\delta_H^* = \sqrt{\mu_0 \rho \nu \eta}/B_0^* = L^*/M$ form on the inner and outer boundaries. The free shear layer, mentioned above, forms about the magnetic field line, which we call $\mathscr{C}$, that touches the outer sphere at its equator. This layer has characteristics similar to the free shear layer caused by current injection and removal by electrodes in channel flow (see Müller & Bühler 2001, Chap. 7) and has the same width $\sqrt{L^* \delta_H^*} = L^*/M^{1/2}$ as sidewall boundary layers (see Roberts 1967*a*). The presence of the $\mathscr{C}$-line shear layers in the shell were clearly identified by the numerical simulations of Dormy *et al.* (1998) (see also Dormy 1997 and the discussion in Starchenko 1998*a,b*). Surprisingly Dormy *et al.* (1998) found that the angular velocity in these $M^{-1/2}$-shear layers exceeded by about 50% the angular velocity Ω_i^* of the inner sphere. We say surprising because Lenz's law says that the Lorentz force acts to retard motion, which locally is evidently not true here. Indeed the situation provides yet another 'warning example to those who might wish to apply Lenz's law in detail!' (Roberts 1967*a*, p. 183). Dormy *et al.*'s (1998) finding was subsequently given further numerical support by Hollerbach (2000, 2001) and Hollerbach & Skinner (2001). Those papers emphasize that the nature of the electromagnetic boundary conditions play an extremely important role. Indeed their numerical results show that when both the inner and outer spheres are electrically conducting, the super-rotation is very large, $O(M^{0.6})$. The sensitivity to boundary conditions can be traced to the role played

by the Hartmann jump conditions on the inner and outer boundaries. We elaborate on this point in § 6, where we offer a tentative explanation for this large power law. A comprehensive analysis of that intriguing case is challenging and lies outside the scope of this present paper.

Though Starchenko (1997) considered the case of a rotating shell ($E \ll 1$), he worked in the large Elsasser number limit for which the boundary layer structures that he isolated are largely similar to those that we consider. Indeed, he proposed a mechanism for super-rotation. The effect he isolated is in fact small but may well produce an $O(M^{-1})$ super-rotation in the equatorial mainstream region, as we explain in § 6. Nevertheless, being small it is not responsible for the $O(1)$ super-rotation that occurs in the $\mathscr{C}$-line shear layer.

In this paper, we develop an asymptotic large-M theory and compare it with numerical integrations of the complete governing equations at large but finite M. Our development is organized as follows. In § 2 we formulate our problem. We describe the mainstream solution, first obtained by Starchenko (1997), valid outside boundary layers and compare it to the numerical solution of the complete governing equations. The differential rotation leads to a current flow from the inner conducting sphere out through the fluid along the meridional magnetic field lines. On arrival at the outer boundary it is carried to the equator inside the Hartmann boundary layer and is returned along the $\mathscr{C}$-line to the inner sphere. In § 3.1 we formulate the $\mathscr{C}$-line shear layer problem and report results of its numerical solution; in § 3.2 we obtain analytic solutions for the narrow gap limit. In § 4 more detailed comparisons are made between the numerical results for the boundary layer and the complete problem. Now it is important to appreciate that a significant fraction of the Hartmann layer current reaches the small equatorial Hartmann layer (the shaded region on figure 7 below), which is only a point on the scale of the $\mathscr{C}$-line shear layer. The current from this point source follows the $\mathscr{C}$-line but spreads laterally causing the azimuthally directed Lorentz force to take opposite signs on either side. The fluid is de-accelerated (accelerated) on the polar (equatorial) side by an $O(1)$ amount. The equator-side acceleration provides the $O(1)$ super-rotation.

Some small discrepancies are found in the numerical comparisons between the full numerics and the shear layer theory. These may be traced to low-order corrections which arise because the free shear layer intersects the outer-sphere boundary in the vicinity of its equator over a relatively long latitudinal length $O(L^* M^{-1/4})$. Here a thin Hartmann layer can still be distinguished but thickens as the equator is approached. Eventually it becomes the equatorial Hartmann layer, which constitutes the source mentioned above, with characteristics more in common with sidewall boundary layers; it has width $O(L^* M^{-2/3})$, extends over the latitudinal length scale $O(L^* M^{-1/3})$ and its existence leads to the source of the dominant correction to the free shear layer. In § 5, we obtain the analytic solution for this layer using a remarkable technique developed by Roberts (1967*b*) (see also Roberts 2000) for a closely related problem. Our result enables us to determine a displacement thickness $\delta^* = O(L^* M^{-2/3})$ for the $M^{-1/2}$-shear layer. By that we mean that the shear layer is effectively triggered on the equatorial plane at a radius $r_o^* - \delta^*$ rather than at the outer boundary r_o^*. With the inclusion of this correction to the shear layer solution, we find excellent agreement with the full numerical simulations.

2. Formulation

We adopt L^*, $L^* \Omega_i^*$ and B_0^* as our units of length, velocity and magnetic field respectively; the superscript star is dropped for all dimensionless quantities.

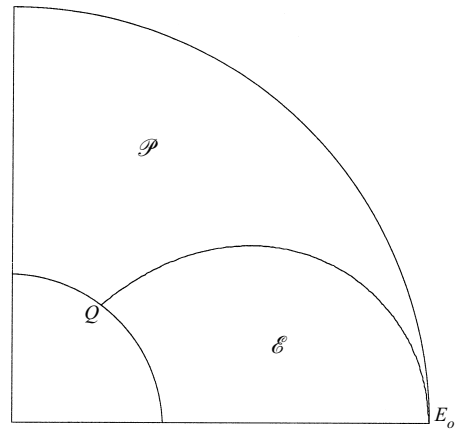

FIGURE 1. The northern hemisphere geometry. At large M, the polar $\mathscr{P}$ and equatorial $\mathscr{E}$ mainstream regions are separated by the shear layer containing the magnetic field line $\mathscr{C}$ joining E_o to Q.

Relative to cylindrical polar coordinates (s, ϕ, z), our applied dipole magnetic field is

$$\boldsymbol{B}_M = \nabla A \times \frac{\hat{\boldsymbol{\phi}}}{s} = -\nabla \Phi = \left(\frac{3sz}{2r^5}, 0, \frac{2z^2 - s^2}{2r^5} \right), \tag{2.1a}$$

where

$$A = \tfrac{1}{2} s^2/r^3, \quad \Phi = \tfrac{1}{2} z/r^3 \quad \left(r := \sqrt{s^2 + z^2} \right). \tag{2.1b}$$

It determines

$$s^{-2}|\nabla A| = |\boldsymbol{B}_M|^2 = \tfrac{1}{4}(s^2 + 4z^2)/r^8. \tag{2.1c}$$

The magnetic field line $\mathscr{C}$: $A = 1/2r_o$ divides the fluid shell up into two domains $\mathscr{P}$: $A < 1/2r_o$ and $\mathscr{E}$: $A > 1/2r_o$. In the former polar domain $\mathscr{P}$ the magnetic field lines intersect both the inner and outer shell boundaries $r = r_i$ and $r = r_o$, where $r_o - r_i = 1$. In the latter equatorial domain $\mathscr{E}$ the magnetic field lines intersecting the inner sphere boundary cross the equator within the fluid and return to the inner sphere without ever meeting the outer spherical boundary. The dividing line $\mathscr{C}$ is important because it has grazing contact with the outer sphere at the equator E_o. There we find it convenient to introduce the alternative Hartmann number

$$\mathscr{M} := \tfrac{1}{2} r_o^{-2} M \tag{2.2}$$

based on the local magnetic field strength $B_0^*/2r_o^3$ ($s = r_o$, $z = 0$ in (2.1c)) and the length r_o^*. We denote the intersection of $\mathscr{C}$ with the inner sphere by Q (see figure 1).

The slow steady azimuthal velocity $(0, s\Omega, 0)$ forced by rotating the inner sphere induces small magnetic field perturbations $(0, R_M B, 0)$. The equations of motion and magnetic induction are linearized on the basis that R_M is small and their ϕ-components give

$$M^2 s^{-1} \boldsymbol{B}_M \cdot \nabla (sB) + \left(\nabla^2 - s^{-2} \right) (s\Omega) = 0, \tag{2.3a}$$

$$s \boldsymbol{B}_M \cdot \nabla \Omega + \left(\nabla^2 - s^{-2} \right) B = 0. \tag{2.3b}$$

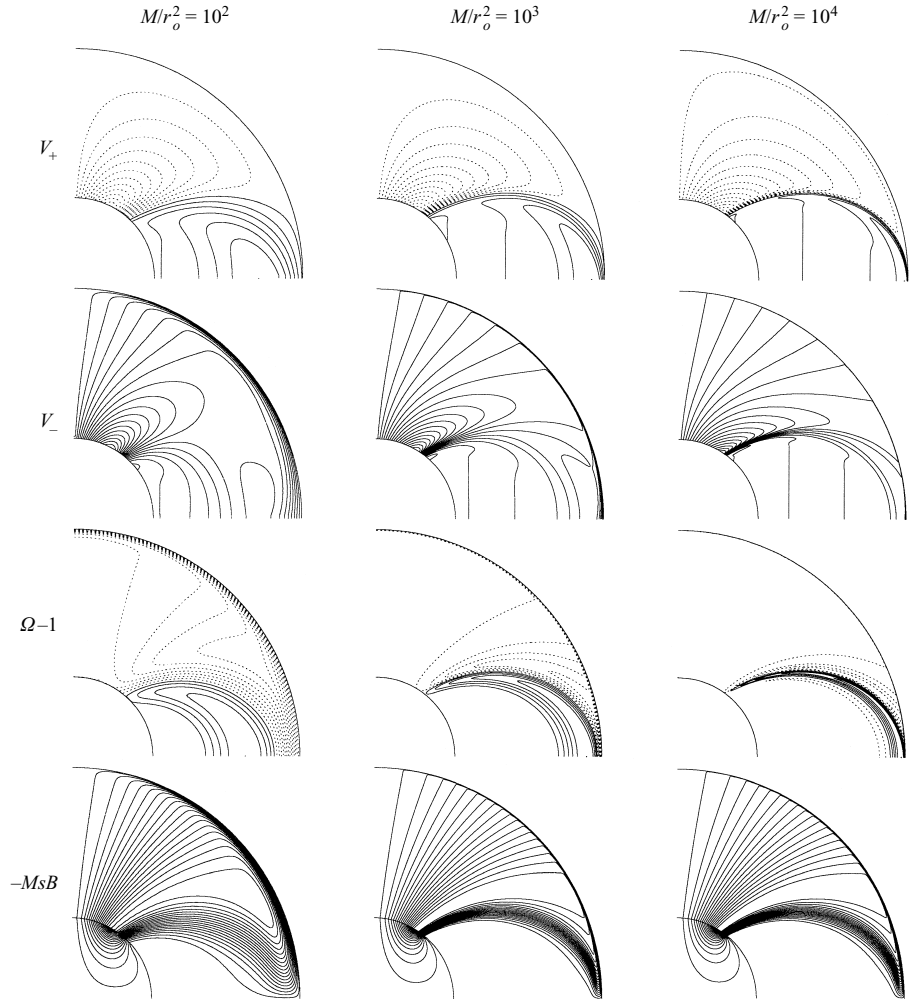

FIGURE 2. The full numerical solutions of the governing equations for the radius ratio $r_i/r_o = 0.35$ at increasing values of M. Contours at uniformly spaced levels of constant positive (negative) isovalues of V_+, V_-, $\Omega - 1$ and $-MsB$ in the meridional plane are indicated by the continuous (dotted) lines.

On the rigid outer insulating boundary ($r = r_o$), we require that

$$\Omega = 0, \quad B = 0, \tag{2.4a, b}$$

while on the inner boundary ($r = r_i$), the no-slip condition requires that

$$\Omega = 1. \tag{2.5a}$$

Since the inner solid sphere is a conductor with the same conductivity as the fluid, we therefore require that

$$B \quad \text{and} \quad \frac{\partial B}{\partial r} \quad \text{are continuous across} \quad r = r_i \tag{2.5b}$$

with B satisfying

$$\left(\nabla^2 - s^{-2}\right) B = 0 \quad \text{in} \quad r < r_i. \tag{2.6}$$

It is also helpful to take advantage of the symmetries corresponding to those of the applied dipole field, $A(s,-z) = A(s,z)$, namely $\Omega(s,-z) = \Omega(s,z)$ and $B(s,-z) = -B(s,-z)$, which respectively imply

$$\frac{\partial \Omega}{\partial z} = B = 0 \quad \text{on the equator} \quad z = 0. \tag{2.7}$$

In the large Hartmann number limit $M \gg 1$ for which our asymptotic analysis is valid, the dissipation in the mainstream exterior to all boundary layers is negligible. With the neglect of viscosity, the Lorentz force vanishes $\boldsymbol{j} \times \boldsymbol{B}_M = \boldsymbol{0}$, where $\boldsymbol{j} = s^{-1}\nabla sB \times \hat{\boldsymbol{\phi}}$ is the electric current measured in appropriate units, implying that the current lines $sB =$ constant are aligned with the meridional magnetic field lines. Likewise with the neglect of Ohmic diffusion, the magnetic field is frozen to the fluid and satisfies Ferraro's (1937) *law of isorotation*, namely that the angular velocity Ω is constant on field lines. From a more formal point of view, (2.3) have solutions with functional form

$$\Omega = \mathscr{F}(A) + O(M^{-1}), \quad sB = -r_o^2 M^{-1}\mathscr{G}(A) + O(M^{-2}) \tag{2.8a, b}$$

(cf. Starchenko 1997, equation (31)), in which the leading-order terms depend on A alone.

In order to understand the nature of the boundary layer structures, we introduce the Alfvén variables

$$V_\pm = s\Omega \pm MB, \tag{2.9}$$

which satisfy (2.3) when

$$\boldsymbol{B}_M \cdot \nabla V_\pm \pm M^{-1}\left(\nabla^2 - s^{-2}\right) V_\pm = s^{-1} B_s V_\mp. \tag{2.10}$$

They should be interpreted as advection–diffusion equations, which are coupled by the source terms on their right-hand sides. The advection is manifested by $\boldsymbol{B}_M$; when $\boldsymbol{B}_M$ directed from the inner to the outer sphere, V_+ (V_-) is convected inwards (outwards). As a consequence, V_+ (V_-) is continuous across the Hartmann layer on the outer (inner) sphere. Continuity of V_+ across the outer Hartmann layer together with the boundary condition (2.4a, b) implies that the mainstream boundary condition on the outer sphere is

$$s\Omega + MB \to 0 \quad \text{as} \quad r \uparrow r_o. \tag{2.11}$$

On the inner boundary, the complete solution of the Hartmann layer equations, which satisfy the boundary conditions (2.5a, b), is

$$B \approx B_i + \frac{1}{M|B_{ri}|}\left(\frac{\partial B}{\partial r}\right)_i \left\{1 - \exp\left[-M|B_{ri}|(r - r_i)\right]\right\}, \tag{2.12a}$$

$$\Omega \approx 1 + \frac{1}{sB_{ri}}\left(\frac{\partial B}{\partial r}\right)_i \left\{1 - \exp\left[-M|B_{ri}|(r - r_i)\right]\right\}, \tag{2.12b}$$

provided that

$$M|B_{ri}|\,|B_i| \gg \left|\left(\frac{\partial B}{\partial r}\right)_i\right|, \tag{2.12c}$$

where B_i and $(\partial B/\partial r)_i$ denote the values of B and its radial derivative inside (but at the boundary of) the solid conductor, while B_{ri} denotes the radial component of $\boldsymbol{B}_M$

normal to the boundary at the location (s_i, z_i). This yields the mainstream boundary conditions

$$B \to B_i + \frac{1}{M|B_{ri}|}\left(\frac{\partial B}{\partial r}\right)_i, \quad \Omega \to 1 + \frac{1}{s_i B_{ri}}\left(\frac{\partial B}{\partial r}\right)_i \quad \text{as} \quad r \downarrow r_i, \tag{2.12d}$$

on the inner sphere.

The mainstream solution, that satisfies the symmetry conditions, $\Omega(s,-z) = \Omega(s,z)$, $B(s,-z) = -B(s,z)$ and the Hartmann jump conditions (2.11), (2.12), is

$$\mathscr{F}(A) = 1 \quad \text{everywhere} \quad (\text{except on} \quad A = A_Q = 1/2r_o) \tag{2.13a}$$

and

$$\mathscr{G}(A) = \begin{cases} A/A_Q & \text{in region } \mathscr{P}\text{: } 0 \leqslant A < A_Q \\ 0 & \text{in region } \mathscr{E}\text{: } A_Q < A \leqslant 1/2r_i \end{cases} \tag{2.13b}$$

(cf. Starchenko 1997, equation (79)). In applying (2.12*d*), we have assumed that $(1/B_i)\,(\partial B/\partial r)_i$ is of order unity, i.e. the radial length scale adopted by the potential solution inside the solid sphere is the same as the latitudinal length scale on its surface. So, since $B = O(M^{-1})$, the mainstream boundary condition (2.12*d*) reduces to $\Omega = 1 + O(M^{-1})$ as $r \downarrow r_i$. Consequently, the terms neglected in our application of the boundary conditions (2.11) and (2.12*d*) are both $O(M^{-1})$ consistent with our assumption (2.8). Note, however, that our error estimates are larger ($O(M^{-1/2})$) near Q, where the $\mathscr{C}$-line shear layer has a short $O(M^{-1/2})$ length scale, but the inequality (2.12*c*) is still met comfortably.

From (2.8*b*) and (2.13*b*) we deduce that the total electric current flowing outwards in the polar region $\mathscr{P}$ is

$$J_{\text{out}} := 2\pi(sB)_{A=A_Q} = -\pi/\mathscr{M} \tag{2.14}$$

(see (2.2)). Since none flows in the equatorial region $\mathscr{E}$, it is all returned along the $\mathscr{C}$-line shear layer.

We performed direct simulations of equations (2.3) up to Hartmann number $2\mathscr{M} := M/r_o^2 = 10^4$ for the radius ratio $r_i/r_o = 0.35$. In order to achieve better comparison with the asymptotics, we considered an initial value problem in which we reinstated inertia into (2.3*a*) by replacing the zero on its right-hand side by $\partial\Omega/\partial t$. It is important to appreciate that this is purely a device to aid convergence and only the final steady state is of interest. The two scalars Ω and B are represented as

$$\Omega = \sum_0^L \Omega_l(r)\mathrm{P}^1_{2l+1}(\cos\theta), \quad B = \sum_1^L B_l(r)\mathrm{P}^1_{2l}(\cos\theta), \tag{2.15a, b}$$

where θ is the colatitude. We calculated B_l and Ω_l on a radial grid stretched so that inner and outer Hartmann layers are well resolved. For $M/r_o^2 = 10^4$ we employed very high resolution (5000 points in radius and harmonics up to $L = 220$). The solutions in meridional planes are illustrated in figure 2. The constancy of sB on magnetic field lines in the polar region $\mathscr{P}$ implied by (2.13*b*) is clear. The absence of contours of constant sB in $\mathscr{E}$ and Ω in both $\mathscr{P}$ and $\mathscr{E}$ is consistent with (2.13). Evidently a free shear layer remains across the dividing field line $\mathscr{C}$: $A = A_Q$, where the mainstream approximations break down. Of course, as this layer thins with increasing M the global resolution of the spectral method becomes more and more difficult to implement and the boundary layer approach is then more attractive. For the boundary layer treatment of the shear layer, the Alfvén variables $V_\pm$ are more

relevant than Ω and B, which is why contours of their constant values are portrayed also on figure 2. We discuss the nature of this free shear layer in the following section.

3. The shear layer $\mathscr{C}$

For reasons that will become clear when we study the equatorial Hartmann layer on the outer sphere in § 5, we introduce the notion of a $\mathscr{C}_M$-field line. It is defined to be the field line $\mathscr{C}_M$: $A = A_M := 1/2r_M$, where $r_M < r_o$ is chosen for our convenience later to be a function of M with the property that $r_M \uparrow r_o$ as $M \to \infty$. More specifically it is a field line that emerges from inside the equatorial Hartmann layer and so $r_o - r_M = O(M^{-2/3})$, which remains small compared to the shear layer thickness $O(M^{-1/2})$.

Points on the $\mathscr{C}_M$-line may be defined parametrically by

$$s = r_M \zeta^{3/2}, \quad z = r_M \zeta (1-\zeta)^{1/2}, \tag{3.1a}$$

where

$$\zeta = r/r_M, \quad \text{and} \quad \zeta_{Mi} = r_i/r_M. \tag{3.1b}$$

An important weighted measure of distance along the line is

$$\begin{aligned} \alpha(\zeta) &= -2\int_{E_M} s^2 \boldsymbol{B}_M \cdot \mathrm{d}\boldsymbol{x} = 2\int_{E_M} s^2 \,\mathrm{d}\Phi \\ &= -2\int_1^{\zeta} \frac{1-\frac{3}{4}\zeta}{(1-\zeta)^{1/2}}\,\mathrm{d}\zeta = (2-\zeta)\sqrt{1-\zeta}, \end{aligned} \tag{3.2}$$

where E_M: $(r_M, 0)$ is the intersection of the $\mathscr{C}_M$-line with the equatorial plane. Thus the weighted distance along $\mathscr{C}_M$ from E_M to its intersection Q_M: (s_{Mi}, z_{Mi}) with the inner sphere is $\alpha_{Mi} := \alpha(\zeta_{Mi})$. Thus we normalize this distance by introducing the coordinate l_M defined by

$$l_M := \int_{Q_M} s^2 \boldsymbol{B}_M \cdot \mathrm{d}\boldsymbol{x} \Big/ \int_{Q_M}^{E_M} s^2 \boldsymbol{B}_M \cdot \mathrm{d}\boldsymbol{x} = 1 - \frac{\alpha(\zeta)}{\alpha_{Mi}}, \tag{3.3a}$$

which has the property that it is zero at Q_M and unity at E_M. Distance normal to $\mathscr{C}_M$ is measured by the stretched flux function coordinate

$$n_M := \sqrt{2M/\alpha_{Mi}}(-A + A_M). \tag{3.3b}$$

Throughout the remainder of this section we consider only the limiting case $r_M = r_o$.

3.1. *The boundary layer formulation*

We adopt boundary layer coordinates $(l, n) \equiv (l_M, n_M)$ in the limit $M \to \infty$. They are

$$l := 1 - \alpha(\zeta)/\alpha_i, \quad n := \sqrt{2M/\alpha_i}(-A + A_Q), \tag{3.4a, b}$$

where

$$\alpha_i := 2\int_Q^{E_o} s^2 \boldsymbol{B}_M \cdot \mathrm{d}\boldsymbol{x} = \alpha(\zeta_i) \quad \text{with} \quad \zeta_i := r_i/r_o. \tag{3.4c}$$

In terms of ζ_i the inner and outer spherical boundaries are located at

$$r_i = \zeta_i/(1-\zeta_i) \quad \text{and} \quad r_o = 1/(1-\zeta_i). \tag{3.4d}$$

Our choice of sign in the definition of n ensures that n is positive in $\mathscr{P}$ and negative in $\mathscr{E}$. Relative to the boundary layer coordinates (l, n), the boundary layer approximations of (2.10) yield

$$\frac{\partial V_\pm}{\partial l} \pm \frac{\partial^2 V_\pm}{\partial n^2} = \frac{1}{s}\frac{\partial s}{\partial l} V_\mp, \quad \text{where} \quad s(l) = r_o \zeta^{3/2} \tag{3.5a, b}$$

is defined implicitly as a function of l via (3.2) and (3.4a). The pair of parabolic partial differential equations (3.5a) are coupled by the term on the right-hand side, which arises due to curvature effects. The strength of the coupling is determined by the size of the coefficient

$$\frac{1}{s}\frac{\partial s}{\partial l} = \frac{3\alpha_i}{4}\frac{\sqrt{1-\zeta}}{\zeta\left(1-\frac{3}{4}\zeta\right)}. \tag{3.5c}$$

Solutions of (3.5a) are required that match with the mainstream solution (2.8). Expressed in our boundary layer coordinates, (2.13) determines the boundary conditions

$$V_\pm \to \begin{cases} s \mp (r_o^2/s)\left(1-\sqrt{\alpha_i/\mathscr{M}}\,n\right) & \text{as} \quad n \uparrow \infty \\ s & \text{as} \quad n \downarrow -\infty \end{cases} \tag{3.6}$$

on $0 < l < 1$, remembering that $s = s(l)$ and $\mathscr{M} = M/2r_o^2$.

To obtain the inner-sphere boundary conditions at $l = 0$, we need to consider the Hartmann layer at Q. Since the shear layer thickness is $O(M^{-1/2})$, that is the latitudinal length scale imposed on B at the surface of the solid inner conductor. The potential solution has the same radial scale and so we estimate that $(\partial B/\partial r)_i = O(M^{1/2}B_i) = O(M^{-1/2})$. Consequently, the Hartmann jump condition (2.12d) becomes $\Omega = 1 + O(M^{-1/2})$, which determines the condition

$$V_- + V_+ = 2s_Q + O(M^{-1/2}) \tag{3.7}$$

at $l = 0$ on the inner sphere.

The situation on the outer sphere is rather more delicate and we need to be aware of its location $\mathscr{S}_o$: $s = s_o(z)$ relative to our boundary layer coordinates. On $\mathscr{S}_o$, the value A_o of A satisfies $A_Q - A_o = z^2/2r_o^3$. Since the $\mathscr{C}$-line and $\mathscr{S}_o$ are tangent to each other at E_o, where $l = 1$, we may assume that, at given l close to unity, we may make the approximations $z \sim r_o(1-\zeta)^{1/2}$ and $\alpha \sim (1-\zeta)^{1/2}$. In this way we obtain, using (3.4a), the approximate results

$$A_o - A_Q \sim \tfrac{1}{2}(1-\zeta)/r_o \quad \text{and} \quad 1 - l \sim \sqrt{1-\zeta}\Big/\alpha_i, \tag{3.8a, b}$$

which together with (3.4b) determines the approximate location

$$n_o = \alpha_i^{3/2}\mathscr{M}^{1/2}(1-l)^2 \tag{3.8c}$$

of the outer-sphere boundary $\mathscr{S}_o$: $n = n_o(l)$. Evidently $\mathscr{S}_o$ eats into the boundary layer up to a distance $|1-l| = O(M^{-1/4})$, as illustrated on figure 7 below. Fortunately this distance tends to zero as $M \to \infty$ and so correct to lowest order the outer-sphere boundary conditions can be applied at $l = 1$.

In the neighbourhood of the equator E_o, the outer-sphere Hartmann jump condition (2.11) requires V_+, to vanish, while symmetry demands that B vanishes on $z = 0$.

Together they yield the boundary conditions

$$V_+ = \begin{cases} 0 & \text{for} \quad n \geqslant 0 \\ V_- \equiv r_o \left(1 - \sqrt{\alpha_i/\mathscr{M}}\, n\right)^{-1} [1 + \Omega_S] & \text{for} \quad n < 0 \end{cases} \tag{3.9a, b}$$

at $l = 1$. Here we have introduced

$$\Omega_S(n) \equiv \Omega - 1, \tag{3.9c}$$

which measures super-rotation on the equatorial plane in the vicinity of E_o.

In addition to the $O(M^{-1/2})$ errors introduced by ignoring the Hartmann layer corrections at $l = 0$ and the higher-order matching terms as $|n| \to \infty$ on $0 < l < 1$, more substantial errors $O(M^{-1/3})$ are incurred at $l = 1$ through not considering the small equatorial Hartmann boundary layer ($|1 - l| = O(M^{-1/3})$ and $n = O(M^{-1/6})$), see figure 7 below. We rectify that deficiency in § 5.

We solved the boundary layer equations (3.5*a*) numerically subject to the lowest-order boundary conditions

$$V_\pm \to \begin{cases} s \mp (r_o^2/s) & \text{as} \quad n \uparrow \infty \\ s & \text{as} \quad n \downarrow -\infty \end{cases} \tag{3.10}$$

on $0 < l < 1$,

$$V_- + V_+ = 2s_Q \tag{3.11}$$

at $l = 0$, and

$$V_+ = \begin{cases} 0 & \text{for} \quad n \geqslant 0 \\ V_- \equiv r_o\,[1 + \Omega_S] & \text{for} \quad n < 0 \end{cases} \tag{3.12}$$

at $l = 1$ on the outer sphere, where the $O(M^{-1/2})$ terms appearing in (3.6), (3.7) and (3.9*a*) have been neglected. Results for the shell radius ratio $\zeta_i = 0.35$ employed for figure 2 are illustrated in figure 3. The curves of constant V_+ clearly indicate how it is advected from the singularity at the equator of the outer sphere E_o: $l = 1$ in the direction of decreasing l. It is essentially reflected at the inner sphere at Q: $l = 0$ and is returned as $2s_Q - V_-$ in the direction of increasing l. The advection–diffusion equations (3.5*a*) for $V_\pm$ are coupled by the source term $(1/s)(\partial s/\partial l)V_\mp$ on their right-hand side. This source term appears to be responsible for the 'nose-like' structures visible on the contours of constant $V_\pm$ for the large Hartmann number solutions in figure 2; they are clearly faithfully reproduced by the boundary layer solutions shown in figure 3.

The value $-B = r_o V_-/2M$ on the outer sphere for $l = 1$ is of some interest. It reduces from $-B = r_o/M$ as $n \uparrow \infty$ to $-B = r_o(1 + \Omega_S(0))/2M$ as $n \downarrow 0$. The fact that it is not zero determines the strength of the equatorial current source

$$J_{\text{source}} = -\tfrac{1}{2}\pi\,[1 + \Omega_S(0)]/\mathscr{M} = \tfrac{1}{2}[1 + \Omega_S(0)]J_{\text{out}}, \tag{3.13}$$

which emanates from the equatorial Hartman layer, where $n = O(M^{-1/6})$ (see § 6 below). The remaining current $J_{\text{out}}[1 - \Omega_S(0)]/2$ is returned directly into the shear layer ($n = O(1)$) from the Hartmann layer itself, where $n \gg M^{-1/6}$. This feature is clearly portrayed by the contours of $-MsB =$ constant in figure 3; some contours stem from the source, while others originate from the Hartmann layer at $l = 1$. There is also evidence of this partitioning of the return current into the source J_{source} and the

continuous distribution $J_{\text{out}} - J_{\text{source}}$ from the full numerics for the case $M/r_o^2 = 10^4$ portrayed in figure 2.

3.2. *The narrow gap limit*

Though the boundary layer problem posed can only be solved numerically in general, some analytic progress can be made in the narrow gap limit

$$\varepsilon = (r_o - r_i)/r_o \ll 1, \tag{3.14a}$$

for which we may make the estimates

$$\frac{r_o - s}{r_o} = O(\varepsilon) \quad \text{and} \quad \frac{1}{s}\frac{\partial s}{\partial l} = O(\varepsilon) \quad \text{noting that} \quad 1 - \zeta_i = \varepsilon. \tag{3.14b}$$

Upon neglecting the $O(\varepsilon)$ terms in the boundary layer equations (3.5a), they then decouple and can be solved successively. Even though the ensuing system is relatively simple, it retains sufficient complexity to demonstrate the super-rotation phenomena. So our prime objective here is to determine the unknown super-rotation $\Omega_S(n)$.

We take (3.12) as our initial data $V_-(n,1) = r_o[1 + \Omega_S(n)]$ at E_o and solve the diffusion problem on $0 < 1 - l < 1$ for V_+. Its value $V_+(n,0)$ at Q provides, via (3.11), the initial data $V_-(n,0) = 2 - V_+(n,0)$ for V_+ on $0 < l < 1$. The solution to both problems can be expressed in the form

$$\frac{V_\pm}{r_o} = 1 \mp \tfrac{1}{2}\,\mathrm{erfc}\left(\frac{-n}{\sqrt{4(1 \mp l)}}\right) \pm \frac{1}{\sqrt{4(1 \mp l)\pi}} \int_{-\infty}^{0} \Omega_S(n') \exp\left(-\frac{(n-n')^2}{4(1 \mp l)}\right) \mathrm{d}n'. \tag{3.15}$$

The requirement, that the final value $V_-(1,n)$ for $n \leqslant 0$ at E_o is the same as the initial value of $V_+(1,n)$ there, leads to the integral equation

$$\Omega_S(n) = \tfrac{1}{2}\,\mathrm{erfc}\left(\frac{-n}{\sqrt{8}}\right) - \frac{1}{\sqrt{8\pi}} \int_{-\infty}^{0} \Omega_S(n') \exp\left(-\frac{(n-n')^2}{8}\right) \mathrm{d}n', \tag{3.16}$$

for $n \leqslant 0$, whose solution in turn determines the complete solution (3.15). In turn, the corresponding values of $s\Omega = (V_+ + V_-)/2$ and $B = (V_+ - V_-)/2M$ (see (2.9)) are readily obtained.

For $n < 0$, the solution of the diffusion problem can be expressed in terms of normal modes periodic in l of half period $l = 2$. Such separable solutions exist with

$$\Omega_S(n) = Re\left\{\sum_{k=0}^{\infty} \hat{\Omega}_k \exp\left[(1+\mathrm{i})\sqrt{(2k+1)\pi}\,\frac{n}{2}\right]\right\} \quad \text{on} \quad n < 0. \tag{3.17a}$$

Here the complex constants $\hat{\Omega}_k$ are the coefficients of the Fourier expansion of a periodic $\mathscr{C}$-line function, which reverses sign under the shift $l \to l + 2$ and is defined by $r_o^{-1}V_+(0, 1-l) - 1$ on $0 \leqslant l \leqslant 1$ and $1 - r_o^{-1}V_-(0, l-1)$ on $1 \leqslant l \leqslant 2$. Of course, the values of $\hat{\Omega}_k$ are unknown, but the form of (3.17a) does provide useful information about the large $-n$ behaviour, namely that

$$\Omega_S(n) \sim |\hat{\Omega}_0| \exp\left(\tfrac{1}{2}\sqrt{\pi}\,n\right) \cos\left(\tfrac{1}{2}\sqrt{\pi}\,n - \varphi_S\right) \quad \text{as} \quad n \downarrow -\infty, \tag{3.17b}$$

where $\hat{\Omega}_0 = |\hat{\Omega}_0| \exp(-\mathrm{i}\varphi_S)$. Essentially, Ω_S oscillates with period $4\sqrt{\pi}$ and decays exponentially in the $-n$-direction.

Though (3.17a) can be used as the basis of a method of solution, it is perhaps more instructive to solve (3.16) by successive iteration. This gives a series expansion

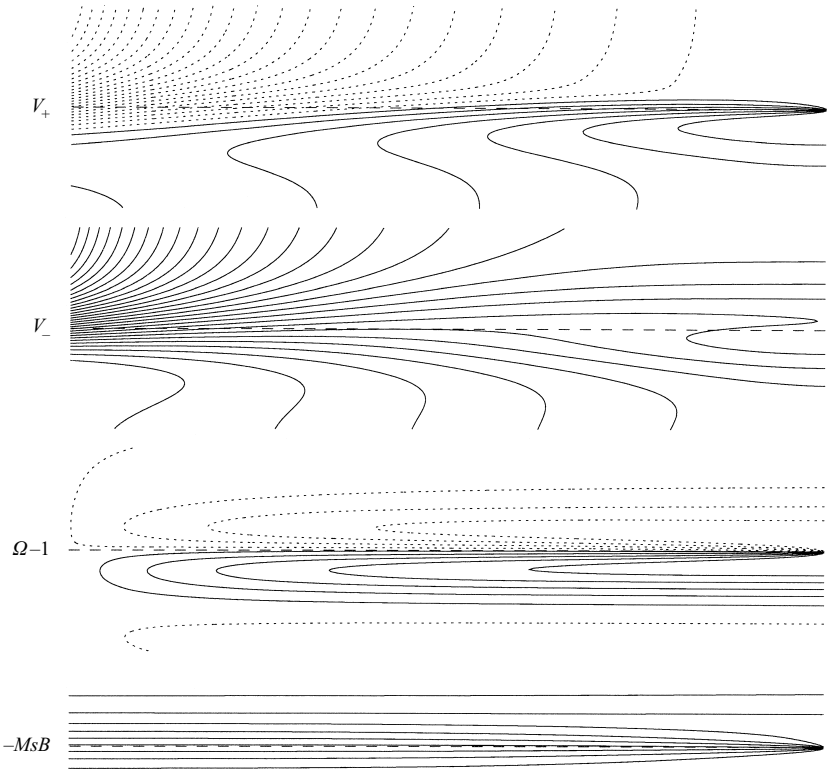

FIGURE 3. The numerical solution of the boundary layer equations (3.5*a*) in the l, n-plane for the radius ratio $r_i/r_o = 0.35$ of figure 2. The l-axis $0 \leqslant l \leqslant 1$ is identified by the horizontal dashed lines; the vertical extent is $-15 \leqslant n \leqslant 15$. As in figure 2, positive (negative) isovalues are indicated by the continuous (dotted) lines.

whose first two terms are

$$\Omega_S(n) = \frac{1}{2}\left[\operatorname{erfc}\left(\frac{-n}{\sqrt{8}}\right) - \frac{1}{\sqrt{8\pi}}\int_{-\infty}^{0} \operatorname{erfc}\left(\frac{-n'}{\sqrt{8}}\right)\exp\left(-\frac{(n-n')^2}{8}\right)\mathrm{d}n' + \cdots\right] \tag{3.18a}$$

which reduces to

$$\Omega_S(n) = \frac{3}{4}\operatorname{erfc}\left(\frac{-n}{\sqrt{8}}\right) - \operatorname{erfc}\left(\frac{-n}{4}\right)\left[\frac{1}{2} - \frac{1}{8}\operatorname{erfc}\left(\frac{-n}{4}\right)\right] + \cdots. \tag{3.18b}$$

The numerical solution for $V_+(1,n)/r_o = 1 + \Omega_S(n)$ obtained by taking the first two terms of (3.18) is illustrated by the dashed curve on figure 4, which according to (3.18*b*) terminates with $\Omega_S = 3/8$ at $n = 0$.

The iterated solution agrees with the numerical solution of the boundary layer equations and they are also shown on figure 4. As n is increased from $-\infty$, the value of Ω_S decreases slightly from zero to a minimum $\Omega_S \approx -0.0070$ at $n \approx -4.3636$ and then increases monotonically through zero at $n \approx -3.4376$. The separation (≈ 0.93) between the minimum and zero of Ω_S is in excellent agreement with the eighth period $\sqrt{\pi}/2(\approx 0.89)$ predicted by the large $-n$ asymptotic result (3.17*b*). Then Ω_S continues to increase, terminating at $n = 0$ with the value $\Omega_S(0) \approx 0.4139$. This lies within the

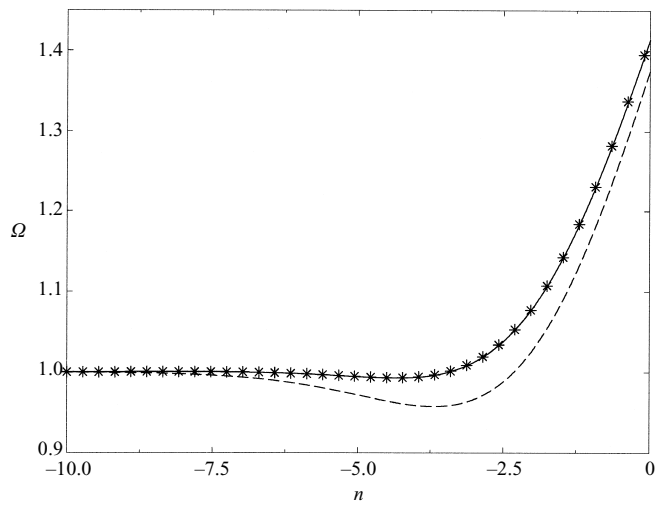

FIGURE 4. The angular velocity $1 + \Omega_S(n)$ on the equatorial plane plotted *vs.* n in the narrow gap limit $\varepsilon \ll 1$. The dashed line denotes the two-term solution (3.18), the continuous line denotes its iteration to 100 terms and the stars denote the numerical solution of system (4.1).

range $0.375 < \Omega_S(0) < 0.5$ suggested by the single-term and two-term expansions of (3.18*a*), which by the alternating nature of the series naturally bound the realized value. Of greater significance is the fact that $\Omega_S > 0$ in the range $-3.4376 < n \leqslant 0$. This feature is obvious even from the simple first term of the series expansion (3.18*a*), while the region of small negative Ω_S is suggested by the two-term representation (3.8*b*).

Our semi-analytic treatment of the narrow gap limit isolates the key mechanisms responsible for super-rotation. In particular, curvature effects, which we neglected in (3.14), are evidently unnecessary. Instead, we need to examine carefully how the electric current circuits are closed inside the electrically conducting fluid; we discuss this issue in the wide gap context in § 4.2 below.

In the next section we describe the numerical procedures adopted to solve the shear layer boundary layer problem. We discuss in more detail the nature of the results and make quantitative comparisons with the numerical solution of the complete governing equations (2.3) illustrated in figure 2 at finite M.

4. Numerical solution of the $\mathscr{C}$-boundary layer equations

The numerical solution of (3.5*a*) subject to the boundary conditions (3.10), (3.11) and (3.12) can be achieved by successively relaxing (3.5a_+) and (3.5a_-). We chose to use a finite difference scheme, well suited for this geometry. It consisted of a second-order scheme to compute the diffusion along n, and an up-wind first-order scheme to compute advection in l.

4.1. *Narrow gap limit*

The solution of the uncoupled system

$$\frac{\partial V_\pm}{\partial l} \pm \frac{\partial^2 V_\pm}{\partial n^2} = 0 \tag{4.1}$$

appropriate to the narrow gap limit does not raise any particular difficulties. We only need to reduce the infinite domain in n to a finite computational domain. Solutions were obtained subject to two distinct sets of boundary conditions at the upper and lower n-boundaries. On the one hand, we applied Dirichlet boundary conditions and, on the other, Robin boundary conditions (exponential decrease). We checked that our computational domain was large enough for both approaches to give the same results. By this device numerical solutions were obtained (see the stars of figure 4) that are in excellent agreement with the iterated analytical solution (3.18) of § 3.2.

4.2. *Wide gap limit*

The numerical solution of the coupled system (3.5*a*) requires some additional care.

As $n \to \pm\infty$, our boundary conditions (3.10) require that n-derivatives vanish. There $V_\pm$ solves

$$\frac{\partial V_\pm}{\partial l} = \frac{1}{s}\frac{\partial s}{\partial l} V_\mp \tag{4.2}$$

with diffusion neglected and its solution is, of course, that defined by (3.10) as $n \to \pm\infty$. In the case of the discrete analogue of (4.2), the boundary condition (3.10) as $n \downarrow -\infty$ is a solution but the boundary condition (3.10) as $n \uparrow \infty$ is not; this is due to the nature of the up-wind discrete operator. Indeed, the error thus introduced if (3.10) is used as the numerical boundary condition does not let the successive relaxations reach a steady solution and the iterative resolution diverges. To overcome this difficulty, we replaced (3.10) as $n \to +\infty$ with the numerical solution of (4.2) imposing $V_+ = 0$ at $l = 1$ and $V_- = 2s_Q - V_+$, at $l = 0$. This numerical boundary condition is consistent in the sense that it tends to (3.10) as the number of l-points tends to infinity.

The numerical approximation of (3.5*a*) itself has inherent difficulties. We add artificial diffusion (often referred to as 'numerical diffusion') to this equation in the l-direction by use of the up-wind operator. This diffusion was kept small by using a large number of points (up to 8000) in this l-direction. For that, the difference between the numerical and exact boundary condition mentioned above is then less that 1%. We employed 600 points in the n-direction and results for the case $\zeta_i = 0.35$ are illustrated on figure 3; they should be compared to the full numerical solution of (2.3) illustrated in figure 2.

A more quantitative comparison between the boundary layer solution and the full numerics is possible by looking at the cross-sections of the shear layer at various values of l as illustrated in figure 5 for the case $\zeta_i = 0.35$. Our boundary layer equations have been solved subject to the conditions that all quantities tend to constants as $n \to \infty$ (see (3.10)). Nevertheless, it is quite clear that the numerical results at finite Hartmann number veer away from those constant values as $n \uparrow \infty$. This is consistent with the $O(M^{-1/2})$ corrections present in the true boundary conditions (3.6). The termination of the finite-M curves at certain positive values of n reflects the fact that the cross-section has either reached the symmetry axis ($l = 0.1$) or the outer sphere $l = 0.4$ and $l = 0.7$; in the extreme case ($l = 1.0$) the outer boundary is reached at $n = 0$ in all cases. The abrupt drops in values of V_- visible in some cases for $l = 0.4$ and 0.7 are manifestations of the Hartmann layer on the outer boundary.

It is important to remember that contours of constant sB are electric current lines (see above (2.8)). In the mainstream region they are almost parallel to the meridional field lines (see (2.8)) and so produce no Lorentz force. That negative electric current

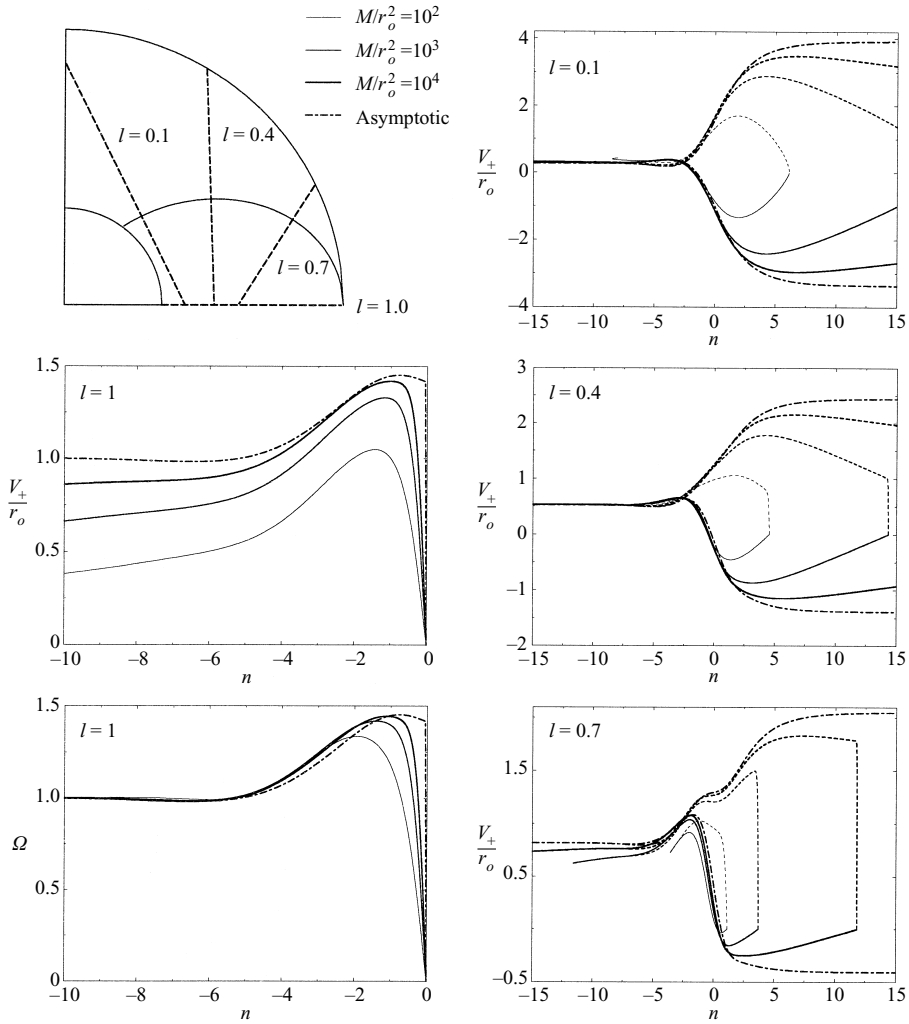

FIGURE 5. For caption see facing page.

($\boldsymbol{j}$ is directed inwards) is returned in the outer Hartmann boundary layer to the equator. Its total magnitude on entering the shear layer is $|J_{\text{out}}|$ (see (2.14)). A small fraction $|J_{\text{out}}|(1-\Omega_s(0))/2$ escapes directly into the shear layer but the larger fraction $|J_{\text{source}}| = |J_{\text{out}}|(1+\Omega_s(0))/2$ (see (3.3)) is returned from the small equatorial Hartmann layer, which on the scale of the shear layer is a point source. The consequences of that are clear in figure 3. The negative current J_{source} emerging from the source spreads with decreasing l ($\boldsymbol{j}$ is directed outwards). Whether the corresponding contours of constant sB cross the contours n =constant from below or above determines the sign of the Lorentz force $\boldsymbol{j}\times\boldsymbol{B}_M$. In figure 3 the contours of $-MsB$ have the correct inclination for negative n to accelerate the fluid. Another measure of the domain, in which the fluid is accelerated, is provided by figure 5. There acceleration occurs when $\partial^2\Omega/\partial n^2 < 0$, which is identifiable for moderate negative values of n. The cross-section $l = 1$ is particularly revealing in this respect, exhibiting features similar to those already seen

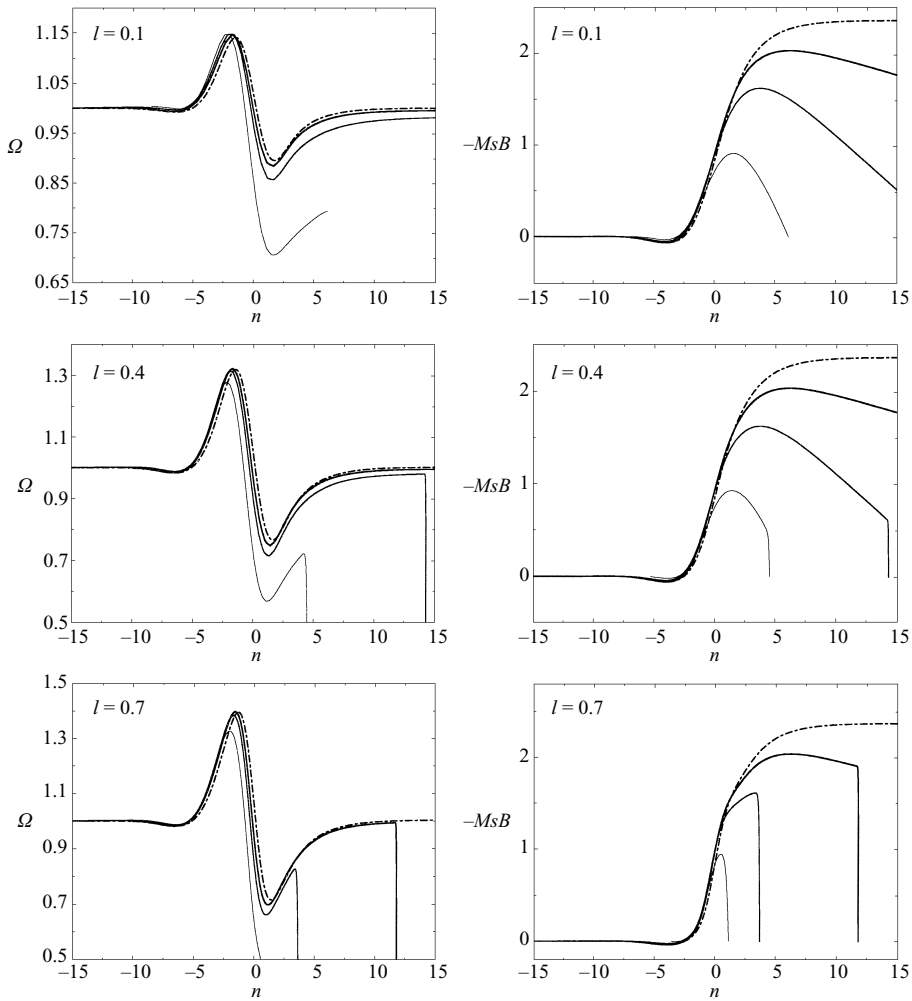

FIGURE 5. The quantities V_+/r_o, V_-/r_o, Ω and $-MsB$ plotted *vs.* n at $l = 0.1$, 0.4, 0.7 and 1.0 for the radius ratio $r_i/r_o = 0.35$. Numerical solutions of the governing equations (2.3) are shown for $M/r_o^2 = 10^2$, 10^3, 10^4 by continuous (except for V_-/r_o dashed) lines of increasing solidity; the numerical solutions of the boundary equations (3.5*a*) are identified by the short-long-dashed curves. The larger the value of M the closer the curve is to the asymptote.

in the narrow gap limit, and is well represented by the asymptotic solution. For that the value of Ω_S decreases slightly from zero at $n = -\infty$, as n is increased; it attains its minimum $\Omega_S \approx -0.01780$ at $n \approx -6.4776$, then increases monotonically through zero at $n \approx -5.1619$ to its maximum $\Omega \approx 0.4530$ at $n \approx -0.7663$, then finally decreasing and terminating at $n = 0$ with the value $\Omega_S(0) \approx 0.4147$ close to the value found in the narrow gap limit.

The fact that the maximum angular velocity Ω is found on the equatorial plane ($l = 1$) not at E_o ($n = 0$) but at a finite distance inside the fluid at $n \approx -0.7663$, is a curious feature special to the finite gap. It is therefore dependent on the coupling term $(1/s)(\partial s/\partial l)V_\mp$ on the right-hand side of (3.5*a*). The plots at $l = 0.7$ on figure 5

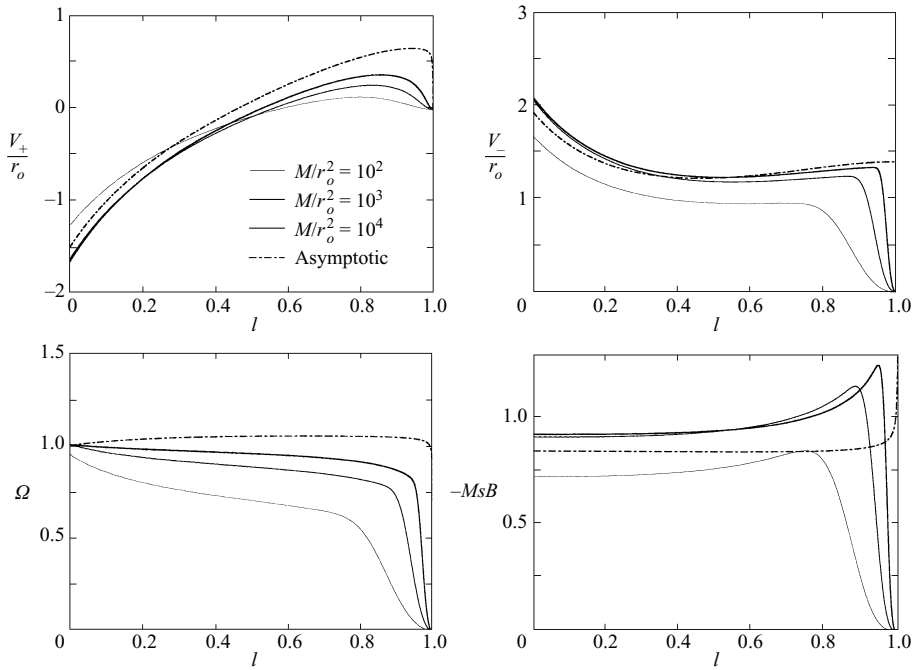

FIGURE 6. As for figure 5 (except for V_- now continuous) but plotted *vs.* l on the $\mathscr{C}$-line $n = 0$.

suggest that the value of V_+ being advected inwards from the equator acts as a sufficiently strong source to alter the outwardly advected V_- giving it a flattened profile at its centre. This is ultimately manifested by the interior local maximum on the equator. Another manifestation of the same effect is identified by an 'S'-shaped contour of V_- at the centre of the layer close to the equator $l = 1$ in figure 3.

An alternative and somewhat more testing comparison is made on figure 6, where quantities are plotted on the $\mathscr{C}$-line ($n = 0$). There some apparently substantial differences between the numerics and asymptotics are visible. The most obvious failure occurs in the neighbourhood of $l = 1$ and can be accounted for by noting that when $|1 - l| = O(M^{-1/3})$ the $\mathscr{C}$-line is inside the equatorial Hartmann boundary layer, where the shear layer boundary layer problem that we have solved ceases to be valid. Outside this equatorial layer it appears that our numerics converge slowly for large M.

Returning to figure 5, we notice that the Ω-profiles appear to be shifted by an amount consistent with a boundary layer displacement induced by the equatorial Hartmann layer. We explore this idea in the next section and isolate such a boundary layer displacement through solving the equatorial Hartmann layer problem. We then redraw the figure 5(a) for Ω at $l = 1$ in figure 9 below but with each finite-M curve displaced by its appropriate amount. In the same spirit, we draw figure 10 below equivalent to figure 6 but the results for the full numerical solution at each given M are plotted on the properly chosen displaced $\mathscr{C}_M$-line. The improvements obtained strongly support our contention that the leading-order corrections stem from a boundary layer displacement.

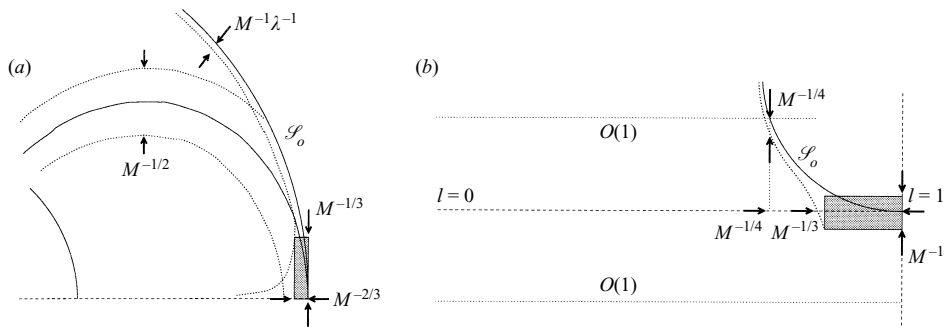

FIGURE 7. A schematic representation of the equatorial Hartmann layers and its neighbouring boundary layers on the outer-sphere boundary $\mathscr{S}_o$. Its relation to the $M^{-1/2}$ $\mathscr{C}$-shear layer and the outer sphere M^{-1} Hartmann layer are shown (*a*) in the meridional plane and (*b*) relative to the l, n boundary layer coordinates of the shear layer.

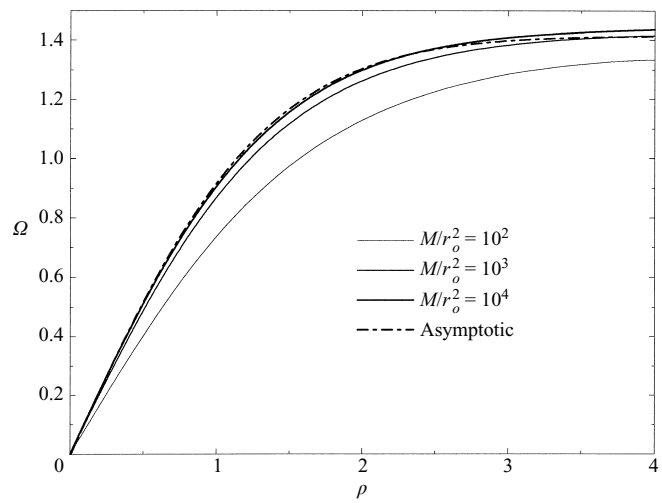

FIGURE 8. The angular velocity profiles Ω plotted *vs.* ρ in the equatorial Hartmann layer on the equator $\tau = 0$ for the radius ratio $r_i/r_o = 0.35$. The curves for $M/r_o^2 = 10^2, 10^3, 10^4$ are identified by continuous lines of increasing solidity, which for small ρ approach the asymptotic solution (5.12) given by the short-long dashed curves.

5. Equatorial Hartmann layer

The length scales for the equatorial Hartmann layer are dictated by the outer-sphere boundary shape (3.8) in the immediate vicinity of E_o and the form of the shear layer equations (3.5*c*). Together they suggest the change of variables

$$1 - l = \alpha_i^{-1} \mathscr{M}^{-1/3}\, \tau, \quad n = -\alpha_i^{-1/2} \mathscr{M}^{-1/6}\, \rho, \tag{5.1a, b}$$

for which the boundary $\mathscr{S}_o$: $n = n_o(l)$ (see (3.8*c*)) is transformed to

$$\xi := \rho + \tau^2 = 0. \tag{5.2}$$

The length scales of the equatorial boundary layer are therefore $|1 - l| = O(M^{-1/3})$ and $n = O(M^{-1/6})$ (or equivalently $r_o - s = O(M^{-2/3})$), as indicated on figure 7. With

these estimates the coefficient $(1/s)(\partial s/\partial l)$ (3.5c) on the right-hand side of (3.5a) is $O(M^{-1/3})$. Therefore, the term on the right-hand side of (3.5a) is smaller than the large derivatives on the left-hand side by a factor $O(M^{-2/3})$ and may clearly be neglected, leaving

$$\frac{\partial V_\pm}{\partial \tau} \mp \frac{\partial^2 V_\pm}{\partial \rho^2} = 0. \tag{5.3}$$

The simplest way to formulate our boundary layer problem is to solve on the infinite interval $-\infty < \tau < \infty$ which includes the other half of the boundary layer in the southern hemisphere $z < 0$. In this way our symmetries imply that $V_\pm$ can be defined in terms of a single function $\Theta(\rho, \tau)$, which solves the diffusion equation

$$\frac{\partial \Theta}{\partial \tau} = \frac{\partial^2 \Theta}{\partial \rho^2} \quad \text{on} \quad \rho > -\tau^2 \tag{5.4}$$

as follows:

$$V_\pm(\rho, \tau) = r_o[1 + \Omega_S(0)]\,[1 - \Theta(\rho, \pm\tau)]. \tag{5.5}$$

The idea is simply that the value of V_- being advected in the shear layer down towards the equatorial Hartmann layer is given by $r_o[1 - \Omega_S(0)]$ as $\tau \uparrow \infty$, namely the leading-order approximation of it for $n = O(M^{-1/6})$. This provides our initial value unity for Θ as $\tau \downarrow -\infty$. It also provides our boundary condition as $\rho \uparrow \infty$. Since both B and Ω vanish on the boundary, our diffusion equation (5.4) must be solved subject to the boundary conditions

$$\Theta \begin{cases} = 1 & \text{on the outer sphere } \rho = -\tau^2 \\ \to 0 & \text{as} \quad \rho \uparrow \infty, \end{cases} \tag{5.6}$$

and the initial condition

$$\Theta = 0 \quad \text{for} \quad \rho > -\tau^2 \quad \text{as} \quad \tau \downarrow -\infty. \tag{5.7}$$

In order to make analytic progress, it is helpful use ξ (see (5.2)) and τ as our dependent variables rather than ρ and τ. Then in place of (5.4), Θ satisfies

$$\frac{\partial \Theta}{\partial \tau} + 2\tau \frac{\partial \Theta}{\partial \xi} = \frac{\partial^2 \Theta}{\partial \xi^2} \quad \text{on} \quad \xi > 0. \tag{5.8}$$

We see at once that the large negative-τ solution has the asymptotic form

$$\Theta = \exp(2\tau\xi) \quad \text{as} \quad \tau \downarrow -\infty. \tag{5.9}$$

Here the exponential simply defines a very thin boundary layer, which for our MHD problem corresponds to the Hartmann layer associated with V_- as it approaches the equator in the shear layer from above. As τ increases, the boundary layer width, $O(-1/\tau)$, thickens. Relative to the latitude $\lambda = \sin^{-1}(z/r_o)$, this corresponds to the radial width of the Hartmann layer thickening proportional to $O(|\lambda M|^{-1})$. The thickening stops at width $O(M^{-2/3})$, when $\lambda = O(M^{-1/3})$, which defines the dimensions of the equatorial Hartmann layer as illustrated in figure 7.

The layer detaches from the boundary at $\tau = 0$ and for large positive τ becomes the shear layer in the neighbourhood of the $\mathscr{C}$-line $\rho = 0$ or equivalently $\xi = \tau^2$. There it has the asymptotic form

$$\Theta = \frac{1}{2}\,\mathrm{erfc}\left(\frac{\rho - \delta}{\sqrt{4\tau}}\right) \quad \text{as} \quad \tau \uparrow \infty \tag{5.10}$$

on $-\tau^2 < \rho < \infty$, where the constant δ of order unity is determined by the solution. To understand the nature of (5.10), we note that with $\delta = 0$ it is the solution of the diffusion equation (5.4) on the infinite interval $-\infty < \rho < \infty$ subject to the initial conditions $\Theta = 0$ on $\rho > 0$ and $\Theta = 1$ on $\rho \leqslant 0$ at $\tau = 0$. This is exactly the boundary condition which we employed at $l = 1$ in the previous § 4, to solve for the free shear layer. The point that we wish to stress is that, when we match the shear layer solution to the equatorial Hartmann layer solution, the shear layer is effectively triggered on the equator at $\rho = \delta$ rather than at $\rho = 0$. In other words, the effective $\mathscr{C}$-line is the $\mathscr{C}_M$-line, which intersects the equatorial plane at

$$n = -\alpha_i^{-1/2} \mathscr{M}^{-1/6} \delta \; ; \tag{5.11a}$$

it determines

$$(r_o - r_M)/r_M = \mathscr{M}^{-2/3} \delta \tag{5.11b}$$

entirely in terms of the local Hartmann number (2.2) appropriate to the equatorial Hartmann layer. We relegate the details of the calculation to the Appendix but note that complete solution (A1) and (A2) yields the result (A12), (A13). From them we deduce

$$\delta = 2 \int_0^\infty \frac{[\mathrm{Ai}(\sigma)]^2 + \sqrt{3}\mathrm{Ai}(\sigma)\mathrm{Bi}(\sigma)}{[\mathrm{Ai}(\sigma)]^2 + [\mathrm{Bi}(\sigma)]^2} \, \mathrm{d}\sigma \approx 1.2551, \tag{5.11c}$$

where Ai and Bi are the usual Airy functions.

The solution (A1), (A2) may also be used to determine the angular velocity

$$\Omega(\rho) = [1 + \Omega_S(0)]\,[1 - \Theta(\rho, 0)] \tag{5.12a}$$

on the equatorial plane, where

$$\Theta(\rho, 0) = \int_0^\infty \left\{ \mathrm{Ai}(\sigma) \left[\frac{\mathrm{Ai}(\rho + \omega^{-1}\sigma)}{\mathrm{Ai}(\omega^{-1}\sigma)} + \frac{\mathrm{Ai}(\rho + \omega\sigma)}{\mathrm{Ai}(\omega\sigma)} \right] + \mathrm{Ai}(\rho + \sigma) \right\} \mathrm{d}\sigma \tag{5.12b}$$

in which $\omega = \exp(\mathrm{i}2\pi/3)$. We plot Ω on figure 8 using the value

$$\Omega_S(0) = 0.4147\ldots \quad \text{for the case} \quad \zeta_i = 0.35 \tag{5.13}$$

determined by the free shear boundary layer calculation reported in § 4. The corresponding values of the angular velocity computed from the full numerical integrations at finite M are also portrayed for comparison.

In order to make a more faithful comparison with the shear layer boundary layer solution and the numerics, we take into account the displacement thickness determined by (5.11) in portraying the finite-M results in figures 9 and 10 below. By that we mean that each finite-M numerical solution is determined as a function of the shear layer boundary layer coordinates (l_M, n_M) defined by (3.3) which are based on the $\mathscr{C}_M$-line defined by $A_M = 1/2r_M$, where r_M given by (5.11b). At any given point in the shear layer, we note that $l - l_M$ is small, $O(M^{-2/3})$, so that the distinction between l_M and l is unimportant, while correct to lowest order we have

$$\begin{aligned} n - n_M &= -\left(\frac{r_o}{2}\right)^{1/3} \left(\frac{2}{\alpha_i}\right)^{1/2} M^{-1/6} \delta \\ &\approx -1.4101 M^{-1/6} \quad \text{for the case} \quad \zeta_i = 0.35, \end{aligned} \tag{5.14}$$

which though small is relatively large and significant.

In figure 9, we redraw the equatorial plot of Ω against n at $l = 1$ displayed in figure 5(a). Now each finite-M solution is plotted against n_M at $l_M = 1$, whereas the

M/r_o^2	100	1000	10000	Asymptotic
$n_{\max}$	−1.95	−1.40	−1.12	−0.77
$\rho_{\max}$	3.74	3.94	4.63	
$\rho_{S\max}$	1.48	2.17	3.18	

TABLE 1. The location of the finite-M maxima of Ω in terms of the boundary layer coordinates $n_{\max}$, $\rho_{\max}$. The asymptotic boundary layer value $n_{\max} = -0.77$ is cast in terms of the equatorial Hartmann layer coordinate $\rho_{S\max}$.

asymptotic solution is left untouched. This plot is most revealing as it confirms that corrections arising from the displacement thickness give excellent agreement between the shear layer solution and the full numerics outside the thin equatorial Hartmann layer. Though good comparisons of Ω inside the equatorial Hartmann layer are also evident in figure 8, the lack of a clear asymptotic trend for large ρ can be attributed to the fact that we are not yet in a true asymptotic regime. This is highlighted by noting the locations $n = n_{\max}$ at which Ω (full numerics) and $1 + \Omega_S$ (the shear layer) are maximum on the equatorial plane and translating them into the boundary layer coordinate values $\rho = \rho_{\max}$ and $\rho_{S\max}$ respectively. We list these values in table 1. Thus the location where the curvature of the free shear layer solution is important remains within the equatorial Hartmann layer even for the largest value of M considered. The implication is that quadratic, as well as linear effects, are influencing the large-ρ trends visible in figure 8.

On figure 10, we repeat the plots of figure 6 but with one crucial difference: each of the finite-M numerical solutions is plotted versus l_M on its $\mathscr{C}_M$-line $n_M = 0$. Though necessary differences between the shear layer solution and the full numerics remain in the equatorial Hartmann layer near $l_M = 1$, the comparisons outside are far better than those reported in figure 6. Yet again the results confirm the reliability of the notion of a displacement thickness that we have developed.

Some bumps on the Ω-profiles can be identified near $l_M = 1$ on figure 10, where the $\mathscr{C}_M$-line $n_M = 0$ enters the equatorial Hartmann layer. These bumps were absent on the $\mathscr{C}$-lines $n = 0$ portrayed in figure 6. Thus these contrasting features provide information about the nature of the equatorial Hartmann layer at finite M.

6. Discussion

We have successfully resolved the mainstream and boundary layer structures, obtaining their solutions by a combination of analytical and numerical techniques. The cornerstone of our development has been the successful implementation of numerical methods to solve the unusual coupled advection–diffusion equations that govern the shear layer. The solution of that problem clearly accounts in a semi-analytic way (certainly in the narrow gap limit) for the phenomenon of super-rotation. The numerical solution of the complete governing equations at large M is also difficult. That results were obtained at sufficiently large M to obtain convincing agreement with the asymptotic theory was most reassuring.

From a more general point of view, the mechanism for super-rotation described in § 4.2 hinges on the electric current flow in our system. Essentially, negative electric current flows outwards along field lines in the polar region $\mathscr{P}$ (total J_{out} see (2.14)), it

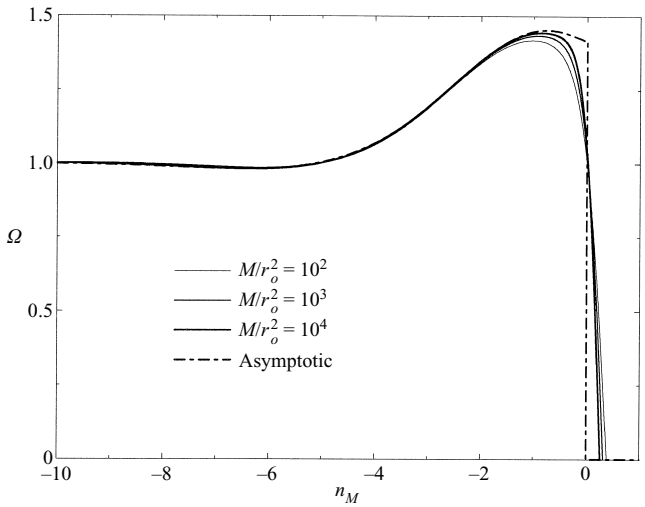

FIGURE 9. As in figure 5(*a*), except that Ω at each M is plotted *vs.* n_M at $l_M = 1$. Note that $n_M \equiv n$ for the asymptotic shear layer solution.

is carried down to the equator in the outer-sphere Hartmann layer and returns to the inner sphere along the $\mathscr{C}$-line shear layer. A substantial fraction J_{source} (see (3.13)), however, reaches the equatorial Hartmann layer, which effectively acts as a current source and thus as the essential mechanism leading to super-rotation. In particular, the current emitted from the source largely follows the $\mathscr{C}$-line but spreads laterally through diffusion. This leads to a Lorentz force, which is largely accelerating on the equatorial side and de-accelerating on the polar side. This phenomenon is well known in the context of channel flow, where current injected from electrodes, which are embedded in the channel boundary, attempts to follow the magnetic field lines (see Müller & Bühler 2001, figures 7.1 and 7.2).

Starchenko (1997) notes that the Hartmann jump condition (2.2*d*) can imply super-rotation in the fluid adjacent to the inner sphere, when $(1/s_i B_{ri})(\partial B/\partial r)_i > 0$ (see his equation (81)). That this is likely to happen in the equatorial region $\mathscr{E}$ is clear from the contours of constant sB inside the solid conducting sphere near the equator seen in our figure 1. Since Ω is constant on meridional field lines, small super-rotation, $O(M^{-1})$, should be present throughout $\mathscr{E}$. The Hartmann jump is stronger, $O(M^{-1/2})$, near Q at the end of the $\mathscr{C}$-line shear layer. Nevertheless, our analysis of the shear layer shows that current diffusion in the shear layer has the dominating $O(1)$ effect and that the Hartmann jump can be ignored. Thus Starchenko's argument is not able to account for the $O(1)$ super-rotation that we find and explain.

Hollerbach (2000) also considers numerically the cases in which the inner and outer spheres are either both insulating or both conducting. The key to understanding the dynamics of these configurations is the role played by the Hartmann layers. We limit our discussion to the later more dramatic conducting case for which the inner-sphere Hartmann layer has solution (2.12), while a similar solution pertains to the outer boundary. Now for our inner conducting and outer insulating problem, we can accept a small $O(M^{-1})$ azimuthal magnetic field B by virtually locking the angular velocity Ω of the mainstream flow to the rotation $\Omega = 1$ of the inner conducting sphere. When both the inner and outer solid spheres are conducting, that is no longer possible. Now

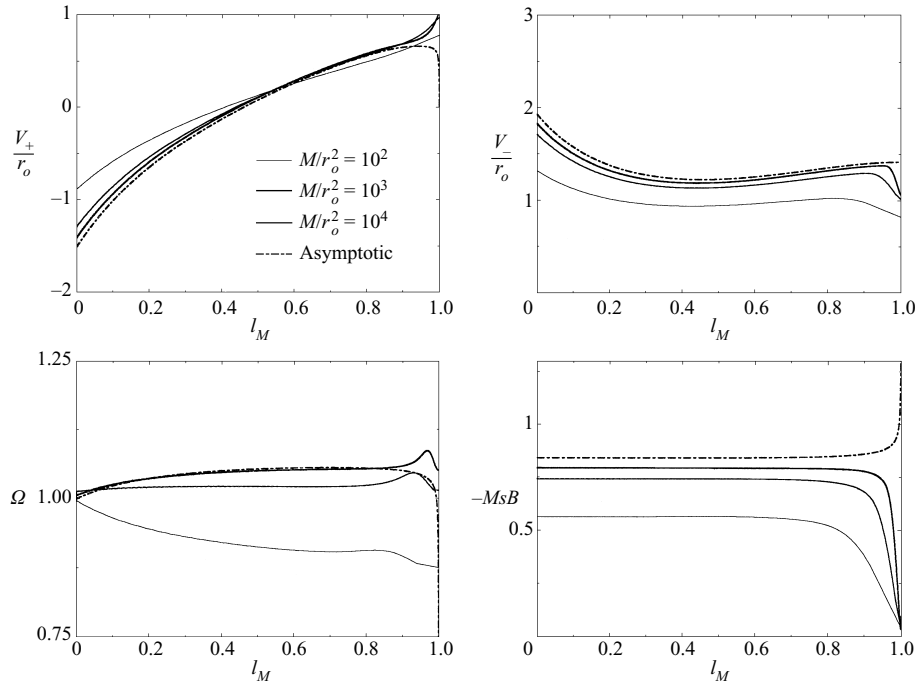

FIGURE 10. As in figure 6 (note that the Ω scale has been stretched), except that solutions at each M are plotted *vs.* l_M on each $\mathscr{C}_M$-line $n_M = 0$. Note that $l_M \equiv l$ for the asymptotic shear layer solution.

both Hartmann layers have to accept an $O(1)$ jump in the angular velocity, which is only achieved with a corresponding azimuthal magnetic field $B = O(1)$ (see (2.12*d*)). A correct physical explanation for this increase in magnitude of B was provided by Hollerbach (2000) in interpreting his numerical results for different boundary conditions. His explanation relies on two facts. First, for insulating outer boundaries, the electric current J_{out} flowing outwards along meridional magnetic field lines in the mainstream polar region $\mathscr{P}$ is transmitted to the equator inside the outer-sphere Hartmann layer, as we repeatedly stress. This leads to Lorentz forces that can achieve $O(1)$ angular velocity jumps for relatively small azimuthal magnetic fields. Secondly, for conducting outer boundaries, the electric currents leak out of the Hartmann layers into the solid conductor. So to obtain a sufficiently strong Lorentz force in the Hartmann layer capable of supporting the angular velocity jump, the entire current flow in the system must be increased by a large factor, $O(M)$.

We tentatively propose the following scenario for Hollerbach's conducting inner and outer spheres. In the mainstream, sB continues to be constant on meridional magnetic field lines, being zero in the equatorial region $\mathscr{E}$ and order unity ($O(1)$) in the polar region $\mathscr{P}$ (i.e. $O(M)$ larger than for our case (2.8*b*)). Then by the magnetic induction equation (2.3*b*), the resulting Ω is also $O(1)$ in the mainstream outside the shear layer $\mathscr{C}$ but no longer constant on field lines in the polar region $\mathscr{P}$. Furthermore, we propose that, unlike our problem, the bulk of the relatively large $O(1)$ electric current flow is returned in the mainstream polar region $\mathscr{P}$. This is accompanied by sB decreasing to zero as the $\mathscr{C}$-line is approached from the polar side. Provided that the decrease is linear, we estimate that the magnetic field, inside the shear layer

on its $O(M^{-1/2})$ width, is $O(M^{-1/2})$. This means that his Alfvén variables would be $O(M^{1/2})$ larger than ours leading to a stronger super-rotation of magnitude $O(M^{1/2})$. This magnitude compares favourably with Hollerbach's (2000) numerical estimate of $O(M^{0.6})$. However, the general picture for the super-rotation mechanism in the shear layer, that we have proposed, should still apply, though, interestingly, this is despite the fact that only a relatively small fraction, $O(M^{-1/2})$, of the entire $O(1)$ current flow follows the $\mathscr{C}$-line. We stress that all these estimates stem from a preliminary theory, which forms the basis for a complete analysis of the problem at present in progress.

Considering that Roberts (1967*b*) had obtained, such a long time ago, an analytic solution for the case of an equatorial Hartmann layer with magnetic field lines bending towards the walls on leaving the equatorial plane, it is surprising that the alternative problem with the field lines bending away does not appear to have been addressed. Though the method of solution in the two cases is essentially the same, the specific details and answer are different. Significantly our derivation of the displacement width δ^* for the free shear layer enabled us to make considerable improvements with our quantitative comparisons with the full numerics. This leads us to believe that we have resolved correctly all the major boundary layer processes.

It should be stressed that a key feature which enables progress to be made with the equatorial boundary layer solution in § 5 is the insulating boundary condition that requires $B = 0$. By implementation of the zero boundary condition on both V_+ and V_-, the two diffusion equations (5.3) remain uncoupled. For more general boundary conditions that is not the case. Whatever the boundary conditions, the corresponding equatorial boundary layer solution only leads to low-order corrections; the dominant leading-order results are not dependent on this layer.

E. D. visited the School of Mathematical Sciences at the University of Exeter in September 1999, while A. M. S. visited IPGP in November 2000; both E. D. and A. M. S. wish to thank their respective host institutions for their hospitality and support. A. M. S. acknowledges support of PPARC grant GR/L40922 and INTAS grant 99-00348, through which he has benefited from discussions with Dr S. Starchenko. E.D. would like to thank Professor Y. Brenier and Dr D. Pissarenko for stimulating discussions about the shear layer problem (3.5), (3.10)–(3.12), while we are all grateful to Dr R. Hollerbach for useful discussions. Numerical resolution of this system was achieved on a Cray SV1 computer at the C.C.R.-Jussieu, whereas solutions of the complete governing equations where computed at the Service Commun de Calcul Intensif de l'Observatoire de Grenoble.

Appendix. The equatorial Hartmann layer solution

We adapt Roberts' (1967*b*) solution to a related problem of Hartmann flow down a circular pipe with a uniform transverse magnetic field applied (see also Waechter 1969). The common feature is the existence of points on the boundary at which the magnetic field is tangent. The problems differ in that our field lines bend away from the boundary into the fluid as the equator is left, whereas his effectively approach the boundary. Put another way, his problem would have been equivalent to ours if his fluid were outside rather than inside the pipe! So though the techniques involved in our solution are similar to his, the details are quite different.

Roberts' (1967*b*) solution relies on the preliminary change of variables

$$\Theta(\xi,\tau) = \exp\left(\tau\xi - \tfrac{1}{3}\tau^3\right)\Phi(\xi,\tau), \tag{A 1a}$$

which satisfies (5.8) when

$$\frac{\partial^2 \Phi}{\partial \xi^2} - \xi \Phi = \frac{\partial \Phi}{\partial \tau}. \tag{A 1b}$$

Guided by Roberts' (1967*b*) analysis, we demonstrate that the solution of the problem specified by (5.4), (5.6) and (5.7) is

$$\Phi = \Phi_{-1} + \Phi_0 + \Phi_1, \tag{A 2a}$$

where

$$\Phi_n = \int_0^\infty \frac{\mathrm{Ai}(\sigma)\mathrm{Ai}(\xi + \omega^n \sigma)}{\mathrm{Ai}(\omega^n \sigma)} \exp(\omega^n \tau \sigma)\, \mathrm{d}\sigma \quad (\omega = \exp(\mathrm{i}2\pi/3)); \tag{A 2b}$$

here ω^{-1}, 1 and ω are the cube roots of unity. Note also that $\Phi_{-1} = \Phi_1^*$ for real ξ and τ, where the star denotes the complex conjugate. It is a trivial matter to verify that (A 2) satisfies (A 1*b*) by direct substitution. It only remains to show that the boundary conditions (5.6) and initial conditions (5.7) (also (5.9)) are met.

A key step in establishing the result (A 2) is to note that the boundary condition (5.6) $\Theta = 1$ at $\xi = 0$ is met simply because of the identity

$$\int_0^\infty \mathrm{Ai}(\sigma) \left[\exp\left(\omega^{-1}\tau\sigma\right) + \exp(\tau\sigma) + \exp(\omega\tau\sigma)\right] \mathrm{d}\sigma = \exp\left(\tfrac{1}{3}\tau^3\right). \tag{A 3a}$$

This is readily established using the power series representations of the exponentials and the identity

$$3\int_0^\infty \sigma^{3m}\mathrm{Ai}(\sigma)\, \mathrm{d}\sigma = \frac{(3m)!}{3^m m!} \quad \text{for} \quad m = 0, 1, 2, 3, \ldots\ . \tag{A 3b}$$

Here the case $m = 0$ is given by Abramowitz & Stegun (1964, equation (10.4.47)), while the cases $m \geqslant 1$ follow by mathematical induction using the property $\sigma\mathrm{Ai}(\sigma) = \mathrm{d}^2\mathrm{Ai}(\sigma)/\mathrm{d}\sigma^2$ and integrating by parts; Roberts (1967*b*) obtained a comparable result (his equation (49)) using integral properties of Bessel functions.

Since all the Airy functions in (A 2*b*) decay exponentially for large positive σ, it is self-evident that the solution (A 2*a*) satisfies the boundary condition $\Phi \to 0$ as $\xi \uparrow \infty$.

As a preliminary step to establish the initial condition (5.7) we note the alternative form

$$\Phi = \tilde{\Phi}_{-1} + \tilde{\Phi}_0 + \tilde{\Phi}_1, \tag{A 4a}$$

where

$$\tilde{\Phi}_n = \int_{\omega^{-n}v_s}^\infty \frac{\mathrm{Ai}(\sigma)\mathrm{Ai}(\xi + \omega^n \sigma)}{\mathrm{Ai}(\omega^n \sigma)} \exp(\omega^n \tau \sigma)\ \mathrm{d}\sigma, \tag{A 4b}$$

where v_s is a positive real chosen for our convenience in (A 6) below. In obtaining (A 4), we have cancelled the contributions from each Φ_n-integral from 0 to $\omega^{-n}v_s$ on the basis of the identity $\omega^{-1}\mathrm{Ai}(\omega^{-1}v) + \mathrm{Ai}(v) + \omega\mathrm{Ai}(\omega v) = 0$ (see Roberts 1967*b*, figure 3 and discussion below it). The idea is to evaluate the remaining integrals (A 4*b*) by the method of steepest descents. For $\tilde{\Phi}_1$, we make the change of variables $\sigma = \omega^{-1}v$, use the appropriate asymptotic form for Ai in the relevant sector on the complex plane (cf. Roberts 1967*b*, figure 2 in the $n = -1$ context) to obtain the asymptotic representation

$$\tilde{\Phi}_1 \sim \int_{v_s}^{v_s + \mathrm{i}\infty} \frac{\exp(g(v))}{\mathrm{i}\sqrt{4\pi}\,(v + \xi)^{1/4}}\, \mathrm{d}v \tag{A 5a}$$

for $-\tau \gg 1$, where

$$g(v) = \tfrac{2}{3}\left[2v^{3/2} - (v+\xi)^{3/2}\right] + v\tau. \tag{A 5b}$$

Like Roberts (1967), we start the integration from the saddle point v_s, which solves

$$g'(v_s) = 2v_s^{1/2} - (v_s+\xi)^{1/2} + \tau = 0. \tag{A 6a}$$

For $\xi \ll \tau^2$, it determines

$$v_s^{1/2} \sim -\tau\left(1 + \frac{\xi}{2\tau^2}\right), \quad (v_s+\xi)^{1/2} \sim -\tau\left(1+\frac{\xi}{\tau^2}\right), \tag{A 6b}$$

from which we obtain

$$g(v_s) \sim \tfrac{1}{3}\tau^3 + \tau\xi. \tag{A 7a}$$

The steepest-descent integration off the saddle in the positive imaginary direction then determines

$$\tilde{\Phi}_1 \sim \tfrac{1}{2}\exp\left(\tfrac{1}{3}\tau^3 + \tau\xi\right). \tag{A 7b}$$

Then the sum $\tilde{\Phi}_{-1} + \tilde{\Phi}_1$ dominate the contributions to $\tilde{\Phi}$ and together with (A 1) yield the initial boundary layer form (5.9) for $-\tau\xi = O(1)$. This conclusion is important as it finally establishes our claim that (A 2) is the solution to our diffusion problem.

To obtain the large positive-τ behaviour we first evaluate the dominant contribution Φ_0, again using the large-argument asymptotic representation for Ai. It yields

$$\Phi_0 \sim \int_0^\infty \frac{\exp(f(\sigma))}{\sqrt{4\pi}\,(\sigma+\xi)^{1/4}}\,\mathrm{d}\sigma \tag{A 8a}$$

for $\tau \gg 1$, where

$$f(\sigma) = -\tfrac{2}{3}(\sigma+\xi)^{3/2} + \sigma\tau. \tag{A 8b}$$

The saddle point σ_s, which solves

$$f'(\sigma_s) = -(\sigma_s+\xi)^{1/2} + \tau = 0 \quad \text{is} \quad \sigma_s = \tau^2 - \xi \equiv -\rho. \tag{A 9a}$$

It determines

$$f(\sigma_s) \sim \tfrac{1}{3}\tau^3 - \tau\xi. \tag{A 9b}$$

For $\rho = O(\tau^{1/2})$, asymptotic evaluation in the neighbourhood of the saddle yields

$$\Phi \sim \tfrac{1}{2}\exp\left(\tfrac{1}{3}\tau^3 - \tau\xi\right)\operatorname{erfc}\left(\frac{\rho}{\sqrt{4\tau}}\right). \tag{A 10}$$

With (A 1*a*) this determines the leading-order approximation to the asymptotic solution (5.10).

To obtain the next-order term we consider Φ_1, which we evaluate using the large-argument expansion of $\mathrm{Ai}(\xi+\omega\sigma)$ alone. It gives

$$\Phi_1 \sim \int_0^\infty \frac{\mathrm{Ai}(\sigma)}{\mathrm{Ai}(\omega\sigma)}\,\frac{\exp(h(\sigma))}{\sqrt{4\pi}\,(\xi+\omega\sigma)^{1/4}}\,\mathrm{d}\sigma, \tag{A 11a}$$

where

$$h(\sigma) = -\tfrac{2}{3}(\xi+\omega\sigma)^{3/2} + \omega\sigma\tau. \tag{A 11b}$$

Since the ratio of the two Airy functions decays exponentially as $\sigma \uparrow \infty$, we expand (A 11*b*) on the basis that $\rho = O(\tau^{1/2})$, $\tau \gg 1$ and $\sigma = O(1)$. To that end, we write $\xi = \tau^2 + \rho$ and retain the first three terms in the binomial expansion of $[\tau^2 + (\rho+\omega\sigma)]^{3/2}$.

It yields

$$h(\sigma) \sim \tfrac{1}{3}\tau^3 - \tau\xi - \frac{(\rho+\sigma\omega)^2}{4\tau}. \tag{A 12}$$

Here the terms proportional to σ are negligible, when $\sigma = O(1)$. In this way, we obtain the leading-order result

$$\Phi_1 \sim \frac{\delta_1}{\sqrt{4\pi\tau}} \exp\left(\tfrac{1}{3}\tau^3 - \tau\xi - \frac{\rho^2}{4\tau}\right), \quad \text{where} \quad \delta_n := \int_0^\infty \frac{\mathrm{Ai}(\sigma)}{\mathrm{Ai}(\omega^n\sigma)}\,\mathrm{d}\sigma, \tag{A 13a, b}$$

with $n = 1$.

Finally we note that, for $\rho = O(\tau^{1/2})$, $\tau \gg 1$, our proposed asymptotic solution (5.10) has the Taylor series expansion

$$\frac{1}{2}\,\mathrm{erfc}\left(\frac{\rho-\delta}{\sqrt{4\tau}}\right) \sim \frac{1}{2}\,\mathrm{erfc}\left(\frac{\rho}{\sqrt{4\tau}}\right) + \frac{\delta}{\sqrt{4\pi\tau}}\exp\left(-\frac{\rho^2}{4\tau}\right). \tag{A 14a}$$

This agrees with our results (A 10) and (A 13) when

$$\delta = \delta_{-1} + \delta_1, \tag{A 14b}$$

which with (A 13*b*) reduces to (5.11*c*).

REFERENCES

Abramowitz, M. & Stegun, I. A. 1964 *Handbook of Mathematical Functions*. Dover.

Dormy, E. 1997 Modélisation numérique de la dynamo terrestre. PhD thesis, IPG Paris.

Dormy, E., Cardin, P. & Jault, D. 1998 MHD flow in a slightly differentially rotating spherical shell, with conducting inner core, in a dipolar magnetic field. *Earth Planet. Sci. Lett.* **160**, 15–30.

Ferraro, V. C. A. 1937 Non-uniform rotation of the sun and its magnetic field. *Mon. Not. R. Astron. Soc.* **97**, 458–472.

Glatzmaier, G. A. & Roberts, P. H. 1995 A three-dimensional convective dynamo solution with rotating and finitely conducting inner core and mantle. *Phys. Earth Planet. Inter.* **91**, 63–75.

Hollerbach, R. 1994 Magnetohydrodynamic Ekman and Stewartson layers in a rotating spherical shell. *Proc. R. Soc. Lond.* A **444**, 333–346.

Hollerbach, R. 2000 Magnetohydrodynamical flows in spherical shells. In *Physics of Rotating Fluids* (ed. C. Egbers & G. Pfister), Lecture Notes in Physics, vol. 549, pp. 295–316. Springer (to appear).

Hollerbach, R. 2001 Super- and counter-rotating jets and vortices in strongly magnetic spherical Couette flow. In *Dynamo and Dynamics, A Mathematical Challenge* (ed. P. Chossat, D. Armbruster & I. Oprea). NATO Science Series II, vol. 26, pp. 189–197. Kluwer.

Hollerbach, R. & Skinner, S. 2001 Instabilities of magnetically induced shear layers and jets. *Proc. Roy. Soc. Lond.* A **457**, 785–802.

Kleeorin, N., Rogachevskii, I., Ruzmaikin, A., Soward, A. M. & Starchenko, S. 1997 Axisymmetric flow between differentially rotating spheres in a dipole magnetic field. *J. Fluid Mech.* **344**, 213–244.

Moore, D. W. & Saffman, P. G. 1969 The structure of free vertical shear layers in a rotating fluid and the motion produced by a slowly rising body. *Proc. R. Soc. Lond.* A **264**, 597–634.

Müller, U. & Bühler, L. 2001 *Magnetofluiddynamics in Channels and Containers*. Springer.

Proudman, I. 1956 The almost-rigid rotation of viscous fluid between concentric spheres. *J. Fluid Mech.* **1**, 505–516.

Roberts, P. H. 1967*a* *An Introduction to Magnetohydrodynamics*. Longmans, London.

Roberts, P. H. 1967*b* Singularities of Hartmann layers. *Proc. R. Soc. Lond.* A **300**, 94–107.

Roberts, P. H. 2000 Magnetohydrodnamics and the Earth's core: Selected works of Paul Roberts. In *The Fluid Mechanics of Astrophysics and Geophysics*, vol. 9 (ed. A. M. Soward). Gordon and Breach (to appear).

Starchenko, S. V. 1997 Magnetohydrodynamics of a viscous spherical layer rotating in a strong potential field. *JETP* **85** (6), 1125–1137 (*Zh. Eksp. Teor. Fiz.* **112**, 2056–2078).

Starchenko, S. V. 1998*a* Magnetohydrodynamic flow between insulating shells rotating in strong potential field. *Phys. Fluids* **10**, 2412–2420.

Starchenko, S.V. 1998*b* Strong potential field influence on slightly differentially rotating spherical shells. *Studia Geoph. Geod.* **42**, 314–319.

Stewartson, K. 1966 On almost rigid rotation. Part 2. *J. Fluid Mech.* **26**, 131–144.

Vidale, J. E., Dodge, D. A. & Earle, P. S. 2000 Slow differential rotation of the Earth's inner core indicated by temporal changes in scattering. *Nature* **405**, 445–448.

Waechter, T. T. 1969 Steady magnetohydrodynamic flow in an insulating circular pipe. *Mathematica* **16**, 249–262.